DISS. ETH NO. 17594

The Evolution of Disk Galaxies in the COSMOS Survey

A dissertation submitted to

ETH ZÜRICH

for the degree of

Doctor of Sciences

presented by

MARK THOMAS SARGENT

Dipl. phys. ETH Zürich

born on September 17th, 1979

citizen of Lüterswil-Gächliwil (SO), Switzerland and Canada

accepted on the recommendation of

Prof. Dr. C. Marcella Carollo, examiner
Prof. Dr. Arnold Benz, co-examiner
Prof. Dr. Lucio Mayer, co-examiner

2007

Cover illustration:

Front cover – Drawings of M51 (top) and M99 (bottom), published in 1850 by the Earl of Rosse [99] based on observations with the 72" telescope *'Leviathan of Parsonstown'* in Birr, Co. Offaly, Ireland.

Back cover – Sketch of M33 made by the same author(s).

Acknowledgements

I am grateful to my supervisor Prof. C. Marcella Carollo for providing a thesis topic which I always felt privileged to pursue even when the daily drudgery of work proved particularly vexing.
I am especially indebted to the people who on many occasions took time to give me advice. Apart from my supervisor these included Claudia, Cristiano, Pascal, my office mates and Prof. Simon Lilly. It is a pleasure to thank Anna, Claudia, Oliver, Peder, Robert and Sebastiano for useful suggestions leading to the correction of many a line of faulty code in misbehaving computer programs. I also appreciated the help of the IT support team of the Physics Department and their willingness to cater for special software needs.
I enjoyed working together with Marcel to prepare questions both for exercises and physics quiz shows and it was also nice to occasionally happen across Padelis and Francesco both in the gym and in the empty corridors of the institute on weekends.

Those closest to my desk – my office mates Anna, Christian, Oliver, Paweł, Robert, Sebastiano and Thomas as well as regular visitors to our office, Annalisa and Simone – will be fondly remembered for shared laughter, confusion and conversations.
Those closest to my heart are assured my deep gratitude for their unfailing support and unconditional backing which saw me through the ups and downs of the Ph.D. studies.

Zurich, December 2007 Mark Sargent

Contents

Acknowledgements **iii**

Contents **viii**

List of Figures **xii**

List of Tables **xiv**

Abstract **xv**

Kurzfassung **xvii**

1 Introduction **1**

1.1 Historical perspective 1

1.2 Hierarchical galaxy formation in a (Λ)CDM universe 2

1.3 Current observational status 6

1.4 Content of this thesis 7

2 Measuring structural properties of distant galaxies **11**

2.1 Two-dimensional fits of analytic surface brightness profiles 12

2.1.1 Tools of the trade 15
2.1.2 Two-dimensional GIM2D fits 17
2.1.3 Reliability of parametric GIM2D fits 20
2.2 Morphological classification of COSMOS galaxies with ZEST 23
2.2.1 Non-parametric quantification of galaxy structure 25
2.2.2 Principal Component Analysis with ZEST 27
2.2.3 ZEST calibration with 56,000 $I < 24$ COSMOS galaxies 29
2.2.4 Summary of the ZEST PC_1-PC_2-PC_3 classification scheme & grid . 34
2.2.5 The performance & reliability of ZEST 36
2.2.6 The advantages of classification with ZEST over other approaches . 44
2.3 Summary 47

3 The evolution of the number density of large disk galaxies 49

3.1 Introduction 49
3.2 Data analysis 51
3.2.1 The initial catalog: 16,538 ACS-selected galaxies 51
3.2.2 Deletion of sources from the original ACS-based catalog 52
3.3 The ZEST morphological classification of our COSMOS sample 53
3.4 The Evolution of the Size Function of disk galaxies in COSMOS 62
3.4.1 ZEBRA photometric redshifts 62
3.4.2 Derivation of the Size Function & assessment of completeness 63
3.4.3 Errors 66
3.4.4 Comparison with the local SDSS galaxy population 66
3.5 Results & discussion 70
3.6 Conclusions 76

4 The role of environment in the evolution of COSMOS disk galaxies 79

4.1 Introduction 79

4.2 Observational data 80

4.2.1 Description of the sample of galaxies 80

4.2.2 Surface brightness fits with GIM2D 82

4.2.3 Completeness 83

4.3 Opacity, surface brightness & histories of star formation since $z \sim 1$ 85

4.3.1 Opacity 85

4.3.2 Surface brightness 91

4.3.3 Star formation histories 102

4.4 The bivariate size-luminosity function 111

4.4.1 Definition 111

4.4.2 Analytic parametrization of the bivariate size-luminosity function . . 116

4.4.3 Luminosity-dependent evolution of disk galaxy sizes at $z < 1$ 121

4.5 The role of environment 126

4.5.1 Estimation of environmental density 126

4.5.2 Results 128

4.6 Discussion & conclusions 130

4.7 Appendix: Errors on $\mu(B)$, $M(B)$, $r_{1/2}$ & $(u^* - V)_0$ 131

5 Summary & Outlook **135**

Appendix **139**

A.1 A local galaxy sample redshifted to $z \sim 0.7$ 139

A.2 The COSMOS Survey 142

A.2.1 Hubble Space Telescope observations 144

A.2.2 Ancillary multi-wavelength observations of the COSMOS field 146

Bibliography **161**

Publications **163**

Curriculum vitæ **165**

List of Figures

2.1 Sérsic profiles 13

2.2 Stamps of an early- & late-type galaxy used for GIM2D & GALFIT tests . 16

2.3 Dependence on parameter initialization for a late-type object 17

2.4 Dependence on parameter initialization for an early-type object 18

2.5 Dependence of Δn on input magnitude 21

2.6 Dependence of $\Delta R_{1/2}$ on input magnitude & size 22

2.7 Variation of best-fit GIM2D parameter values with PSF 23

2.8 Dependence of A, M_{20}, G, C & ϵ on S/N 28

2.9 Relations between the non-parametric quantities 30

2.10 Variance of ZEST principal components 32

2.11 Pictorial representation of ZEST classification grid 33

2.12 Slices through 3-dimensional ZEST principal component space 36

2.13 Schematic 3D view of the ZEST classification grid 43

2.14 Results of applying ZEST to a set of local galaxies 44

2.15 $\langle \Delta(PC) \rangle = \sum_i |PC_i - PC_{i,0}|)/3$ as a function of S/N 45

2.16 Displacement in 3-D ZEST PC-space as a function of S/N 46

2.17 Overlap of parameter distributions among different ZEST classes 47

3.1 Satisfactory fits with high χ^2_{GIM2D} due to internal structure 53

3.2a Example GIM2D fits of ZEST type 1 galaxies 55

3.2b Example GIM2D fits of ZEST type 2.3 galaxies 55

3.2c Example GIM2D fits of ZEST type 2.2 galaxies 56

3.2d Example GIM2D fits of ZEST type 2.1 galaxies 56

3.2e Example GIM2D fits of ZEST type 2.0 galaxies 57

3.2f Example GIM2D fits of ZEST type 3 galaxies 57

3.3 Correlations between GIM2D & ZEST parameters 58

3.4 Distribution of Sérsic indices for different ZEST types 59

3.5 Distribution of galaxy sizes for different ZEST types 59

3.6 $M(B)$ vs. z for Cycle 12 galaxies. 61

3.7 Size-luminosity diagrams for disk galaxies at $z < 1$. 64

3.8 Evolution of the size function since $z \sim 1$ (all disk galaxies) 67

3.9 Evolution of the size function since $z \sim 1$ (diff. B/D-categories) 68

3.10 Comparison of physical properties of $\mathrm{SDSS}_{z=0.7}$ & COSMOS galaxies . . 69

3.11 $\mathrm{SDSS}_{z=0.7}$ & COSMOS size functions at $z \sim 0.7$ (all disk galaxies) 72

3.12 $\mathrm{SDSS}_{z=0.7}$ & COSMOS size functions at $z \sim 0.7$ (diff. B/D-categories) . 73

3.13 Evolution of the relative number densities of disk galaxies since $z \sim 1$ . . 74

3.14 Evolution of the relative number densities in diff. B/D-categories 75

4.1 Illustration of sample completeness 84

4.2 Size-luminosity diagram for $\mathrm{SDSS}_{z=0.7}$ galaxies 86

4.3 Distribution of axis ratios in different B/D-categories 87

4.4 Inclination-dependence of disk surface brightness 88

4.5 Best-fit trend lines to the relation $\mu(B)$ vs. $\log(b/a)$ 90

4.6a Evolution of $\mu(B)$ in different disk galaxy samples ($r_{1/2} \geq 5$ kpc) 92

4.6b Evolution of $\mu(B)$ in different disk galaxy samples ($r_{1/2} \geq 7$ kpc) 93

4.7 Evolution of $\overline{\mu(B)}$ in COSMOS compared with CFRS & GEMS 96

4.8a Evolutionary trends of $\overline{\mu(B)}$ for disk galaxies with $r_{1/2} \geq 5$ kpc 100

4.8b Evolutionary trends of $\overline{\mu(B)}$ for disk galaxies with $r_{1/2} \geq 7$ kpc 101

4.9a Evolution of (u^*-V) for different disk galaxy samples ($r_{1/2} \geq 5$ kpc) . . . 104

4.9b Evolution of (u^*-V) for different disk galaxy samples ($r_{1/2} \geq 7$ kpc) . . . 105

4.10a Tracks of synthetic/real ($r_{1/2} \geq 5$ kpc) galaxies w.r.t. $\Delta M(B)$ & (u^*-V) . 108

4.10b Tracks of synthetic/real ($r_{1/2} \geq 7$ kpc) galaxies w.r.t. $\Delta M(B)$ & (u^*-V) . 109

4.11 Evolution of real/synthetic bulged disks w.r.t. to $\Delta M(B)$ & (u^*-V) . . . 110

4.12a 3-D views of $\Phi(M, \log(r_{1/2}), z)$ (all disk galaxies) 113

4.12b 3-D views of $\Phi(M, \log(r_{1/2}), z)$ (pure disks) 114

4.12c 3-D views of $\Phi(M, \log(r_{1/2}), z)$ (disk galaxies w/ intermediate bulges) . . 115

4.12d 3-D views of $\Phi(M, \log(r_{1/2}), z)$ (bulge-dominated disk galaxies) 116

4.13a Contour plot of biv. size-luminosity fct. (all disk galaxies) 119

4.13b Contour plot of biv. size-luminosity fct. (pure disks) 120

4.13c Contour plot of biv. size-luminosity fct. (disk gal.s w/ intermed. B/D) . 121

4.13d Contour plot of biv. size-luminosity fct. (bulge-dominated disk galaxies) . 122

4.14a Evolution of characteristic sizes in evolving magnitude bins 124

4.14b Evolution of comoving density at characteristic size 125

4.15a Evolution of $\overline{\mu(B)}$ & (u^*-V)-colour as a fct. of δ ($r_{1/2} \geq 5$ kpc) 128

4.15b Evolution of $\overline{\mu(B)}$ & (u^*-V)-colour as a fct. of δ ($r_{1/2} \geq 7$ kpc) 129

A.1 Examples of original & artificially redshifted SDSS galaxy images 140

A.2 Normalization of the luminosity function of the SDSS$_{z=0.7}$ sample 141

A.3 Comparison of COSMOS with other HST surveys 145

List of Tables

2.1 Overview of ZEST morphological classes 24

2.2 Results of the ZEST principal component analysis 31

2.3 COSMOS ZEST classification grid. (Continued on next page.) 34

2.3 *cont.* 35

3.1 Physical properties of the galaxies shown in Figures 3.1 to 3.2f 54

3.2 Distribution of galaxies with z (after application of a $\chi^2_{\rm phz}$-cut) 60

3.3 Distribution of galaxies with z (without a $\chi^2_{\rm phz}$-cut) 60

3.4 Parameters of straight line fits to size functions of COSMOS galaxies 70

3.5 Parameters of straight lines fit to size functions of $\mathrm{SDSS}_{z=0.7}$ galaxies . . . 71

3.6 Normalized number densities of large disk galaxies. 76

4.1 Number of galaxies as a function of redshift and morphological class. 81

4.2 Number of large disk galaxies as a function of z and B/D-category 82

4.3 Best fit values of the opacity parameter C 89

4.4 Evolution of inclination-corrected $\overline{\mu(B)}$ for different COSMOS disk samples 94

4.5 $\overline{\mu(B)}$ (w/ incl. correction) for different disk galaxy categories in the SDSS$_{z=0.7}$ sample 95

4.6 Evolution of $\overline{\mu(B)}$ (uncorrected) for different COSMOS disk samples 97

4.7 $\overline{\mu(B)}$ (uncorr.) for different disk galaxy categories in the SDSS$_{z=0.7}$ sample 98

4.8 Best-fit evolutionary trend to the values of $\overline{\mu(B)}$ 99

4.9 Evolution of the (u^*-V)-colours of COSMOS disk galaxies 103

4.10 (u^*-V)-colours for different simulated SDSS$_{z=0.7}$ disk samples 106

4.11 Parameters of the best-fit trend lines to the evolution of (u^*-V) 106

4.12 Best-fit parameters of the bivariate size-luminosity functions 118

Abstract

In this Ph.D. thesis we study the evolution of the disk galaxy population since redshift $z \sim 1$, i.e., during the last eight billion years. To this purpose we use data from the Cosmic Evolution Survey (COSMOS). COSMOS is currently the largest look-back survey with data from the radio wave band to X-rays acquired in a 2 deg^2 equatorial field (about ten times the area of the moon) in order to study the evolution of the galaxies as a function of environment since $z \sim 3$. The program includes the largest single observational Hubble Space Telescope (HST) project ever carried out. Thanks to the high resolution and the depth of the I-band HST images – the pixel scale of the space-based exposures is 0.4 kpc at $z \sim 1$ – the morphological properties of galaxies at optical wavelengths can be measured for galaxies observed when the universe was less than half as old as it is today.

Two techniques to measure galactic structure for intermediate redshift galaxies imaged with HST are adopted (cf. Chapter 2). Following the so-called "parametric" approach to quantify morphology, an analytic law – the Sérsic [114] profile – is fit to the projected two-dimensional surface brightness distribution of COSMOS galaxies. This is complemented by a "non-parametric" classification scheme, The Zurich Estimator of Structural Types (ZEST), in which measures of concentration, asymmetry, clumpiness, etc. are used to separate early-type from disk and irregular galaxies. Disk galaxies are further split into three categories according to the bulge-to-disk (B/D) ratio.

The COSMOS survey makes it possible to address unresolved questions concerning the evolution of disk galaxies (i.e., evolution of surface brightness, size, etc.) with a data set that is significantly larger – and suffers significantly less from cosmic sampling variance – than any sample employed in previous reports. Furthermore, the large statistical sample provided by COSMOS, and the large volumes of the survey, covering all scales of the large scale structure at all redshifts of relevance for our work, allow us to investigate the dependence of evolutionary trends in the disk galaxy population on (1) bulge-to-disk ratio B/D, and (2) environmental density.

In Chapter 3 we study the evolution of the size function of large disk galaxies between $z \sim 1$ and the present using a sample of >11,000 disk galaxies with $I \leq 22.5$, extracted from the central 38% of the COSMOS field. Chapter 4 is dedicated to the evolution of the bivariate size-luminosity function and of the opacity and surface brightness of large disk galaxies at $z < 1$. This analysis is based on the complete sample of >27,500 disk galaxies present over the entire area of the COSMOS field. In the same chapter we also investigate the history of star formation in disk galaxies, as well as the effects of environment on the detected evolutionary trends. The thesis ends with a summary of the presented analyses in Chapter 5. The Appendix provides a brief overview of the COSMOS survey and of the properties of the comparison sample of local SDSS galaxies, used as a local reference sample to calibrate our COSMOS data.

The most important findings of this thesis are as follows: (1) On average, the bulk of the large disk galaxy population had completed its growth by $z \sim 1$. Specifically, however, bulgeless disks were more frequent at high redshift than nowadays, while the fraction of bulge-dominated disks has grown steadily since $z \sim 1$. Processes of secular evolution have built up – or at least added stellar mass to – the bulge components of disk galaxies over the same period. (2) The typical sizes of bulgeless disk galaxies have hardly changed over the past eight billion years; the typical sizes of bulge-dominated galaxies have increased by about 30% over this time span. The changes in the relative abundance of bulged and bulgeless disks conspire to produce a weaker evolution in surface brightness in the disk galaxy population as a whole in comparison with the individual B/D classes. (3) Environment affects the evolution of disk galaxies. In particular, the colour evolution of disks becomes progressively weaker the denser the environment. Surface brightness and luminosity evolution on the other hand are apparently independent of environment.

The implications of these results provide a strong stimulus for future work on this subject; suggestions are outlined in Chapter 5.

Kurzfassung

Die vorliegende Doktorarbeit ist der Evolution von Scheibengalaxien seit Rotverschiebung 1 gewidmet, d.h. während der vergangenen acht Milliarden Jahre. Der Datensatz, der hierzu verwendet wird stammt aus im Rahmen des Cosmic Evolution Survey (COSMOS) durchgeführten Beobachtungen in einem ca. 2 Quadratgrad großen äquatorialen Beobachtungsfeld (selbiges ist damit rund 10 Mal größer als der Mond). COSMOS ist die bisher ambitionierteste Studie mit dem Ziel die Evolution von Galaxien und deren Variation in unterschiedlichen kosmischen Umgebungen zu verstehen. Das bisher aufwändigste je durchgeführte Beobachtungsprogramm mit dem Hubble Weltraumteleskop (HST) ist ein essentieller Bestandteil der zahlreichen Messkampagnen im COSMOS-Feld, welche das elektromagnetische Spektrum vom Radio- bis in den Röntgenbereich abdecken. Dank des hohen Auflösungsvermögens der HST-Aufnahmen im I-Filter und dank der langen Belichtungszeit können die strukturellen Eigenschaften von Galaxien bei sichtbaren Wellenlängen sogar noch für Objekte, die wir zu einer Zeit beobachten, als das Universum erst halb so alt war wie heute, auf Skalen von 0.4 kpc vermessen werden.

Zwei Methoden zur Quantifizierung galaktischer Morphologie anhand der COSMOS HST-Aufnahmen werden vorgestellt (siehe Kapitel 2). Es ist dies einerseits der sogenannte „parametrische“ Ansatz, bei dem eine analytische Funktion – das Profil von Sérsic [114] – zur Beschreibung des radialen Verlaufs der Oberflächenhelligkeit an die (projizierte) zweidimensionale Helligkeitsverteilung einer Galaxie angepasst wird. In Ergänzung dazu wird der auf „nicht-parametrischen“ Strukturindikatoren (z.B. Asymmetrie, Konzentration oder Klumpigkeit der Helligkeitsverteilung) basierende ZEST-Algorithmus (der ‘Zurich Estimator of Structural Types’) verwendet, um elliptische Galaxien von Scheibengalaxien und irregulären Systemen zu unterscheiden. Die Scheibengalaxien werden zudem je nach der relativen Intensität ihrer Scheibe und zentralen sphäroidalen Komponente noch in vier Unterklassen eingeteilt.

Das COSMOS-Projekt ermöglicht es, ungeklärte Aspekte der Galaxienevolution (z.B.

die Entwicklung der Oberflächenhelligkeit, der Galaxiengrößen, etc.) mit einem weit grösseren Datensatz als bislang zur Verfügung stand zu untersuchen und daraus statistisch zuverlässige Schlüsse zu ziehen. Aufgrund der großen Datenmenge und des erheblichen kosmischen Volumens, welches mit COSMOS beobachtet wird, kann man Galaxienentwicklung auch gezielt für spezifische Galaxienklassen untersuchen, etwa für Scheibengalaxien mit unterschiedlich ausgeprgter Sphäroidkomponente oder Galaxien in dicht oder dünn besiedelten Regionen des Universums.

Im 3. Kapitel betrachten wir die Entwicklung der Grössenverteilung (die sog. 'size function') grosser Scheibengalaxien zwischen $z \sim 1$ und der Gegenwart. Wir verwenden dazu über 11'000 Scheibengalaxien aus dem inneren Bereich des COSMOS HST Feldes (38% des gesamten Beobachtungsgebiets). Kapitel 4 ist der Evolution der parallelen Entwicklung von Galaxiengrösse und -helligkeit gewidmet sowie der Evolution der Oberflächenhelligkeit grosser Scheibengalaxien. Die Analyse stützt sich hierzu auf 27'500 Scheibengalaxien welche, über das gesamte COSMOS Beoachtungsfeld verteilt, mit HST zwischen $z \sim 0.2$ und 1 detektiert wurden. Gleichzeitig untersuchen wir in diesem Kapitel auch den Verlauf der Sternbildungsaktivität und die optische Dicke von Scheibengalaxien sowie den Einfluss der Umgebung auf die Entwicklung von Scheibengalaxien. Die Disseration schliesst mit einer Zusammenfassung der Ergebnisse dieser Doktorarbeit in Kapitel 5, gefolgt vom Anhang, in dem das COSMOS Projekt und der Satz lokaler SDSS Galaxien, der für Vergleiche mit den Galaxien bei mittlerer Rotverschiebung verwendet wurde, kurz vorgestellt werden.

Folgende Resultate zählen zu den wichtigsten Ergebnissen, die im Rahmen dieser Doktorarbeit gewonnen wurden: (1) Die Mehrzahl der großen Scheibengalaxien hat ihr Wachstum vor acht Milliarden Jahren vollendet. In derselben Zeit haben jedoch Prozesse, die im Fachjargon als 'secular evolution' bezeichnet werden, zum Aufbau oder gar zur Neubildung von Sphäroidkomponenten im Zentrum der Scheibengalaxien geführt. Als Folge davon ist der Anteil der Scheibengalaxien mit Sphäroidkomponente seit $z \sim 1$ stetig gestiegen, während reine Scheibengalaxien heute weniger zahlreich sind als früher. (2) Die Abmessungen von reinen Galaxienscheiben hat sich in den letzten acht Milliarden Jahren kaum geändert, wogegen die typische Größe einer Scheibengalaxie mit Sphäroidkomponente in derselben Zeit um ca. 30% zugenommen hat. Die Verschiebung der relativen Anteile von reinen und Sphäroid-dominierten Scheibengalaxien bewirkt, daß die für die gesamte Population gemessene Hellikeitsentwicklung (in Form einer Abnahme seit $z \sim 1$) kleiner ist als für die verschiedenen Kategorien von Scheibengalaxien einzeln betrachtet. (3) Die kosmische Umgebung beeinflußt die Entwicklung von Scheibengalaxien dahingehend, daß Galaxienfarben sich in Regionen geringer Dichte stärker entwickeln als in dichter besiedelten. Die Abnahme der Oberflächenhelligkeit andererseits hängt kaum von der Umgebung ab.

Diese Erkenntnisse werfen viele neue Fragen auf, die wir im Kapitel 5 kurz erläutern werden.

"Explain all that," said the mock turtle.
"No, no! The adventures first," said the gryphon in an impatient tone:
"Explanations take such a dreadful time."

The Lobster Quadrille, *Alice's Adventures in Wonderland* [22]

1 Introduction

1.1 Historical perspective

Our own galaxy, the Milky Way, has apparently evolved under comparatively peaceful conditions for the last 10 billion years. As its inhabitants, the formation and evolution of disk galaxies is therefore of immediate interest to us. Is the history of our galaxy typical of the evolution suffered by all disk galaxies we see around us? Can we regard our galaxy as a representative "laboratory" for observational astronomy in which we can perform measurements that may be generalized to other disk galaxies, near and far? These questions are not just important due to mankind's cosmographic settings. They are also worth addressing in the general context of structure formation in the universe. In the hierarchical framework of galaxy formation (e.g., Toomre [126], White and Frenk [133]), disks are one of the most fundamental building blocks of the cosmic web in that they are believed to be systems which have experienced no disruptive mergers with other galaxies. Their properties should thus directly reflect the processes controlling the coalescence of baryons at the centre of dark matter haloes where they form the distribution of luminous matter we observe today.

The first ideas and insights on the formation and evolution of disk galaxies necessarily came from observations of the Milky Way and objects that were recognized to be local galaxies at the beginning of the 20th century. In 1750 Wright [137] coined the idea that the Milky Way was an optical effect owing to the sun being embedded in an assembly of stars. His ideas were embraced by Kant [63] who pointed out that the bright ribbon of the Milky Way traced the shape of a great circle on the sky and thus exactly the geometry expected of a planar system containing the Earth-bound observer. He subsequently suggested that many of the fuzzy nebular objects in the sky were actually distinct stellar systems of their own. In the same work, and following an idea of Swedenborg [124], Kant outlined a nebular theory of the solar system's origin. The nebular hypothesis was elaborated

upon 40 years later by Laplace [69] and proved an influential concept for one and a half centuries. Originally conceived to explain the origin of the solar system from a rotating nebula, its potential applicability to structure formation on larger scales may have dawned on astronomers by the middle of the 19th century. The discovery of spiral structure in nebulæ between 1842 and 1850 by Lord Rosse [99] clearly indicated rotational motion which could be interpreted as the remnant eddy of primeval turbulence. Indeed, the cosmic turbulence theory was held to be a valid candidate to explain galaxy formation in the 1940s and 50s as expressed in the work of von Weizsäcker [131] and Gamow [50], partly because gravitational instability was thought to be too slow to form galaxies out of statistical fluctuations as a consequence of Jeans instabilities (Jeans [58]) developing in an expanding universe (Gamow and Teller [51]).
The tide turned in favour of the gravitational instability theory shortly after the discovery of the 2.7° K cosmic microwave background (CMB) radiation (Penzias and Wilson [90]). The imprints of minuscule density fluctuations (Smoot et al. [119], Spergel et al. [121]) on top of the otherwise perfectly Planckian character of radiation from a hot big bang are nowadays regarded as the seeds of the cosmic web. In the following section we summarize the theoretically expected properties of disk galaxies that form in a (Λ)CDM universe.

1.2 Hierarchical galaxy formation in a (Λ)CDM universe

With the discovery of the CMB it became thinkable to determine a causal link between the layout of the universe at redshift[1] $z \sim 0$ and its configuration during the epoch of recombination at $z \sim 1500$. The first calculations of the required amplitude of the density fluctuations at that epoch however revealed a discrepancy; if the fluctuations at recombination were to grow into the presently observed density contrasts, as delineated by the luminous matter, the expected relative density excesses $\Delta\rho/\langle\rho\rangle$ with respect to the mean density $\langle\rho\rangle$ would have had to be of the order of 10^{-4} to 10^{-3}. Although the instruments of the time would have been sensitive enough to detect such fluctuations at this level, they found none. A way out of this apparent impasse was offered if a weakly interacting dark matter particle (e.g., neutrinos or supersymmetric partners of baryonic particles) existed which was only susceptible to the pull of gravity. With these properties it would have been free to coalesce[2] and enhance density perturbations once the pre-radiation universe became matter-dominated. Fluctuations in the baryonic matter component on the other hand were continuously dissipated on all but the largest scales (larger then approximately $10^{14} M_{\odot}$, which is referred to as the Silk [116] mass) due to Thomson scattering of the electrons in the radiation-dominated plasma. After the universe became neutral at recombination, the pressure of the baryonic matter component arising from this scattering decreased, in the new neutral state, to that of an ideal gas. The baryonic Jeans mass

[1] Redshift is operationally defined as $z = (\lambda_{\text{obs.}} - \lambda_{\text{em.}})/\lambda_{\text{em.}}$. Cosmological redshift is a measure of the size of the expanding universe as reflected by its relation to the scale factor: $a(z=0)/a(z) = 1 + z$.

[2] A medium composed of dark matter particles that do not interact through the electromagnetic force does not feel pressure. The speed of sound in such a medium is vanishingly small, resulting in the Jeans mass for dark matter being effectively zero.

$$M_J = \frac{1}{6}\pi\langle\rho\rangle\left(\frac{\pi c_s^2}{G\langle\rho\rangle}\right)^{3/2} \tag{1.1}$$

thus abruptly decreased from $10^{14}M_\odot$ to the mass of a globular cluster ($10^5 M_\odot$) due to the smaller speed of sound, c_s. The growth of baryonic density fluctuations then became possible and the neutral baryons were drawn into the deep potential wells of the dark matter, soon reaching comparable overdensites $\Delta\rho/\langle\rho\rangle$ as the universe continued to expand:

$$(\Delta\rho/\langle\rho\rangle)_{\text{bar.}} = (\Delta\rho/\langle\rho\rangle)_{\text{DM}}\left(1 - \frac{a(z_{\text{rec.}})}{a(z)}\right) \ . \tag{1.2}$$

(The subscripts 'DM' and 'bar.' denote the dark and baryonic matter density excesses. $a(z)$ is the scale factor of the universe at redshifts lower than the redshift of recombination, $z_{\text{rec.}}$.) It was subsequently shown that this alleviated the disagreement between predicted and observed amplitude of CMB fluctuations. With hot dark matter this would have led to top-down structure formation whereas structure formation from the bottom up (i.e., with small units decoupling from the Hubble-flow first and then merging into larger units, a sequence of event termed "hierarchical clustering") would have ensued in the presence of cold dark matter (CDM). Blumenthal et al. [11] showed that the latter mechanism matched observations better; hot dark matter models predicted galaxy clusters to form as the first structures at $z \sim 2$ with smaller objects fragmenting from them which clearly was at odds with the ages of globular clusters and the ages of stars in normal and dwarf galaxies.

Meanwhile, based on the power spectrum $\langle|\Delta_k|^2\rangle \propto k^n$ (here Δ_k is the relative density excess $\Delta\rho/\langle\rho\rangle$ on scales described by the wave number $k = 2\pi/L$) of the primordial density fluctuations the work of Press and Schechter [93] provided an analytic recipe for the build-up of mass through hierarchical clustering and predicted the relative abundances of bound structures with different masses at a given epoch. It was soon realized that the Press-Schechter formalism in fact was an adequate description of the distribution of dark matter structures. Furthermore, an adaptation of the Press-Schechter mass function, the so-called Schechter function

$$\Phi(L)dL = \Phi^*\left(\frac{L}{L^*}\right)^\alpha \exp\left(-\frac{L}{L^*}\right)\frac{dL}{L^*} \ , \tag{1.3}$$

was soon thereafter introduced (Schechter [108]) to describe the luminosity function of elliptical galaxies in clusters and field galaxies in general.

With the spectrum of dark matter mass units predicted by the Press-Schechter formalism the question remains how the galaxies form within the dark matter haloes. In the local

universe the abundance ratio of elliptical to disk galaxies to irregular galaxies is found to be E:S:Irr $\simeq$ 0.11:0.83:0.06 (Fukugita et al. [49]). Conversely, the ratio of the stellar mass in ellipticals and bulges of spiral galaxies to that in disks and irregulars is spheroid:disk $\simeq$ 0.74:0.26 (Fukugita and Peebles [48]).
What determines the morphology and dynamics of a galaxy? Which processes shape a disk galaxy like our own Milky Way? Their rotational nature seemed hard to explain by the aforementioned turbulence theory since any primeval turbulence that may have existed would have inevitably been damped out in the expanding universe if angular momentum is conserved. In the CDM scenario for galaxy formation it is reasonable to assume that the density profile of the halo, its shape and its distribution of angular momentum determine the structure, size and rotation curve of the galaxy at its centre. The theory indeed offered a natural explanation for the rotation of galaxies. Density perturbations are not intrinsically spherical but ellipsoidal and their associated quadrupole moment can thus exert gravitational torques on neighbouring dark matter structures during the phase of linear growth of a fluctuation (Peebles [87], White [132]). Angular momentum growth comes to an abrupt end as soon as the density perturbation reaches the order of unity after which its nonlinear collapse proceeds quickly and gravitational torquing becomes negligible due to the small extent of the structure. The amount of angular momentum that a dark matter halo can acquire scales with the amount of time it spends in its phase of linear growth and is expressed by the dimensionless spin parameter λ which is the square root of the ratio between centrifugal and gravitational acceleration:

$$\lambda = \frac{J\sqrt{|E|}}{GM^{5/2}} \ . \tag{1.4}$$

Here J is the total angular momentum, E the gravitational binding energy, and M the mass of the dark matter halo. N-body simulations of structure formation in a CDM-universe find that the distribution of spin parameters λ follows a log-normal curve

$$p(\lambda)d\lambda = \frac{1}{\sqrt{2\pi\sigma_\lambda^2}} \exp\left(-\frac{\left[\ln\left(\lambda/\overline{\lambda}\right)\right]^2}{2\sigma_\lambda^2}\right)\frac{d\lambda}{\lambda} \tag{1.5}$$

which peaks around $\overline{\lambda} \simeq 0.05$ and has a width of $\sigma_\lambda \simeq 0.5$ (Barnes and Efstathiou [6]). This result does not seem to vary much with the initial power spectrum nor with the details of the cosmological model. The low values of λ are consistent with the slow rotation of spheroidal systems, i.e., ellipticals or central bulges in disk galaxies, but they cannot provide the amount of rotational support disk galaxies require to maintain their structure. The material destined to form a disk thus needs to contract further by cooling out of the hot gaseous halo associated with the dark matter potential well[3] and the simplest

[3] In this discussion the topic of how units of collisionless cold dark matter become gravitationally bound and form virialized systems as a consequence of hierarchical clustering in less than a Hubble time has been skipped. The process by which this happens is the so-called "violent relaxation" which leads to the swift

assumption was that, in doing so, it would preserve its specific angular momentum (Fall and Efstathiou [40]). Because of the centrifugal barrier these authors found that the gas settles into a rotationally supported disk with rotation curves and exponential scale lengths that were in qualitative agreement with the observations of the time. In the course of the collapse the linear extent of the gas distribution shrinks by about an order of magnitude but the developing systems still reflect the properties of the host halo in that their size (parametrized by the disk scale length r_d) is predicted to be proportional to both the size and the angular momentum of the halo (Mo et al. [81]; note that this also implies a log-normal distribution for disk galaxy sizes in keeping with equation (1.5)):

$$r_d = \frac{1}{\sqrt{2}} \left(\frac{j_d}{m_d} \right) \lambda r_{200} \tag{1.6}$$

Here r_{200} stands for the virial radius of the dark matter halo and j_d and m_d are the fractions of the total angular momentum and mass of the system contained in the disk, respectively. Since the virial radius is inversely proportional to the Hubble parameter $H(z)$ this also had implications for the expected size evolution of disks as a function of redshift.

The considerations of the previous paragraph have left a crucial question unanswered: under which circumstances are disk galaxies formed and what conditions favour the creation of an elliptical? Since the relaxation time scales for (essentially collisionless) stellar systems are longer than the Hubble time it is unlikely that one type evolved into the other. In semi-analytic models of hierarchical galaxy formation spheroids are formed from mergers of disk galaxies with similar masses (Kauffmann et al. [65]) but this explanation is not entirely satisfactory since it appears that the more massive ellipticals cannot have been formed through binary mergers of disk galaxies, at least if these have the properties of disk galaxies we observe today (Naab and Ostriker [84]). An alternative explanation lies with the influence of initial conditions or of the environment. In view of the prediction of White [132] that the angular momentum of linear perturbations grows with time as $t^{5/3}$ (this is strictly valid only in an Einstein-de Sitter universe which is, however, a reasonable approximation at early cosmic times) it could be envisaged, for example, that ellipticals formed from fluctuations which had turned around quickly whereas disk-like systems were able to acquire angular momentum for a longer time. Barnes and Efstathiou [6] propose that the cooling time of the gas within a protogalaxy is critical; appropriate conditions for the development of a disk might prevail if the cooling time were longer than the Hubble time such that the bulk of the gas will not collapse until most of the substructure in the halo has been erased. Short cooling times and an inhomogeneous protocloud on the other hand could lead to the formation of an elliptical if the clumps of gas lose angular momentum as they spiral in toward their common centre of mass (van Albada [130]). Finally, internal processes can also play a role and determine the morphology of a galaxy.

equipartition of energy in the rapidly fluctuating potential of a newly forming dark matter halo (cf. Eggen et al. [37]).

Observations at different redshifts are essential to understand galaxy formation. This thesis is primarily about the formation and evolution of disk galaxies, and in particular about placing experimental constraints on the state of the disk galaxy population as a function of cosmic time. Numerical simulations of disk galaxy formation still have difficulties in producing a pure disk without any spheroidal component and which matches all scaling relations. Significant progress has been made in this field and has lead to the (numerical) creation of disk galaxies which possess some properties observed in real objects (e.g., Governato et al. [54], Robertson et al. [97], Sommer-Larsen et al. [120]). Nevertheless disk galaxies developing from *ab initio* cosmological boundary conditions into full-flegged replicas of their observational counterparts have not yet been successfully reproduced in simulations. To set the stage for the remainder of the thesis, in the next section, we give an overview of the current observational knowledge on disk galaxy evolution.

1.3 Current observational status

How well do the most basic theoretical predictions of the previous section compare with reality? Simard et al. [117] and Ravindranath et al. [94] claimed that no noticeable surface brightness or luminosity evolution has taken place since $z \sim 1$, in disagreement with the pioneering CFRS results of Schade et al. [106, 107] and Lilly et al. [71]. In the mid 1990s the CFRS survey presented evidence that late-type galaxies were brighter at intermediate redshift than in the local universe. This is attributed to a 3-fold higher rate of star formation at $z \sim 0.7$ than nowadays. The enhanced star formation activity manifests itself in both a surface brightness increase by about 1.2-1.6 mag at $z \sim 0.75$ (Schade et al. [105, 107]), as well as in the evolution by about 1 mag of the luminosity function of objects bluer than present-day Sbc galaxies (Lilly et al. [72]) at $0.5 < z < 0.75$.
Further work on larger samples, e.g., the GEMS analysis of Barden et al. [5], confirmed the CFRS results and showed that the surface brightness and luminosity of disk galaxies as a whole have indeed evolved by $\sim$ 1-1.5 mag in the last eight billion years.

The evolution of disk sizes at $z < 1$ still remains rather controversial. While measurements of the number density of large disk galaxies find no large changes since $z \sim 1$ (Lilly et al. [71], Sargent et al. [101]) others claim that there is evidence of inside-out growth of disk galaxies by about 25% in the same period (Trujillo and Pohlen [128], Barden et al. [5]). All studies agree, however, that disk galaxy sizes have evolved less in the last half of the Hubble time than predicted by theoretical models.

All the studies of disk galaxy evolution mentioned above were possible thanks to increasingly large photometric or spectroscopic surveys in the past decade that have mapped out considerable volumes of the universe, both in space and time, combined with the availability of high resolution images from the Hubble telescope which permit astronomers to measure galactic structure reliably out to at least redshift 1. Nevertheless, such studies have been limited by small statistical samples extracted from volumes so small not to allow any investigation as a function of galaxy structure, and to be severely hampered by

cosmic variance.

The COSMOS survey[4] is the largest HST survey to date, and covers an area of about 2deg^2. Following the HST observations, the COSMOS field has been observed at all accessible wavelengths from the ground and from space, from radio to the X-ray wavelengths; the spectroscopic followup of COSMOS at the ESO VLT is collecting spectroscopic redshifts and diagnostics for over 35,000 COSMOS galaxies (Lilly et al. [73]). COSMOS finally provides the statistics to dissect the disk galaxy population into different categories with different physical properties (e.g., bulge-to-disk ratio), and, unprecedented so far, to study the evolutionary trends of the disk galaxy population in the different environments provided by the large-scale structure filaments, voids, sheets and clusters.
The study the evolution of the disk galaxy population since $z = 1$ as a function of (1) bulge-to-disk ratio (B/D), and (2) environmental density is the aim of this thesis.

1.4 Content of this thesis

Starting from an introduction to the methods used to classify and measure galactic structure we will study the evolution of the sizes, of the surface brightness and luminosity and of the properties of the stellar populations in disk galaxies of varying B/D-ratio in different environments. The text is divided into four chapters, namely:

In **Chapter 2** "parametric" and "non-parametric" methods to describe the structural properties of COSMOS galaxies at intermediate redshift will be presented.
In particular, the properties of the Sérsic profile – an analytical law capable of reproducing the radial fall-off of light in both late- and early-type galaxies – will be discussed. Several algorithms used to measure the Sérsic profile will be discussed and the optimization of one of these (Gim2d) and its application to the COSMOS data described in some detail. An estimate of systematic errors on the Gim2d measurements will be given based on simulations of mock galaxies.
The Zurich Estimator of Structural Types (ZEST) is the topic of the second half of this chapter. It will be shown (by means of a principal component analysis) how linear combinations of a basic set of 5 non-parametric quantities can be used to define a three-dimensional parameter space in which galaxies of different morphological classes occupy distinct regions. This finding will be used to classify COSMOS galaxies as either early-type, late-type or irregular galaxies and, moreover, to distinguish bulge-dominated disk galaxies from pure disk systems. The capability of ZEST to consistently classify both distant and local galaxies will be demonstrated and the robustness of the approach tested to a magnitude of $I_{ACS,AB} = 24$. Finally, it will be argued that the newly developed galaxy classification scheme allows for a more accurate selection of morphologically defined sam-

[4] More information on the COSMOS survey can be found in section A.2 of the appendix. There the scientific goals of the survey, the survey field and some of the data sets are discussed (with emphasis on the HST ACS I-band imaging of the COSMOS field, which for our measurements is the primary source of information).

ples than frequently in the literature so far.

In **Chapter 3** we will study a sample of approximately 16,500 galaxies with $I_{ACS,AB} \leq 22.5$ in the central 38% of the COSMOS field to measure the evolution of the size function of disk galaxies since $z \sim 1$.
The galaxy sample used for the analysis of this chapter is selected from the HST Cycle 12 ACS F814W COSMOS data set and structural information on the galaxies is derived by fitting single Sérsic models to their two-dimensional surface brightness distributions. Focusing on the disk galaxy population (as classified by ZEST) we will investigate the evolution of the number density of disk galaxies larger than approximately 5 kpc between redshift $z \sim 1$ and the present epoch. Specifically, the measurements of the half-light radii derived from the Sérsic fits will be used to construct, as a function of redshift, the size function $\Phi(r_{1/2}, z)$ of both the total disk galaxy population and of disk galaxies split in four bins of bulge-to-disk ratio. In each redshift bin the size function specifies the number of galaxies per unit comoving volume and per unit half-light radius $r_{1/2}$. Furthermore, a selected sample of roughly 1800 SDSS galaxies will serve to calibrate our results with respect to the local universe. It is found that:
(1) The number density of disk galaxies with intermediate sizes ($r_{1/2} \sim$ 5-7 kpc) remains nearly constant from $z \sim 1$ to today. Unless the growth and destruction of such systems exactly balanced in the last eight billion years, they must have neither grown nor been destroyed over this period.
(2) The number density of the largest disks ($r_{1/2} > 7$ kpc) decreases by a factor of about 2 out to $z \sim 1$.
(3) There is a constancy – or even slight increase – in the number density of large bulgeless disks out to $z \sim 1$; the deficit of large disks at early epochs seems to arise from a smaller number of *bulged* disks.
The results of the analysis presented in this chapter indicate that the bulk of the large disk galaxy population had completed its growth by $z \sim 1$ and support the theory that secular evolution processes produce – or at least add stellar mass to – the bulge components of disk galaxies.

In **Chapter 4** the surface brightness evolution of large disk galaxies, the evolution of the bivariate size-luminosity function and environmental variations in the evolution of the history of star formation will be investigated.
In this chapter the complete sample of 27,500 disk galaxies covering the entire 1.64 deg^2 field of the HST COSMOS survey is used. The sample has photometric redshift estimates obtained from ground-based photometry and is brighter than $I_{ACS,AB} = 22.5$. As in Chapter 3, (a) structural information on the galaxies is derived by fitting a single Sérsic law to their surface brightness distribution and the sample is further split – by means of the automated morphological classifying scheme ZEST – into different morphological categories based on the importance of the galaxies' bulge component; (b) a complementary data set of roughly 1800 local SDSS galaxies serves as a local anchor to the measurements performed on the COSMOS galaxies and allows us to relate them to the average properties of the local disk galaxy population.
Based on measurements of surface brightness, galaxy colours and the bivariate size-luminosity distribution we will argue that the following changes have shaped the disk

galaxy population in the redshift range $z < 1$:
(1) The surface brightness of large disk galaxies decreases by about 1-1.4 mag since $z \sim 1$. Both pure disk galaxies and the most bulge-dominated systems display a similar fading in surface brightness.
(2) The star formation history in galactic disks is similar regardless of the size of the central bulge. The amount of luminosity evolution since $z \sim 1$ can be explained by an exponentially declining star formation activity with an exponential time constant of about 5 Gyr.
(3) The bivariate size-luminosity distribution is well fit by a log-normal distribution in size and a Schechter function in luminosity. For pure disk galaxies the peak of the size distribution has not changed since $z \sim 1$. The size distribution of disk galaxies which possess a bulge has evolved towards larger sizes in the last 8 billion years. On average disk galaxies with a non-negligible bulge-component are about 70% of their current size at $z \sim 1$.
(4) The relative abundance of bulged and pure disk galaxies changes with cosmic time; bulge-dominated systems have become more abundant since $z \sim 1$ while the number density of pure disk galaxies declines.
(5) The evolution of the disk galaxy population slightly depends on environment: in high density regions galaxy colours evolve less than in sparsely populated regions while surface brightness evolution does not vary as a function of environment. This suggests that disks in denser environments have had a globally accelerated evolution compared to disks in low density environments.

In **Chapter 5** the results of the Ph.D. thesis will be summarized and used to give an outline of future foreseen developments and open questions pertaining to the topic of disk galaxy evolution.

Finally, the thesis is concluded with the

Appendix, in which the comparison sample of artificially redshifted SDSS galaxies at $z \sim 0.7$ is briefly presented (Section A.1) and the multi-wavelength surveys conducted in the COSMOS field are described (Section A.2). In this section the COSMOS HST Legacy survey which has provided the data for this thesis and ancillary ground-based photometry used for photometric redshift estimates are given special attention.

Throughout the thesis, we consistently use AB magnitudes (Oke [86]), and thus drop the subscript 'AB' from our notation when quoting magnitudes. Galaxy magnitudes and colours are calculated assuming the transmission characteristics of the filters used in the multi-wavelength photometry for the COSMOS survey, i.e., those of the B, g', V, r', i' and z' of SuprimeCam at the Subaru telescope and of the u^*-filter of MegaPrime at CFHT (see also the description of these instruments in Section A.2).
We adopt $\Omega_m = 0.25$, $\Omega_\Lambda + \Omega_m = 1$ and a present day Hubble parameter of H_0 =70 km s^{-1} Mpc^{-1}. The redshift range we consider ($0 < z < 1$) spans a look-back time of 7.9 billion years in our cosmological model. The age of the universe at redshift $z \sim 1$ was 6.2 billion

years. At redshifts 0.2, 0.4, 0.6 and 0.8 – values which will be used often to define redshift slices in which the properties of the galaxy population will be assessed – the look-back time was 2.4, 4.3, 5.8 and 7 billion years, respectively.
We will be dealing frequently with the sizes of galaxies and state them in units of kpc. 1 pc is 3.086×10^{16} m which corresponds to about 3.262 light-years. The Milky Way has a half-light radius of about 4 kpc which is about half the distance between the sun and the centre of our galaxy. A typical absolute magnitude of a disk galaxy with the size of the Milky Way is around -20 at optical wavelengths. This compares, e.g., with a B-band absolute magnitude of the sun of 5.5 implying that the luminosity of the Milky Way in blue light is approximately $L_{MW,B} \simeq 2 \times 10^{10} L_{\odot,B}$ where $L_{\odot,B} = 5.2 \times 10^{25}$ W is the B-band luminosity of the sun. (In terms of (baryonic) mass the ratio is $M_{MW}/M_{\odot} \simeq 6 \times 10^{11}$ (Karachentsev and Kashibadze [64]) where $M_{\odot} = 2 \times 10^{30}$ kg is the solar mass.)

An inconceivably numerous host of stars must be here arranged together [...], because their free positions towards each other would otherwise have presented irregular forms and not exact figures.

Immanuel Kant, *Universal History and Theory of the Heavens* [63]

2 Measuring structural properties of distant galaxies

Parts of Section 2.1 are based on Sargent et al. [101]
(`http://adsabs.harvard.edu/abs/2007ApJS..172..434S`).
Section 2.2 is extracted from Scarlata, Carollo, Lilly, Sargent et al. [103]
(`http://adsabs.harvard.edu/abs/2007ApJS..172..406S`).

The two-dimensional morphological information contained in today's high resolution astronomical CCD images can be described in alternative ways which all have advantages and disadvantages. The principal focus of this section will be the so-called "parametric" (see Section 2.1) and "non-parametric" methods (see Section 2.2). Non-parametric quantification of galactic structure is versatile because no *a priori* assumptions about the functional form of the distribution of light are made. This approach is clearly appropriate for irregular or disturbed systems (e.g., for galaxies in the early universe when the Hubble sequence had not yet been established). However, it has the disadvantage that it is sensitive to the depth or noise level of the images because it cannot resort to a parametric law to extrapolate morphological features to faint fluxes.
Parametric methods, on the other hand, are less flexible than a non-parametric description of galactic structure but they permit the extrapolation to low flux levels thanks to their rigorously defined functional form (under the assumption that the adopted parametrization is indeed valid for such flux components as well, of course). They are thus especially suitable for estimates of total galaxy luminosity or size, or for the dissection of galaxies into distinct morphological components such as disks, bulges or bars. Since they are commonly used to describe the global properties of galaxies they are also a useful tool to derive measurements for comparison with theoretical or numerical predictions.

This chapter contains a description of the efforts to both measure and classify galactic structure for COSMOS galaxies. The catalog of objects on which we perform morpholog-

ical measurements was produced by applying the source extraction software SExtractor (Bertin and Arnouts [9]) to the HST ACS images. More information on the procedure is given in Section 3.2.1. In the following section we describe the fitting of the analytic Sérsic profile (Sérsic [114]) to COSMOS disk galaxies with $I \geq 22.5$ and in Section 2.2 their classification by non-parametric means is presented.

2.1 Two-dimensional fits of analytic surface brightness profiles

The choice of a mathematical law to describe the structure of a galaxy does not imply that there is a unique strategy for determining the pertinent parameters from astronomical images. In general, a measurement scheme will be either a one-dimensional or a two-dimensional method. In the one-dimensional case either a transect along the major or minor axis of the galaxy is chosen or, instead, an azimuthally averaged surface brightness profile. While this method works in low S/N conditions and is simple and fast it also has its drawbacks. If isophote fitting is used to construct an azimuthally averaged profile, for instance, changes in ellipticity and position angle at consecutive isophotes lead to a profile which effectively runs along an arc rather than a straight line. Spiral arms or bars are especially likely to have this distorting effect. Alternatively, profiles may be extracted along the semi-major or minor axis in which case information is inevitably lost (Baggett et al. [4]). Moreover, the positioning of major and minor axes may be ambiguous or dominated by different morphological components for the two axes (e.g., the bulge along the minor axis). In two dimensional fitting, all information contained in the image is accounted for to build a model of a galaxy's structure and thus differences in projected ellipticities and orientation may even be of advantage as they can help to distinguish between different morphological components.

One-dimensional techniques, by virtue of being fast and not placing high demands on computational resources, have been used for a long time. Two-dimensional fitting algorithms, on the other hand, only started making their appearance about a decade ago when computers became fast enough to implement this method. Examples are the fitting packages Gim2d (Marleau and Simard [77], Simard et al. [118]), Galfit (Peng et al. [89]), or Budda (de Souza et al. [30]). Many of them have been written with a specific purpose in mind (e.g., edge-on or face-on samples, early-type cluster galaxies) and are, at least under favourable conditions, capable of performing bulge-to-disk decomposition or even include additional components like nuclear point sources, bars, etc. The large complexity of such structural models is reflected in the number of free parameters which may be as large as a few dozen in the most sophisticated decompositions.

Even at the high spatial resolution offered by the HST ACS camera, a reliable bulge-to-disk decomposition is a delicate task at the depth of the COSMOS F814W exposures. In the present work we will thus adopt a fairly simple law – the so-called Sérsic profile – with 8 free parameters to describe the radial surface brightness dependence of the galaxies in our sample.

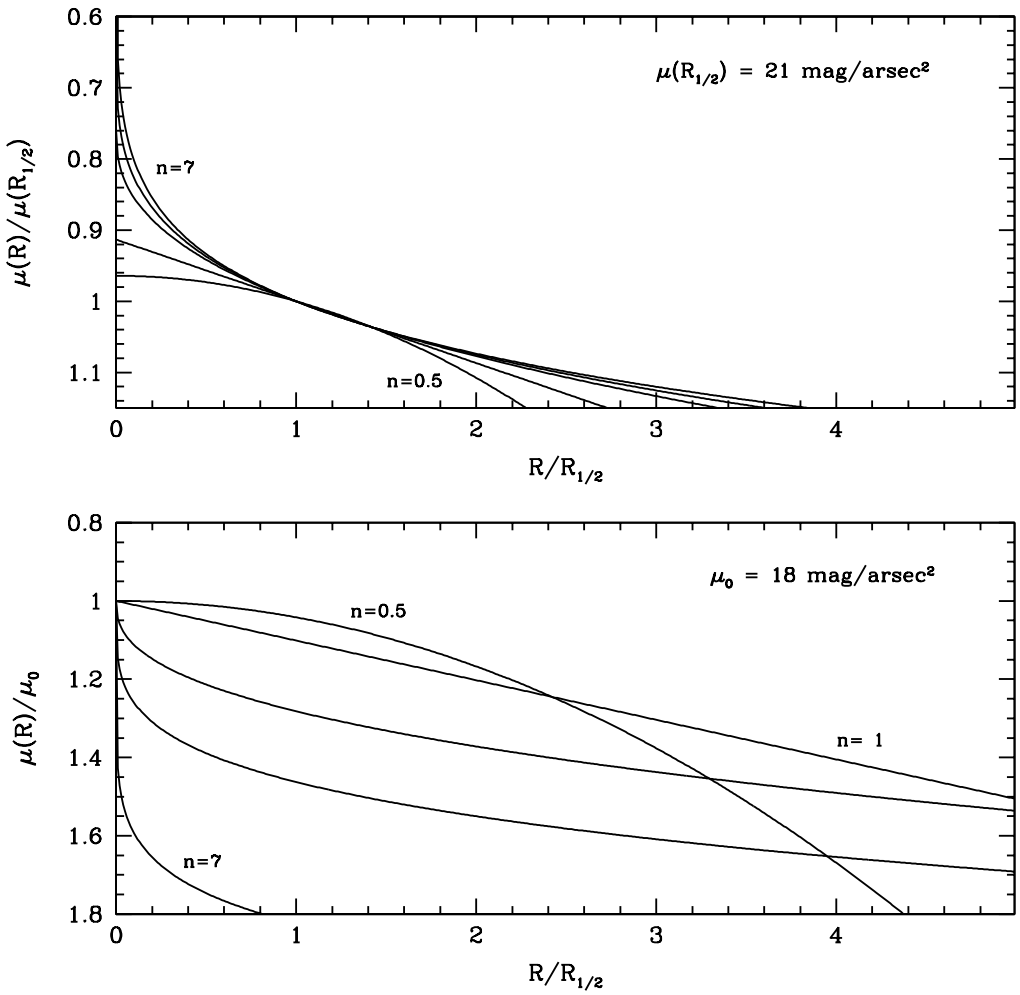

Fig. 2.1 — Sérsic surface brightness profiles (cf. equations (2.2a/2.2b)), normalized to the surface brightness $\mu(R_{1/2})$ at the half-light radius (*top*) and the central surface brightness μ_0 (*bottom*). In both panels five Sérsic models are shown, namely profiles for $n = 0.5$, 1, 2.5, 4 and 7.

The widely used $R^{1/n}$ model was introduced by José Luis Sérsic for the compilation of his atlas of galaxies in the southern hemisphere (Sérsic [114]). It is most commonly stated as a surface intensity profile $I(R)$ (i.e., in units of flux per area), in which case it reads

$$I(R) = I(R_{1/2}) \exp\left\{-k(n)\left[\left(R/R_{1/2}\right)^{1/n} - 1\right]\right\} , \tag{2.1}$$

where $I(R_{1/2})$ is the surface intensity at the half-light radius $R_{1/2}$[1]. The value of $k(n)$ is chosen such that $R_{1/2}$ represents the semi-major axis of the ellipse containing half of the

[1] Throughout this manuscript we adopt the convention that $R_{1/2}$ stands for the apparent half-light

total flux for each value of Sérsic index[2] n. The half-light radius is related to the so-called "scale length" R_d of the disk by $R_{1/2} = 1.678 \cdot R_d$. Multiplying the negative logarithm of equation (2.1) by 2.5 yields the surface brightness profile (in units of mag arcsec^{-2})

$$\mu(R) = \mu(R_{1/2}) + \frac{2.5\ k(n)}{\ln(10)} \left[\left(R/R_{1/2}\right)^{1/n} - 1 \right] \tag{2.2a}$$

$$= \mu_0 + \frac{2.5\ k(n)}{\ln(10)} \left(R/R_{1/2}\right)^{1/n} \tag{2.2b}$$

which in the equation above is expressed both in terms of the surface brightness $\mu(R_{1/2})$ at the half-light radius (equation (2.2a)) and as a function of the central surface brightness μ_0 (equation (2.2b)). The shape of the Sérsic profile is shown for five different values of the Sérsic index n in Figure 2.1. For $n < 1$ profiles are shallow at small sizes ($\lesssim R_{1/2}$) and drop rapidly with increasing radius. Conversely, profiles with $n > 1$ are steep at small radii but then flatten out as R increases. This means that for an exponential profile with $n = 1$, 99.8% of the total flux resides within 5 $R_{1/2}$, while for a $n = 4$ profile the inner 5 $R_{1/2}$ enclose only 88.4 % of the total light.

The strength of the Sérsic law is that it allows a flexible description of surface brightness ranging from objects with profiles more shallow than that of an exponential disk to those canonically assumed for elliptical galaxies.
Notwithstanding its versatility, the Sérsic profile is an *empirical* law. It was traditionally assumed to reflect varying contributions of an exponential $n = 1$ disk and a classical de Vaucouleur $n = 4$ spheroid component in images lacking the resolution to allow a proper separation into a bulge and a disk component. Since its first appearance in the literature, however, many studies have shown that bulges display $R^{1/n}$ profiles with a broad range of power law indices. The empirical nature of the Sérsic profile distinguishes it from the exponential and the de Vaucouleurs profile. Disk formation in a cosmological framework may only result in an exponential profile in the inner few (approx. 3) scale lengths if the angular momentum of gas clouds being accreted is conserved (Gunn [56]), but the viscous redistribution of gaseous material and thus of angular momentum – if it happens on time scales similar to those for star formation – can generate an exponential profile over at least half a dozen scale lengths (Ferguson and Clarke [43], Lin and Pringle [74]). In the case of the elliptical galaxies, dissipationless collapse starting from irregular initial conditions successfully produces objects obeying the $R^{1/4}$ law provided collapse factors are large (e.g., van Albada [130]).

Although it appears to have no direct theoretical basis as of yet, the Sérsic law incon-

radius on the image, measured in pixels or seconds of arc, while $r_{1/2}$ denotes the physical half-light radius in units of kpc. Similarly a capital variable R describes a general observed radial coordinate in arcsec while small r stands for the radial position in kpc.

[2] See, e.g., Ciotti and Bertin [24] for series expansions allowing a precise calculation of $k(n)$ over a wide range of Sérsic indices, or Graham and Driver [55] for a collection of formulæ pertaining to the $R^{1/n}$ law.

testably does provide an excellent fit to the radial falloff of light in most galaxies and as such is very useful to quantify the evolution of galactic structure with cosmic time. In the following sections we thus describe the procedures involved in the analytical fitting of COSMOS galaxies.

2.1.1 Tools of the trade

Four codes for the automated fitting of surface brightness profiles are in common use[3]. In addition to having catchy acronyms (e.g., Galaxy IMage 2D – GIM2D (Marleau and Simard [77], Simard et al. [118]); GALaxy FITting – GALFIT (Peng et al. [89]); BUlge/Disk Decomposition Analysis – BUDDA (de Souza et al. [30]); Galaxy Automatic Surface PHOTometry – GASPHOT (Pignatelli et al. [92])) they also have certain methodological properties in common. The first three (GIM2D, GALFIT and BUDDA), for example, can be termed genuine two-dimensional methods based on the discussion in the previous paragraph, while GASPHOT stays close to the one-dimensional approach in that it merely fits the luminosity profiles along the combination of major and minor axes. The last three (GALFIT, BUDDA and GASPHOT) all perform a gradient search in parameter space to derive the best fit while GIM2D uses the Metropolis algorithm to find the parameter combination with the minimal χ^2. Finally, they also vary in the extent of accessible free parameter space: GASPHOT can only fit single Sérsic profiles to galaxy images, with GIM2D double component fits (and thus bulge-to-disk decomposition) are feasible and both BUDDA and GALFIT allow the inclusion of, among others, bars and nuclear point sources in addition to the standard bulge and disk components. The codes thus reflect the purpose for which they were designed, namely the study of nearby, well resolved galaxies in the case of GALFIT or distant galaxies in the case of GIM2D.

GALFIT and GIM2D are currently the two most frequently used codes. Both have been employed to measure the evolution of galactic structure in late-type and early-type galaxies (e.g., Barden et al. [5], Marleau and Simard [77], McIntosh et al. [78] or Trujillo et al. [129]) in the last half of the Hubble time.
To ascertain which was more stable and suitable for the study of the COSMOS data we tested both GALFIT and GIM2D. We show the outcome of several dozen runs in which the fits to a late-type and an early-type galaxy (shown in Figure 2.2) were launched with a broad range of input parameter values in order to assess the stability of the corresponding best-fit models with respect to input parameter combinations. For both galaxies a basic set of input parameters (for a single Sérsic profile) was chosen based on a visual inspection of the galaxy images. One of these input parameters was then varied over a representative range of values while all others remained at their default initial estimate. The outcome of this test is shown in Figure 2.3 for the late-type object and in Figure 2.4 for the early-type

[3] Online documentation for these is available on the world-wide web at:
`http://www.mpa-garching.mpg.de/~dimitri/budda.html` (BUDDA),
`http://www.ociw.edu/~peng/work/galfit/galfit.html` (GALFIT),
`http://web.pd.astro.it/pignatelli/GASPHOT/` (GASPHOT), and
`http://www.hia-iha.nrc-cnrc.gc.ca/STAFF/lsd/gim2d/` (GIM2D).

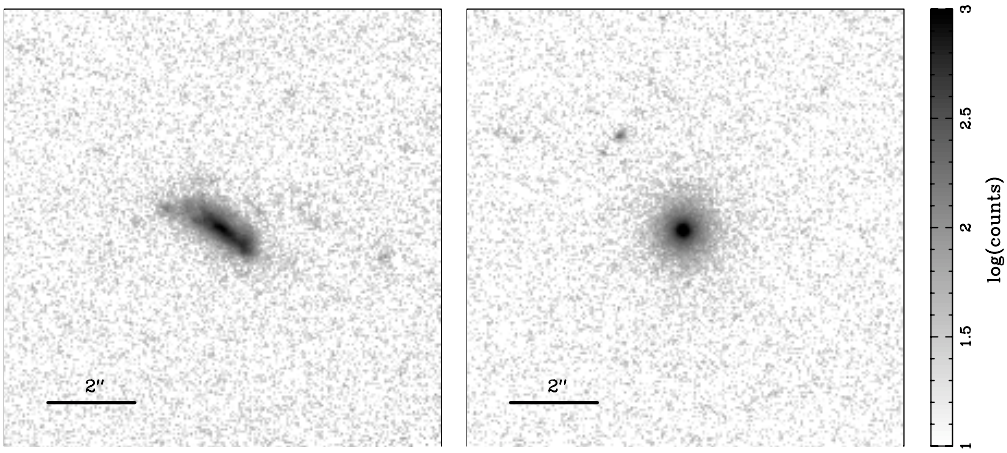

Fig. 2.2 — Examples of a late-type (*left*) and an early-type (*right*) galaxy in the COSMOS sample with which the performance of two parametric fitting codes (GIM2D and GALFIT) was tested when initial parameter guesses were systematically varied (see Section 2.1.1).

galaxy. Solid lines in different colours (one for each of the five Sérsic parameters, namely magnitude I, half-light radius $R_{1/2}$, Sérsic index n, axis ratio b/a and position angle ϕ; see also explanation of colour scheme in the lower right corner of the figures) show the best fit model parameters put out by GIM2D while dotted lines mark those returned by GALFIT. The output Sérsic index n has been normalized to the theoretical value expected for a disk and an elliptical galaxy, i.e., $n = 1$ and $n = 4$, respectively. In each of the five panels a different input quantity is varied.
For the late-type galaxy it is immediately obvious from Figure 2.3 that both codes return very similar best-fit parameters. Moreover, the values of the best-fitting parameters depend neither on the variation of a given individual input quantity (the only exception being the jumpy behaviour displayed by GALFIT for position angles smaller than 90° in the panel in the lower left corner) nor on which input quantity is varied.
In the case of the early-type galaxy the set of best-fit parameters put out by either of the codes individually are still robust with respect to both the variation of a given input quantity and the variation of different input parameters. In this example GIM2D and GALFIT only return consistent best-fit values for the axis ratio. Of the other parameters, the divergent results for the position angle can be explained by the fact that the investigated object is nearly circular.

Despite their similar performance when working properly, in the testing phase the algorithm of the GALFIT package failed to converge more frequently than GIM2D. When dealing with a sample of several 10,000 galaxies, a lack of reliability is a serious drawback as it requires frequent manual interventions. We thus gave preference to GIM2D for the automated fitting of the COSMOS galaxy images. The steps involved in running GIM2D on our sample and the optimization of the code for our purposes are the topic of the following section.

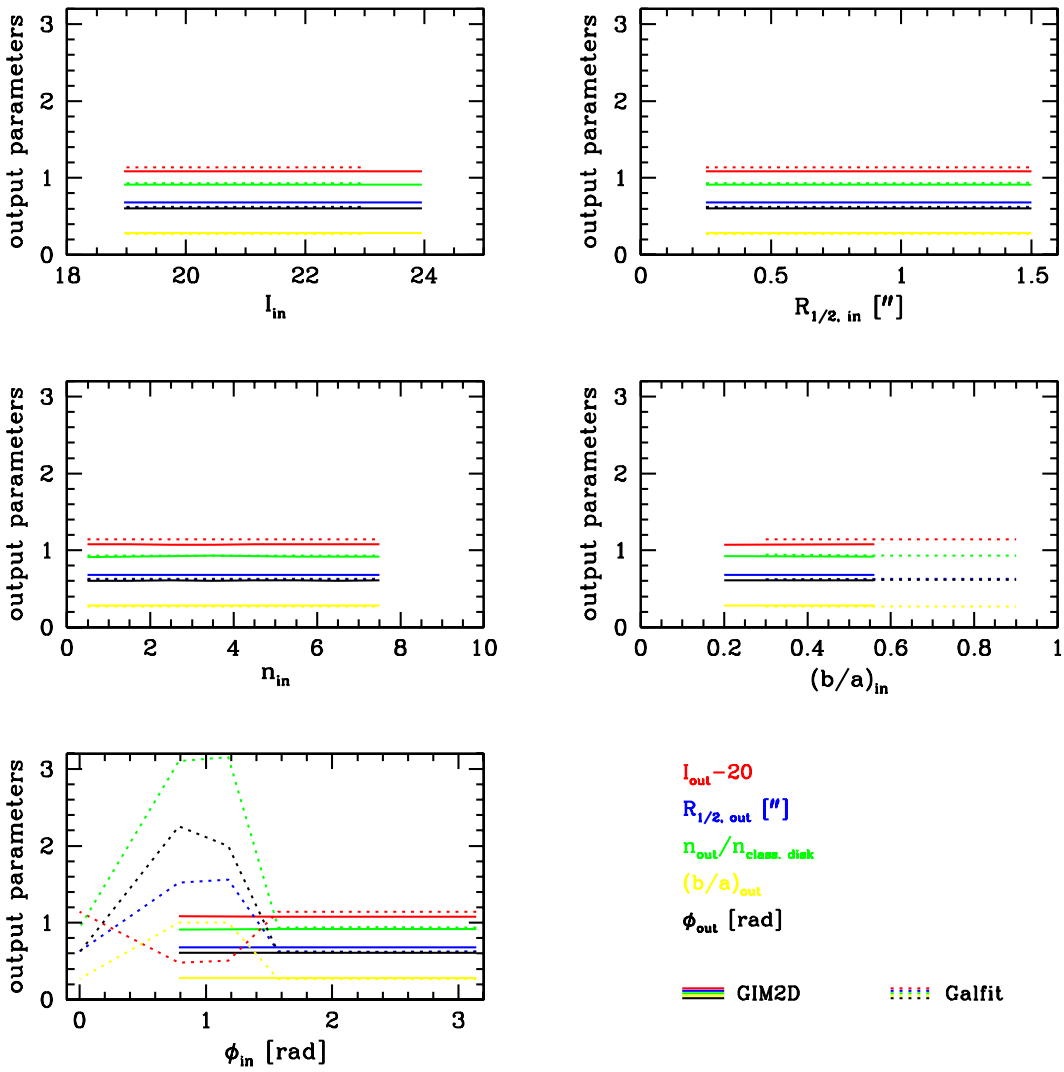

Fig. 2.3 — Dependence of best-fit parameters returned by GIM2D (solid lines) and GALFIT (dashed lines) on initial parameter estimates. The fitting was performed on the disk galaxy shown in the left half of Figure 2.2. Different colours represent the best fitting values of five structural parameters describing a Sérsic profile (magnitude I (rescaled to the plotting range by subtracting 20), half-light radius $R_{1/2}$, Sérsic index n (normalized to the theoretical value of an exponential disk), axis ratio b/a, and the position angle ϕ). In each of the five panels the input parameter that is varied changes.

2.1.2 Two-dimensional GIM2D fits

The `iraf` software package GIM2D (Marleau and Simard [77], Simard et al. [118]) uses the Metropolis algorithm to converge to the analytical model, i.e., it carries out a Monte Carlo sampling of the likelihood function $P(w|D, M)$, which measures the probability that

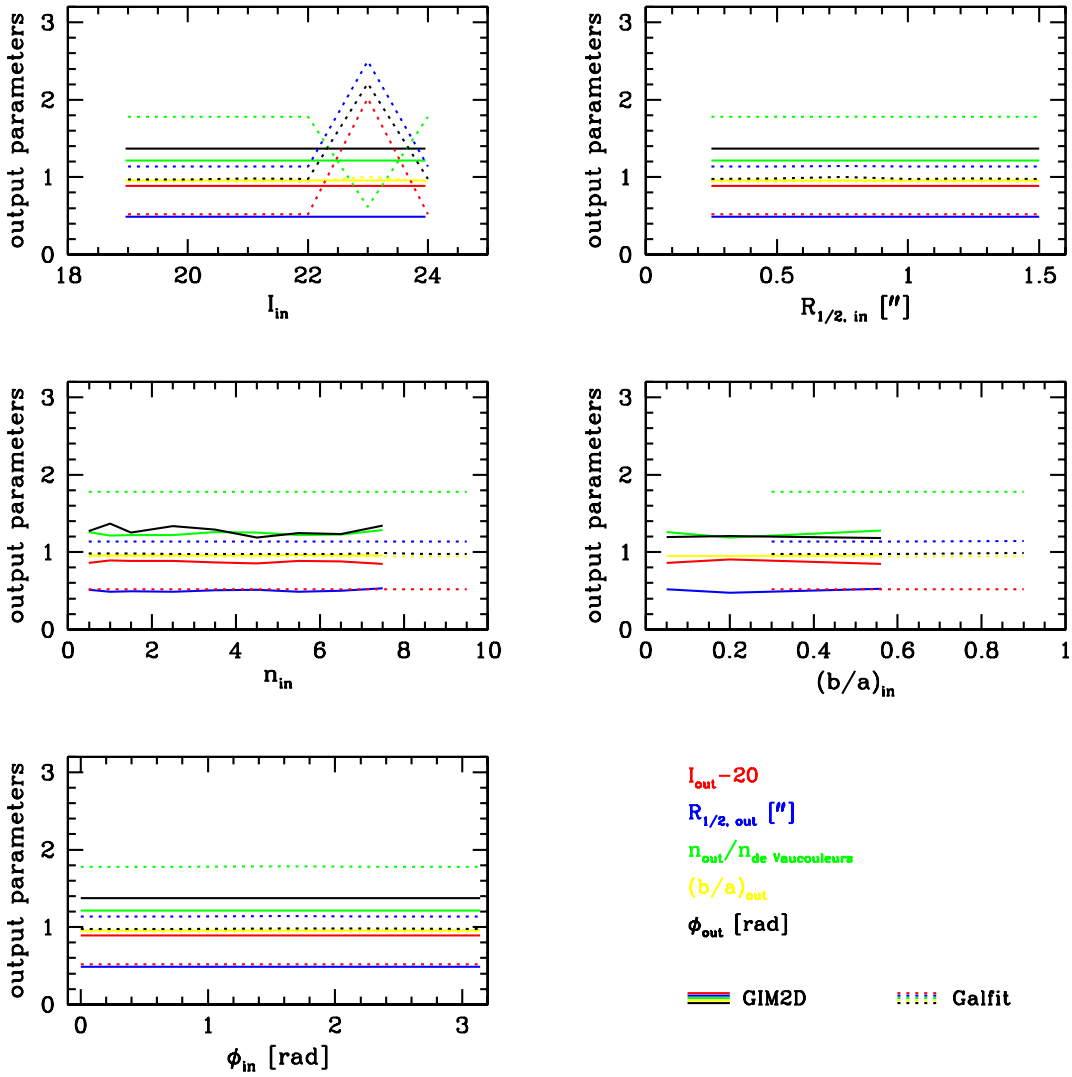

Fig. 2.4 — Same as in Figure 2.3 but for the early-type galaxy depicted in the right half of Figure 2.2. (Note that the values of the Sérsic index n have been normalized to the value of de Vaucouleur profile rather than an exponential profile as in the previous figure.)

the parameter combination w is the correct one given the data D and the model M. The Monte Carlo approach of sampling the complex multidimensional topology of parameter space has the virtue of converging consistently to the same best fit model for a wide range of initial guesses.

In our analysis, we adopt the simple single Sérsic (Sérsic [114]) profile of equation (2.1) to describe the two-dimensional surface brightness distribution of a galaxy. The flexible form of the Sérsic law has the advantage of parametrizing, through the variable exponent n, surface brightness distributions including the exponential radial falloff of the light profile in bulgeless disks ($n = 1$), and the classical de Vaucouleur profile encountered in elliptical

galaxies ($n = 4$).
In the case of a single Sérsic model, GIM2D seeks the best fitting values for the following eight parameters: the total flux F_{tot} (integrated to $R = \infty$); the half-light radius $R_{1/2}$; the ellipticity $e = 1 - b/a$, where a and b are the semimajor and semiminor axes of the brightness distribution; the position angle ϕ; the offsets dx and dy from the initially specified centre of the galaxy; the residual background level db and the value of the Sérsic index n.

The procedure followed to obtain Sérsic models for the galaxies in our sample involved the following steps:

- *Definition of the area to fit.* – For each galaxy, GIM2D was instructed (by means of a *mask image*) to fit the distribution of light within an elliptical area with a semimajor axis equal to 1.5 Petrosian radii[4] (Petrosian [91]) of the target galaxy and an ellipticity equal to the flattening of the SExtractor segmentation map (the latter defines the pixels associated with the object). The orientation of this Petrosian ellipse is also provided by SExtractor. During the fitting, the algorithm considers both pixels assigned to the objects of interest and those flagged as background in the *mask image*. The goodness of the fit (i.e., χ^2), on the other hand, is estimated based on the difference betweeen image and model for pixels within the Petrosian ellipse.

- *Generation of stamp images.* – For each galaxy we extracted a *stamp image*, centered on the coordinates of the ACS-based catalog, from the reduced ACS images. The *stamp images* were (1) no smaller than $10'' \times 10''$ and (2) always sufficiently large to guarantee a proper computation of the local background for all target galaxies. Point (2) is ensured by choosing the stamp size such as to contain at least the same number of "background" pixels outside the masking area as lie within an ellipse with semimajor axis equal to a single Petrosian radius, centered on the target galaxy.

- *Generation of cleaned images.* – To optimize the quality of the fits, we allowed GIM2D to improve the determination of the center of the galaxy with respect to the coordinates specified in the catalog. Furthermore, GIM2D computed the value of the background prior to starting the fit. Bright objects that are located near the galaxy to be fit can cause an inaccurate calculation of the background, and an incorrect estimate of the galaxy center. To prevent these potential errors from affecting the quality of our Sérsic models, we cleaned the galaxy stamp images of all close companions. In this cleaning procedure pixels in the stamp image that were associated with sources other than the one of interest were replaced by values reproducing the properties of the surrounding background (this was based on a segmentation map

[4] The Petrosian radius r_P is the radius at which the surface brightness in a thin annulus equals a given fraction of the average surface brightness within that radius, in our case a fraction of 20%. Since it is computed from the ratio of two surface brightness values, the Petrosian radius is effectively *independent of redshift*. That is, because surface brightness dimming does not change the shape of a galaxy's light profile it also does not affect the estimate of the Petrosian radius r_P. It thus provides a robust and consistent definition of the area over which to perform our GIM2D fits.

accompanying the ACS catalog; see Scarlata et al. [103] for details). We used these *cleaned images* in the following steps.

- *Symmetrization of galaxy images.* – We used GIM2D to produce a symmetrized version of the cleaned galaxy image. This was done by rotating the galaxy by 180°, subtracting the rotated image from the cleaned image, setting all pixels with values smaller than 2σ of the *cleaned image*'s background in the difference image to zero, and, finally, subtracting this clipped difference image from the *cleaned image*. These *symmetrized images* were used as input to GIM2D in order to converge to a satisfactory model of the galaxy light distribution more reliably and quickly.

- *Initial launch parameters and allowed parameter space.* – Given the robustness of GIM2D with respect to changes in the initial parameters (see sections 2.1.1 and 2.1.3), we started all our fits with the same initial values of galaxy structural parameters, namely, $I = 21$, $R_{1/2} = 10$ px, $\epsilon = 0.5$, $\phi = 0°$ and $n = 4$. The calculation of a pure Sérsic profile is achieved by fixing the ratio of flux in the bulge to the total flux, B/T, to unity. Structural parameters were allowed to vary within the following ranges: $I \in$ [17.5, 26.7], $R_{1/2} \in$ [1 px, 50 px], $\epsilon \in$ [0, 1], $\phi \in$ [-180°, 180°] and $n \in$ [0.2, 9]. We inspected the relatively small number of galaxies that appeared to genuinely require values outside these ranges, and allowed the parameters to converge to best fits outside those boundaries when our visual inspection confirmed the quality of the fits.

- *Adopted Point Spread Functions (PSFs).* – We select a different PSF for each individual object based on its position on the tile and the current focal length of the ACS due to in-orbit breathing at the time of the exposure (Rhodes et al. [95]).

The outcome of the GIM2D profile fitting is illustrated for selected galaxies of different morphological types (cf. Section 2.2) in Chapter 3. In particular, Figure 3.1 and Figures 3.2a to 3.2f in show examples of input, model and residual stamps.

2.1.3 Reliability of parametric GIM2D fits

Simulations

To quantitatively test the robustness of the GIM2D fits, we performed a set of simulations of an equal number of pure exponential disks ($n = 1$) and pure de Vaucouleur galaxies ($n = 4$) with a range of half-light radii and magnitudes (and ellipticities) covering the observed parameter space.
The simulated galaxies were generated with the `iraf` task `mkobjects`, which automatically adds a component of Poisson noise to the flux of the source. Source-independent background noise was estimated from five regions of pure sky in different ACS-tiles of the COSMOS survey. An average standard deviation from these regions was used to scale a

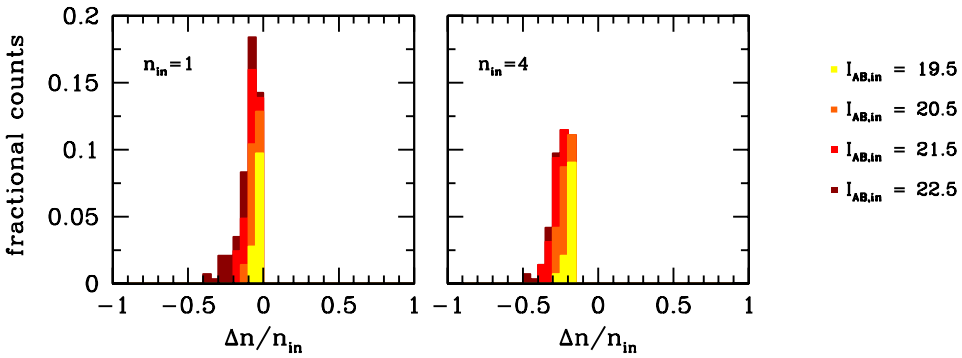

Fig. 2.5 — Dependence of the error in the recovered Sérsic index n on input magnitude I_{in}. On the left we plot the distribution of normalized difference between the nominal n value and the Sérsic index recovered by GIM2D for $n_{in} = 1$ galaxies, on the right the same for objects with a nominal Sérsic index of $n_{in} = 4$.

Gaussian white noise distribution, in order to match the average background characteristics of the COSMOS images. The SExtractor measurements and the GIM2D fits for the simulated galaxies were carried out in an analogous way to the measurements and fits of the COSMOS galaxies (cf. Section 2.1.2).

Figures 2.5 and 2.6 summarize the main results obtained with the galaxy simulations. Figure 2.5 shows the distribution of normalized difference between the input and the recovered Sérsic indices n, as a function of galaxy magnitude and separately for both the $n = 1$ (left) and the $n = 4$ galaxies (right). Figure 2.6 shows the comparison between the input half-light radii and those derived from the GIM2D fits; in particular, the figure shows the distribution of the normalized difference between GIM2D and input half-light radii – separately for the $n = 1$ and the $n = 4$ galaxies as in the previous figure – as a function of magnitude (upper half) and of galaxy size (lower half).
The GIM2D fits tend to underestimate the galaxy sizes. It does so to varying degrees, depending on galaxy magnitude and size, and on the shape of the profile. For example, the radii are underestimated by 3% and 10% for $n = 1$, $I > 21$ galaxies with half-light radii smaller or equal to, or larger than, 10 pixels, respectively. The corresponding comparison for the $n = 4$ galaxies yields systematic uncertainties on the order of 20% and 40%, respectively.

It should be emphasized that the vast majority of disk galaxies in our sample is well described by a $n = 1$ Sérsic profile (see e.g., Figure 3.4) and that none of the galaxies in our sample selected to be disk galaxies are well represented by a smooth, pure de Vaucoleur profile which would be appropriate for a disk-less spheroid. By construction, the ZEST-selected disk galaxies of our study posess a visible disk component, even if the single-Sérsic fits that we have performed return an n =4 profile. Nonetheless, we included the limiting pure de Vaucouleur cases in our simulations, to be able to derive conservative estimates for the systematic errors in our GIM2D measurements.

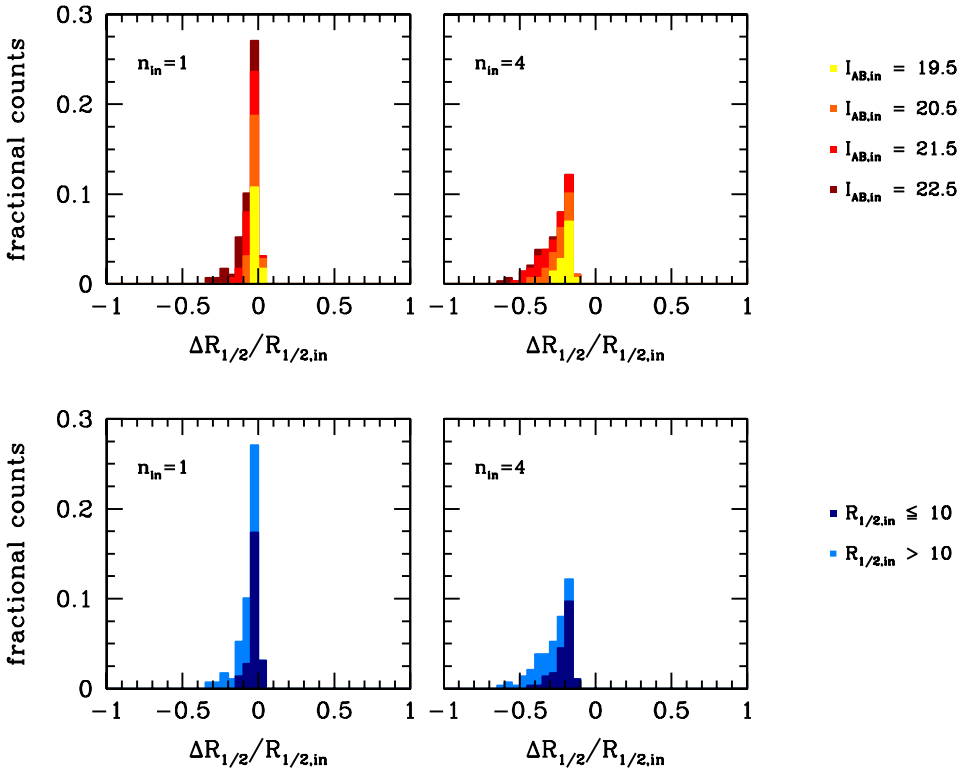

Fig. 2.6 — *Upper panel*: Distribution of normalized difference between the nominal input half-light radius of the simulated galaxies and the half-light radii recovered with the GIM2D fits as a function of magnitude. – *Lower panel*: As above, but showing the distribution for galaxies with input half-light radii smaller and larger than 10 pixels.

Susceptibility to PSF Variations

Although we did not expect the outcome of single Sérsic fits to depend strongly on small variations of the PSF, we carried out tests with varying PSFs on a few COSMOS galaxies. The outcome of such a test for one of these objects is illustrated in Figure 2.7. The six panels show the distribution of parameters put out by GIM2D if the galaxy is fitted with 250 different PSFs extracted in a (spatially) regular fashion from the total of 2500 PSFs generated by Rhodes et al. [95] for each ACS tile to study weak lensing maps. The results of the PSF tests confirm that the GIM2D fits are very robust to possible variations of the PSF as can occur due to spatial variations across the ACS-tiles. Changes in the Sérsic index and half-light radius were found to lie well below a level of 10%.

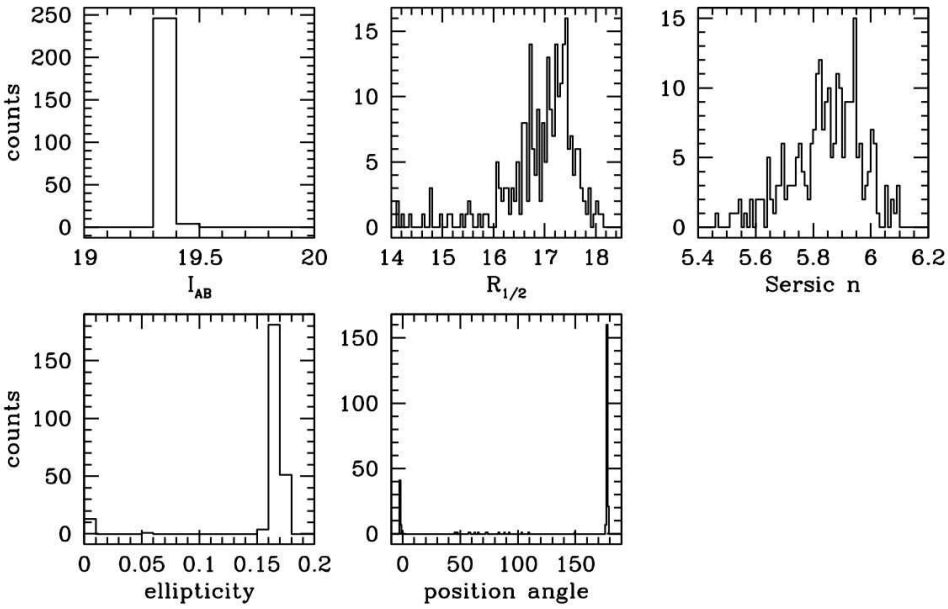

Fig. 2.7 — Variation of GIM2D output for a specific galaxy when fit using 250 different point spread functions from the collection of PSFs employed in our work. The PSFs have been derived for different individual ACS tiles, and vary as a function of position within a single tile.

2.2 Morphological classification of COSMOS galaxies with the 'Zurich Estimator of Structural Types' (ZEST)

We developed the Zurich Estimator of Structural Type (ZEST) to facilitate an automated and quantitative morphological description of the galaxies in the large COSMOS data set. ZEST combines:

- a Principal Component Analysis (PCA) of five non-parametric measures of galaxy structure, i.e., asymmetry A, concentration C, Gini coefficient G, 2nd-order moment of the brightest 20% of galaxy pixels M_{20} (e.g., Abraham et al. [2], Lotz et al. [75]), and the ellipticity ϵ. The PCA reduces the redundancy of information that is present in these five quantities, without substantial loss of information on galaxy structure, and
- a parametric description of the galaxy light, i.e., the exponent n of a single-component Sérsic fit to its surface brightness distribution.

ZEST classifies galaxies based on their location in the three-dimensional space defined by the main three eigenvectors PC_1, PC_2 and PC_3 that contain most of the variance of the

Tab. 2.1 — The ZEST classification scheme.

Parameter	Type 1 Early Types (no visible disk)	Type 2 Disk Galaxies	Type 3 Irregular Galaxies
Bulgeness	...	from 0 (massive bulge) to 3 (bulgeless disk)	...
Elongation	from 0 (face on) to 3 (edge on)	from 0 (face on) to 3 (edge on)	...
Irregularity	from 0 (regular) to 2 (highly irregular)	from 0 (regular) to 2 (highly irregular)	...
Clumpiness	from 0 (smooth) to 3 (very clumpy)	from 0 (smooth) to 3 (very clumpy)	...

Note. — Summary of the ZEST classification scheme. Type 1 (early-type galaxies) are spheroids with no visible disk (including face-on S0 galaxies, for which the identification of the disk component is difficult). Type 2 are disk galaxies, and Type 3 are irregular galaxies. A clumpiness parameter is assigned to each to each galaxy depending on the ZEST unit cube in which it is found. Early-type and disk galaxies are assigned an elongation parameter in four steps from 0 (face-on) to 3 (edge-on), and an irregularity parameter (from 0 for regular to 2 for highly irregular galaxies). Type 2 disk galaxies are split in four "bulgeness" categories, namely 2.0, 2.1, 2.2 and 2.3 for sources ranging from bulge-dominated to bulgeless disks, respectively. Relatively inclined S0 galaxies occupy cubes classified as $T = 2.0$.

original non-parametric quantities. The Sérsic indices are used to refine the classification of disk galaxies by splitting these into four separate categories according to the value of a bulgeness parameter which correlates with the bulge-to-disk (B/D) ratio. To each galaxy the ZEST classification scheme assigns (see also 2.1):

1. a morphological type (1, 2 or 3 for early-type, disk and irregular galaxies, respectively),

2. a bulgeness parameter for the type 2 disk galaxies, which coarsely correlates with the B/D ratio; the disk galaxies are split in four bins, from pure disk galaxies ($T = 2.3$) to bulge-dominated disks ($T = 2.0$),

3. an elongation parameter (four bins, respectively from 0 for face–on to 3 for edge–on galaxies)

4. irregularity and clumpiness parameters for type 1 and 2 galaxies, which indicate whether the galaxy light distribution is regular and smooth or rather distorted and clumpy.

2.2.1 Non-parametric quantification of galaxy structure

The following paragraphs describe which steps were taken to construct the ZEST classification grid. It also contains an assessment of the inherent uncertainties and systematics in the measurements of non-parametric estimators of galaxy structure.

Methodology

The advantage of a principal component analysis in general and of the ZEST PCA in particular is that the number of different but not independent structural variables is reduced to a new and smaller set of variables (the principal components) which are linear combinations of the initial quantities. ZEST uses four widely adopted non-parametric measurements of the light distribution in galaxies (e.g., Abraham et al. [2], Lotz et al. [75]), plus a measurement of the ellipticity of a galaxy's distribution of light, as its basic quantities:

1. The concentration quantifies the central density of galaxy light. It is computed according to

$$C = 5\ \log\left(\frac{r_{80}}{r_{20}}\right)\ , \tag{2.3}$$

   where r_{80} and r_{20} stand for the radii including 80% and 20% of the total galaxy light, respectively,

2. The asymmetry parameter A describes the degree of rotational symmetry of a galaxy's flux. A is measured by calculating the normalized difference between the galaxy image and the image rotated by 180°. A correction for background noise is also applied (as in Conselice et al. [26], Lotz et al. [75]), i.e.:

$$A = \frac{\sum_{x,y} |I_{(x,y)} - I_{180(x,y)}|}{2\sum |I_{(x,y)}|} - B_{180}; \tag{2.4}$$

   where I is the galaxy flux in pixel (x, y), I_{180} is the image rotated by 180° about the galaxy's central pixel, and B_{180} is the average asymmetry of the background.

3. The Gini coefficient G expresses how uniformly the flux is distributed among galaxy pixels. G can vary from 0, in which case a galaxy's light is homogeneously distributed among all galaxy pixels, to 1 if all the light is concentrated in one pixel (regardless of its position in the galaxy). After ordering the pixels by increasing flux, G is computed according to:

$$G = \frac{1}{\overline{X}n(n-1)} \sum_{i}^{n} (2i - n - 1)X_i, \tag{2.5}$$

where n is the number of pixels assigned to a galaxy, and $\overline{X}$ is the mean pixel value (Glasser [53]).

4. The second order moment of the brightest 20% of a galaxy's pixels is given by

$$M_{20} = \log\left(\frac{\sum_i M_i}{M_{tot}}\right), \quad \text{while} \quad \sum_i f_i < 0.2 f_{tot} \ . \tag{2.6}$$

Here

$$M_{tot} = \sum_i^n M_i = \sum_i^n f_i \left[(x_i - x_c)^2 + (y_i - y_c)^2\right]$$

is the total second order moment. For centrally concentrated objects, M_{20} correlates with the concentration C; however, M_{20} is also sensitive to bright off-centered knots of light.

5. The ellipticity $\epsilon = 1 - b/a$ of the light distribution is measured by SExtractor (Bertin and Arnouts [9]). SExtractor computes the semi-major axis a and semi-minor axis b from the second order moments of galactic light; specifically, a and b are the maximum and minimum spatial variance (rms) of the object, along the direction θ where the variance is maximized:

$$\begin{aligned} a^2 &= \frac{\overline{x^2} + \overline{y^2}}{2} + \sqrt{\frac{\left(\overline{x^2} - \overline{y^2}\right)^2}{4} + \overline{xy}^2}, \\ b^2 &= \frac{\overline{x^2} + \overline{y^2}}{2} - \sqrt{\frac{\left(\overline{x^2} - \overline{y^2}\right)^2}{4} + \overline{xy}^2}, \end{aligned}$$

where the second order moments $\overline{x^2}$, $\overline{y^2}$, and $\overline{xy}$ are given by:

$$\begin{aligned} \overline{x^2} &= \frac{\sum_i I_i x_i^2}{\sum I_i} - \overline{x}^2, \\ \overline{y^2} &= \frac{\sum_i I_i y_i^2}{\sum I_i} - \overline{y}^2, \\ \overline{xy} &= \frac{\sum_i I_i x_i y_i}{\sum I_i} - \overline{xy}. \end{aligned}$$

The values of a and b are thus representative of the galaxy ellipticity at large radii, and are rather insensitive to details in the internal structure (e.g., bars in disk galaxies, knots of star formation, etc.).

Uncertainties and systematics in the morphological measurements

To quantify the errors in the measurement of C, A, G, M_{20} and ϵ for the COSMOS galaxies, and to assess systematic trends as a function of galaxy brightness, extensive simulations based on real, bright COSMOS galaxies were performed. They involved 35 isolated COSMOS galaxies with magnitude between $I = 17.5$ and $I = 18$, each of which was used to create 40 S/N-degraded versions of the original image. This was done by dividing the original frame by a factor f such that the final magnitude of the object was $2.5 \log(f)$ fainter than the original one. The factor f was chosen such that each galaxy uniformly sampled the magnitude range from 18 to 24. The scaled images were then added back to an ACS tile, in randomly-selected positions. Before adding the rescaled image, the original ACS tile was multiplied by a factor k, to preserve the noise properties in the final image. If $\sigma_{\rm orig}$ denotes the background noise in the image containing one of the 35 bright galaxies, the background noise after the rescaling became $\sigma_{\rm orig}/f$. Adding the rescaled image to the ACS original image increases the noise in the final image to $\sigma^2_{\rm final} = \sigma^2_{\rm orig} + \sigma^2_{\rm orig}/f^2$. The factor k was therefore computed by requiring that $\sigma^2_{\rm final} = \sigma^2_{\rm orig} = \sigma^2_{\rm orig}/k^2 + \sigma^2_{\rm orig}/f^2$.

The results of this set of simulations are illustrated in Figure 2.8 where the fractional change of each parameter is given as a function of the magnitude of the S/N-degraded galaxy. Lines connect the variation of the parameters for each of the 35 galaxies as a function of magnitude.
For all parameters (except ϵ) the scatter remains below about 10-20% and no strong systematic effects are observed down to $I \sim 22$. At magnitudes $I > 22$ the scatter increases and all parameters are systematically underestimated up to a maximum of ∼20% in the faintest magnitude bin. The behavior of ϵ shows a different trend, with the scatter starting to increase already at bright magnitudes (at a level of ∼10%) and systematic effects start to be important at $I \sim 23$. The asymmetry A is systematically underestimated at the 10% level for $I-$band magnitudes of order 21, and degrades down to a 20% underestimate for $I = 24$.

2.2.2 Principal Component Analysis with ZEST

The quantities above provide complementary, but also redundant information on galaxy structure. Thus a PCA analysis was performed using the measurements of A, C, M_{20}, G and ellipticity ϵ as basic variables.

The PCA is a classical statistical method for multivariate analysis which reduces the dimensionality of a dataset without a significant loss of information. This is done by transforming the observed variables into a new set of orthogonal variables, the *principal components* "PC_i", (with $i = 1, \ldots\ n$, and n the number of basic parameters, i.e., initial variables). The PC_i are ordered so that the first few of them retain most of the variance present in the original dataset. They represent a linear combination of the original variables, and define a new coordinate system obtained by rigid rotation of the original space.

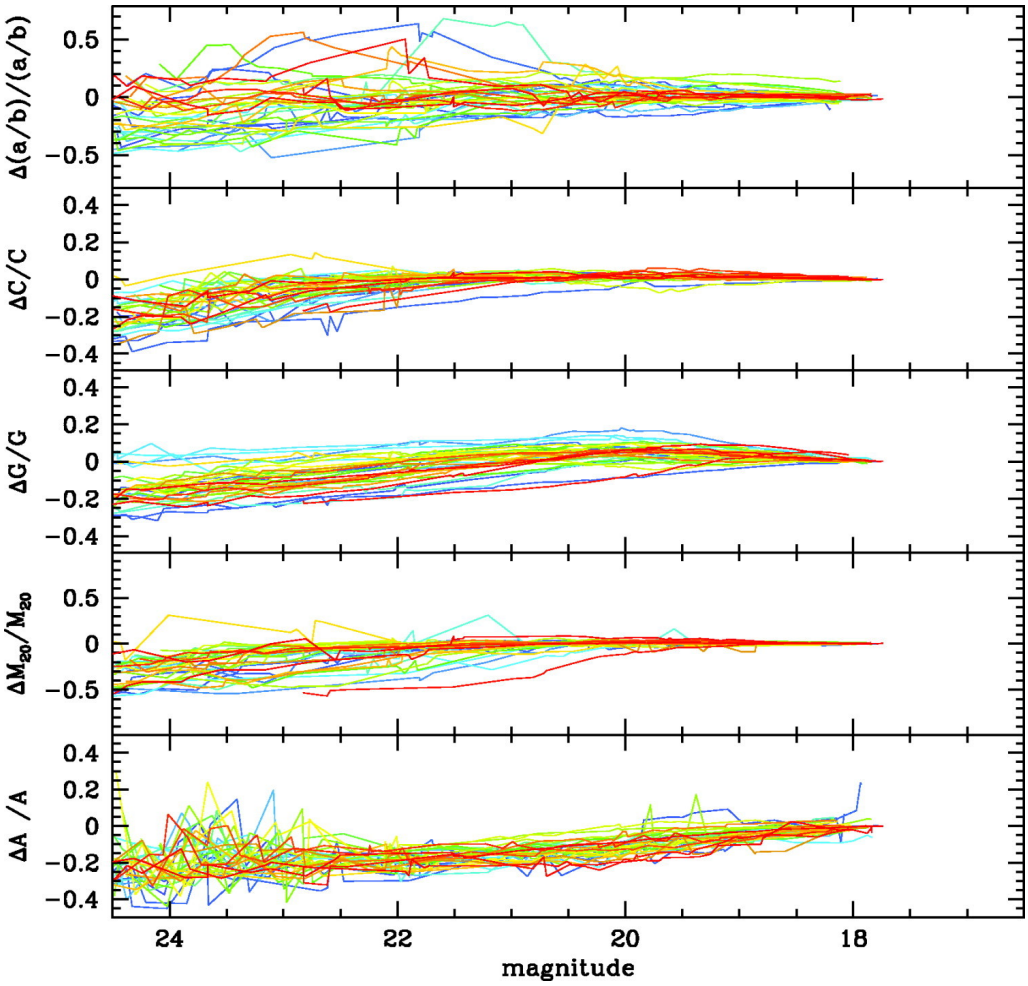

Fig. 2.8 — Results of the simulations performed by degrading the S/N of real galaxies (see text for details) to assess systematic changes in non-parametric estimators of galaxy structure. Lines in each panel show the fractional variation of the parameter as a function of magnitude (each line shows a different galaxy). From top to bottom we show the relative changes in ellipticity, concentration, Gini, M_{20}, and asymmetry. Systematic effects are <20% over the whole range of observed magnitudes.

In the new system, the axes define the directions of maximum variability in the original $n-$dimensional distribution of points.
In the present case the dataset is described by an $n \times m$ data matrix, where $n = 5$ in the current version of ZEST and m is the number of galaxies with measured basic parameters. All variables are standardized before performing the analysis by subtracting their median value (indicated with an overline in the following expressions) and normalizing them with their standard deviation. Therefore the five variables considered in the ZEST PCA are defined as $x_1 = (C - \overline{C})/\sigma_C$, $x_2 = (M_{20} - \overline{M_{20}})/\sigma_{M_{20}}$, $x_3 = (G - \overline{G})/\sigma_G$, $x_4 = (\epsilon - \overline{\epsilon})/\sigma_\epsilon$, and $x_5 = (A - \overline{A})/\sigma_A$.

The direction of the principal components is derived by calculating the eigenvectors of the $n \times n$ covariance matrix of the x_j variables (i.e., of the matrix $S_{ij} = \langle (x_i - \langle x_i \rangle)(x_j - \langle x_j \rangle) \rangle$). The matrix $S \geq 0$ is real and symmetric and as such admits real, positive eigenvalues λ_i. By sorting the eigenvectors in order of decreasing eigenvalues, an ordered orthogonal basis is obtained, with eigenvectors aligned along directions of decreasing variance $(\lambda_i / \sum_j \lambda_j)$ in the data. The first few principal components that account for most of the power – i.e., most of the total variance, $\sum_j \lambda_j$, in the data set – are then used to replace the original n variables without any significant loss of information (so the assumption).

2.2.3 ZEST calibration with 56,000 $I < 24$ COSMOS galaxies

Once the new axes in parameter space (defined by the orientation of the eigenvectors derived in the course of the principal component analysis, see previous section) are defined, the next step in the development of a morphological galaxy classification scheme is to identify in which part of parameter space different types of objects reside. This "calibration" of the ZEST classification grid was carried out using a sample of ∼56,000 $I <$ 24 COSMOS galaxies detected in the 260 ACS F814W images acquired during the HST Cycle 12 observing period. The total area covered by this fraction of the COSMOS field is 0.74 deg^2.

For each COSMOS galaxy, we measured the basic non-parametric quantities described in Section 2.2.1 by computing them on the galaxy pixels (defined using Petrosian apertures). Figure 2.9 shows the behavior of each basic non-parametric diagnostic as a function of the others. The contours in each panel enclose, respectively, 30%, 80% and 98% of the COSMOS galaxies in our sample. Some global correlations are known to exist between various non-parametric coefficients. For example, a relatively tight relation is observed between G, M_{20}, and C, with objects of high C tending to have low M_{20} and high G. Any value of C may occur for small values of A, while high values of A are preferentially observed in low-C galaxies. These trends have already been noted in the literature, and indeed highlight the redundancy of information present in this set of parameters. As expected, the ellipticity ϵ does not correlate with any of the other parameters, except for a mild positive correlation with the concentration for $\epsilon > 0.6$. This is a geometric effect, since edge-on galaxies preferentially have high C values.

The results of the PCA on the normalized COSMOS dataset are presented in Table 2.2. Columns 2-6 refer to the five principal components derived in the analysis. The first row gives the eigenvalue (i.e., the variance) of the data along the direction of the corresponding PC. The second row shows the fraction of the variance that is explained by each of the PCs, i.e., the fraction of the "power" that is contained in each PC; the third row lists the cumulative fraction of the variance. In the bottom part of the table, each column lists the weights assigned to a given input variable (listed in column 1) in the linear combination that defines the direction of the specific principal component (e.g., $PC_1 = -0.54 \times x_1 + 0.60 \times x_2 - 0.56 \times x_3 + 0.20 \times x_4 + 0.02 \times x_5$).

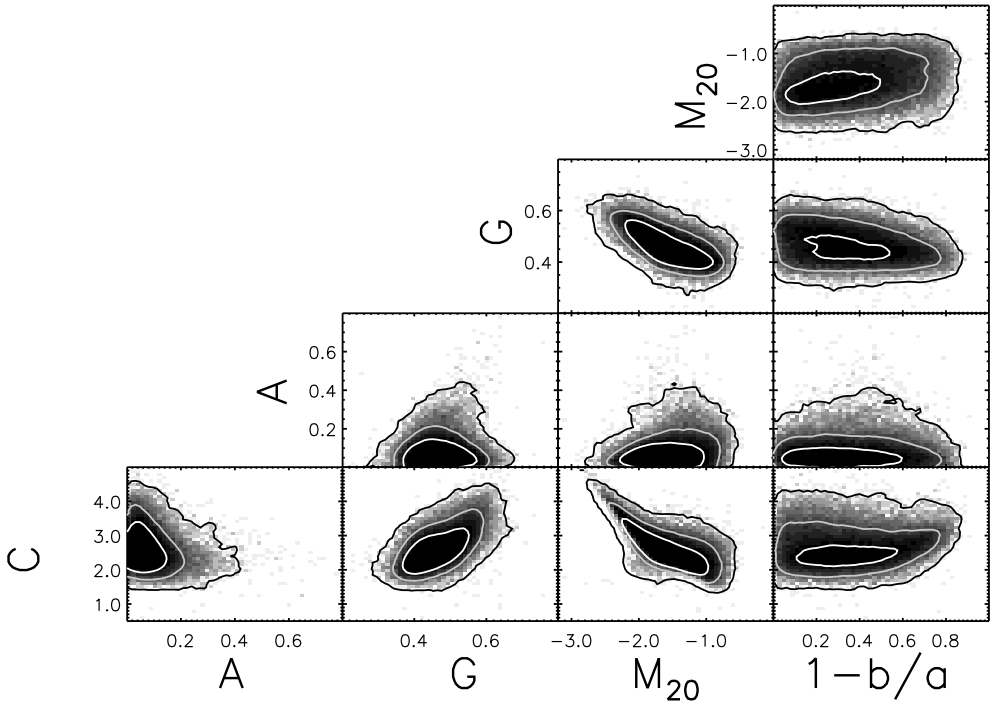

Fig. 2.9 — Relations between the non-parametric diagnostics (M_{20}, G, A, C, and $\epsilon = 1 - b/a$). Contours enclose ∼30% (white contour), 80% (grey contour), and 98% (black contour) of the galaxies. The main correlations among some of the parameters, such as M_{20}, C, and G, are clearly visible in these diagrams.

In Figure 2.10 we show the fraction of the total variance contained in each of the five principal components. Solid circles refer to the PCA applied to the COSMOS galaxies in the considered $I \leq 24$ sample. Open squares refer to the same analysis when it is restricted to COSMOS galaxies brighter than $I = 22.5$. The horizontal line denotes the threshold for the eigenvalues which is expected if each of the five variables were uncorrelated. The comparison of the results for the samples with $I \leq 22.5$ and $I \leq 24$ demonstrates the stability of the analysis down to the faintest magnitudes in the sample.

As discussed in Section 2.2.1, the scatter in the measured variables that define the PCs increases with increasing magnitude (the scatter at $I = 24$ is twice the scatter measured at $I = 22$). While the larger scatter in the data could potentially wash out correlations present in the original parameters, this effect is negligible down to the considered $I = 24$ magnitude limit: e.g., the fraction of variance in PC_1 is only ∼3% larger for galaxies with $I \leq 22.5$ relative to a sample including all objects down to $I \leq 24$.

Several methods have been proposed in the literature to establish the number of PCs which are sufficient to fully describe the properties of the sample; all methods require some degree of judgment. For example Kaiser [61] proposes the rule-of-thumb of rejecting all

Tab. 2.2 — Results of the ZEST principal component analysis

Variable (1)	PC_1 (2)	PC_2 (3)	PC_3 (4)	PC_4 (5)	PC_5 (6)
Eigenvalue	2.46	1.19	0.92	0.25	0.17
Proportion	0.49	0.24	0.18	0.05	0.03
Cumulative	0.49	0.73	0.92	0.97	1.00
Concentration ($=x_1$)	−0.54	0.35	0.18	−0.34	−0.66
M_{20} ($=x_2$)	0.60	−0.04	0.03	0.39	−0.70
Gini ($=x_3$)	−0.56	−0.20	0.14	0.79	−0.02
Ellipticity ($=x_4$)	0.20	0.57	0.74	0.16	0.26
Asymmetry ($=x_5$)	0.02	−0.71	0.64	−0.29	−0.08

Note. — Columns 2-6 refer to the five principal components in ZEST. The first row gives the eigenvalue (i.e., variance) of the data along the direction of the corresponding PC. The second and third row show the fraction of the variance and the cumulative fraction of each PC, respectively. The bottom part of the table lists the weights assigned to each input variable in the linear combination that defines the direction of the principal component (i.e., $PC_i = \alpha \mathrm{x}_1 + \beta \mathrm{x}_2 + \gamma \mathrm{x}_3 + \delta \mathrm{x}_4 + \phi \mathrm{x}_5$, with the coefficients α,... , ϕ given by the numbers listed, for each PC, in the bottom part of the table).

components that contain less power than the variance expected for uncorrelated variables (in our case of 5 variables, less than 20%); Jolliffe [60] adopted instead a lower threshold value. To classify galaxy structure, we will use the first three PCs; these explain 92% of the total variance. The ZEST classification grid is therefore constructed in a three-dimensional space in which galaxies are ranked, according to their structural properties, in unit cubes along the ZEST PC_1, PC_2, PC_3 axes.

Morphological classification of the PC_1-PC_2-PC_3 unit cubes

COSMOS Galaxies with different structural properties occupy different regions of PC_1-PC_2-PC_3 space. For example, PC_1 is dominated by C, M_{20}, and G. Highly negative values of PC_1[5] are populated by highly centrally-concentrated galaxies. PC_2 is, on the other hand, dominated by ellipticity and asymmetry: round asymmetric objects are found at negative values of PC_2, and symmetric flattened systems are preferentially located at high positive values of PC_2. PC_3 is also mostly a combination of asymmetry and ellipticity, but in PC_3 these parameters contribute both with positive weights to the absolute value of PC_3. Highly asymmetric and elongated objects are thus located at high values of PC_3.

To associate a (dominant) morphological class to different regions of the PC_1-PC_2-PC_3 space, the latter was partitioned into a regular 3-D grid with unit steps in each of

[5] M_{20} is always negative.

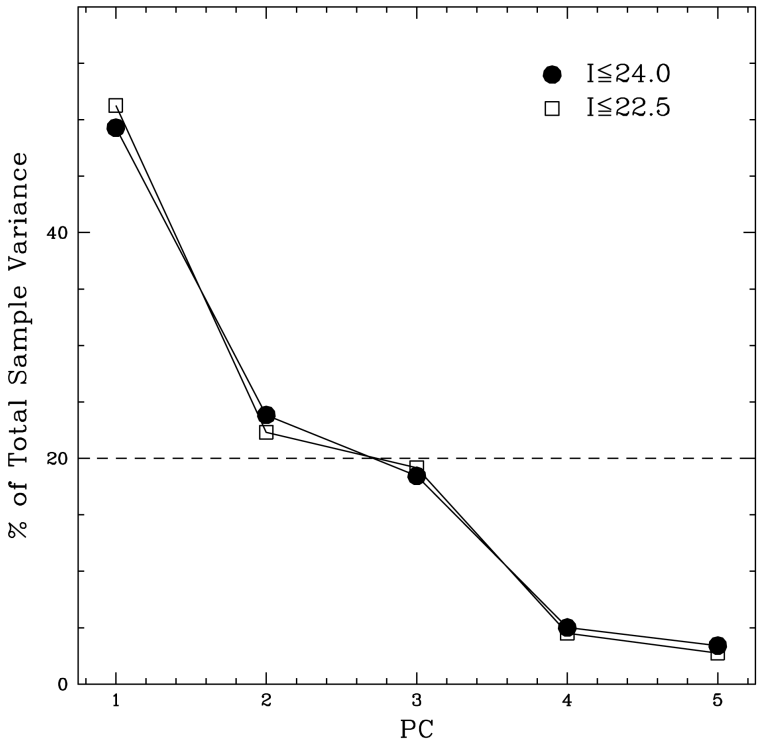

Fig. 2.10 — Fraction of the total variance explained by each principal component as a function of the corresponding principal components for all galaxies down to $I = 24$ in the ACS–catalog (solid circles). Open squares refer to the same analysis performed only on those objects with magnitude brighter than $I = 22.5$. The horizontal line indicates 20% of the total variance, i.e., the value for the five eigenvalues for a sample of 100% uncorrelated variables.

the coordinates, and *all galaxies* in our COSMOS sample within each unit PC_1-PC_2-PC_3 cube were visually inspected. Each unit cube was then assigned a *morphological type* ($T =$ 1, 2 or 3 for early-type, disk and irregular galaxies, respectively; face-on S0 galaxies would of course be found in cubes classified as $T = 1$, while more inclined S0 galaxies would be in cubes classified as $T = 2$), and a *clumpiness parameter* in unit steps, ranging from 0 for smooth surface density distributions, to 2 for very clumpy morphologies). For galaxies with $T = 1$ or 2, we furthermore assigned an *elongation parameter* (in unit steps, from 0 for face-on galaxies, to 3 for edge-on galaxies), and an *irregularity parameter* (in unit steps, ranging from 0 for regular surface density distributions, to 2 for disturbed $T = 1$ or 2 morphologies). A measure of the galaxy sizes (i.e., their Petrosian radii) is also available for all ZEST-classified galaxies, as a by-product of our analysis.

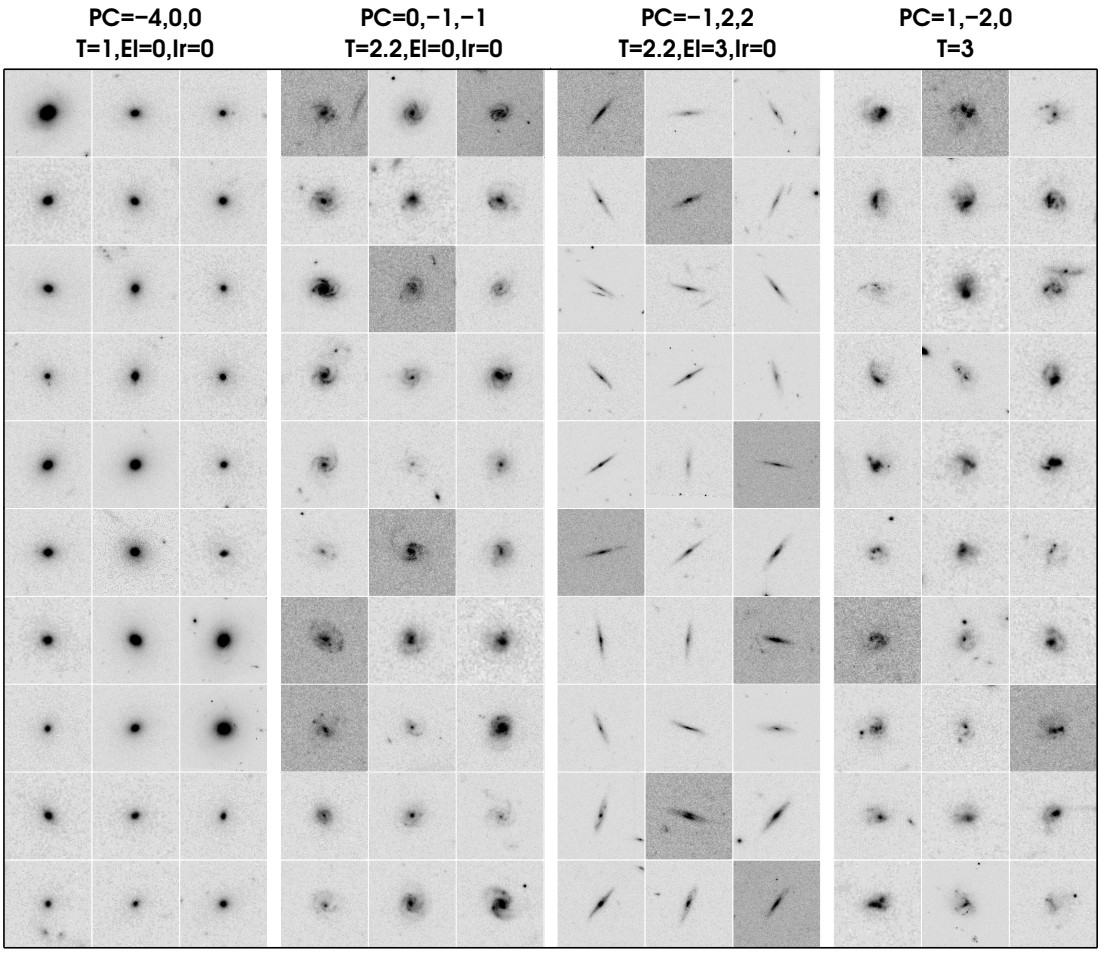

Fig. 2.11 — Illustration of the performance of the ZEST grid in locating COSMOS galaxies with different structural properties in different parts of the three-dimensional PC_1, PC_2, PC_3 space. Four separate unit cubes of PC_1-PC_2-PC_3 are depicted which are centered on the values reported in the labels. In every unit cube, those galaxies shown are representative of the general population of objects in a particular bin.

Bulge-to-disk ratios: Parametric surface brightness fits

To refine the ZEST structural classification of $T = 2$ disk galaxies GIM2D single Sérsic fits (cf. Section 2.1.2) were incorporated in the analysis. This information is available for a subsample of $I \leq 22.5$ COSMOS galaxies. In particular, the statistical distribution of Sérsic indices n was considered within each unit cube of PC_1-PC_2-PC_3 with a $T = 2$ classification. In this manner it was possible to assign a *bulgeness parameter* to each $T = 2$ cube. Specifically, the $T = 2$ unit cubes are split in four bins, i.e, $T = 2.3$, 2.2, 2.1 and 2.0, depending on the value of the median Sérsic index $\overline{n}$ of the galaxies in that cube ($T = 2.3$, 2.2, 2.1, 2.0 for $0 < \overline{n} < 0.75$, $0.75 \leq \overline{n} < 1.25$, $1.25 \leq \overline{n} < 2.5$, and $\overline{n} \geq 2.5$,

Tab. 2.3 — COSMOS ZEST classification grid. (Continued on next page.)

	PC_1									
PC_2	−6	−5	−4	−3	−2	−1	0	1	2	3
					$PC_3 = -2$					
−4										
−3										
−2										
−1						2.2	2.2	2.3	2.3	2.3
0					2.1	2.2	2.2	2.3	2.3	2.3
1					2.2	2.2	2.2	2.2	2.2	2.2
2										
3										
					$PC_3 = -1$					
−4										
−3										
−2					1	2.2	2.2	2.3	3	3
−1			1	1	2.1	2.1	2.2	2.3	2.3	2.3
0			1	2.0	2.1	2.1	2.2	2.3	2.3	2.3
1			2.0	2.0	2.1	2.1	2.2	2.3	2.3	2.3
2										
3										
					$PC_3 = 0$					
−4										
−3					2.1	3	3	3	3	3
−2			1	1	2.0	2.1	3	3	3	3
−1		1	1	1	2.1	2.1	2.2	2.3	2.3	3
0	1	1	1	2.0	2.1	2.1	2.2	2.3	2.3	2.3
1		1	1	2.0	2.1	2.1	2.2	2.3	2.3	2.3
2			2.0	2.1	2.1	2.1	2.2	2.2	2.3	2.3
3										

Note. — COSMOS-calibrated ZEST grid in each plane of constant PC_3, going from PC_3 = -2 (first panel of the table) to PC_3=3 (last panel). In each panel, the ZEST classification into either Type 1, 2 or 3 is specified for each combination of PC_1 and PC_2. For Type 2 disk galaxies, the "bulgeness" parameter associated with the cube is also given. (See also Figure 2.12 for a graphical representation of the information in this table. Note that in Figure 2.12 the PC_2 axis is flipped about the horizontal axis with respect to the layout of this table.)

respectively). This refinement of the Type 2 ZEST classification grid can be interpreted as a classification of disk galaxies in terms of their bulge-to-disk ratio into four bins. Cubes with T = 2.0, 2.1, 2.2 and 2.3 contain galaxies with decreasing B/D ratio (ranging from Type 2.0 – bulge-dominated galaxies, including relatively inclined S0 galaxies – to the bulgeless disks of Type 2.3).

2.2.4 Summary of the ZEST PC_1-PC_2-PC_3 classification scheme & grid

The final ZEST classification scheme is summarized in Table 2.1, and the distribution of distinct morphological families within the COSMOS-calibrated ZEST grid is given in Table 2.3.

Tab. 2.3 — *cont.*

	PC_1									
PC_2	−6	−5	−4	−3	−2	−1	0	1	2	3
					$PC_3 = 1$					
−4										
−3						3	3	3	3	3
−2			1	2.0	2.0	3	3	3	3	3
−1		1	1	2.0	2.0	2.1	2.2	3	3	3
0	1	1	2.0	2.0	2.1	2.1	2.2	2.3	2.3	3
1	1	1	2.0	2.0	2.1	2.2	2.2	2.3	2.3	2.3
2			2.0	2.1	2.1	2.2	2.2	2.3	2.3	2.3
3						2.2	2.2	2.2	2.3	
					$PC_3 = 2$					
−4						3	3	3	3	3
−3					1	3	3	3	3	3
−2				1	1	3	3	3	3	3
−1			1	2.0	2.0	3	3	3	3	3
0		2.0	2.0	2.0	2.1	2.1	2.2	2.3	3	3
1	2.0	2.0	2.0	2.0	2.1	2.2	2.2	2.3	2.3	2.3
2		2.0	2.0	2.0	2.1	2.2	2.3	2.3	2.3	2.3
3				2.1	2.1	2.2	2.3	2.3	2.3	
					$PC_3 = 3$					
−4							3	3	3	
−3							3	3	3	
−2				2.0	2.0	3	3	3	3	
−1				2.0	2.1	2.1	3	3	3	
0			2.0	2.0	2.1	2.1	2.2	2.3	2.3	
1			2.0	2.0	2.1	2.1	2.2	2.3	2.3	
2			2.1	2.1	2.1	2.2	2.2	2.3	2.3	
3										

To show the performance of ZEST in disentangling galaxies with different structural properties, a representative selection of the $I \leq 24$ COSMOS galaxies is plotted in Figure 2.11. These example objects occupy four different unit cubes of PC_1-PC_2-PC_3. Furthermore, in Figure 2.12 we show, in sequential planes of constant PC_3 = -2, -1, 0, +1, +2, +3, a representative galaxy in each of the (PC_3-)PC_1-PC_2 unit bins. Arrows in the lower left corner of each panel (i.e., a plane of constant PC_3) indicate the directions of the steepest (positive) variation for the quantities specified as labels of the arrows. Arrows labeled as "bulgeness" or "irregularity", for instance, show the direction of maximal increase of the "degree of bulgeness" and of irregularity among galaxies occupying a given plane of constant PC_3.

In Figure 2.13 the COSMOS-calibrated ZEST classification grid is illustrated in a schematic way. In each plane of fixed PC_3, different symbols represent the different morphological types, and the different values of the elongation and bulgeness parameter. As indicated in the figure, ellipses represent the $T = 1$ early-type galaxies; concentrical double circles indicate $T = 2$ disk galaxies, and stars represent irregular galaxies classified as $T = 3$. The size of the internal ellipse of $T = 2$ galaxies is proportional to their bulgeness parameter. The continuity of properties in PC_1-PC_2-PC_3 space is immediately

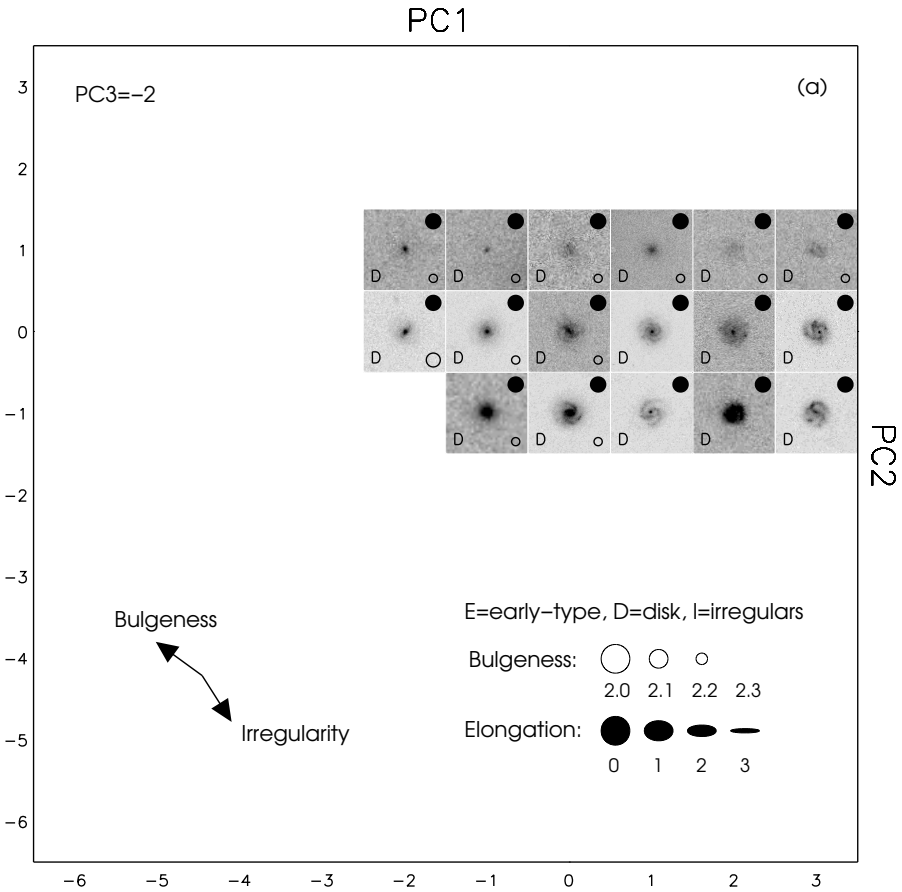

Fig. 2.12 — The stamp of a representative galaxy is shown for each cube of PC, arranged in planes of constant PC_3 in six different panels (a) to (f). In particular the panels show sequentially the PC_3 = -2, -1, 0, 1, 2, 3 planes. Galaxy structural properties – and thus galaxy types – change smoothly through the PC_1-PC_2-PC_3 space.

evident from Figure 2.13. For example, the transition from early-type morphologies (T = 1), to bulge-dominated disks (T = 2.0), to pure disk galaxies (T = 2.3) is smooth both across the PC_1-PC_2 planes, and along the PC_3 direction. The bulge-dominated galaxies are found preferentially at intermediate values of PC_3, and, as expected, at low values of PC_1.

2.2.5 The performance & reliability of ZEST

Before demonstrating the robustness of the ZEST classification it is important to realize that in generally the appearance of a galaxy depends on the rest-frame wavelength at which it is observed. Since only F814W ACS images are available for the COSMOS galaxies it is important that any comparison of morphology for galaxies at different redshifts is treated

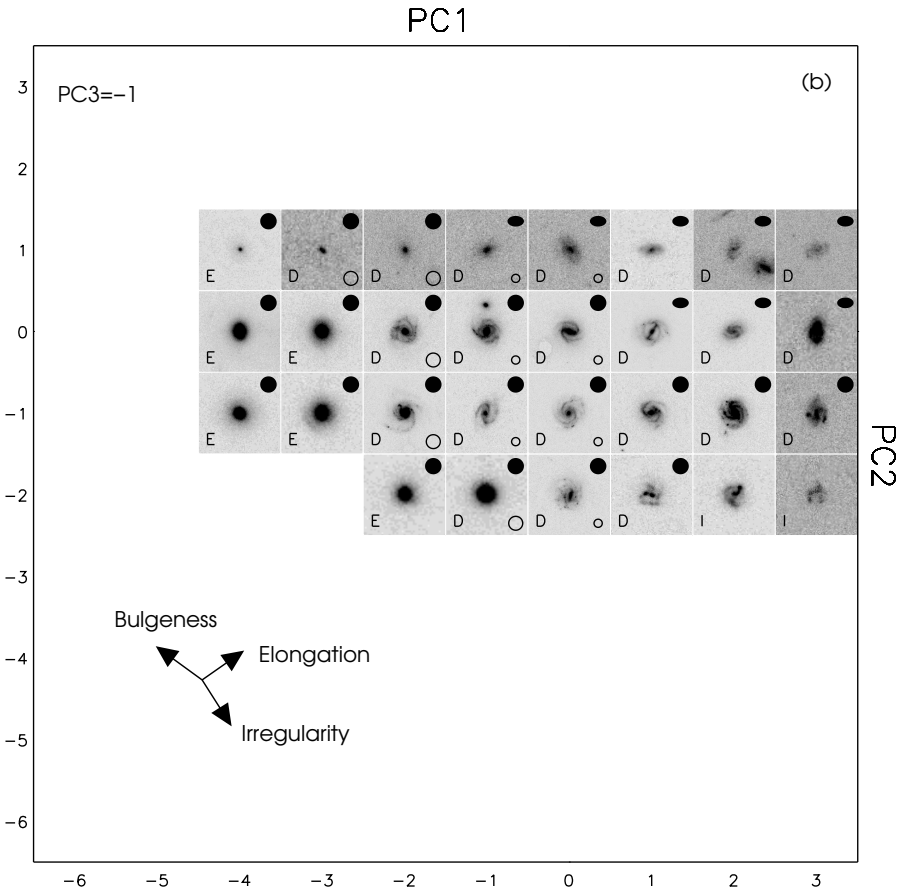

Fig. 2.12 — *cont.*

with caution. At low and intermediate redshifts (0.2< $z \leq 1.0$) which are those covered in the present sample, the central wavelength of the F814W filter covers the rest-frame 4000-6700Å window, where morphological K-corrections are negligible for most galaxies.

Testing ZEST on $z = 0$ galaxies

To assess the performance and reliability of the ZEST classification grid the code was applied to a catalog of 80 representative galaxies at $z = 0$ published by Frei et al. [47]. They (a) have Hubble types available from the RC3 catalog (de Vaucouleurs et al. [31]), (b) were observed (at the 1.1 meter telescope of the Lowell Observatory) in the B_J band ($\lambda_{eff} = 4500$Å) with a pixel scale of 1.35″ per pixel, and (c) have a PSF-FWHM smaller than 5.0″. Three galaxies in the Frei at al. sample for which the available images were too small to get a reliable estimate of the background were excluded from the analysis. The set of local galaxies includes Hubble types from Ellipticals (T = -5) to Sd (T = 10) and has been used as a $z = 0$ benchmark for assessing galaxy morphologies at higher redshifts

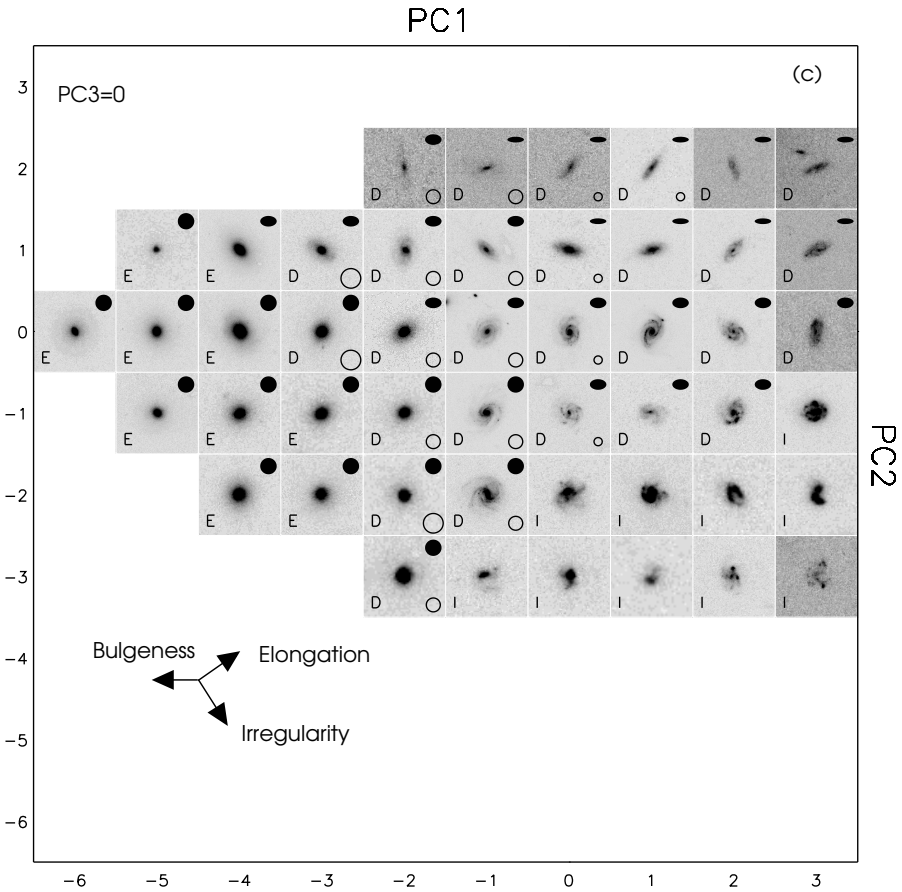

Fig. 2.12 — *cont.*

in a number of other works (Bershady et al. [8], Lotz et al. [75], Simard et al. [118]).

In the left half of Figure 2.14 we show the fraction of objects with a given RC3 classification (E, S0-Sab, Sb-Scd and Sd and later) that have been assigned ZEST types $T = 1$, 2.0, 2.1, 2.2, 2.3, and $T = 3$, respectively. The agreement between the two classifications is excellent, and highlights the power of the the ZEST algorithm to recover the physically motivated Hubble classification of galaxies.
There are only a few objects which have significantly different classifications in RC3 and in the ZEST grid. In the right-hand half of Figure 2.14 postage stamps of these most discrepant galaxies are displayed. A detailed analysis of these galaxies shows that:

1. NGC 4621 and NGC 4564, classified as -5 by the RC3 but as Type 2.0 by ZEST, have a disk component (Emsellem et al. [38], Michard and Marchal [79], Mizuno and Oikawa [80], Scorza and Bender [111]).

2. NGC 4710 has a ZEST Type 2.2 and a Hubble Type S0. As the image shows (see also Michard and Marchal [79]), this edge-on galaxy displays a very bright ring and

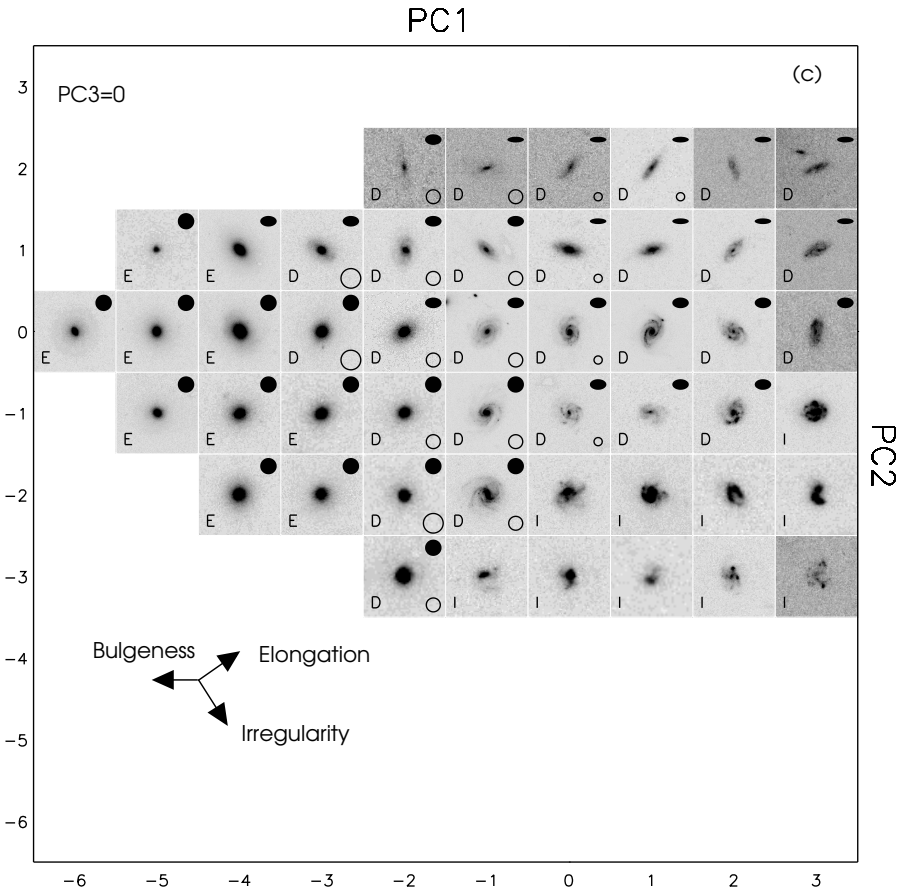

Fig. 2.12 — *cont.*

an important equatorial dust lane, which causes its visual classification to be highly uncertain: indeed, in the UGC catalog this galaxy is classified as an S0a.

3. The two galaxies classified as Type 1 by ZEST and as S0-Sa in RC3 are seen nearly face-on. Their surface brightness varies smoothly with radius and shows no signs of spiral arms or star formation, with the exception of a smooth ring around NGC 4340.

4. NGC 4088, classified by ZEST as $T = 3$ and by the RC3 as Sb-Scd, is described as an irregular and distorted spiral by Dahari [27].

5. Finally, for the few galaxies which are classified by ZEST as bulge dominated (Type 2.0) galaxies and have RC3 classification of Sb-Scd, the single Sérsic fit to their surface brightness profile returned concentrated light distributions, with Sérsic indices $n \geq 3$, which confirms our ZEST classification as Type 2.0 galaxies.

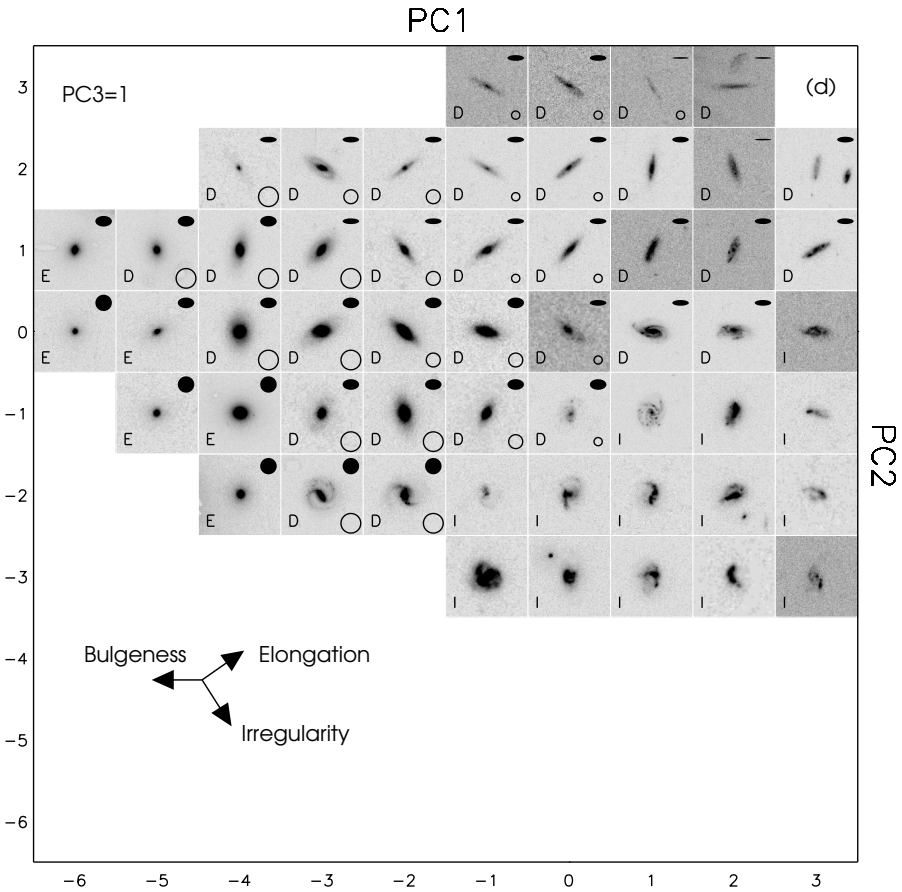

Fig. 2.12 — *cont.*

Quantification of uncertainties in the ZEST morphological classification of COSMOS galaxies

In Section 2.2.1 a detailed assessment of uncertainties and systematic errors on the measured structural parameters was conducted as a function of signal-to-noise ratio (S/N). These tests were carried out using a sample of bright COSMOS galaxies, which were progressively dimmed to fainter magnitudes (lower S/N). Here we summarize to what extent the COSMOS-calibrated ZEST morphological classification grid is affected by the S/N of the individual galaxies. The test was performed by using the same sample of bright test galaxies as in Section 2.2.1. For each of them, all parameters involved in the ZEST classification were computed during the progressive degradation to lower S/N levels. The PC_i ($i = 1, 2, 3$) coordinates were then determined for each galaxy as a function of S/N level, and the ZEST morphological classification corresponding to the relevant unit cube of PC_1-PC_2-PC_3 was assigned to each of the original and artificially faintened galaxies. Finally, the change in galaxy type (ΔT) that occurred due to degraded S/N was estimated as a function of magnitude.

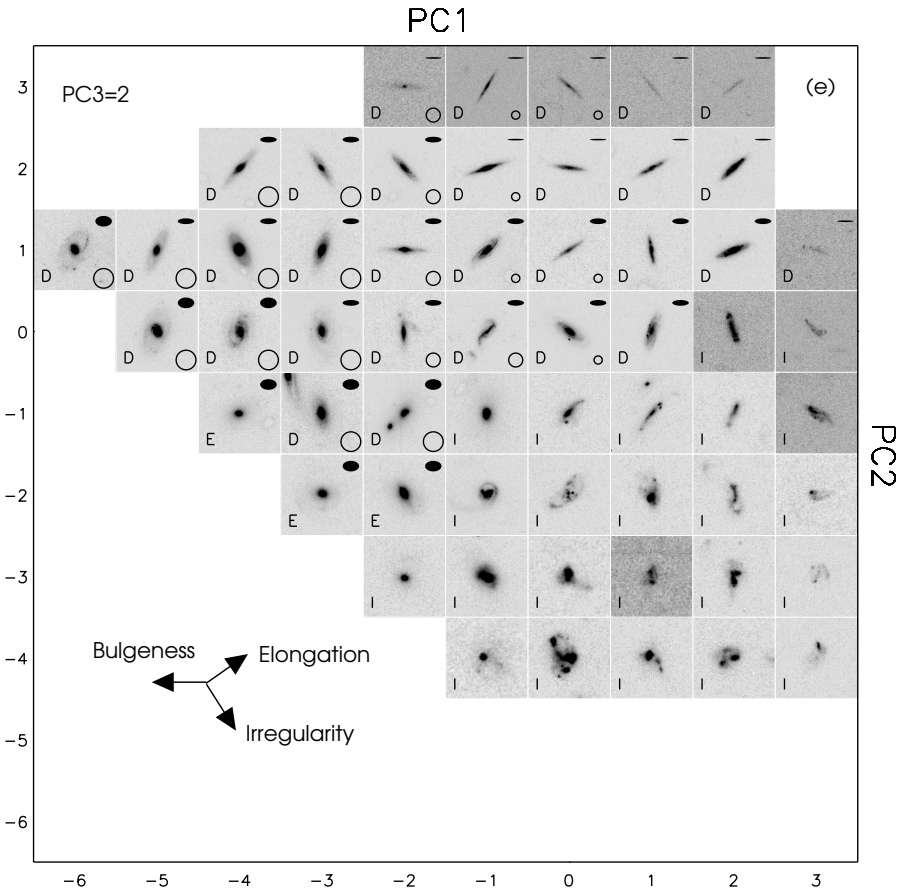

Fig. 2.12 — *cont.*

The ZEST classification is robust down to $I = 24$. For magnitudes $I \leq 22.5$, more than 90% of the galaxies do not change morphological class. The remaining galaxies change morphological type by smoothly moving through the PC_1-PC_2-PC_3 space; in fact, a change of ZEST morphological type with varying S/N happens typically for galaxies which are originally classified in PC_1-PC_2-PC_3 cubes that are close to a "type transition-wall" in PC space. The fraction of galaxies with $\Delta T = 0$ remains larger than ∼75% down to magnitudes $I = 23.0$, and even in the faintest magnitude bin ($23.5 < I < 24$), the fraction of galaxies with $\Delta T = 0$ is still as high as 65%. This is illustrated in Figure 2.15, where we show the distribution of the average absolute variation in PC_i, namely $\langle \Delta(PC) \rangle = (\sum_i |PC_{i,f} - PC_{i,0}|)/3$ (with $i = 1$, 2, 3 and $PC_{i,0}$ denominating the initial values of the PC_is, and $PC_{i,f}$ the measured value of PC_i after S/N degradation). The *solid* histograms show the distribution of $\langle \Delta(PC) \rangle$ for all galaxies in each of the four considered magnitude bins (ranging from $I = 22$ on the upper left to $I = 24$ in the lower right panel). *Hatched* histograms show the distribution of $\langle \Delta(PC) \rangle$ for galaxies which change morphological class due to S/N degradation.

Figure 2.16 shows a few examples of how galaxies move through PC space as the S/N

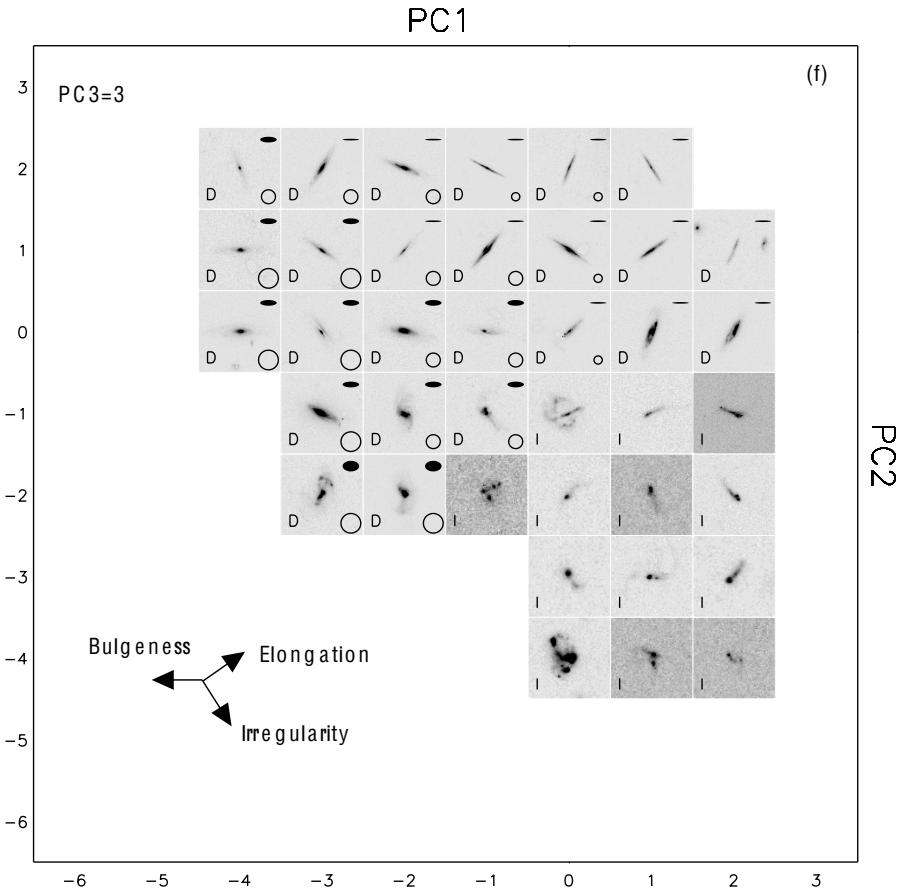

Fig. 2.12 — *cont.*

of the galaxy images decreases. Initial and final values for the PC_i coordinates of these galaxies are indicated at the beginning and end of the track that describes the movement of a particular test galaxy in PC space. Note that galaxies can have a $\langle\Delta(PC)\rangle$ as high as $\langle\Delta(PC)\rangle = 2$, without changing their morphological class if their path in PC_i space lies within a region uniformly assigned to a specific morphological type. As stressed above, virtually all galaxies that change morphological class are located initially in bins of PC_1-PC_2-PC_3 that border on regions with a different morphological classification.

The most noticeable effect of S/N degradation is a contamination, at the faintest magnitudes, of at most ∼30% from low S/N early-type galaxies to the Type 2 or Type 3 galaxy populations (see also Abraham et al. [1], Lotz et al. [75]). This in turn implies that at most 30% of early-type galaxies at the faintest magnitudes should be removed from the early-type sample due to a misclassification as a disk or irregular galaxy arising from their lower S/N values.

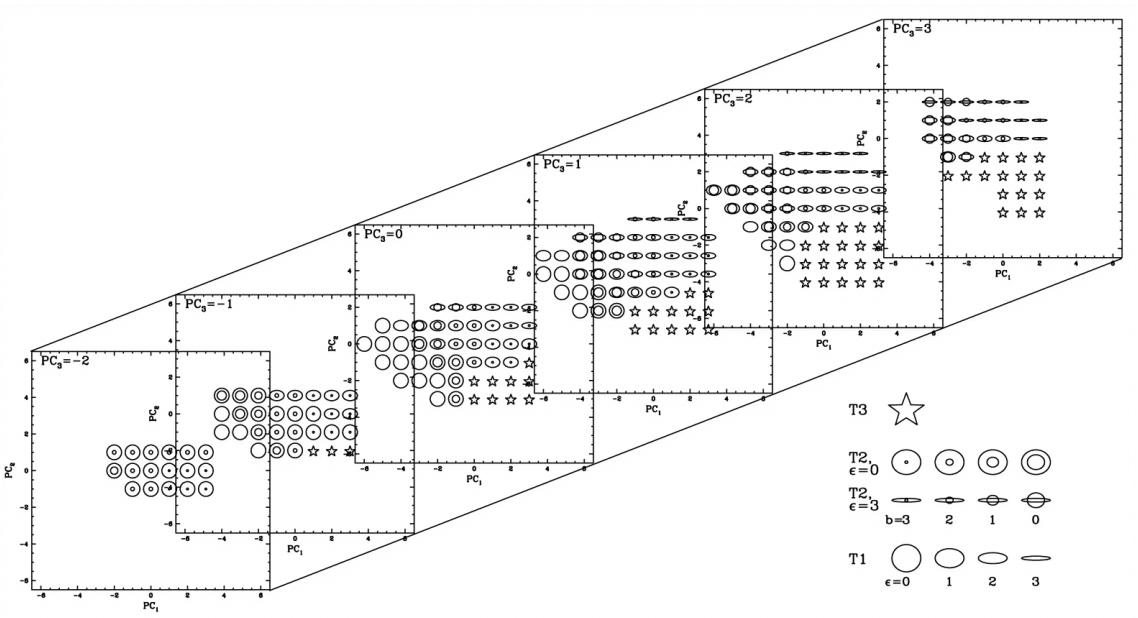

Fig. 2.13 — Schematic view of the ZEST morphological classification. Slices at constant PC_3 are shown in three-dimensional PC space. While PC_1 and PC_2 vary in a given slice, the value of PC_3 increases from bottom-left to upper-right. In each unit cube the symbol indicates the ZEST classification associated with that cube (according to the legend shown in the bottom-right corner of the Figure). In particular, stars represent $T = 3$ galaxies, and single ellipses $T = 1$ galaxies. The double ellipses indicate $T = 2$ galaxies, for which the size of the inner ellipse increases with growing importance of the bulge component.

Effects of the Point-Spread-Function

For very compact objects, the structural parameters computed for the COSMOS galaxies from the HST-ACS images can be affected by the instrumental PSF (FWHM $\sim 0.1'$). In order to determine the limiting size and magnitude at which the effects of the PSF become important in our classification algorithm, a set of simulations based on synthetic galaxy images were performed. They consisted of artificial images of about 2500 galaxies with magnitudes in the range $21 \leq I \leq 24$, with surface brightness profiles described either by a deVaucouleur (i.e., $n = 4$) or an exponential ($n = 1$) profile, and with half-light radii $R_{1/2}$ in the range $0.05'' \leq R_{1/2} \leq 1.0'$. These artificial images were convolved with the TinyTim (Krist and Hook [68]) HST PSF, and with a PSF constructed from stars present in the COSMOS ACS field. Similar results are obtained with either of these PSFs; in the following, we discuss the results obtained with the TinyTim PSF.

Both the original and the PSF-convolved artificial galaxies were analyzed and classified in a similar way as the COSMOS data. Comparison of the results obtained on the original and on the PSF-convolved images revealed that galaxies with the exponential ($n = 1$) surface brightness profile are always classified as Type 2 disk galaxies, and no change of

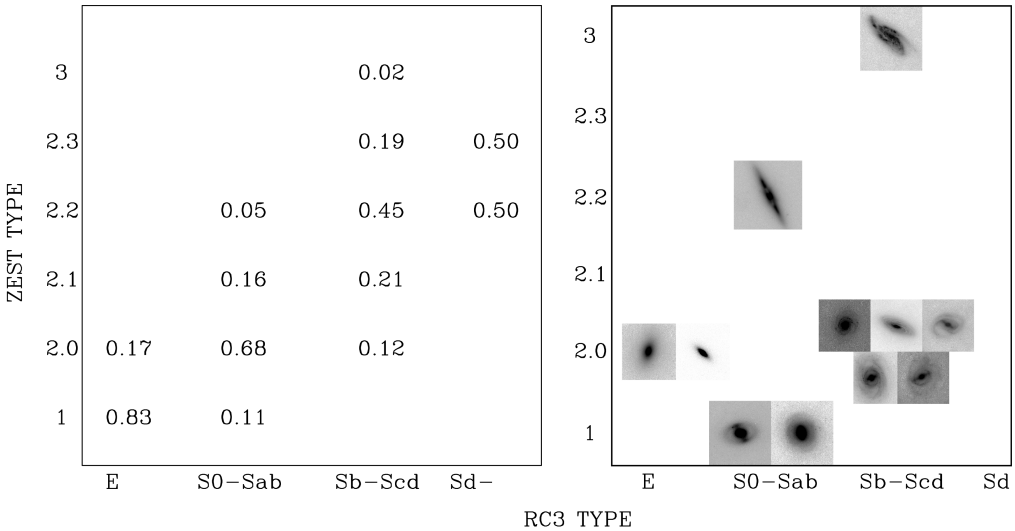

Fig. 2.14 — *Left:* The fraction of objects with a given RC3 classification (E, S0-Sab, Sb-Scd, and Sd and later) that are classified as $T = 1$, 2.0, 2.1, 2.2, 2.3, and $T = 3$ by ZEST. – *Right:* Images of the $z = 0$ Frei et al. galaxies with discrepant ZEST and RC3 classifications.

class is observed over the entire range of half-light radii and magnitudes explored. All $n = 4$ galaxies are classified as Type 1 (early-type galaxies) when the analysis is performed on images which were not convolved with a PSF. When the convolved images are considered, about 15% of all galaxies with half-light radius larger than $0.17''$ changes class from Type 1 to Type 2; 85% of these systems have $I > 23$. All $n = 4$ galaxies with a measured $R_{1/2} < 0.17''$ change class from Type 1 to Type 2.
The fraction of such objects in our COSMOS sample which has a measured $R_{1/2} < 0.17''$ is about 4% down to our magnitude limit of $I = 24$. For this small fraction of the sample, the ZEST morphological classification is therefore likely affected by convolution with the ACS-HST PSF.

2.2.6 The advantages of classification with ZEST over other approaches

Recent classifications of nearby and high-z galaxies have been based typically on combinations of two or three of the non-parametric diagnostics that are used in ZEST (e.g., Ferreras et al. [45], Lotz et al. [75], and references therein) or on a threshold in Sérsic index n (most notably the SDSS defined early-type galaxies as those objects with $C \geq 2.87$ or $n \geq 2.5$; all other galaxies were classified as "late-type"). Such approaches can be seen as projections of the ZEST grid onto a lower-dimensional space, and lead to galaxy samples that are contaminated by systems with rather different structural properties.

As an illustration of this, two-dimensional planes defined by G and M_{20} (upper row),

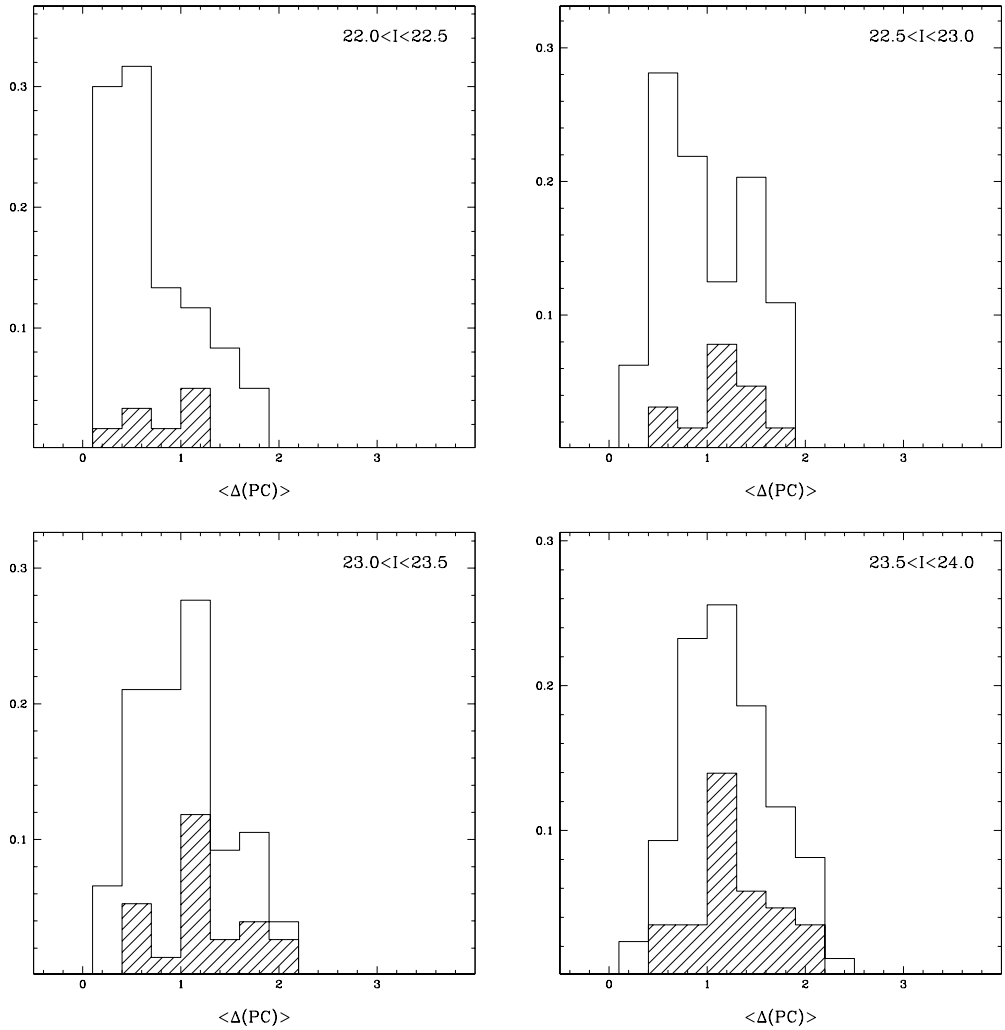

Fig. 2.15 — Change in ZEST morphological class $\Delta(PC)$ as a function of S/N. The solid histograms show the distribution of $\langle\Delta(PC)\rangle = \sum_i |PC_i - PC_{i,0}|)/3$, with $i = 1$, 2, 3. $PC_{i,0}$ is the initial value of any of the three PCs and PC_i the measured PC after signal-to-noise degradation of a set of images of bright COSMOS galaxies with $17.5 < I < 18$. The degraded galaxies are grouped in four different magnitude bins ranging from $I = 22$ (top left panel) to $I = 24$ (bottom right panel). The hatched histograms show the distribution of $\langle\Delta(PC)\rangle$ for the galaxies with $\Delta T \neq 0$.

C and M_{20} (middle row), and C and A (lower row) are shown in Figure 2.17. The total density of galaxies is colour-coded with a grey scale is all cases. In the different panels (i.e., from left to right) the regions of space that are populated by a given ZEST morphological class are outlined in different colours: the color contours enclose ∼99% of the COSMOS galaxies with the specified ZEST morphological class. To avoid crowding we show in the left panels the location of the $T = 1$ early-type galaxies (red contours), in the central panels the $T = 2$ disk galaxies (blue contours, with increasing intensity from bulge-dominated

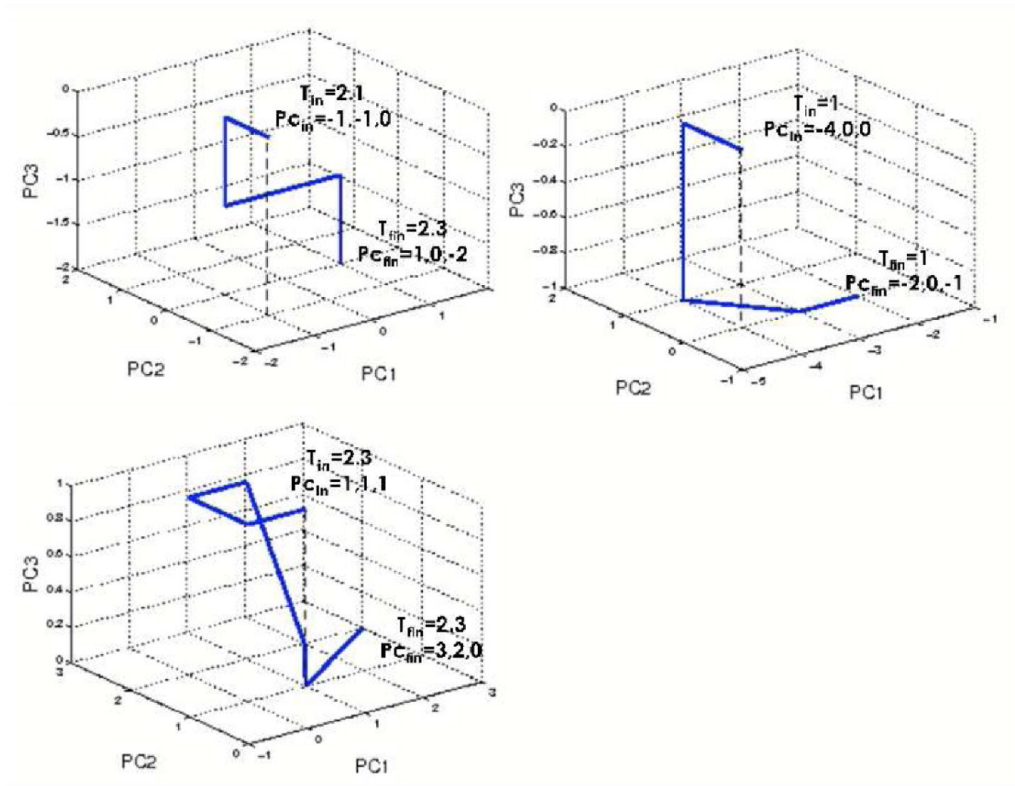

Fig. 2.16 — Three examples of how galaxies move in the PC space as the signal-to-noise of the galaxy image decreases. The starting and finishing points in PC-space are indicated by $PC_{\rm in}$ and $PC_{\rm fin}$, respectively.

$T = 2.0$ galaxies to $T = 2.3$ bulgeless disks), and in the right panels the $T = 3$ irregular galaxies (green contours).

It is clear from Figure 2.17 that there is significant overlap from different galaxy types in all regions of these two-dimensional planes. In the $C - M_{20}$ plane, for instance, $T = 1$ early-type galaxies form a tight sequence, well visible in the left panel of Figure 2.17. That region of the plot however includes not only the majority of $T = 2.0$ bulge-dominated disk galaxies, but also a substantial fraction of galaxies with a lower bulge-to-disk ratio ($T =$ 2.2 or 2.1). If the galaxies lying above the solid black line running diagonally across the $C - M_{20}$ plane were classified as "early-types", ZEST would return the following galaxy population mixture in the selected region: 38% of the desired $T = 1$ early-type galaxies, 23% of $T = 2.0$ galaxies, and 26% and 10% of $T = 2.1$ and of $T = 2.2$ galaxies, respectively. Even adding up $T = 1$ and 2.0 galaxies (which might be desired for some scientific reasons), the sample selected in this way would still be affected by a contamination of some 40% contributed by galaxies with a lower B/T ratio. Similar levels of mixing are found when the other two-dimensional planes of Figure 2.17 or a simple cut in Sérsic index n are used to morphologically classify galaxies, as has been done frequently in the pertinent literature.

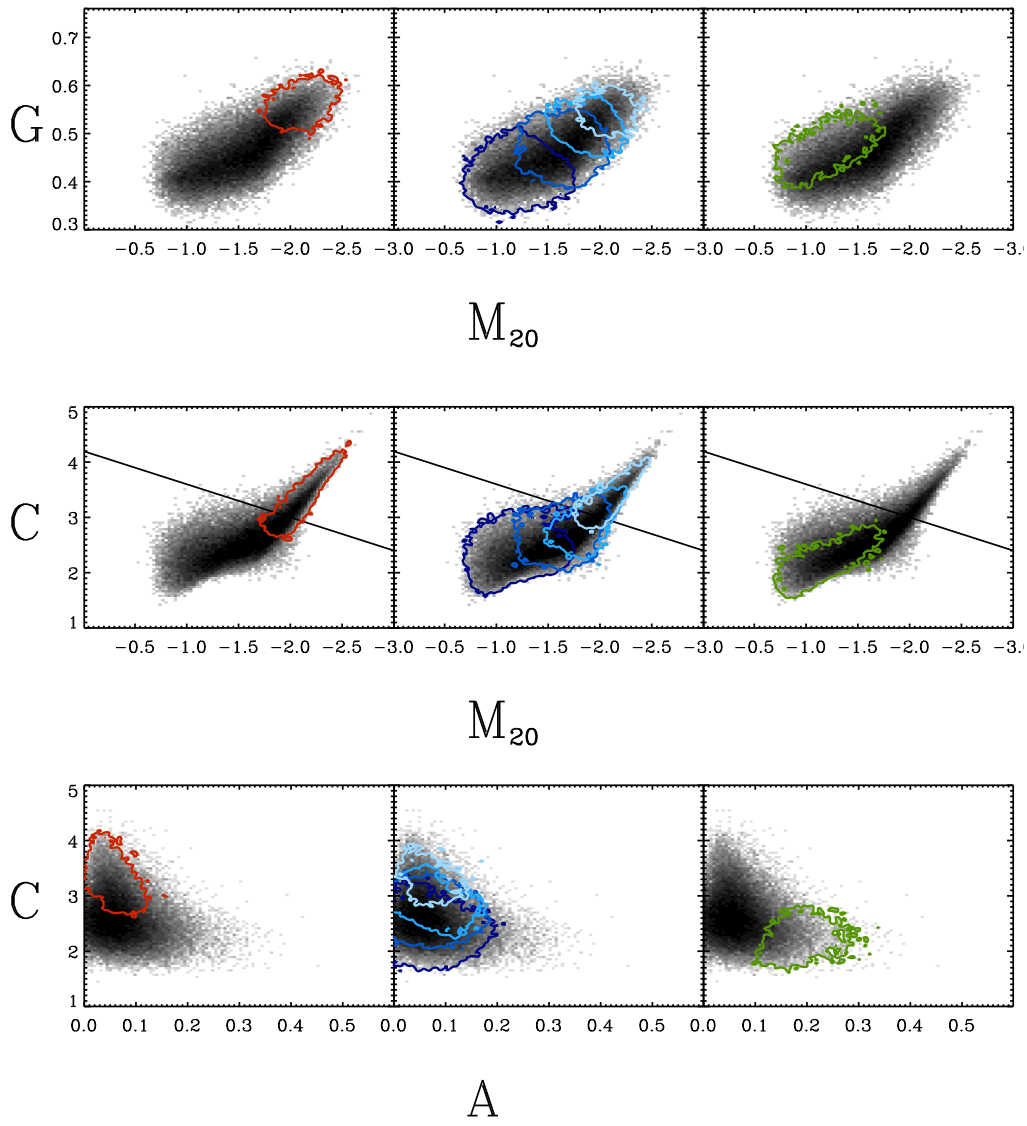

Fig. 2.17 — Distribution of our ∼56000 $I \leq 24$ COSMOS galaxies in the $G - M_{20}$ plane (top panels), $C - M_{20}$ plane (middle panels), and $C - A$ plane (bottom panels). In each column we highlight the position of a different ZEST morphological class by drawing the contours enclosing 99% of the objects in that ZEST class. In the first, second and third columns we show respectively $T = 1$, 2 and 3 galaxies (red, blue and green contours). The blue color for $T = 2$ galaxies ranges from light blue for bulge-dominated $T = 2.0$ galaxies to dark blue for $T = 2.3$ bulgeless disks.

2.3 Summary

Both the "parametric" and the "non-parametric" approach of quantifying galaxy structure have been successfully applied to COSMOS galaxies from redshift $z \sim 0.1$ to 1.2. The

Sérsic profile is a flexible analytic law with the capability of describing the smooth and azimuthally symmetric component of the light emitted by both early-type galaxies and disk galaxies. Using the package GIM2D we have derived structural parameters for more than 30,000 COSMOS galaxies. They provide estimates of galaxy size (the half-light radius $R_{1/2}$), galaxy luminosity and of the radial fall-off of galaxy light as parametrized by the Sérsic index, which is also an indicator of the morphological type or bulge-to-disk ratio of an object.
The Zurich Estimator of Structural Types (ZEST) uses the Sérsic index n of the fits to the galaxy surface brightness distributions, and five basic non-parametric quantities to classify galaxies according to their morphology. The ZEST classification scheme divides galaxies in three main types (early-types, disk galaxies and irregular galaxies), assigns a bulgeness parameter related to the B/D ratio (quantized in four bins) to disk galaxies, and ranks galaxies according to the elongation, irregularity and clumpiness of their light distribution.

In the remainder of this thesis we use the 27,500 galaxies classified as *disk* galaxies by ZEST (from the most bulge-dominated to the pure disk galaxies the relative contributions to the total sample are: 13.2% of type 2.0, 28.2% of type 2.1, 32.5% of type 2.2 and 26.1% of type 2.3 galaxies) to study the evolution of the size, number density at a given size, surface brightness and rest-frame colours of disk galaxies over the last 8 billion years.

Since 'tis nature's law to change,
Constancy alone is strange.

John Wilmot

3 The evolution of the number density of large disk galaxies

The content of this chapter is based on Sargent et al. [101]
(`http://adsabs.harvard.edu/abs/2007ApJS..172..434S`).

3.1 Introduction

A detailed quantitfication of galaxy structure as a function of redshift is an essential tool in the study the evolution of galaxies through cosmic time. In particular, the evolution of galaxy sizes is a direct diagnostic of the history of their star formation and mass assembly. For disk galaxies several theoretical predictions have been made, which are now testable with observations. For example, under the assumption that the scale lengths of disks scale with their virial radii, their sizes are predicted to evolve as $r_d \propto H(z)^{-2/3}$ at a fixed halo mass Fall and Efstathiou [40], Mo et al. [81]). In contrast to this, Bouwens and Silk [12] assume a dependence of the star formation rate on the local gas density within the disk and the infall of metal-free gas, and predict the sizes of disks to evolve as $r(z)/r(0) = 1-0.27\cdot z$.

Pioneering observations, however, generally appear to support a substantially weaker size evolution of the disk galaxy population than predicted by theory. Data from the Canada-France Redshift Survey (CFRS) for a few tens of large disk galaxies up to redshift $z \sim 1$ indicate about a magnitude of surface brightness evolution for the disks, and a constant number density of large disks over this period (Lilly et al. [71], Schade et al. [105, 106]). Similar results are reported by Roche et al. [98]. In contrast, Simard et al. [117] interpret their data as indicating no surface brightness evolution in disks over the same redshift range. The work of Trujillo and Aguerri [127], on the other hand, provides further evidence for surface brightness evolution in galaxy disks, although a possible decrease in

the sizes of disks by approximately 30% at $z \sim 0.7$ is also proposed as an alternative to explain the data. Using 1500 disk galaxies at redshifts $0.25 < z < 1.25$ from the GOODS survey, Ravindranath et al. [94] find at most a very modest decrease of the number of disks with half-light radius $r_{1/2} > 4$ kpc. The GEMS survey has been used to investigate the evolution with redshift of the luminosity-size relation for disk galaxies (Barden et al. [5]; see also Trujillo et al. [129]), but no analysis of the evolution of the number density of disk galaxies as a function of galaxy size has been presented based on the GEMS data. Therefore, the observational evidence for a relatively constant number of (large) disks since $z \sim 1$ relies on very small samples extracted from small areas in the sky.

In this chapter we use the COSMOS survey (Scoville et al. [113]) to investigate how the number density of disk galaxies with sizes above 5 kpc – the threshold above which our sample is reasonably complete – evolves with cosmic time from $z \sim 1$ to $z = 0$. Thanks to the good statistics of COSMOS, we are able to extend the investigation so as to study this evolution as a function of the bulge-to-disk ratio of disk galaxies. Specifically, we use the ACS COSMOS database, and select a $I \leq 22.5$ sample from the 38% of the COSMOS area that was imaged by the HST during Cycle 12. The complete $I \leq 22.5$ sample contains more than 16,000 galaxies. We perform two-dimensional GIM2D (Marleau and Simard [77]) fits to their surface brightness distributions, which we describe with a single Sérsic law (Sérsic [114]). Free parameters in the fits are: the total flux F_{tot}, the Sérsic index n, the half-light radius $R_{1/2}$, the ellipticity $\epsilon = 1 - b/a$ (with a and b the semimajor and semiminor axes, respectively), and the position angle ϕ. (See Section 2.1.2 for a description of how the GIM2D profile fitting was optimized for the current analysis.)

We compare the structural parameters obtained with the GIM2D surface brightness fits with the structural measurements derived using the Zurich Estimator of Structural Types (ZEST; Scarlata et al. [103]). ZEST uses individual measurements of four non-parametric diagnostics of galaxy structure, namely, the concentration C, the asymmetry A, the Gini coefficient G, and the second order moment of the brightest 20% of the galaxy pixels, M_{20} (see Section 2.2 or Scarlata et al. [103] and references therein), plus the elongation of the distribution of the light, to classify galaxies in three morphological types: early-types, disk galaxies or irregular and peculiar galaxies. The disk galaxies are further split by ZEST into four classes of bulge-to-disk ratio (B/D). At any redshift, the multi-dimensional ZEST classification grid substantially reduces the intermixture of structurally different galaxy populations compared with simpler approaches. The comparison of our parametric structural quantities with the diagnostics supplied by ZEST shows the expected correlations (e.g., between Sérsic index n and concentration C) and, by doing so, illustrates the robustness of the results of our GIM2D fits. It also demonstrates that studies of selected galaxy populations which are classified by a simple cut in Sérsic index n – as customarily done, for instance, in studies of the SDSS galaxy population and in other surveys of the high-z universe – are affected by mixing of galaxies with different structural properties.

We use the ZEST classification to extract, from the total $I \leq 22.5$ sample, the subsample of approximately 12,000 disk galaxies (with different B/D ratios), and use the half-light radii provided by our Sérsic fits to compute the number of disk galaxies per unit comoving volume and per unit half-light radius $r_{1/2}$ as a function of redshift (the *size function*

$\Phi(r_{1/2}, z)$). In order to compare the results at higher redshift with the local universe, we use a suitably selected sample of about 1800 SDSS galaxies, which have been "redshifted" to $z = 0.7$ by properly re-scaling for flux dimming, distance and image resolution (cf. Section A.1 or Kampczyk et al. [62]).

We find that the number density of disk galaxies with intermediate sizes $r_{1/2} \sim$ 5-7 kpc remains nearly constant from $z \sim 1$ to today, while that of the largest disks ($r_{1/2} > 7$ kpc) shows a drop by a factor of approximately two. This deficit appears to stem mostly from a lower number density of *bulged* disks at early epochs.

3.2 Data analysis

3.2.1 The initial catalog: 16,538 ACS-selected galaxies

We use a sample of 16,538 COSMOS galaxies with $I \leq 22.5$, detected in the 259 ACS F814W images acquired during the HST Cycle 12 observing period (Scoville et al. [112]). Details on the processing of the ACS data are given in Koekemoer et al. [66]; a discussion of the ACS-detected catalog used as the starting point to build our sample is presented in Leauthaud et al. [70]. In the following we give a brief overview of the steps leading to the production of the catalog:

- The ACS-detected catalog was generated by running SExtractor (Bertin and Arnouts [9]) twice on the reduced ACS images; the first time in a "cold" run with a configuration optimized for the detection of large, bright objects, and then in a "hot" run with a configuration optimized for small and faint sources.
- The two resulting samples were then merged together to produce a final catalog by retaining all the "cold" detections plus the "hot" detections which fell outside the SExtractor segmentation map of any galaxy detected in the "cold" run. This ACS-based catalog contains approximately 55,700 galaxies down to $I = 24$.
- Stars were removed by deleting the sources with SExtractor CLASS_STAR> 0.6 from the catalog.
- The ACS-based catalog was inspected to remove all remaining over-deblended large galaxies as well as false detections from it. About 4.5% of the sources in the original ACS-based catalog were deleted from our final catalog after this visual check.

The final, cleaned ACS-based catalog contains 55,651 galaxies down to $I = 24$, 16,538 of which have $I \in [16, 22.5]$ and an ACS-stellarity parameter smaller than 0.6[1]. These

[1] Note that by applying the customary cut at a value of the stellarity parameter of 0.9 some very bright stars would be included in the sample. We inspected the sources with stellarity larger than 0.6 to ensure that no galaxy was excluded from our sample.

roughly 16,500 galaxies constitute the sample that we study in this chapter.

3.2.2 Deletion of sources from the original ACS-based catalog

A clear assessment of the selection effects is essential to perform statistical studies of the evolution of galaxy populations. Sources had to be removed from our initial sample of 16,538 ACS-selected, Cycle 12 COSMOS galaxies with $I \in [16, 22.5]$ and ACS-stellarity smaller than 0.6 due to a variety of reasons:

1. A total of 465 sources (i.e., about 2.8% of the sample) were deleted from our final sample, due to the failure of GIM2D to converge.
2. Twenty-nine additional sources were also excluded on the basis of the χ^2 of the GIM2D fits. After inspection of the GIM2D residuals and of the $\chi^2_{\rm GIM2D}$ distribution, we fixed the threshold for deleting sources from our sample at $\chi^2_{\rm GIM2D} = 15$. While this may seem an exceedingly generous criterion, visual inspection of all GIM2D fits and their residuals for objects with $\chi^2_{\rm GIM2D} > 1.5$ showed that, in the vast majority of the cases, GIM2D produces a fair model of the diffuse galaxy light, and the high values of $\chi^2_{\rm GIM2D}$ in these objects were produced by structure such as knots of star formation, spiral arms or bars.
   Figure 3.1 and the first three entries in Table 3.1 display and list three random examples of objects with $\chi^2_{\rm GIM2D} \in [5, 15]$. It is clear from the figure that the presence of spiral and other structure can lead to high values of $\chi^2_{\rm GIM2D}$ even if the underlying symmetric component is reproduced well by the Sérsic model.
3. Of the galaxies in our sample, 344 (2.1%) lacked ground-based photometric information in at least five of eight bands; therefore, no accurate photometric redshifts could be derived for these sources.
4. A fourth selection criterion for the rejection of objects was applied in part of the analysis, based on the value of $\chi^2_{\rm phz}$ supplied by ZEBRA (see Section 3.4.1). As a test to evaluate the impact of high values of $\chi^2_{\rm phz}$ in the photometric redshift estimates, we adopted the approach of calculating the size functions (Section 3.4.1) both by applying no $\chi^2_{\rm phz}$ cut, and by deleting from our sample sources with a $\chi^2_{\rm phz}$ above a threshold given by the value corresponding to two standard deviations in an ideal χ^2 distribution of a varying number of degrees of freedom (which in our case is the difference between the number of filters for which ground-based photometric measurements are available and the number of free parameters, i.e., redshift, SED template and template normalization). This cut, when applied, reduces the sample by 1369 objects (8.2%).
5. Finally, objects with one ground-based set of coordinates but two distinct coordinates in the ACS-selected catalog must be expected to have ambiguous photometric information, and they were therefore removed as well. A total of 271 objects (1.6%) fell in this category.

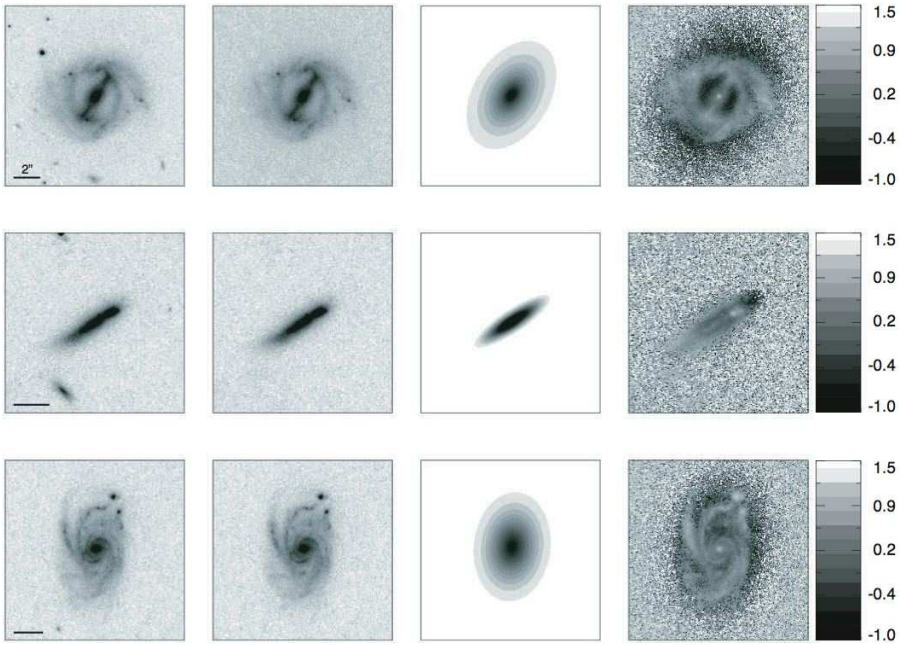

Fig. 3.1 — Selection of objects with high values of $\chi^2_{\rm GIM2D}$ but satisfactory fits to the smooth component of the surface brightness profile of the galaxy. From left to right, the figure shows the original stamp image, the cleaned image, the GIM2D model and the residual image (see footnote on following page). For each object, the bar in the original galaxy image indicates a scale of $2''$. An intensity scale for the normalized residual images is reported on their right-hand side. Model parameters are listed in Table 3.1.

3.3 The ZEST morphological classification of our COSMOS sample

All COSMOS galaxies in our sample have been classified with ZEST, the Zurich Estimator of Structural Types, discussed in Section 2.2 or Scarlata et al. [103]. ZEST is a multi-dimensional classification grid that simultaneously uses: (1) the non-parametric diagnostics of asymmetry A, concentration C, Gini coefficient G, and the second order moment of the brightest 20% of galaxy pixels M_{20}, (e.g., Lotz et al. [75]), plus (2) the elongation of the galaxy's distribution of light, to classify galaxy types. For each galaxy, the final ZEST classification provides quantitative information on galaxy structure, and a classification into either of the types 1, 2 or 3 for early-type, disk and irregular or peculiar galaxies, respectively. ZEST further splits the disk galaxies into four sub-classes of bulge-to-disk ratio, ranging from bulgeless disks (type 2.3) to bulge-dominated spirals (type 2.0). The Sérsic indices presented in this chapter were employed in ZEST to check and refine the four B/D categories of disk galaxies.

Figures 3.2a to 3.2f show, for the different ZEST types and for disk galaxies with

Tab. 3.1 — Physical properties of the galaxies shown in Figures 3.1 to 3.2f.

redshift	M_B	I	size [kpc]	n	type	e	χ^2_{GIM2D}
0.271	-21.558	18.303	11.17	1.19	2.0	0.36	7.651
0.097	-18.008	19.740	2.06	0.55	2.0	0.77	5.378
0.340	-21.604	18.765	9.56	0.78	2.0	0.30	5.364
0.511	-21.465	19.882	3.43	4.06	1	0.09	1.148
0.572	-20.762	20.933	4.21	5.48	1	0.35	1.059
1.085	-22.453	21.881	4.76	3.45	1	0.23	1.044
0.751	-22.890	19.808	9.89	0.90	2.3	0.05	1.640
0.212	-18.525	20.914	3.28	0.90	2.3	0.46	1.242
0.850	-21.100	22.016	5.65	0.68	2.3	0.23	1.031
0.215	-19.500	19.894	4.99	1.19	2.2	0.33	1.167
0.075	-15.416	20.964	1.92	1.22	2.2	0.63	1.014
0.854	-20.951	22.179	3.86	1.47	2.2	0.44	1.016
0.391	-20.440	20.023	8.55	2.00	2.1	0.86	1.176
0.742	-21.678	20.958	7.59	2.48	2.1	0.43	1.181
1.080	-22.371	21.913	5.40	3.04	2.1	0.54	1.065
0.755	-22.543	20.179	7.49	1.40	2.0	0.33	2.164
0.729	-22.636	19.911	13.45	1.81	2.0	0.42	2.505
0.343	-19.272	20.830	1.71	4.21	2.0	0.72	1.207
0.300	-20.363	19.912	5.17	1.67	3	0.24	1.584
0.649	-21.299	20.906	6.18	1.36	3	0.48	1.124
0.682	-20.542	21.826	4.77	0.62	3	0.44	1.040

Note. — The galaxies are listed in the order in which they appear in Figures 3.1 to 3.2f, i.e., the first galaxy listed is the uppermost one in Figure 1, the third one the lowermost object in Figure 3.1, the fourth entry the uppermost galaxy in Figure 3.2a, and so forth.

different B/D ratios, a few examples of GIM2D fits chosen randomly from representatives of the morphological class in question. In each figure we plot (from left to right) the original stamp image, the cleaned image, the GIM2D model and the fractional residuals[2] between the observed galaxy and the analytical model. It is clear from these examples that early-type and disk galaxies are well described by the analytical fits with the Sérsic profile. They do well in reproducing the smooth component underlying the galactic light and, as is visible in the residuals, leave behind only the sub-structure within the galaxies, such as spiral arms and bars. On the other hand, the GIM2D fits for the irregular galaxies are understandably less reliable, as the smooth and symmetric analytical models cannot capture the richness of structure of this class of objects.

To further highlight the robustness of the GIM2D fits, we show in Figure 3.3 the com-

[2]The pixel values $R_{(x,y)}$ of the fractional residual are calculated by subtracting the GIM2D model ($I_{(x,y),\text{model}}$) from the original image ($I_{(x,y),\text{orig.}}$) and then dividing the difference image by the original image:

$$R_{(x,y)} = \frac{I_{(x,y),\text{orig.}} - I_{(x,y),\text{model}}}{I_{(x,y),\text{orig.}}} \ .$$

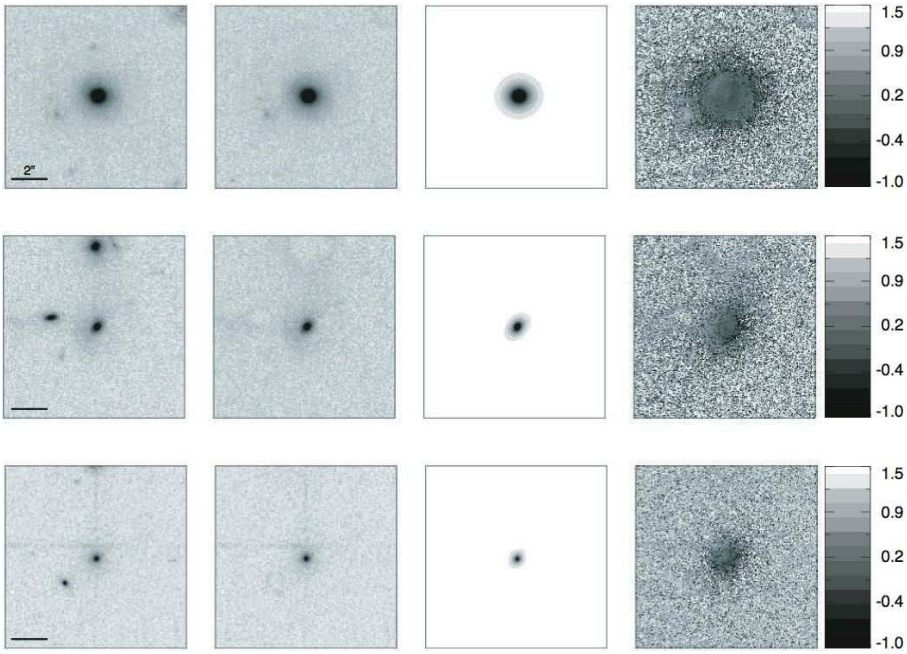

Fig. 3.2a — Original and cleaned image, GIM2D model and residual image for three galaxies of ZEST type 1 (values of the physical parameters are listed in Table 3.1).

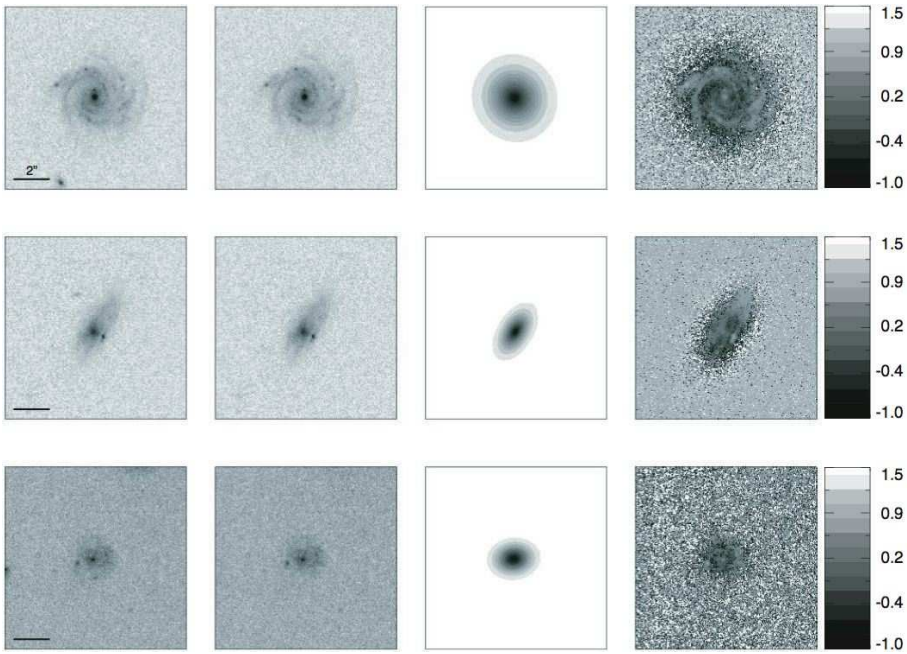

Fig. 3.2b — As Figure 3.2a but for galaxies of ZEST type 2.3.

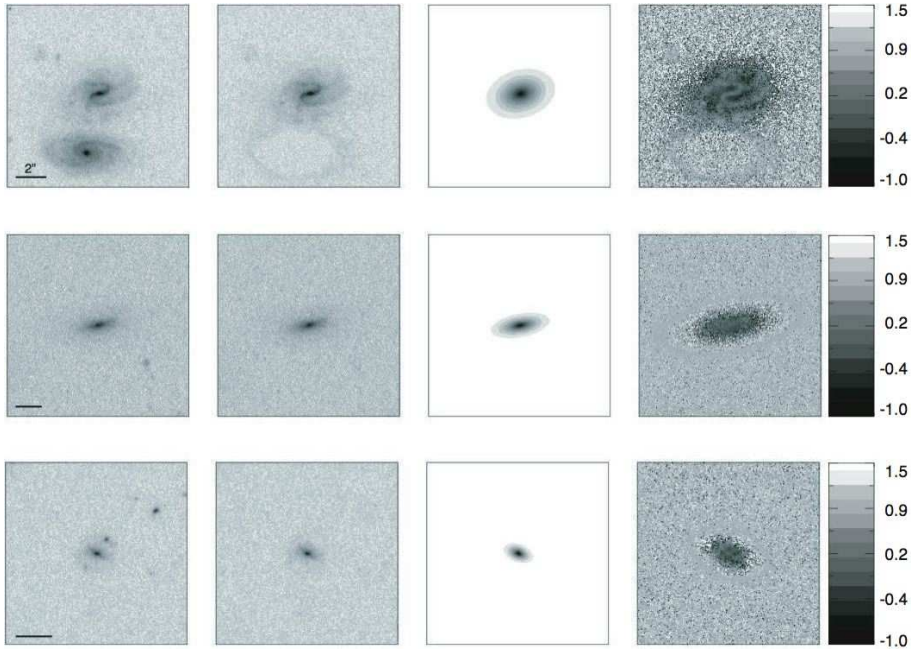

Fig. 3.2c — As Figure 3.2a but for galaxies of ZEST type 2.2.

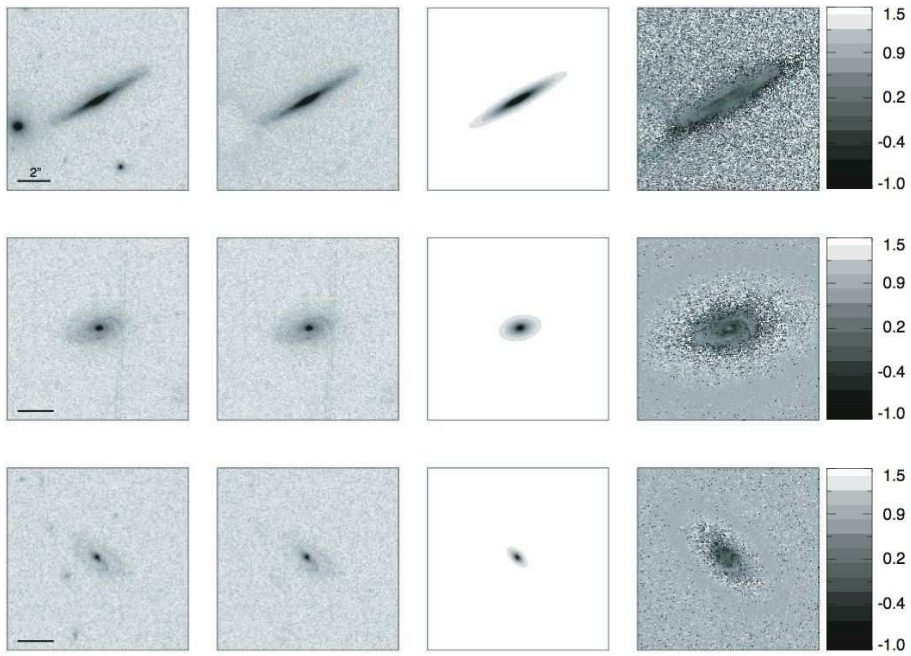

Fig. 3.2d — As Figure 3.2a but for galaxies of ZEST type 2.1
.

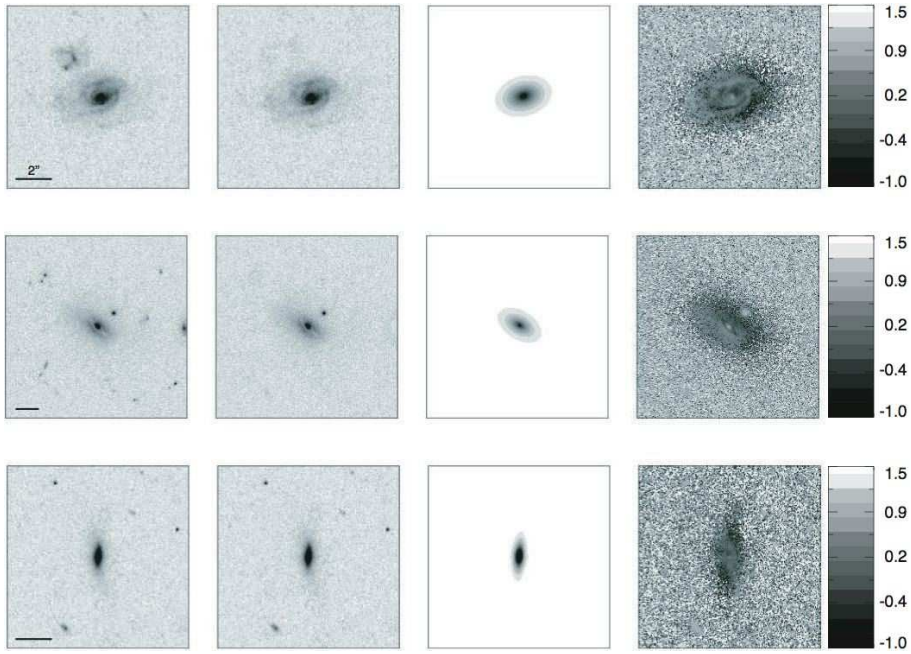

Fig. 3.2e — As Figure 3.2a but for galaxies of ZEST type 2.0.

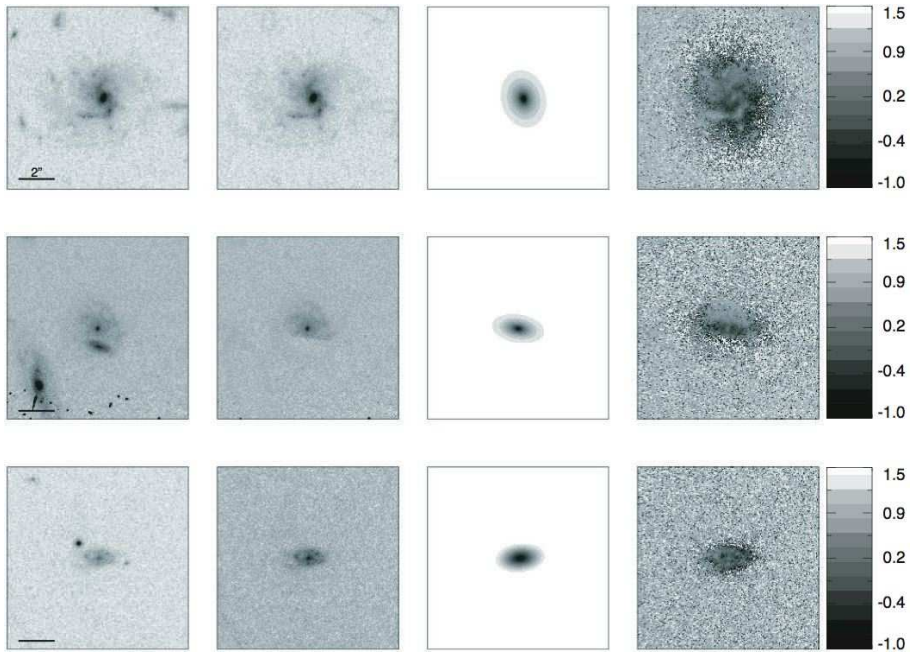

Fig. 3.2f — As Figure 3.2a but for galaxies of ZEST type 3. Due to the irregular distribution of light in these objects, their GIM2D fits are less reliable.

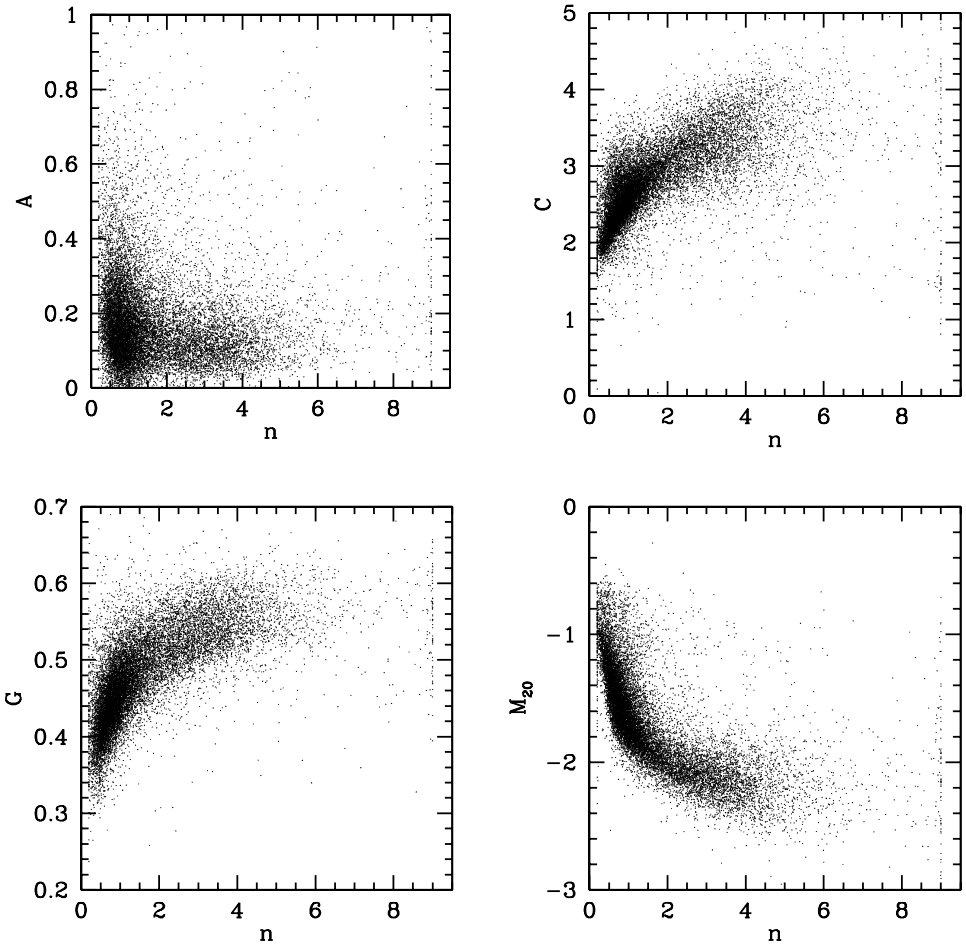

Fig. 3.3 — The comparison of the non-parametric diagnostics A (asymmetry), C (concentration), M_{20} (second order moment of the brightest 20% of the pixels) and G (Gini coefficient) with the Sérsic index n. The regular trends and tight relations in these plots support the reliability of the GIM2D fits. The clustering of points at $n = 9$ reflects our restriction of the Sérsic index to the interval $n \in [0.2, 9]$.

parison of our values of the Sérsic index with the non-parametric structural parameters A, C, G and M_{20}. The expected correlations between diagnostics such as concentration and Sérsic index, as well as the tightness of these relationships, are an independent confirmation of the reliability of the analytical fits.

The left hand side of Figure 3.4 shows the distribution of Sérsic indices n as a function of ZEST galaxy type. The figure illustrates that, as expected, the bulk of late-type galaxies (including the type 3 irregular galaxies) typically shows low values of n and preferentially lies close to the typical value $n = 1$ of disk-like exponential profiles. The distribution of early-type galaxies, on the other hand, reaches its peak at $n \sim 3.5$. The right panel of the

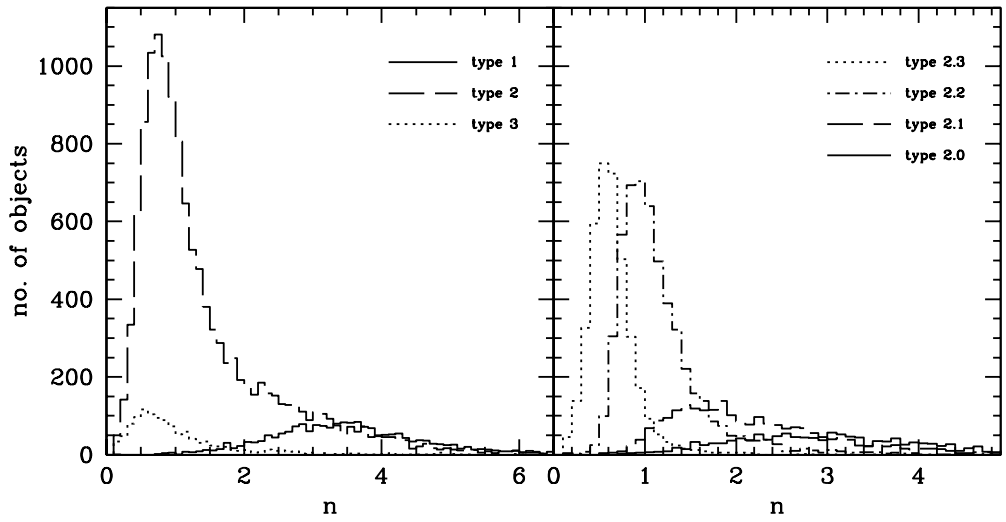

Fig. 3.4 — *Left half*: Distribution of Sérsic indices for galaxies classified by ZEST as type 1 (early-types), type 2 (disk galaxies) and type 3 (irregular and peculiar galaxies). *Right half*: Distribution of Sérsic indices for sources ranging from purely exponential disks (type 2.3) to bulge-dominated disks (type 2.0).

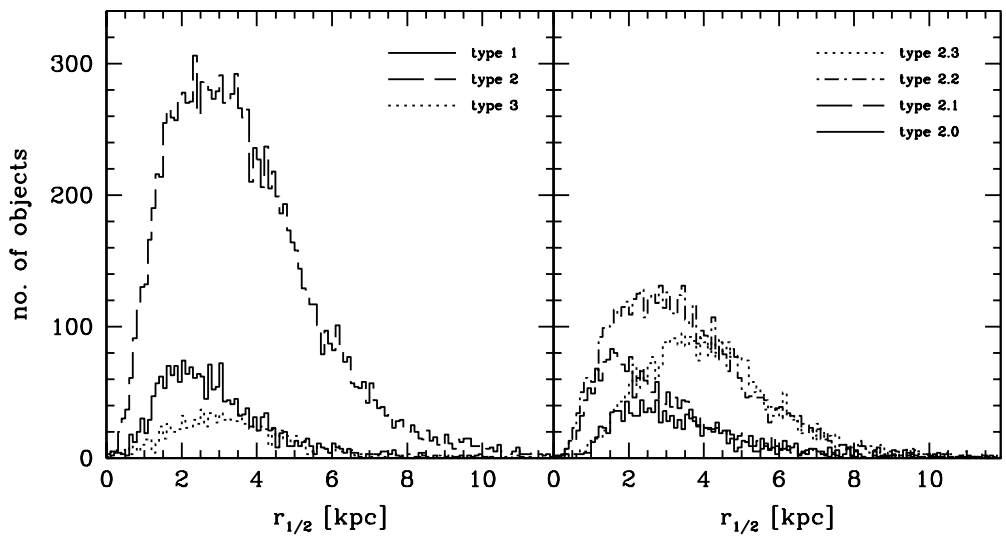

Fig. 3.5 — *Left half*: Distribution of half-light radii (measured in kpc) for galaxies classified by ZEST as type 1, type 2 and type 3. *Right half*: Distribution of half-light radii for objects ranging between pure exponential disks (type 2.3) and strongly bulge-dominated objects (type 2.0).

Tab. 3.2 — Number of galaxies as a function of redshift when a 2σ-cut in $\chi^2_{\rm phz}$ is applied

redshift	total sample	type 2.3	type 2.2	type 2.1	type2.0	type 1	type 3
$0.2 \leq z < 0.4$	3967	813	1733	571	276	425	132
$0.4 \leq z < 0.6$	2634	714	969	346	188	256	153
$0.6 \leq z < 0.8$	3313	813	873	506	357	540	219
$0.8 \leq z < 1$	2508	761	493	347	234	416	249
$1 \leq z < 1.2$	527	167	114	77	32	54	82

Tab. 3.3 — Number of galaxies as a function of redshift without a 2σ-cut in $\chi^2_{\rm phz}$

redshift	total sample	type 2.3	type 2.2	type 2.1	type2.0	type 1	type 3
$0.2 \leq z < 0.4$	4180	841	1791	601	309	465	149
$0.4 \leq z < 0.6$	2859	758	1045	381	214	279	171
$0.6 \leq z < 0.8$	3616	871	953	559	387	583	248
$0.8 \leq z < 1$	2840	800	552	415	287	507	270
$1 \leq z < 1.2$	661	188	134	96	52	93	96

figure shows the distribution of n for disk galaxies of different B/D ratio; by construction, the mode shifts to ever higher values of n as the bulge component gains in importance. It is evident from Figure 3.4 that a separation of galaxy types according to a simple cut in Sérsic index brings about a significant mixture of different galaxy populations. Depending on the scientific goals, however, it may be important to use samples as uncontaminated as possible by other galaxy types. In the following we thus adopt the more precise ZEST classification of galaxy types – rather than a cut in Sérsic index – to investigate the evolution of the size function of disk galaxies in Section 3.4.2.

As a final illustration of the COSMOS sample under investigation, we show the distributions of physical sizes $r_{1/2}$ in kpc in Figure 3.5. ZEST types and sub-types are displayed with different line styles, as in Figure 3.4 The distribution of half-light radii of disk-dominated galaxies (morphological type 2) peaks at roughly 2.75 kpc, that of elliptical galaxies (type 1) around 2 kpc. In the right panel of the figure, the peaks of the distribution of half-light radii shift to progressively smaller sizes with increasing B/D-ratio, as is expected for objects with successively more centrally concentrated surface brightness profiles. The only exception to this trend are the most bulge-dominated sources among the disk galaxy population (type 2.0), which break out of this sequence. The ZEST class 2.0 is defined as containing objects with a spheroidal component (and Sérsic index) similar to the type 1 early-type galaxies, but, as opposed to the latter, showing an obvious disk component as well. For many scientific applications, it might prove beneficial to merge this morphological class with the type 1 early-type galaxies (see, for instance, Scarlata et al. [104] for a discussion on the evolution of early-type galaxies in COSMOS, in which

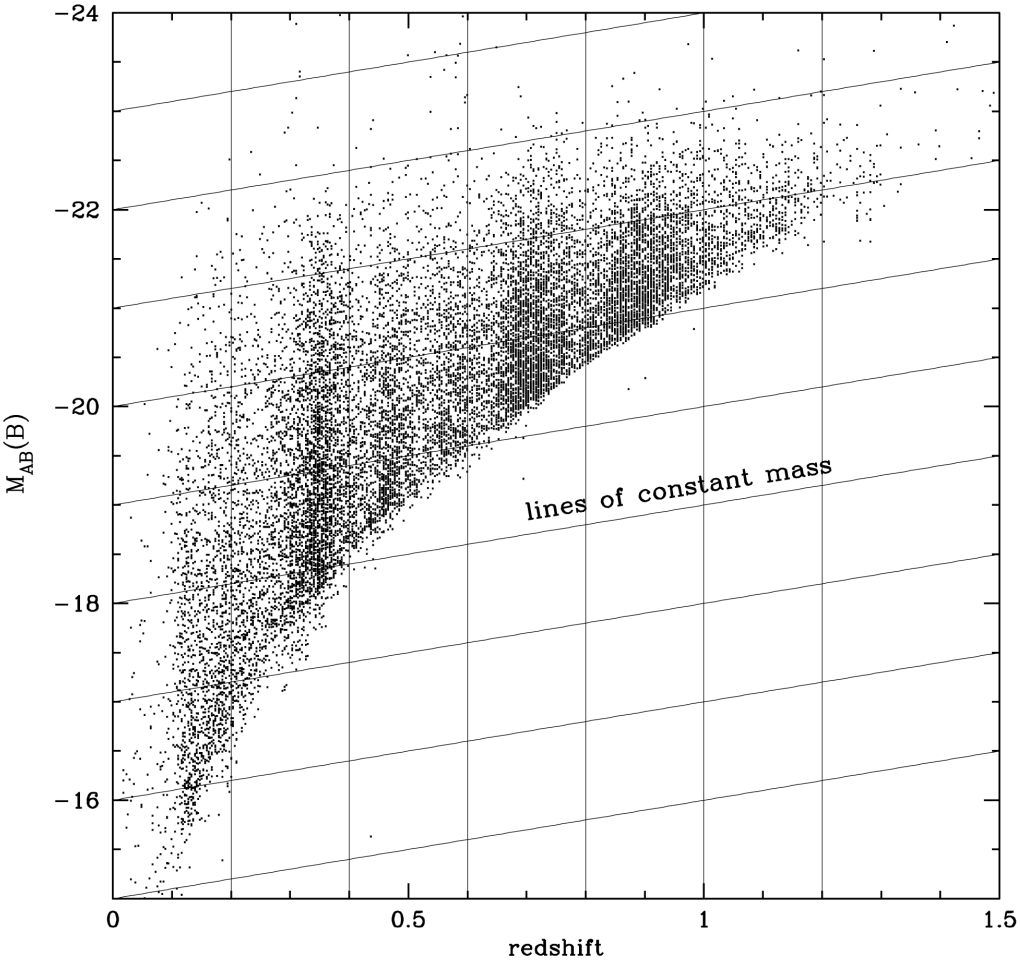

Fig. 3.6 — The distribution of all Cycle 12 COSMOS galaxies with $I \in [16, 22.5]$ and absolute B-band magnitude $M(B)$ at redshifts $z < 1.5$.

the effects of including the ZEST type 2.0 class in the sample is discussed in detail). Here we emphasize that the $I \leq 22.5$ COSMOS sample under scrutiny encompasses, for each galaxy type individually, a broad range in physical sizes and allows for statistically sound statements thanks to the large number of available objects. Thus, with proper care given to the effects of incompleteness, this permits us to study the evolution with cosmic time of the comoving number density of galaxies of a given size.

In this analysis we focus exclusively on the disk galaxies - classified as such by ZEST - and postpone the investigation of other galaxy populations to future publications. Of the 14,520 galaxies reliably fitted with GIM2D that remain in the sample after applying the selection criteria in magnitude, stellarity parameter, $\chi^2_{\rm GIM2D}$, $\chi^2_{\rm phz}$ and photometric reliability (see Section 3.2.2), 11,744 galaxies are classified as disk galaxies on the ZEST COSMOS classification grid. If no cut based on the value of $\chi^2_{\rm phz}$ is applied, the remaining sample of disk galaxies contains 12,701 objects. Figure 3.6 shows the distribution with

redshift of the galaxies in our sample and Tables 3.2 and 3.3 summarize in more detail how the disks and other galaxy types are assigned to the different investigated redshift bins up to $z \sim 1$. This information is provided both for the case when a cut based on the value of $\chi^2_{\rm phz}$ is applied to the sample, and when no such cut is applied. We have tested that the results obtained with and without the cut in $\chi^2_{\rm phz}$ do not differ significantly (see Section 3.5). We therefore show our results using the sample *with* the cut in $\chi^2_{\rm phz}$. Doing so implies the exclusion of a total of 8% of the original ACS-based $I \leq 22.5$ Cycle 12 COSMOS sample.

3.4 The Evolution of the Size Function of disk galaxies in COSMOS

3.4.1 ZEBRA photometric redshifts

Several codes and approaches have been used to derive accurate photometric redshifts for COSMOS galaxies down to faint magnitudes (see Mobasher et al. [82] for a review). In our work, we adopt the photometric redshift estimates obtained by Feldmann et al. [41] for the COSMOS galaxies of our ACS-selected $I \leq 22.5$ galaxy sample. These are computed with the Zurich Extragalactic Bayesian Redshift Analyzer (ZEBRA)[3].

ZEBRA produces two separate estimates of the photometric redshifts of individual galaxies: A maximum likelihood estimate and a fully two-dimensional Bayesian estimate in the space of redshift and templates. In both approaches, ZEBRA uses an iterative technique to automatically correct the original set of galaxy templates to best represent the spectral energy distributions of the galaxies in different redshift bins. The availability of a "training set" of spectroscopically derived zCOSMOS redshifts (see Lilly et al. [73]) for a small fraction of the whole considered photometric sample allows for a precise calibration of the ZEBRA photometric redshifts and thus for an optimal correction of the galaxy templates.

ZEBRA uses the available ancillary ground-based multi-band photometry to estimate the photometric redshifts of the COSMOS galaxies. The B, V, g', r', i', and z' fluxes are measured with Subaru (Taniguchi et al. [125]), u^* fluxes with CFHT and the 4 m telescopes at Kitt-Peak and CTIO provide the K_s photometry (Capak et al. [14], see also Section A.2.2 for more details on ancillary photometric measurements in the COSMOS field).

In the following, we use the ZEBRA maximum likelihood photometric redshifts of Feldmann et al. [41] for our discussion of the evolution of the size function of disk galaxies. The maximum likelihood ZEBRA photometric redshifts (in the ZEBRA release of spring 2006) have, at all redshifts of interest, an accuracy of $\Delta z/(1+z) \sim 0.03$ if compared with

[3] ZEBRA is documented on-line at `http://www.exp-astro.phys.ethz.ch/ZEBRA/`.

the zCOSMOS spectroscopic redshifts (Lilly et al. [73]). The application of ZEBRA to our sample shows some dependence of the photometric redshifts on whether small systematic offsets (of order approximately 0.05 mag or smaller), which are detected by the code, are applied to the calibration of the Subaru data. This has, however, no substantial impact on our analysis, as we show in the following by using, when relevant, the two ZEBRA estimates of the photometric redshifts obtained with and without corrections for these photometric offsets. The inclusion or exclusion of bad ZEBRA fits (cf. Tables 3.2 and 3.3) from our final sample does not change the conclusions of this manuscript either.

3.4.2 Derivation of the Size Function & assessment of completeness

In each redshift bin, the size function $\Phi(r_{1/2}, z)$ measures the number of galaxies per unit comoving volume and per unit half-light radius $r_{1/2}$. In order to chart the evolution of the number density of disk galaxies with a given size as a function of redshift up to $z \sim 1$, we split our sample of disk galaxies into four different redshift slices of width $\Delta z = 0.2$, centred on the redshifts 0.3, 0.5, 0.7, and 0.9.

There are two different considerations in constructing the size function which should be clearly distinguished. The first is the variation of sampling volume for different individual objects that are included in the sample. This can be fully taken into account using the $V_{\rm max}$-formalism (Felten [42], Schmidt [110]) in which each galaxy is weighted with the reciprocal of the comoving volume it could occupy while still satisfying the selection criteria of the sample. For bright objects this volume will be larger, thus leading to a smaller weight and correcting for their relative rarity with respect to fainter members of the galaxy population:

$$\Phi(r_{1/2}, z) \times \Delta r_{r_{1/2}} = \sum_{\gamma} \frac{1}{V_{\rm max,\gamma}} \ . \tag{3.1}$$

The summation is carried out over all sources γ with a photometric redshift within the redshift bin in consideration. Using that the comoving distance $D(z)$ in a ΛCDM cosmological model with $\Omega_\Lambda = 0.75$ and $\Omega_m = 0.25$ is given by

$$D(z) = \left(\frac{c}{H_0}\right) \int_0^z \frac{dz}{\sqrt{\Omega_\Lambda + \Omega_m \ (1+z)^3}} \ , \tag{3.2}$$

the volume $V_{\rm max}$ is calculated for each source according to

$$V_{\rm max} = \left(\frac{c}{H_0}\right)^3 \ d\Omega \ \left[\int_{z_{\rm min}}^{z_{\rm max}} \frac{dz}{\sqrt{\Omega_\Lambda + \Omega_m \ (1+z)^3}}\right]^3 \ . \tag{3.3}$$

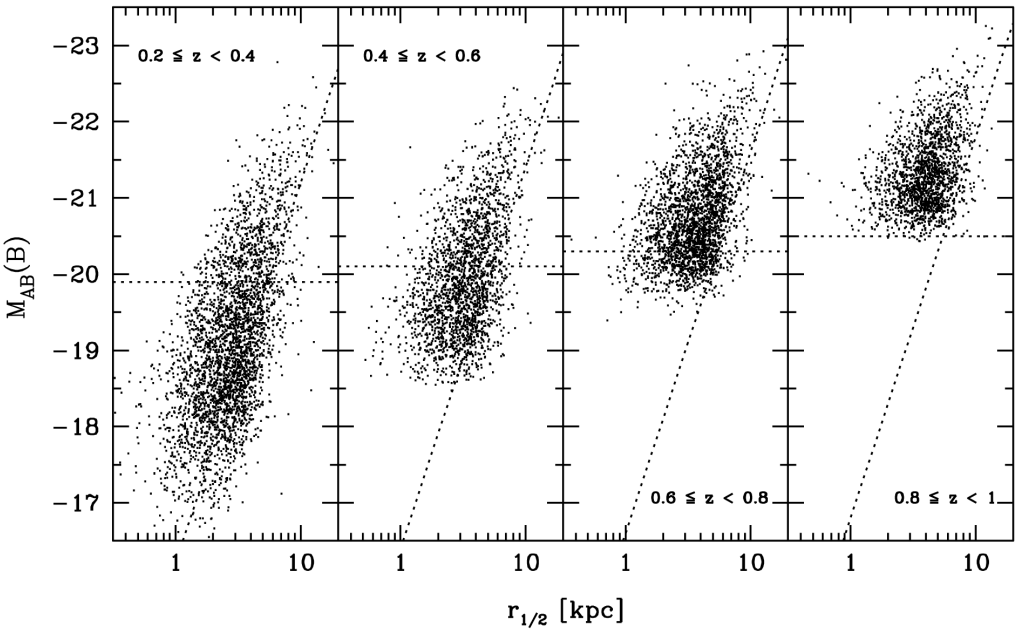

Fig. 3.7 — Distribution of absolute B-band magnitude $M(B)$ vs. physical size for type 2 disk galaxies as a function of redshift. Horizontal lines show the average magnitude cuts applied in the derivation of the size function within the different redshift bins (cf. Section 3.4.2) and inclined dotted lines are lines of constant surface brightness.

Here $d\Omega$ is the effective solid angle covered by the survey during Cycle 12, which is 2734 arcmin^2.

The lower and upper bounds of integration, $z_{\rm min}$ and $z_{\rm max}$, define the redshift range within which any particular galaxy in the sample could have entered the sample. It is constrained in three ways: (1) the minimum and maximum redshifts of the relevant redshift bin, $z_{\rm min,\ bin}$ and $z_{\rm max,\ bin}$; (2) the minimum and maximum redshifts at which the sample magnitude limits are satisfied, $z_{\rm min,\ mag}$ and $z_{\rm max,\ mag}$; and (3) the minimum and maximum redshifts at which the size limits of the sample are fulfilled ($z_{\rm min,\ size}$ and $z_{\rm max,\ size}$). The size limit of relevance is that the object must have sufficient pixels to be classified by ZEST (FWHM $> 0.15''$) and can be calculated from the condition that the galaxy have the same physical size $r_{1/2} \propto D_A \cdot R_{1/2}$ [px] at all redshifts, regardless of its observed scale:

$$\frac{D_A(z_{\rm max,\ size})}{D_A(z_{\rm obs})} = \frac{R_{1/2,\rm obs}}{R_{1/2,\rm min}} \ .$$

(Here the subscript 'obs' indicates the actually measured value of both quantities.) In practice the size constraint is the least significant because of the small variation in angular diameter with redshift at high redshifts and because of the high angular resolution of the

HST images. Of more importance are the limits in redshift imposed by the magnitude cuts. In the case of a bounding magnitude of $I_{\rm lim}$ – in the present analysis either $I = 16$ or $I = 22.5$ – the requirement of identical absolute magnitude leads to the condition

$$M(B) = I_{\rm lim} - 5\,\log\left[D_L(z_{\rm lim})/(10{\rm pc})\right] + K_{F814W,B}(z)\ ,$$

which must be solved for the limiting redshift $z_{\rm lim}$[4].

There may also be an observational surface brightness selection. It is, however, unimportant in practice when compared with the surface brightness constraint induced by a selection in absolute magnitude. The difficulty is that the size function is only partially sampled, because of the magnitude limits of the sample. Thus the size function constructed above represents the integral of the bivariate size-luminosity function above some limiting luminosity. We adopt the approach of Lilly et al. [71] to deal with this problem and (a) limit the sample in equation (2) to objects lying within a specified range of luminosity, and allow this luminosity range to change with redshift according to the expected luminosity evolution of individual galaxies. The integration over luminosity of the bivariate function is thus explicit, albeit model-dependent. Second, we (b) consider, at each redshift, the limiting size above which one can be fairly confident that the sample is more or less "complete", i.e., that there are rather few objects of this size, or greater, lying below the magnitude limit because of their low surface brightness. Of course, luminous low surface brightness galaxies are known to exist and the sample can never be absolutely complete, but we may assume that the size function above this limiting size will be a good approximation to reality and it will, in any case, represent a lower limit to the actual number density. It is important to appreciate that this apparent surface brightness selection arises from the inevitable selection in absolute magnitude (at a given size) rather than any direct observational surface brightness selection (see Lilly et al. [71] for a detailed discussion of this matter).

Figure 3.7 shows the distribution of $M(B)$ and $r_{1/2}$ in the sample as a function of redshift. As discussed in the previous paragraph, we limit the set of galaxies to those above a redshift-dependent magnitude limit of $M(B) = (-19.6 - z)$. It reflects an assumed luminosity evolution by about 1 mag due to a passively aging stellar population since $z \sim 1$. The horizontal dotted lines in Figure 3.7 illustrate the effect of the cut as it would be applied at the lower limiting redshift of the different bins. Their loci change from an absolute magnitude of $M(B)$ = -20.5 at redshift 0.9 to $M(B)$ = -19.6 at redshift zero. In Figure 3.7 the inclined dotted lines are lines of constant surface brightness, shifted according to the assumed surface brightness evolution. The figure illustrates that our sample is fairly complete above $r_{1/2} \sim 5$ kpc; i.e., the bulk of galaxies with sizes above this threshold lies above the horizontal line at all redshifts. We therefore limit our analysis to galaxies with half-light radii exceeding this size.

[4] Here $K_{F814W,\ B}$ denotes the K-correction as defined through the equation $I = M(B) + 5\,\log(D_L(z)/10\ pc) + K_{I,B}$ (see Hogg et al. [57]).

3.4.3 Errors

Sizes, magnitudes and photometric redshifts are all subject to uncertainty. In order to assess the resulting inaccuracy of the size function $\Phi(r_{1/2}, z)$, we varied these quantities according to a Gaussian distribution centred on the measured values and having an appropriate standard deviation. In the case of the photometric redshifts, for instance, the standard deviation rises with increasing redshift as $\sigma_z \approx 0.03 \cdot (1+z)$. For the magnitude, we used the standard deviation σ_I given in the ACS-COSMOS catalog. Errors for the sizes are tabulated for each galaxy by GIM2D in the form of upper and lower 99% confidence levels, corresponding to $3\sigma_{R_{1/2}}$ for the half-light radii.

From the results of 101 test runs with errors introduced on all three of the above quantities, we calculated the resulting scatter for each bin of the size function. The size of the errors given on the grounds of these tests corresponds to the interquartile range of the 101 values at every measurement point on the curve $\Phi(r_{1/2}, z)$. The interquartile range spans 50% of a data set, and eliminates the influence of outliers by effectively removing the highest and lowest quarters of the data range. The distance from the median of the 101 error realisations to the first and third quartile give the lower and upper error bar respectively. In the plots of the size function (see Figures 3.8 and 3.9) these asymmetric errors have been reported in each individual data point and the area between them shaded in grey.

The Poisson noise in each bin of the size function (owing to the statistical manner in which each bin is populated) remains, however, the dominant source of random error in the size function. The Poisson error is given by:

$$\sigma_P = \sqrt{\sum_{\gamma} \frac{1}{V^2_{\mathrm{max},\gamma}}} \tag{3.4}$$

with the summation carried out over all objects γ in a given bin. Poisson errors are reported symmetrically around the data points in each bin of the size function.

Systematic uncertainties in the GIM2D measurements of the half-light radii (discussed in Section 2.1.3) could affect the slope of the size functions presented in Figures 3.8 and 3.9 for the COSMOS galaxies, and in Figures 3.11 and 3.12 for our comparison sample of SDSS galaxies (Section 3.4.4 below). It should be noted that any systematic errors arising from the fits would be identical at $z = 0$ and $z = 0.7$ and thus the *SDSS-normalized* densities of Figures 3.13 and 3.14 – on which we base our discussion and conclusions – are free of such systematics.

3.4.4 Comparison with the local SDSS galaxy population

To quantitatively assess the redshift evolution of the number density of disk galaxies of a given size (and as a function of B/D-ratio), it is important to realize that a large

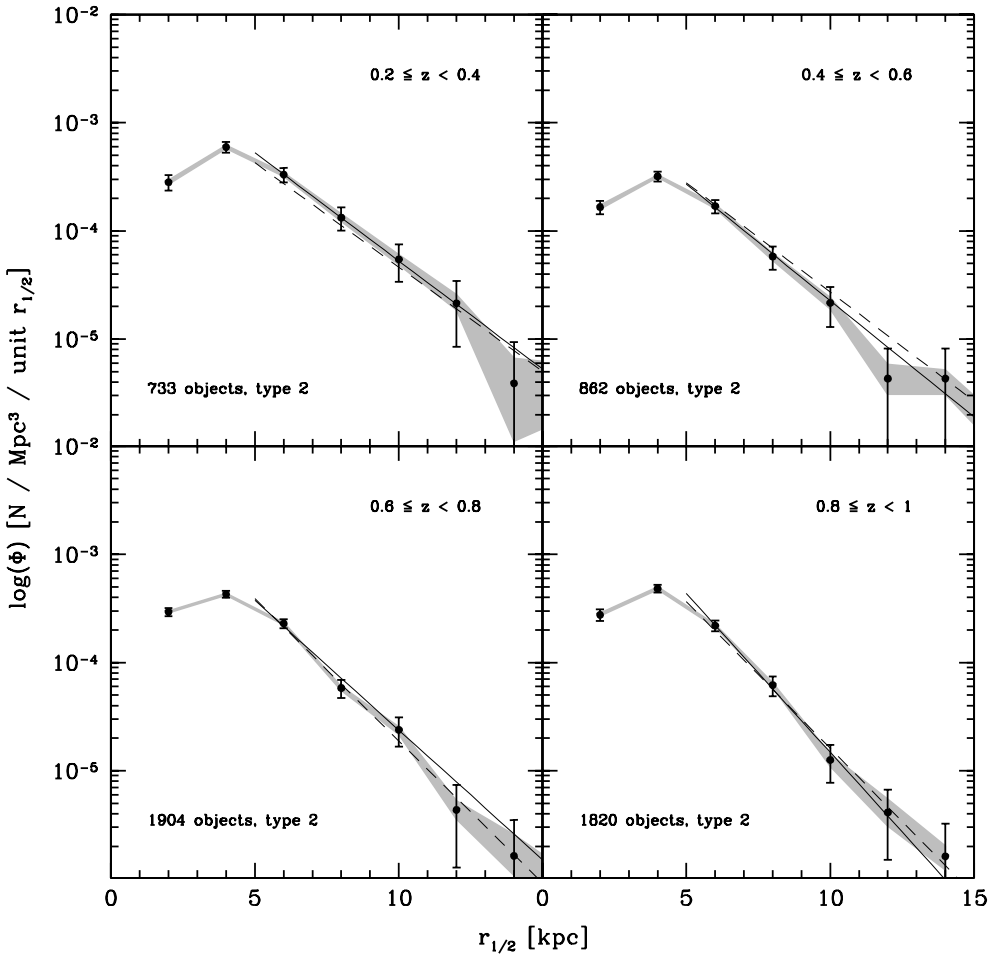

Fig. 3.8 — Evolution of the size function between redshift 0.2 and 1 for the entire sample of disk galaxies. Four different bins of redshift, centred at $z \sim 0.3$, 0.5, 0.7 and 0.9, are displayed. The vertical error bars reproduce the Poisson errors. Areas shaded in grey indicate the errorbar on the size function induced by random errors in redshift, size and observed magnitude (cf. Section 2.1.3). The solid and dashed lines in black show fits to the relation $\log(\Phi) = \alpha \cdot r_{1/2} + \beta$ above 5 kpc, calculated for two sets of ZEBRA photometric redshifts obtained without and with corrections to the photometric catalogs, respectively (cf. Section 3.4.1). Table 3.4 lists the best fit parameters of the solid lines.
Apart from a modest steepening of the slope with increasing redshift, the size function of disk galaxies is roughly constant in the range $0.2 < z < 1.0$.

overdensity in the COSMOS field at $z < 0.4$ affects the number counts in the lowest COSMOS redshift bin. Therefore, to carry out our comparison and determine how the number of disk galaxies with scalelengths larger than about 5 kpc changes with redshift from $z \sim 1$ to $z \sim 0$, we repeated our analysis on a set of 1876 galaxies extracted from the SDSS Data Release 4. To fully include all observational effects, the images of the SDSS

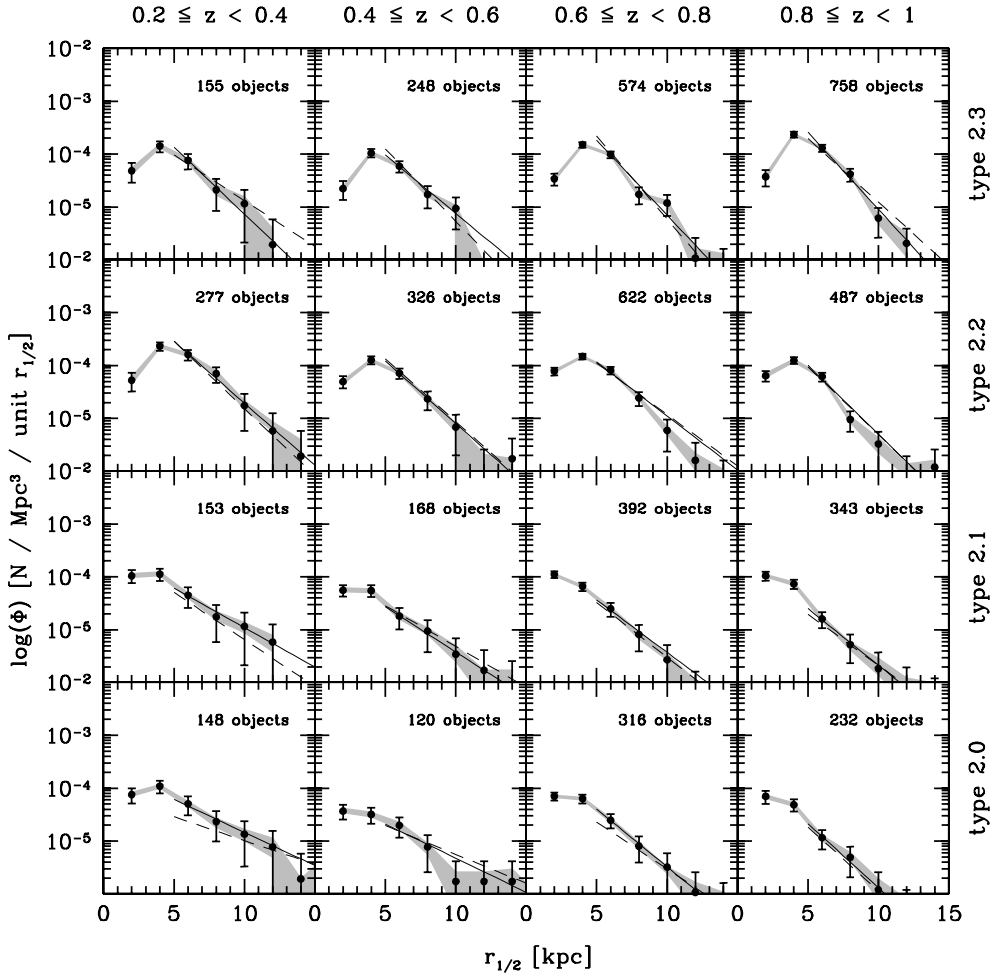

Fig. 3.9 — The evolution of the size function shown individually for all sub-classes of the disk galaxy population in COSMOS. The sub-classes are displayed by increasing B/D-ratio from top to bottom. The errors and the solid and dashed black lines are as in Figure 3.8.

galaxies were degraded so as to appear as they would in the COSMOS images at $z = 0.7$. The generation of these simulated images is described in detail in Kampczyk et al. [62] (see also Section A.1 for a brief overview). To summarize, the $\mathrm{SDSS}_{z=0.7}$ galaxies were selected from the redshift range $z \in [0.015, 0.025]$. Their g-band images were then transformed to how such galaxies would appear in the F814W COSMOS ACS images if they were to lie at $z = 0.7$, at which redshift the passbands are well matched. Thus, this "redshifting" of the SDSS galaxies needed only to take into account the different pixel scales, and point spread function, and the cosmological surface brightness dimming. Two sets of images were produced, one without surface brightness evolution and one with an assumed brightening to high redshift of $\Delta\mu = z$ mag arcsec^{-2}. (We will henceforth refer to these two samples as "unbrightened" and "brightened", respectively). No size evolution

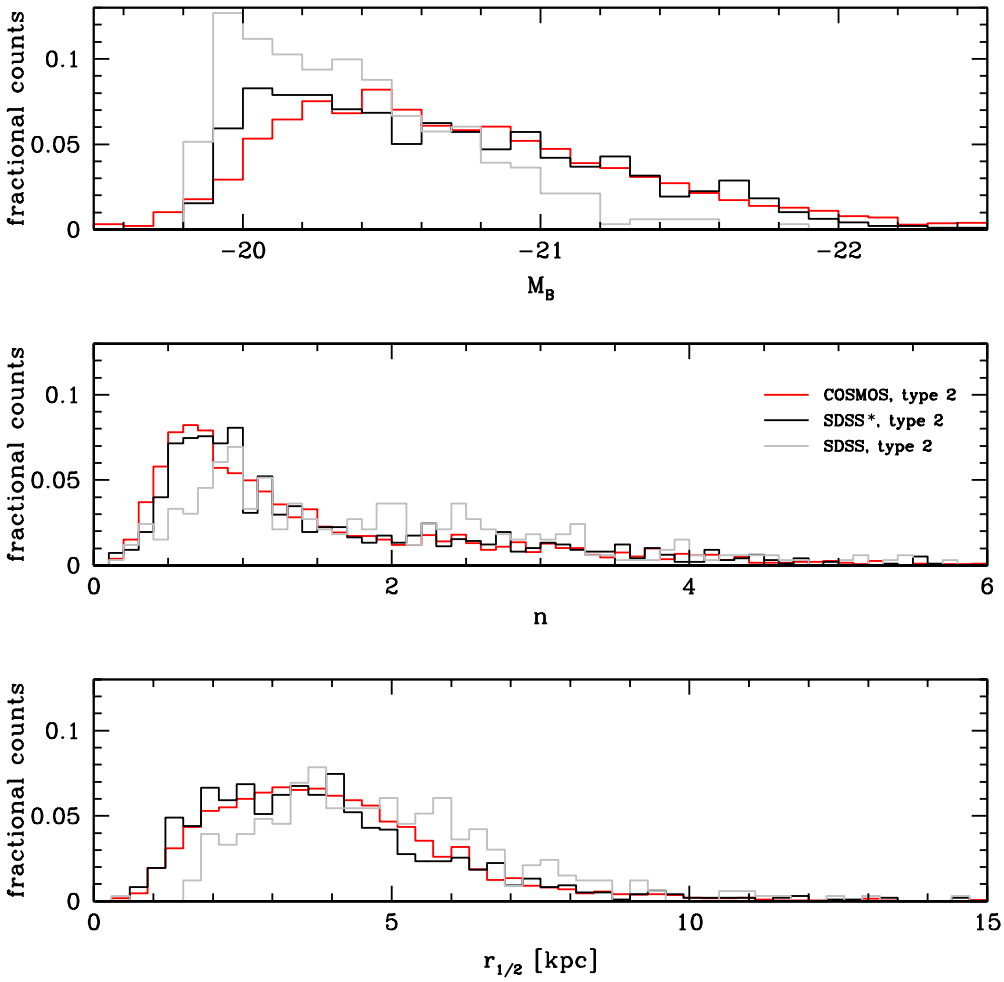

Fig. 3.10 — Normalized distribution of absolute B-band magnitudes (*top*), Sérsic indices (*centre*) and half-light radii (*bottom*) in the sample of artificially redshifted SDSS galaxies (black histogram; brightened sample ('SDSS*') - grey histogram; unbrightened sample ('SDSS')) and the COSMOS data set (red histograms) in the range $z \in [0.6, 0.8[$.

was considered. The simulated galaxies at $z = 0.7$ were then added into the COSMOS ACS images to reproduce also the same issues of image crowding and noise. These $z = 0.7$-"simulated" SDSS galaxies were then analyzed following the identical procedure adopted for the real COSMOS objects. Stamps sized $10'' \times 10''$ or more were extracted for all galaxies. As before, the original images were cleaned if necessary and then symmetrised prior to performing the GIM2D fits. After applying exactly the same selection criteria with respect to magnitude and $\chi^2_{\rm GIM2D}$, 457 and 1294 objects remained in the unbrightened and brightened samples, respectively. The distribution of absolute B-band magnitudes, half-light radii and Sérsic indices among the two sets of artificially redshifted SDSS galaxies is compared to that of COSMOS galaxies in the range $z \in [0.6, 0.8[$ in Figure 3.10.

Tab. 3.4 — Line parameters of the COSMOS size function for radii $r_{1/2} > 5$ kpc.

type	redshift	α	β	χ^2
type 2	0.3	-0.200 ± 0.021	-2.278 ± 0.167	0.912
	0.5	-0.215 ± 0.024	-2.494 ± 0.180	0.834
	0.7	-0.240 ± 0.017	-2.225 ± 0.125	5.363
	0.9	-0.294 ± 0.031	-1.891 ± 0.215	0.311
type 2.3	0.3	-0.253 ± 0.070	-2.602 ± 0.501	0.204
	0.5	-0.221 ± 0.071	-2.910 ± 0.485	0.279
	0.7	-0.283 ± 0.034	-2.321 ± 0.237	2.940
	0.9	-0.291 ± 0.049	-2.130 ± 0.331	0.800
type 2.2	0.3	-0.234 ± 0.039	-2.372 ± 0.293	0.457
	0.5	-0.236 ± 0.039	-2.735 ± 0.291	1.641
	0.7	-0.204 ± 0.022	-2.913 ± 0.171	6.963
	0.9	-0.260 ± 0.035	-2.696 ± 0.254	4.164
type 2.1	0.3	-0.149 ± 0.061	-3.468 ± 0.500	0.088
	0.5	-0.171 ± 0.050	-3.710 ± 0.446	0.060
	0.7	-0.198 ± 0.043	-3.446 ± 0.330	1.562
	0.9	-0.214 ± 0.046	-3.528 ± 0.377	0.155
type 2.0	0.3	-0.125 ± 0.029	-3.585 ± 0.303	0.981
	0.5	-0.129 ± 0.031	-4.031 ± 0.326	2.274
	0.7	-0.218 ± 0.046	-3.304 ± 0.354	0.082
	0.9	-0.242 ± 0.068	-3.458 ± 0.533	0.136

Note. — Line parameters and χ^2 of the linear regressions of the form $\log(\Phi) = \alpha \cdot r_{1/2} + \beta$ applied to the size functions of Figures 3.8 and 3.9 at sizes $r_{1/2} > 5$ kpc (solid black lines in the figures). The values of slope α and y-axis intercept β are given for the morphological class type 2 as a whole, and for the different B/D-ratio sub-classes. See Figures 3.8 and 3.9 for the graphical representation of the size function derived from the COSMOS galaxies.

Absolute B-band magnitudes for the SDSS$_{z=0.7}$ galaxies were derived by determining the best fit spectral energy distribution template with ZEBRA, and then calculating the K-correction for that spectral type, and the corresponding distance modulus, at redshift $z \sim 0.7$. The SDSS sample of Kampczyk et al. [62] was extracted as a volume limited sample from the local Universe; its equivalent volume was obtained by computing the luminosity function for the 1876 SDSS galaxies, and setting it equal to the global SDSS luminosity function (see Section A.1 for more details). We used the equivalent volume derived in this way to compute the size function for the SDSS$_{z=0.7}$ sample.

3.5 Results & discussion

Figures 3.8 and 3.9 show the size functions for the total disk galaxy population and for disk galaxies of different B/D-ratios, derived as a function of redshift above an evolving absolute magnitude limit $M(B) = (-19.6 - z)$ (see Section 3.4.2). As discussed before,

Tab. 3.5 — Line parameters of the size function derived from artificially redshifted SDSS galaxies for radii $r_{1/2} > 5$ kpc.

sample	type	α	β	χ^2
SDSS	type 2	-0.159 ± 0.027	-3.051 ± 0.234	2.589
	type 2.3	-0.172 ± 0.056	-3.449 ± 0.494	0.429
	type 2.2	-0.110 ± 0.034	-3.877 ± 0.341	1.942
	type 2.1	-0.128 ± 0.080	-4.013 ± 0.675	1.351
	type 2.0	-0.100 ± 0.304	-4.158 ± 2.046	0.002
SDSS*	type 2	-0.197 ± 0.026	-2.470 ± 0.201	0.939
	type 2.3	-0.176 ± 0.040	-3.060 ± 0.326	2.434
	type 2.2	-0.217 ± 0.055	-2.727 ± 0.404	0.402
	type 2.1	-0.107 ± 0.050	-4.031 ± 0.503	0.244
	type 2.0	-0.142 ± 0.048	-3.743 ± 0.431	1.683

Note. — Line parameters and χ^2 of the linear regressions of the form $\log(\Phi) = \alpha \cdot r_{1/2} + \beta$ applied to the size functions of the brightened (denoted as 'SDDS*' in the table) and unbrightened (denoted 'SDDS') artificially redshifted SDSS galaxies at sizes $r_{1/2}$ >5 kpc. The values of slope α and y-axis intercept β are given for the morphological class type 2 as a whole, and for the different B/D-ratio sub-classes. See Figures 3.11 and 3.12 for the graphical representation of the size function derived from the $\mathrm{SDSS}_{z=0.7}$ galaxies.

these size functions should be most complete for sizes larger than roughly 5 kpc. Above this threshold we have thus fit them with straight lines of $log(\Phi)$ vs. $r_{1/2}$, i.e., with an exponential size function. The fits of the aforementioned functional form were calculated for two sets of photometric ZEBRA redshifts; one obtained without (solid line) and the other with (dashed line) corrections to the photometric catalog (with no significant change to our conclusions). The reported size function is based on the uncorrected photometry and the parameters of the corresponding solid black lines are given in Table 3.4. The size function of disk galaxies as a whole appears remarkably constant with redshift across the range $0.2 < z < 1$. We detect, however, a weak trend for the slope of the size function to steepen with redshift, a result which applies to the global disk population and also separately to all categories of bulge-to-disk ratio.

These findings are strengthened by comparing directly the COSMOS size function in the range $z \in [0.6,\ 0.8[$ with that derived from the local SDSS sample ("redshifted" to $z \sim 0.7$). In Figures 3.11 and 3.12, the SDSS-based size functions are plotted together with the COSMOS size functions in the bin $z \in [0.6,\ 0.8[$. The size function of the brightened $\mathrm{SDSS}_{z=0.7}$ sample is reported with solid grey points and error bars (and labeled as 'SDSS*'); the grey circles show the unbrightened one (labeled as 'SDSS'). The difference is due to the brightening of the galaxies which, in combination with the luminosity cut at $M(B) \sim$ -20.3 at $z = 0.7$ (see Figure 3.7) leads to a greater number of smaller objects in the brightened set of SDSS galaxies. Given the evidence for luminosity evolution in all classes of galaxies, we would expect the brightened sample to provide the best comparison and in Figure 3.10 the latter indeed matches the distributions of $M(B)$, n and $r_{1/2}$ of COSMOS galaxies best. The line parameters of a linear regression on the $\mathrm{SDSS}_{z=0.7}$ size functions in the same range of sizes as in the COSMOS data set are listed in Table 3.5.

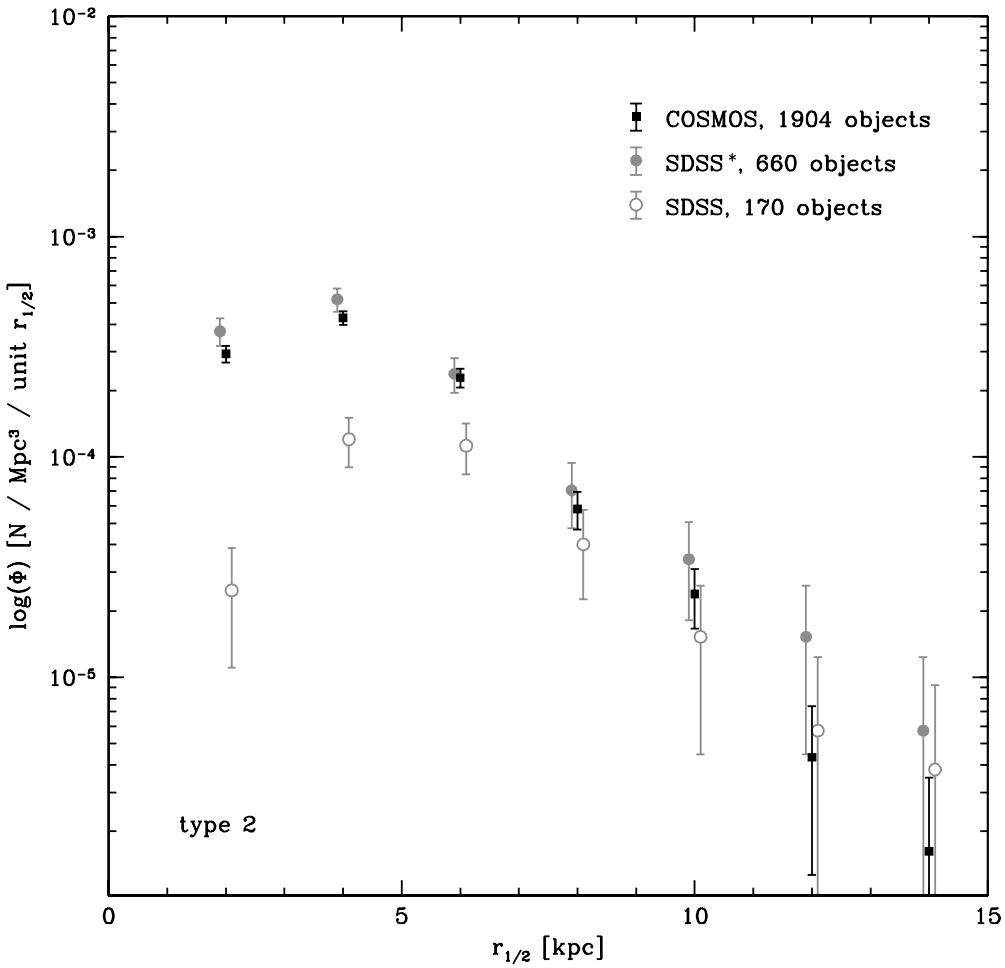

Fig. 3.11 — Size function for COSMOS disk galaxies as plotted in Figure 3.8 (black squares) in the range $z \in [0.6, 0.8[$ and for brightened (filled grey points) and unbrightened (empty grey points) artificially redshifted SDSS galaxies. The data points of the $\mathrm{SDSS}_{z=0.7}$ size functions have been slightly offset from their nominal value of $r_{1/2}$ for better legibility. Systematic effects on the GIM2D size measurements are identical to those discussed for the COSMOS sample (see caption of Figure 3.8, and secction 2.1.3).
The COSMOS size function in the range $z \in [0.6, 0.8[$ and that of the simulated $\mathrm{SDSS}^*_{z=0.7}$ galaxies closely resemble each other. The steeper slope of the size function in COSMOS relative to that of artificially redshifted SDSS galaxies confirms the tendency observed in Figures 3.8 and 3.9, implying a small deficit of the largest disks ($r_{1/2} > 7$ kpc) in the COSMOS sample compared to the local universe.

Figures 3.11 and 3.12 show a striking similarity in the shape of the size function over half the Hubble time. Furthermore, the steepening of the size function in COSMOS relative to locally is confirmed in that there is a small deficit of the largest disks ($r_{1/2} > 7$ kpc) in the COSMOS sample compared to the artificially redshifted local sample.

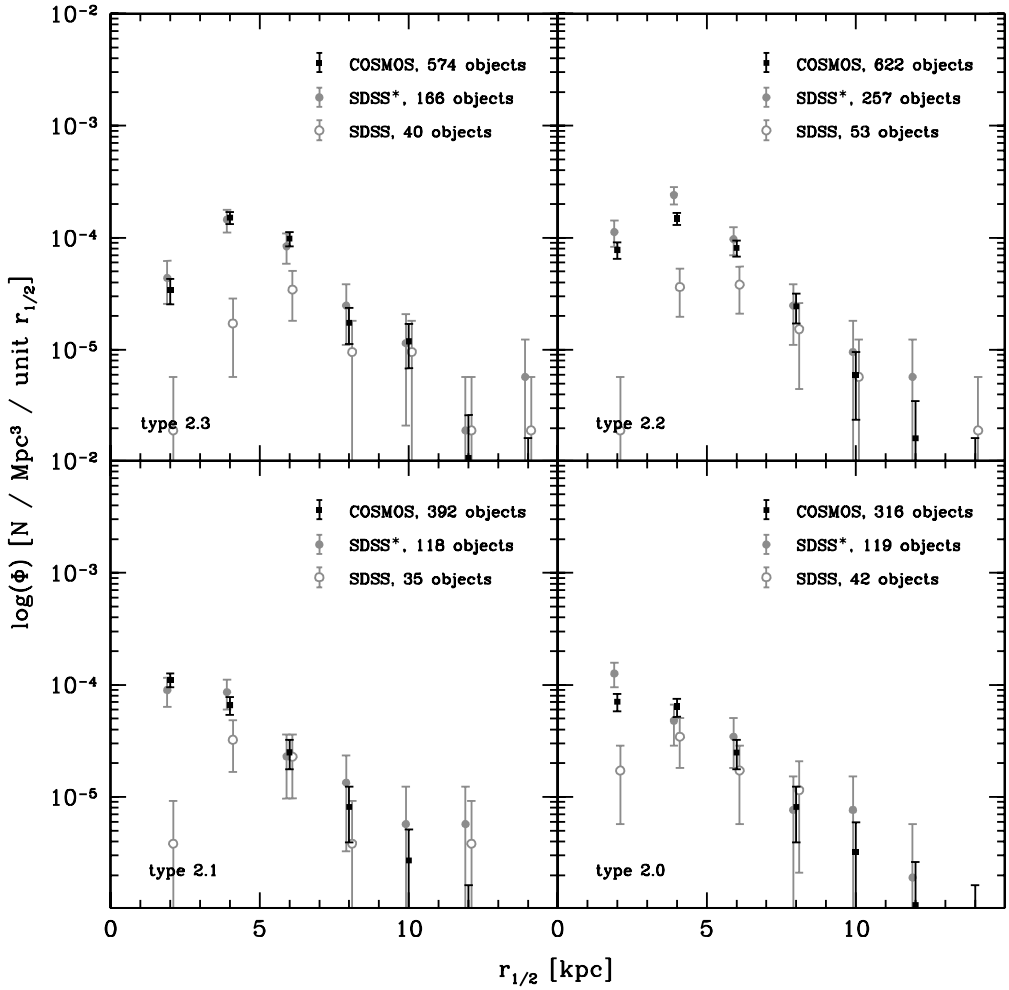

Fig. 3.12 — Size function for COSMOS disk galaxies (reported with black squares and split by relative importance of the bulge component) in the range $z \in [0.6, 0.8[$ (as plotted in Figure 3.9) and for brightened (filled grey points) and unbrightened (empty grey points) artificially redshifted SDSS galaxies.
Broadly speaking, a general constancy of the size function over half the Hubble time is seen for galaxies of all bulge-to-disk ratios. However, the four panels above indicate that the steepening of the slope of the size function is more pronounced for galaxies with measurable bulges than for bulgeless disks. Therefore, the deficit of large disks at earlier epochs is apparently caused by a deficit of *bulged* disk galaxies at high redshift.

To further investigate this issue we show in the two following figures the density of disk galaxies in COSMOS normalized to the local size function of (brightened) SDSS sources for two size bins, for all disks (Figure 3.13) and differentiated by bulge-to-disk ratio (Figure 3.14). In Table 3.6 we list the relative densities $\widetilde{\rho} = \Phi_{COSMOS}/\Phi_{SDSS^*}$ for disk galaxies as a function of redshift and B/D-category. Here Φ_{COSMOS} denotes the comoving number density per unit size, as presented in Figures 3.8 and 3.9 for the COSMOS sample in

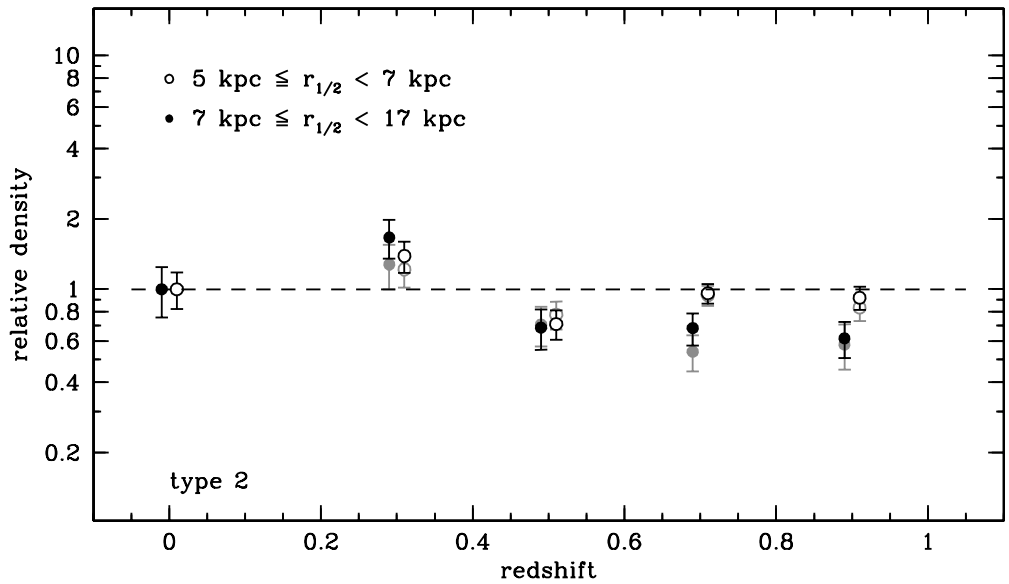

Fig. 3.13 — The density of COSMOS disk galaxies with half-light radii in the range 5-7 kpc and > 7kpc, normalized to the corresponding brightened SDSS sample, as a function of redshift (see Table 3.6 for the values of the relative density $\widetilde{\rho} = \Phi_{COSMOS}/\Phi_{SDSS^*}$). The point at $z = 0$ (equal to 1 by definition since $\widetilde{\rho} = \Phi_{SDSS^*}/\Phi_{SDSS^*}$) is plotted to show the error on the $z = 0$ measurement based on the SDSS$_{z=0.7}$ sample. The evolution of the SDSS-normalized density is not affected by the systematic errors in the GIM2D estimates of the half-light radii discussed in Section 2.1.3. Black and grey symbols refer to the two sets of photometric redshifts from ZEBRA, obtained without and with correction to the photometric catalogs (cf. Section 3.4.1 and Figures 3.8 and 3.9). Uncertainties in the estimates of the photometric redshifts do not change our conclusions.

the studied redshift bins. The variable Φ_{SDSS^*} stands for the (artificially redshifted and brightened) SDSS density in the $z \in [0.6, 0.8[$ redshift bin (as presented in Figure 3.11 for the entire disk galaxy sample, and in Figure 3.12 for the sample split in the four B/D ratio bins). In the table, $\widetilde{\rho}_<$ stands for the relative density of disks with intermediate sizes of $r_{1/2} \in [5, 7[$ kpc and $\widetilde{\rho}_>$ for that of large disks with $r_{1/2} \in [7, 17[$ kpc. At $z = 0$, the normalized density point $\Phi_{SDSS^*}/\Phi_{SDSS^*} = 1$ has been plotted as well, so as to show the error bar on the SDSS $z = 0$ density estimate. Within the uncertainties (and excluding the lowest redshift bin from COSMOS because of the large cosmic variance), there is no evidence for a variation with redshift in the size function of disks in the range $r_{1/2} \in [5$ kpc, 7 kpc$[$. Disk galaxies of these intermediate sizes have neither grown nor been destroyed from $z = 1$ to $z = 0$ or, alternatively, the growth and destruction of such systems exactly balanced over this period. The larger disks, however, show a weak decline by a factor of nearly 2 over the same time span, even though the sample should be more complete for these larger disks as discussed before.

Figures 3.9, 3.12 and especially Figure 3.14 and the values of the slopes α given in

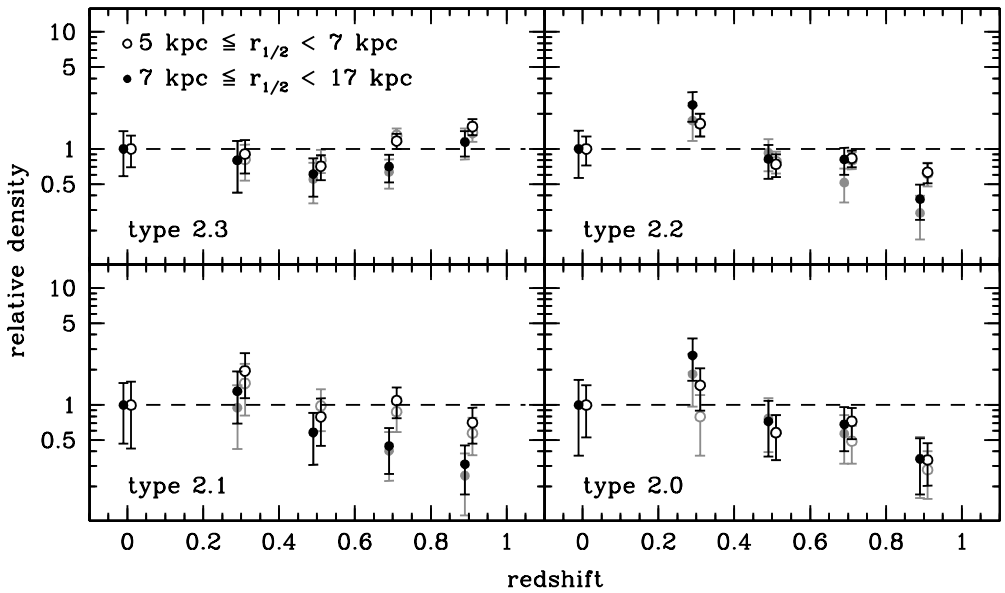

Fig. 3.14 — As in Figure 3.13, but shown individually for disk galaxies with different B/D-ratio. Black and grey symbols too are as in Figure 3.13.
A constant (or possibly even slightly higher) number density of large bulgeless disks is observed at $z \sim 1$, while disk galaxies with a prominent bulge are three time less frequent than in the local universe at that redshift.

Table 3.4, consistently show the steepening of the slope of the size function to be more pronounced for galaxies with higher B/D-ratios. This suggests that the deficit of large disks at earlier epochs is primarily due to a deficit of *bulged* disk galaxies. In principle disks with the highest bulge-to-disk ratio could be classified as early-types by ZEST and thus excluded from our sample, yet the direct comparison with the $\mathrm{SDSS}_{z=0.7}$ sample – which was classified in precisely the same fashion – argues against this interpretation. Moreover, the stated result remains valid even if type 2.0 galaxies are omitted from the discussion. Morphological K-corrections could play a role in the observed disappearance of about 60% of the large disks with bulges, due to color differences between bulges and disks; we are studying this issue in more detail.

The constancy – or even slight increase – of the number density of *bulgeless* disks out to $z \sim 1$ is at variance with models based on hierarchical formation or infall scenarios (e.g., Bouwens and Silk [12], Mo et al. [81]). On the other hand, a constant or slightly increasing number density of large bulgeless disks at $z \sim 1$, in combination with a decrease of similarly sized *bulged* disks to this redshift, supports a scenario in which secular evolution processes form or at least increase the sizes of bulges at late stages in the history of the universe. Independent evidence for bulge-building secular evolution within disk galaxies comes from numerical experiments (e.g., Debattista et al. [32, 33, 34], Norman et al. [85]), observations of nearby "young" bulges with disk-like stellar density profiles (see Kormendy and Kennicutt [67] and Carollo [16] for reviews and references; Carollo [17], Carollo et al.

Tab. 3.6 — Relative densities $\widetilde{\rho} = \Phi_{COSMOS}/\Phi_{SDSS^*}$ as a function of redshift.

type	redshift	$\widetilde{\rho}_<$	$\widetilde{\rho}_>$
type 2	0.3	1.386 ± 0.327	1.664 ± 0.513
	0.5	0.710 ± 0.163	0.686 ± 0.214
	0.7	0.960 ± 0.196	0.681 ± 0.197
	0.9	0.920 ± 0.195	0.616 ± 0.185
type 2.3	0.3	0.904 ± 0.398	0.798 ± 0.502
	0.5	0.710 ± 0.274	0.610 ± 0.336
	0.7	1.169 ± 0.393	0.706 ± 0.349
	0.9	1.550 ± 0.528	1.142 ± 0.551
type 2.2	0.3	1.639 ± 0.585	2.379 ± 1.241
	0.5	0.737 ± 0.262	0.819 ± 0.445
	0.7	0.832 ± 0.270	0.811 ± 0.411
	0.9	0.632 ± 0.215	0.372 ± 0.205
type 2.1	0.3	1.954 ± 1.392	1.311 ± 0.934
	0.5	0.792 ± 0.573	0.582 ± 0.415
	0.7	1.089 ± 0.706	0.446 ± 0.305
	0.9	0.707 ± 0.473	0.311 ± 0.217
type 2.0	0.3	1.473 ± 0.903	2.651 ± 1.973
	0.5	0.578 ± 0.364	0.724 ± 0.584
	0.7	0.725 ± 0.403	0.681 ± 0.513
	0.9	0.338 ± 0.209	0.345 ± 0.279

Note. — Relative densities $\widetilde{\rho} = \Phi_{COSMOS}/\Phi_{SDSS^*}$ for disk galaxies as a function of redshift and B/D-category. Here Φ_{COSMOS} and Φ_{SDSS^*} denominate the comoving number density per unit size as reported in the plots of the size function in Figures 3.8 and 3.9 for the COSMOS sample in the redshift range $z \in [0.6, 0.8[$, and in Figures 3.11 and 3.12 for the artificially redshifted and brightened sample of the SDSS galaxies. $\widetilde{\rho}_<$ stands for the relative density of disks with intermediate sizes of $r_{1/2} \in [5, 7[$ kpc and $\widetilde{\rho}_>$ for that of large disks with $r_{1/2} \in [7, 17[$ kpc.

[18, 19, 20, 21]), and also from the lack of evolution in the fraction of large-scale bars in disk galaxies since redshift 1 (Jogee et al. [59], Sheth et al. [115]). Our work provides strong evidence that, by $z \sim 1$, the disks have not only grown to their current sizes, but also that they have become massive and stable enough to allow for large-scale internal dynamical instabilities to take place and to grow bulges inside disks, thereby shaping the Hubble sequence that we observe today.

3.6 Conclusions

We have used measurements of the half-light radii obtained with analytic fits to the surface brightness distribution of roughly 12,000 disk galaxies in COSMOS to chart the evolution of the number density of intermediate-sized and large disks since redshift $z \sim 1$.

Our analysis has shown a general constancy of the size function for disk galaxies with half-light radii larger than about 5 kpc. This constancy, initially proposed by Lilly et al. [71] based on much smaller statistics, and here clearly demonstrated from a much larger

sample of disk galaxies of any bulge-to-disk (B/D) ratio, suggests that the massive disk galaxy population was largely in place with its current properties when the universe was only half as old as today.

Among the observed general constancy of the size function there is evidence for some subtler and possibly quite important trends: (1) The number density of disk galaxies of all B/D-ratios in the intermediate size range $r_{1/2} \in [5, 7[$ kpc remains constant to a good approximation up to $z \sim 1$. (2) The number density of the largest disks with half-light radii $r_{1/2} \in [7, 17[$ kpc at $z \sim 1$ appears however to be only 60% of today's value in the disk galaxy population as a whole. (3) When this population of large-sized disk galaxies is split by the values of their B/D-ratio we find that the deficit at high redshift stems from disk galaxies with a bulge component. It is conceivable that color differences between bulges and disks contribute to this result and we will study their effect in more detail. Bearing this in mind, however, it is nevertheless likely that we might be witnessing a secular transformation of bulgeless disks into disks with a bulge component.

THESE ARE VERY DEEP WATERS.

Sherlock Holmes, *The Adventure of the Speckled Band* [35]

THESE ARE MUCH DEEPER WATERS THAN I HAD THOUGHT.

Sherlock Holmes, *The Adventure of the Reigate Squires* [36]

4 The role of environment in the redshift evolution of disk galaxies in COSMOS: Surface brightness, sizes & star formation histories

The content of this chapter is being prepared for publication in the Astrophysical Journal (Sargent et al. [102]).

4.1 Introduction

After some initial debate (Ravindranath et al. [94], Simard et al. [117]), several studies have indicated that there is a surface brightening of disk galaxies of roughly one magnitude at $z \sim 1$ (Barden et al. [5], Lilly et al. [72], Schade et al. [105, 107]). The interpretation of such brightness evolution, and in particular, the evolution of disk sizes over the same cosmic period remain, however, rather controversial. While measurements of the number density of large disk galaxies have found no large changes out to $z \sim 1$ (Lilly et al. [71], Sargent et al. [101], hereafter S07, see Chapter 3), others studies suggest an inside-out growth of disk galaxies by about 25% over the past 8 Gyr (Barden et al. [5], Trujillo and Pohlen [128]).

Nevertheless, all studies agree that disk galaxy sizes have evolved less in the last half of the Hubble time than theoretically expected by the most popular disk evolution models. For example, under the assumption that the scale lengths of disks are proportional to the size of the virial radii of host halos, their sizes are predicted to evolve as $r_d \propto H(z)^{-2/3}$ at a fixed halo mass (Fall and Efstathiou [40], Mo et al. [81]). In contrast to this, Bouwens and Silk [12] assume a dependence of the star formation rate on the local gas density

within the disk, and the infall of metal-free gas, and predict the sizes of disks to evolve as $r(z)/r(0) = 1 - 0.27\ z$. In both cases one would expect about a 30% decrease in the size of disk galaxies to be detected at $z \sim 1$.

Several questions remain open, as the modest sizes of the previous surveys do not allow for a splitting of the disk galaxy population at $z \sim 1$ into sub-components, and have thus precluded a study of the detailed evolution of disks as a function of, e.g., the bulge-to-disk ratio (B/D) and the environmental properties. This chapter specifically tackles the question of how disk surface brightness, size and star formation histories vary as a function of B/D and environmental density. The suitably large statistical sample of disk galaxies is provided by the COSMOS survey, the largest HST survey to date of the distant universe (see 5).

This chapter is structured as follows: Section 4.2 briefly describes the COSMOS data set that we use in the current analysis, and lists the most important properties of the SDSS sample of galaxies which we use to calibrate the measurements at high redshift with the local universe (see also Sections 3.4.4 and A.1). In Section 4.3 we investigate the opacity and surface brightness evolution, and the star formation histories, of disk galaxies since $z \sim 1$. This is followed by the construction of the bivariate size-luminosity function in Section 4.4. The environmental effects of the derived evolution are described in Section 4.5. Section 4.6 summarizes the findings of this chapter.

4.2 Observational data

4.2.1 Description of the sample of galaxies

The parent galaxy sample contains all the 32,287 galaxies with $I \leq 22.5$ detected over the entire 1.64 deg^2 of the COSMOS-survey in the COSMOS ACS $I(F814W)$ images; most galaxies belong to the 'bright spectroscopic sample' of the zCOSMOS redshift survey (Lilly et al. [73]).

For all but 0.3% of the galaxies it was possible to derive photometric redshifts using ground-based measurements in the eight following filters: B, V, g', r', i', and z' (Suprime-Cam at Subaru; Taniguchi et al. [125]), u^* fluxes (CFHT) and K_s-band (4 m Kitt Peak and CTIO; Capak et al. [14]). The Zurich Extragalactic Bayesian Redshift Analyzer (ZEBRA; Feldmann et al. [41]) was employed to compute the photometric redshifts with the maximum likelihood method (see Section 3.4.1). The accuracy of the ZEBRA photometric redshifts for the current sample is $\Delta z/(1+z) \sim 0.022$ over the whole redshift range up to $z = 1$.

All galaxies were assigned a morphological class by means of the Zurich Estimator of Structural Types (ZEST; see Section 2.2). 27,672 galaxies were classified as disk galaxies

Tab. 4.1 — Number of galaxies as a function of redshift and morphological class.

redshift	all types	type 2	type 2.3	type 2.2	type 2.1	type 2.0	type 1	type 3
$z < 0.2$	3348	2921	566	1301	799	255	166	230
$0.2 \leq z < 0.4$	8150	6879	1326	2854	1918	781	625	599
$0.4 \leq z < 0.6$	7513	6079	1479	1999	1792	809	661	721
$0.6 \leq z < 0.8$	7997	6123	1946	1565	1722	890	801	1030
$0.8 \leq z < 1$	5846	4182	1406	918	1147	711	720	904
$1 \leq z < 1.2$	1669	1072	347	236	323	166	207	359
$z > 1.2$	671	416	156	115	107	38	30	186
$z < 0.2$	3016	2679	516	1219	732	212	121	190
$0.2 \leq z < 0.4$	7920	6729	1295	2801	1880	753	577	574
$0.4 \leq z < 0.6$	7193	5834	1422	1919	1725	768	620	696
$0.6 \leq z < 0.8$	7594	5821	1872	1491	1624	834	756	985
$0.8 \leq z < 1$	5450	3888	1348	841	1059	640	654	876
$1 \leq z < 1.2$	1485	953	335	215	268	135	167	339
$z > 1.2$	525	315	121	87	78	29	21	155
SDSS @ 0.7	478	351	75	92	108	76	74	48

Note. — The first set of seven entries gives the number of galaxies if *no* 2σ-cut in χ^2_{phz} (but all other selection criteria with respect to magnitude and goodness-of-fit) is applied, the second set of 7 entries lists the number of galaxies if a 2σ-cut in χ^2_{phz} *is* applied to the sample. The final line in the table states the number of artificially redshifted SDSS galaxies of each galaxy class.

by ZEST and therefore constitute the sample for our analysis. Disk galaxies are split by ZEST into four categories of bulge-to-disk (B/D) ratio. The convention used is: type 2.3 - pure disk galaxy, type 2.2 - disk galaxy with a small bulge, type 2.1 - disk galaxy with moderate bulge, and type 2.0 - bulge-dominated disk galaxy.

An overview of how the galaxies of the different morphological types are distributed with redshift is provided in Tables 4.1 and 4.2. Table 4.1 contains the statistics for all morphological classes and B/D-categories of the 27,672 disk galaxies with $I \leq 22.5$ in the COSMOS field. This global overview is complemented by Table 4.2 where we list how many objects our sample contains of the different B/D-categories with physical sizes larger than 5 kpc and 7 kpc. In the current study we will use these size thresholds to split the disk galaxies into "intermediate" and "large" disks, following the nomenclature of S07.

We emphasize that we limit our study only to galaxies with FWHM $> 0.15''$ (or 3 pixels), since this is the smallest possible size that allows a morphological classification with ZEST. In Section 4.4.1 (see also Section 3.4.2) we use the $V_{\rm max}$-formalism to compute the comoving number density of our sources as a function of redshift, and highlight again, as done in Section 3.4.2, how this formalism allows us to account for potential selection effects arising from this restriction. A further inspection of the parent sample to exclude stars was done using the stellarity parameter calculated by SExtractor: sources were

Tab. 4.2 — Number of disk galaxies of different B/D-categories and sizes larger than 5 (*left half*) and 7 kpc (*right half*) as a function of redshift. The table's row structure matches that of Table 4.1.

redshift	type 2.3	type 2.2	type 2.1	type 2.0	type 2.3	type 2.2	type 2.1	type 2.0
	$r_{1/2} \geq 5$ kpc				$r_{1/2} \geq 7$ kpc			
$z < 0.2$	10	38	31	21	1	9	9	9
$0.2 \leq z < 0.4$	167	331	206	145	39	81	74	70
$0.4 \leq z < 0.6$	393	379	224	124	96	86	87	53
$0.6 \leq z < 0.8$	723	415	260	137	187	107	85	45
$0.8 \leq z < 1$	660	307	181	90	188	86	46	27
$1 \leq z < 1.2$	152	94	74	18	34	25	16	4
$z > 1.2$	89	45	18	8	29	12	3	4
$z < 0.2$	8	34	25	13	1	7	6	2
$0.2 \leq z < 0.4$	163	322	200	134	36	77	69	61
$0.4 \leq z < 0.6$	377	358	213	115	90	78	81	44
$0.6 \leq z < 0.8$	691	390	238	128	175	97	75	40
$0.8 \leq z < 1$	632	269	166	73	176	72	43	23
$1 \leq z < 1.2$	148	88	57	15	32	21	9	2
$z > 1.2$	71	34	16	7	21	8	2	4
SDSS @ 0.7	52	42	36	14	18	13	15	3

considered to be point-like and excluded from our sample if the stellarity parameter was larger than 0.8; sources with stellarity in the range between 0.6 and 0.8 were visually inspected to eliminate any remaining stars.

Further cuts to the final sample of disk galaxies adopted in our studies are imposed by details in the surface brightness fits, as discussed below.

4.2.2 Surface brightness fits with GIM2D

The GIM2D structural parameters discussed in Chapter 2 and also used in Chapter 3 were employed for this analysis. We remind that the two-dimensional surface brightness fits provide the total flux F_{tot} (integrated to $r = \infty$); the semi-major axis half-light radius $R_{1/2}$; the ellipticity $e = 1 - b/a$, where a and b are the semi-major and semi-minor axes of the fitted Sérsic profile; and the value of the Sérsic index n. The strategy we adopted to prepare and carry out the measurements with GIM2D is laid out in Section 2.1.2. The steps used are:

- extraction of stamps centred on each source; stamp sizes were chosen such as to ensure that there were sufficient pixels to estimate the local background,
- generation of cleaned stamps by substituting pixel values reproducing the properties of the local background whenever a pixel on a stamp was associated with a nearby

object,

- creation of an elliptical mask with a semi-major axis of 1.5 Petrosian radii (the Petrosian radius was calculated using elliptical annuli with a fixed position angle and ellipticity based on image moments) which defines the area on which the χ^2 of the fit is calculated,
- symmetrization of the cleaned images, and
- selection of the point spread function based on the location of the object on the ACS tile and the time of the exposure.

As done in S07 we excluded from our study a small fraction of disk galaxies which failed to satisfy a number of conditions, namely:

- Galaxies for which GIM2D did not converge or returned a value of χ^2 larger than 15 (428 objects or 1.5% of the sample). Up to four attempts, using different random number seeds, were made to fit each galaxy with GIM2D. A visual inspection of GIM2D fits and their residuals for objects with $\chi^2_{\rm GIM2D} > 1.5$ showed that GIM2D usually produces a fair model of the diffuse galaxy light, and that their high values of $\chi^2_{\rm GIM2D}$ are often the result of sub-structure such as knots of star formation, spiral arms or bars (see Figure 3.1 in Chapter 3). For this reason we impose the generous criterion of cutting at $\chi^2_{\rm GIM2D} = 15$ rather than at a smaller value.
- Galaxies with a $\chi^2_{\rm phz}$ for the ZEBRA photometric redshift above a threshold corresponding to two standard deviations in an ideal χ^2-distribution (with the number of degrees of freedom equal to the difference between the number of filters used for deriving the redshift and the number of free ZEBRA parameters, namely three, i.e., the redshift, the template type and the template normalization). This criterion lead to the elimination of 1097 objects (4%). Another 92 disk galaxies (<0.5%) were discarded as no estimate of their photometric redshift could be obtained.
- Galaxies separated by less than $0.6''$ from their closest neighbour, leading to a ground-based photometric measurement which mixes fluxes from the two sources (a total of 363 disk galaxies, i.e., 1.3%).

4.2.3 Completeness

As done in Chapter 3 (see Figures 3.6 and 3.7) it is necessary to explore the completeness properties of our sample.
The upper half of Figure 4.1 shows the spread in the values of rest-frame B-band magnitude (calculated from the ACS F814W Kron magnitude, i.e., the SExtractor `MAG_AUTO` value) as a function of redshift for our entire disk galaxy sample. Superimposed in blue is the track of an Scd galaxy from Coleman et al. [25] (CWW) and in red the track of a CWW

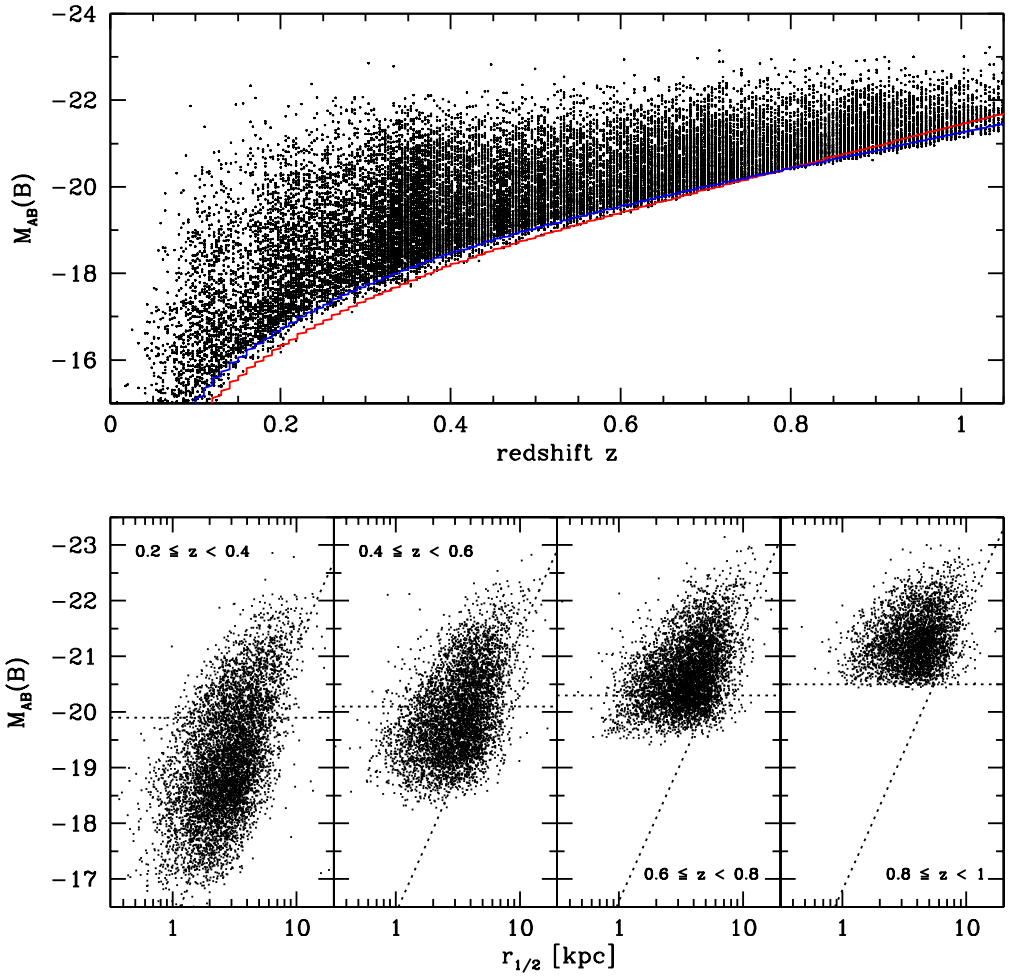

Fig. 4.1 — *Upper panel*: Values of rest-frame B-band magnitude $M(B)$ found in the disk galaxy population between $z \sim 0$ and 1. The red line shows the locus of an S0 galaxy as it is moved out in redshift, the blue line the locus of an Scd galaxy, both with an apparent magnitude at the faint sample limit of $I = 22.5$.
Lower panel: Distribution of rest-frame B-band magnitude $M(B)$ vs. physical size $r_{1/2}$ for all disk galaxies as a function of redshift. Horizontal dotted lines show the limiting magnitude below which the sample is complete at all redshifts. This limit shifts to fainter magnitudes with decreasing redshift according to an assumed brightening of one magnitude per unit in redshift. The inclined dotted lines of constant surface brightness have been evolved in the same way. The projection of the intersection of the two dotted lines onto the horizontal axis defines the threshold in physical size above which the studied sample has a high degree of completeness out to $z \sim 1$ (see text of Section 4.2.3 for details).

S0 galaxy, both types having an apparent magnitude right at the faint survey limit of $I = 22.5$. A comparison of the distribution of the galaxies in the $(z, M(B))$-plane and the loci of the two galaxies as they are moved out in redshift shows that the blue galaxies define

the completeness limit in magnitude at redshifts lower than 0.7, while the opposite applies beyond this redshift.

Following the approach taken in S07, our analysis is primarily concerned with galaxies larger than about 6 kpc in physical half-light size $r_{1/2}$. Above this size one can be confident that our sample has a satisfactory degree of completeness. The lower half of Figure 4.1 illustrates this point. Along the vertical axis the rest-frame B-band magnitude $M(B)$ is plotted as a function of physical size $r_{1/2}$ in kpc at different redshifts. In the bin of $z \in [0.8, 1[$ at the far right, the dotted horizontal line marks the lower envelope of the cloud of points (i.e., the faintest magnitude values measured in this redshift slice). This limit shifts to fainter magnitudes with decreasing redshift according to an assumed brightening of one magnitude per unit redshift. The diagonal line is a line of constant effective surface brightness (averaged within the half-light radius). The intersection of the two dotted lines defines the size (roughly 6 kpc; this threshold is independent of the Sérsic index of the surface brightness profile of a galaxy) above which the sample is more or less complete if there are *few low surface brightness galaxies with sizes in excess of this value.*
Completeness above a certain size implies that there should be no sources in the lower-right part of the diagram defined by the vertical size threshold and the horizontal (dotted) magnitude limit. A threshold of 6 or 7 kpc implies a completeness of 78% and 82%, respectively. Given the fuzzy boundary for the completeness of our sample, the approach we take in this work is to duplicate each step of the analysis assuming a bold completeness threshold of 5 kpc and a conservative one of 7 kpc. The advantage of including also objects in the range $r_{1/2} \in [5,\ 7[$ kpc is that this enlarges the sample significantly (by about a factor of 5) as there are only few of the biggest objects (see Table 4.2) even in the large volume of space the COSMOS field samples at high redshift.

In Figure 4.2 we show the information corresponding to the panels in the lower half of Figure 4.1 for the comparison sample of SDSS galaxies in the range $z \in [0.015,\ 0.025]$. The sample is described in Section 3.4.4 and Appendix A.1.

4.3 Evolution of disk galaxies since $z \sim 1$: Opacity, surface brightness & star formation histories

4.3.1 Opacity

When studying the surface brightness evolution of the disk galaxy population and its subclasses it is important to examine whether disks are optically thin or thick, and whether there is evolution in dust opacity with redshifts.

The distribution of axis ratios b/a is a first indication of the amount of extinction occurring in disks. In Figure 4.3 we show the relative frequency of axis ratios for different B/D-categories of the disk galaxy population. In the first row we plot the histograms

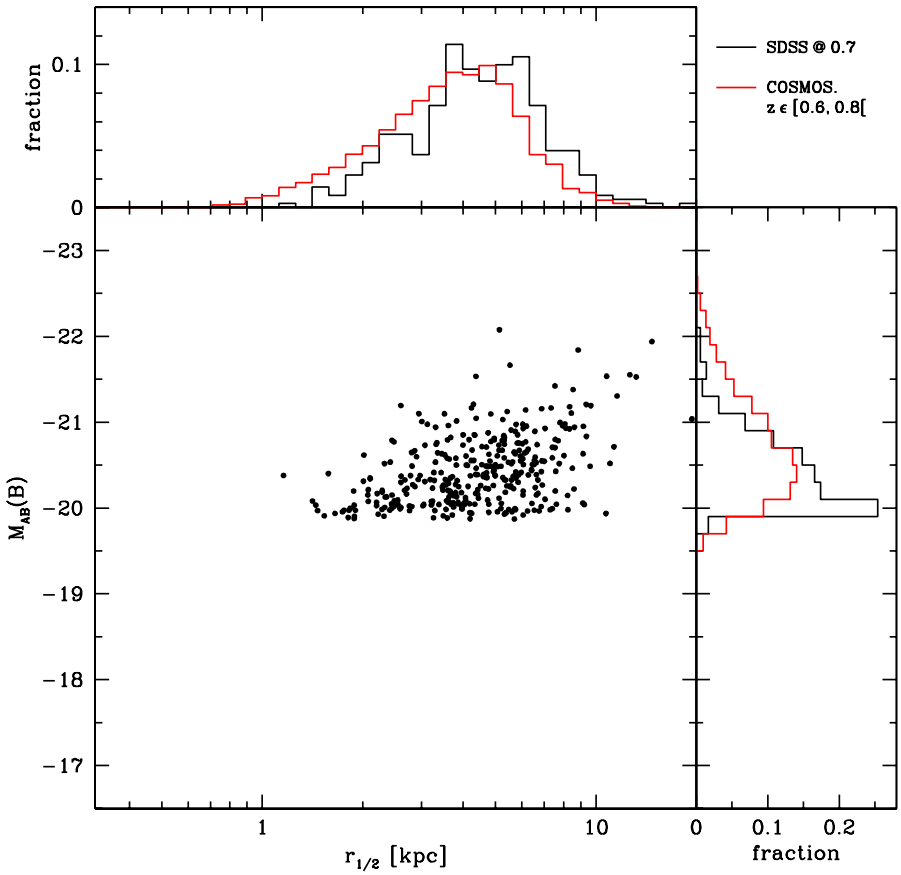

Fig. 4.2 — Plot of $M(B)$ vs. $r_{1/2}$ (*main panel*) for the artificially redshifted local SDSS galaxies. The histograms on the upper and right hand edges show the relative frequency of objects with respect to rest-frame B-band magnitude and size for the SDSS$_{z=0.7}$ comparison sample (black lines) and the COSMOS sources in the redshift interval $z \in [0.6, 0.8[$ (red lines). The size distributions are offset but similar in shape, while the distribution of the sources in magnitude are different in shape but hardly offset.

for SDSS galaxies in our local comparison sample, in rows 2 to 5 the distributions for COSMOS disk galaxies. Grey histograms show the distribution for the total population of a given B/D-category while red histograms specify the distribution for objects with a half-light radius larger than 7 kpc; the black line refers to the sample with half-light radius above 5 kpc. The plot is presented as a function of axis ratios from the single Sérsic fits with GIM2D; however, the histograms look alike if the SExtractor estimate of b/a is used instead.

The large contribution of the bulge component to the total flux of the bulge-dominated sources results in peaked distributions which reflect the roundness of the spheroidal component. The shape of the histograms for the largest disk-dominated galaxies indicates the presence of dust opacity. In particular, the evolution of the distribution of galaxies with

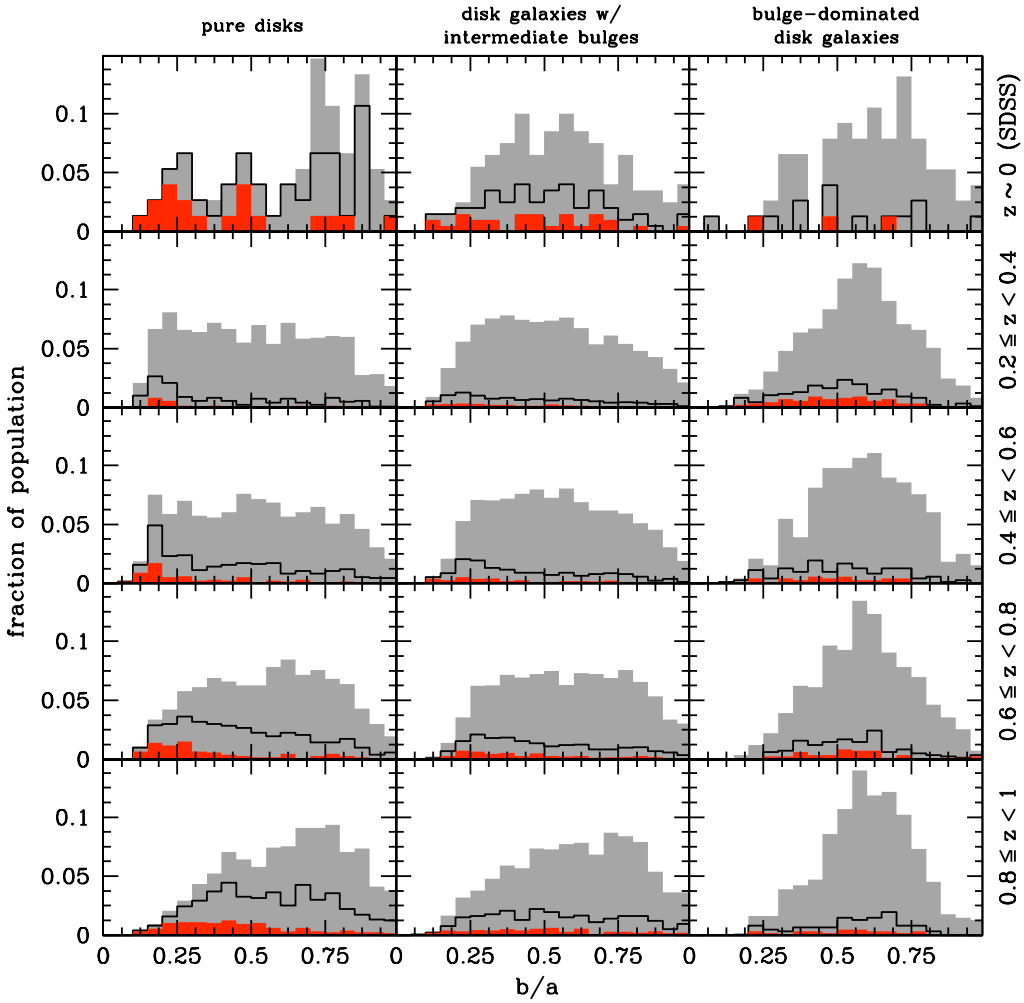

Fig. 4.3 — Distributions of axis ratios b/a of the GIM2D Sérsic fits for three different B/D-categories (see labels on upper edge of the figure) of disk galaxies as a function of redshift. The measured abundance of axis ratios is normalized to the total number of galaxies of each category within a specific redshift slice. The distributions of axis ratios in the total population are shown in grey, those of disks with $r_{1/2} \geq 5$ kpc with a black outline and those with $r_{1/2} \geq 7$ kpc in red. In the first row we plot the histograms for SDSS galaxies in our local comparison sample, in rows 2 to 5 the distributions for COSMOS disk galaxies are given.

respect to axis ratio in our sample suggests that disk opacity increases with redshift.

Figure 4.4 shows the effective rest-frame B-band surface brightness within the observed half-light radius, $\mu(B)$, as a function of axis ratio and redshift for all pure disk galaxies with size larger than 5 kpc (upper half of figure) and 7 kpc (lower half of figure). The local SDSS galaxies are plotted on the left, and the COSMOS galaxies at successively higher redshift afterwards. Despite PSF effects, the finite thickness of disks and their

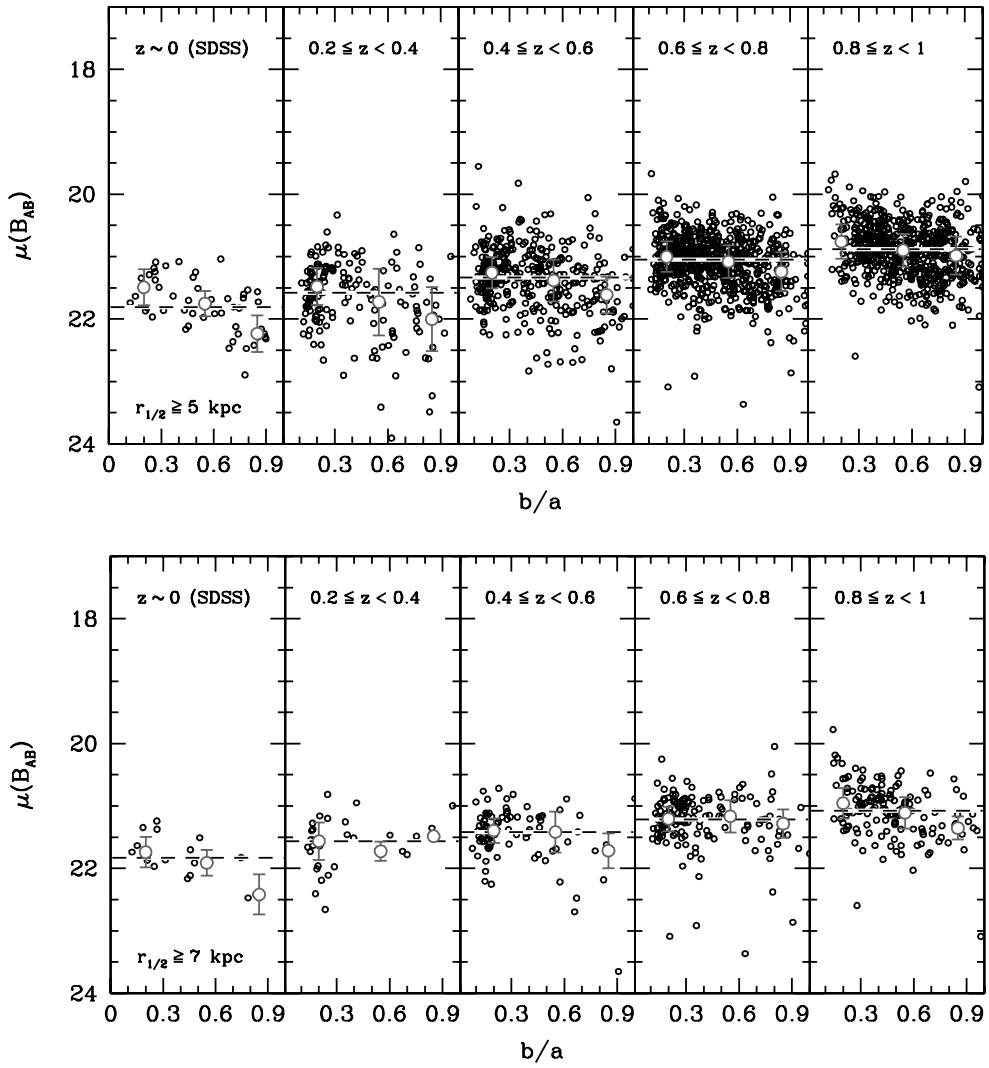

Fig. 4.4 — Dependence of rest-frame B-band effective surface brightness $\mu(B)$ on the axis-ratio b/a of pure disk galaxies in the range $z < 1$. The horizontal dashed lines show the median of the effective surface brightness of pure disk galaxies in a specific redshift bin. In the upper panel only sources with physical size $r_{1/2} \geq 5$ kpc have been used, in the lower panel only objects larger than $r_{1/2} = 7$ kpc. The empty grey circles with error bars (which mark the 1st and the 3rd quartile) at $b/a = 0.2$, 0.55 and 0.85 mark the median values of $\mu(B)$ in three bins of axis ratio, namely $b/a \in [0, 0.4[$, $b/a \in [0.4, 0.7[$ and $b/a \in [0.7, 1]$. Median values of surface brightness at low inclination (i.e., high b/a) tend to lie below the global median, while those at high inclination are often slightly raised with respect to the median over all axis ratios. This tendency diminishes as a function of redshift.

small, yet non-negligible intrinsic ellipticity (e.g., Ryden [100]), the value of b/a can be taken as a reasonable approximation to the galaxies' orientation. Optically thin galaxies would preferentially have a higher surface brightness when viewed edge-on rather than

Tab. 4.3 — Best fit values of the opacity parameter C introduced to account for the effects of optically thick dust on the rest frame B-band average surface brightness and its variation with axis ratio b/a)

category	redshift	C	dC	$\langle\mu_{face-on}\rangle$ [a]	$d\langle\mu_{face-on}\rangle$
pure disks	0 (SDSS)	0.456	0.149	22.187	0.146
(type2.3)	0.3	0.415	0.181	22.104	0.177
	0.5	0.231	0.088	21.579	0.087
	0.7	0.186	0.074	21.261	0.073
	0.9	0.180	0.023	21.021	0.023

[a] $\langle\mu_{face-on}\rangle$ denotes the value of the best fit trends lines at $b/a = 1$.

face-on because of the larger flux density of photons coming from the stellar light which is predominantly confined to a thin plane rather than being distributed over a circular area as for galaxies seen face-on. As can be seen in Figure 4.4 galaxies with small axis ratios do have a higher surface brightness than sources with b/a approaching 1. This tendency is less pronounced in the higher redshift bins than at low redshift in agreement with the conclusions drawn above from the distribution of axis ratios. To measure the amount of extinction we have fit an inclination correction of the form

$$\mu_{face-on} = \mu_{obs} - C \cdot 2.5\ log(b/a) \tag{4.1}$$

to the distribution of $\mu(B)$ vs. b/a for galaxies with half-light radius larger than 5 kpc. Specifically, we fit relation (4.1) to the median values of $\mu(B)$ in three bins of axis ratio centered on $b/a = 0.2$, 0.55 and 0.85. (In equation (4.1) μ_{obs} is the surface brightness calculated according to equation (4.2). The constant C is unity for perfectly transparent disks and zero for opaque disks; for non-zero C the inclination will thus reduce the measured surface brightness of disks inclined with respect to the observer's line of sight to the value of $\mu(B)$ when the galaxy is seen face-on.) The medians are marked by empty grey circles in Figure 4.4 and are reported again in Figure 4.5 where we show the measured trend lines for pure disks with $r_{1/2} \geq 5$ kpc derived with a least-squares fit. The asymmetric error bars on the medians extend to the 1st and 3rd quartile of the surface brightness distribution in each bin of b/a. In Table 4.3 the values of the opacity constant C describing the slopes of the lines in the figure are listed. In the subsequent assessment of the surface brightness evolution in the disk galaxy population since $z \sim 1$ we use the best-fitting values of C to correct the measured surface brightness to the face-on value.

At all redshifts disks are non-negligibly optically thick since the estimates of C range from 0.46±0.15 to 0.18±0.02 as a function of increasing redshift. The fact that the SDSS sample has a steeper slope than that measured in the COSMOS data set at redshifts $z \in [0.6, 0.8[$ which it was constructed to match in terms of rest-frame wavelengths, suggests

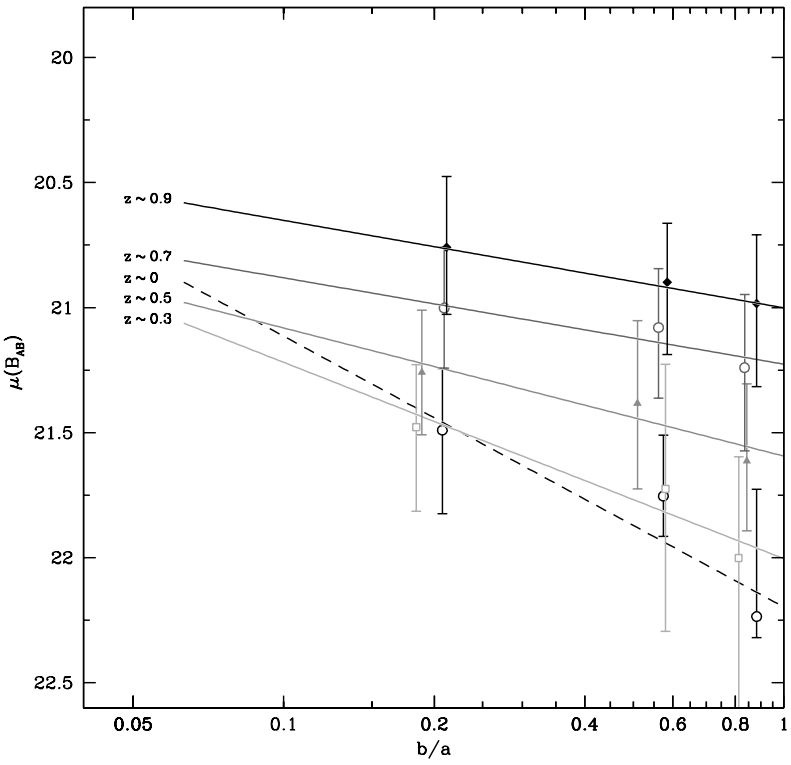

Fig. 4.5 — Best-fit trend lines to the relation between rest-frame B-band effective surface brightness $\mu(B)$ and axis-ratio b/a among pure disk galaxies with $r_{1/2} \geq 5$ kpc. The lines show the result of fitting equation (4.1) to the measurements given in the upper half of Figure 4.4. The values of the constant C which measures the opacity are given in Table 4.3. They indicate that disks become increasing optically thick at higher redshift. Data points and error bars correspond to those given in the individual panels of Figure 4.4.

that disk opacity indeed increases with redshift and that we do not purely detect the effect of sampling bluer (and thus more attenuated) wavelengths.

Note, however, that at 5 kpc our sample may still suffer from incompleteness (see Section 4.2.3). Values of the opacity constant C are reduced by 30-50% when a sample restricted to $r_{1/2} \geq 7$ kpc is considered. We therefore investigate the evolutionary trends for the two bracketing cases of perfectly optically thick disks (i.e. $C = 0$) and disks described by the values of $C(z)$ given in Table 4.3. The comparison of the two approaches provides an estimate of the uncertainty in the analysis which is introduced by adopting an opacity correction that may be influenced by incompleteness of the sample.

4.3.2 Surface brightness

We estimate the surface brightness evolution by calculating the values of surface brightness on an individual basis for each galaxy and then determining the median value of the surface brightness distribution of objects with $r_{1/2}$ greater than our completeness threshold. Median statistics, applied to a set of surface brightness values, will minimize the influence of outliers in the population that could otherwise affect the fitting of a line described by equation (4.2) to the magnitude-size relation.

While other studies adopt the value of the central surface brightness μ_0 to investigate evolutionary trends in the brightness of disks, the fact that we have fitted our galaxies with a single Sérsic law which includes the bulge component prevents us from using this quantity. We therefore adopt the effective surface brightness $\langle\mu\rangle_{R_{1/2}}$ as a tracer of brightness evolution. The angle brackets with the subscript '$R_{1/2}$' emphasize that the effective surface brightness represents an average quantity obtained by distributing half (hence the factor $\log(2)$ in equation (4.2)) of the total GIM2D flux over an ellipse with a semi-major axis given by the observed half-light radius $R_{1/2}$ and a semi-minor axis calculated with the GIM2D value for the axis ratio q. If $R_{1/2}$ is expressed in units of arcseconds the expression used to calculate an effective rest-frame B-band surface brightness reads

$$\mu(B) = I + 2.5\,\log(2) + 2.5\,\log\left(\pi R_{1/2}^2\right) + 2.5\,\log(q) - 10\,\log(1+z) - K_{F814W,B}(z)\ . \quad (4.2)$$

The surface brightness computed according to this expression is not yet corrected for inclination. In keeping with Section 4.3.1 we apply an inclination correction $-C(z)\cdot 2.5\,\log(b/a)$ (derived for the sample with $r_{1/2} \geq 5$ kpc) to the observed surface brightness which varies with redshift and deduce the evolutionary trend based on the median surface brightness values in each redshift bin. We also calculated the evolutionary trend resulting from values of $\mu(B)$ which were not corrected for inclination (corresponding to the case of perfectly optically thick disks) in order to estimate the uncertainties in the analysis introduced by the opacity of the disks. To what extent disk opacity will affect the measured flux of inclined disk galaxies depends not only on redshift but also on B/D-ratio. Accounting for the different fractional contributions of the disk component to the total flux of a disk galaxy in order to apply a correction for opacity which depends on the B/D-ration necessitates assumptions on the shape and the opacity of the bulge component which both are not well constrained. In view of these uncertainties we simply apply the opacity correction derived in Section 4.3.1 to all B/D-categories. In equation 4.2 we have dropped (and will continue to do so from now on) the angle brackets in the expression for the effective surface brightness in the interest of easier legibility. I is the observed magnitude computed with the GIM2D total flux. In the conversion from an observed to a rest-frame B-band surface brightness we use the K-correction $K_{F814W,B}$ which is derived from the best-fit ZEBRA template assigned to each galaxy. The K-correction is defined through the equation $I = M(B) + 5\,\log(D_L(z)/10\ pc) + K_{I,B}$.

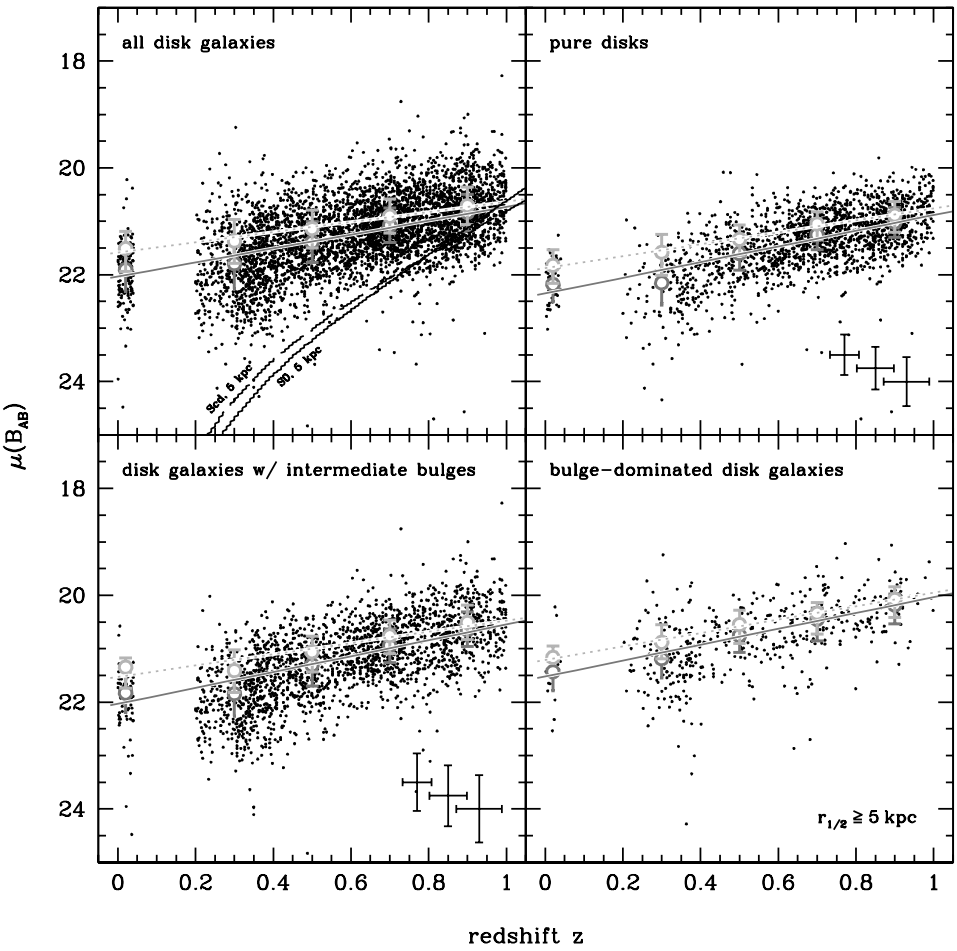

Fig. 4.6a — Evolution of the rest-frame B-band effective surface brightness $\mu(B)$ since $z \sim 1$ for the whole population of disk galaxies with $r_{1/2} \geq 5$ kpc (*upper left*), for pure disk galaxies (*upper right*), for disk galaxies with an intermediate bulge component (*lower left*) and disk galaxies with a large bulge (*lower right*). The median values $\overline{\mu(B)}$ of the inclination-corrected surface brightness are reported in dark grey and the corresponding linear evolutionary trend shown with a solid line (cf. Tables 4.4, 4.5 and 4.8). The evolution inferred when no inclination correction is applied is marked with a dotted light grey line fitted through the light grey data points (cf. Tables 4.6, 4.7 and 4.8).

In Figures 4.6a and 4.6b the values of inclination-corrected effective surface brightness $\mu(B)$ are plotted as a function of photometric redshift for COSMOS disk galaxies with physical size $r_{1/2}$ larger than 5 and 7 kpc, respectively. Starting at a lower limit of $z = 0.2$, we split the redshift interval out to $z = 1$ into four slices of width $\Delta z = 0.2$ and calculated the median $\overline{\mu(B)}$ of the surface brightness measurements in each redshift bin. In both parts of Figure 4.6 this median is drawn as an open grey point (dark grey for inclination-corrected $\mu(B)$; light grey for uncorrected $\mu(B)$) at the centre of the bin. The spread in the population – indicated by the 2nd and the 3rd interquartile range (on the

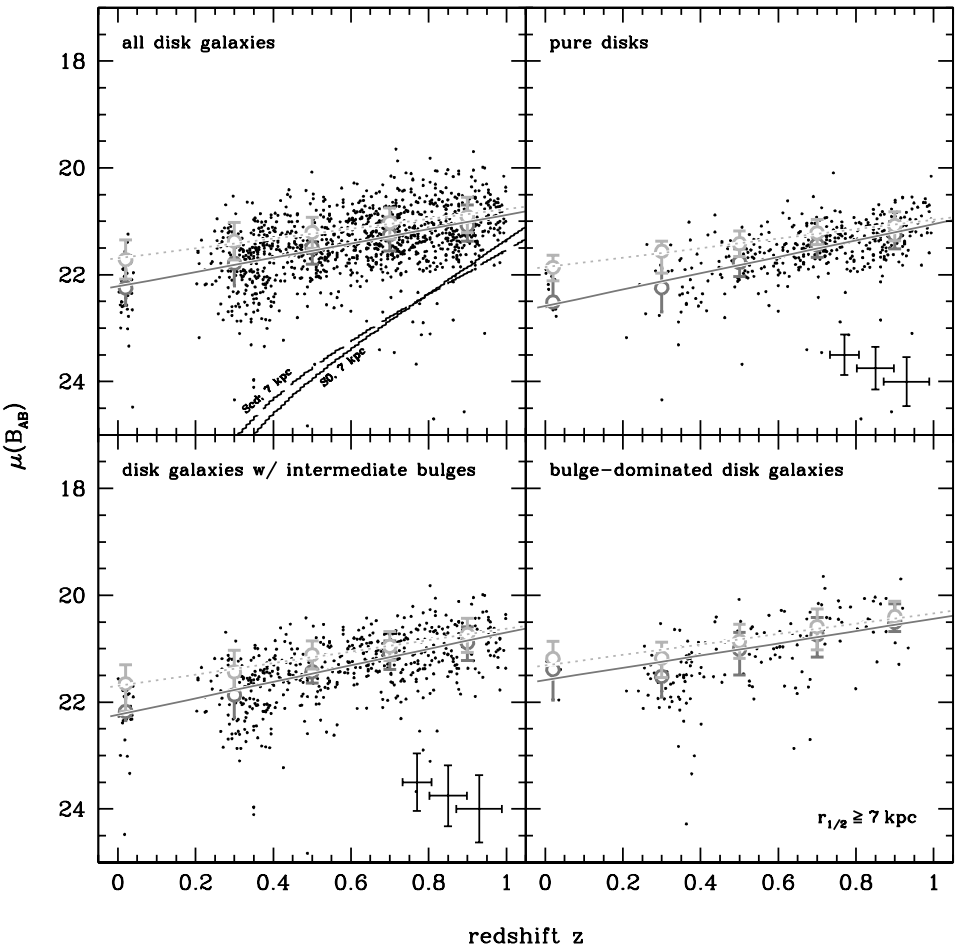

Fig. 4.6b — As in previous figure but using only galaxies with $r_{1/2} \geq 7$ kpc. Median values of inclination-corrected $\mu(B)$ (dark grey points and solid trend line) and their associated errors shown in this figure are listed in Table 4.4 for the COSMOS sources and in Table 4.5 for the SDSS comparison sample. Tables 4.6 and 4.7 give the according information for the case when no inclination correction is applied (light grey points and dotted trend line).

bright and faint side of the median, respectively) – is indicated by the error bars on the median. To estimate the formal error on the determination of median values we also calculated the standard error of the median. These numbers, which in most cases are significantly smaller than the semi-quartile range, are listed in Table 4.4 (Table 4.6 for the case without inclination correction). They, as well as the standard error of the median of any other quantity x which we investigate in this work, were computed according to

$$\Delta x = \frac{x_{0.84} - x_{0.16}}{\sqrt{N}} \ , \tag{4.3}$$

Tab. 4.4 — Average inclination-corrected surface brightness properties of different COSMOS disk samples (only including objects with $r_{1/2} \geq 5$ kpc and $r_{1/2} \geq 7$ kpc, in column 3 and 4, respectively) in four bins of redshift. The information in this table is graphically represented in Figs. 4.6a and 4.6b.

T [a]	redshift	$\overline{\mu(B)}$ [b] $r_{1/2} \geq$5 kpc	$\overline{\mu(B)}$ $r_{1/2} \geq$7 kpc
type 2	0.3	$21.793^{+0.475}_{-0.472}$ ($\pm$0.047)	$21.785^{+0.428}_{-0.349}$ ($\pm$0.083)
	0.5	$21.391^{+0.377}_{-0.386}$ ($\pm$0.035)	$21.489^{+0.314}_{-0.304}$ ($\pm$0.063)
	0.7	$21.076^{+0.319}_{-0.330}$ ($\pm$0.027)	$21.252^{+0.307}_{-0.329}$ ($\pm$0.047)
	0.9	$20.835^{+0.356}_{-0.339}$ ($\pm$0.031)	$21.078^{+0.292}_{-0.383}$ ($\pm$0.057)
type 2.3	0.3	$22.151^{+0.417}_{-0.367}$ ($\pm$0.087)	$22.245^{+0.453}_{-0.371}$ ($\pm$0.188)
	0.5	$21.600^{+0.315}_{-0.287}$ ($\pm$0.046)	$21.768^{+0.264}_{-0.253}$ ($\pm$0.080)
	0.7	$21.251^{+0.281}_{-0.252}$ ($\pm$0.031)	$21.438^{+0.240}_{-0.225}$ ($\pm$0.055)
	0.9	$21.018^{+0.285}_{-0.278}$ ($\pm$0.034)	$21.252^{+0.260}_{-0.244}$ ($\pm$0.064)
type 2.2/	0.3	$21.844^{+0.426}_{-0.432}$ ($\pm$0.056)	$21.866^{+0.424}_{-0.403}$ ($\pm$0.100)
type 2.1	0.5	$21.304^{+0.393}_{-0.327}$ ($\pm$0.046)	$21.429^{+0.213}_{-0.308}$ ($\pm$0.079)
	0.7	$20.939^{+0.325}_{-0.311}$ ($\pm$0.039)	$21.096^{+0.293}_{-0.241}$ ($\pm$0.064)
	0.9	$20.646^{+0.310}_{-0.333}$ ($\pm$0.050)	$20.890^{+0.333}_{-0.300}$ ($\pm$0.085)
type 2.0	0.3	$21.190^{+0.355}_{-0.321}$ ($\pm$0.095)	$21.518^{+0.388}_{-0.333}$ ($\pm$0.112)
	0.5	$20.752^{+0.319}_{-0.264}$ ($\pm$0.094)	$21.009^{+0.480}_{-0.313}$ ($\pm$0.174)
	0.7	$20.451^{+0.402}_{-0.210}$ ($\pm$0.086)	$20.742^{+0.419}_{-0.327}$ ($\pm$0.227)
	0.9	$20.183^{+0.349}_{-0.205}$ ($\pm$0.097)	$20.505^{+0.174}_{-0.344}$ ($\pm$0.181)

[a] ZEST morphological class.

[b] Median of surface brightness measurements in the redshift range in question. Errors in brackets specify the standard error of the median (calculated according to equation (4.3). Errors in superscript and subscript immediately after the value of the median provide a measure of the spread of surface brightness values in the population; they denote the first and third quartile, respectively.

where N is the number of galaxies in the sample used to calculate the median and $x_{0.84}$ and $x_{0.16}$ denote the 84th and 16th percentile of the distribution. These values would correspond to 1σ errors if the underlying distribution were Gaussian.

In addition to the uncertainty of the median and the spread in the population, representative examples of errors on the individual data points are also shown with crosses in selected panels of Figure 4.6a and 4.6b. In the appendix (Section 4.7) of this chapter we summarize and give estimates of the factors contributing to systematic errors in the profile fitting process which ultimately lead to the presented error bars. Those shown in the plot are generously estimated errors on an *individual measurement* and should not be interpreted as the uncertainty on the determination of the average properties of the disk galaxy population or sub-categories thereof. The uncertainty on the photometric redshift of an object at $z \sim 0.25$, 0.6 and 0.95 (from leftmost to rightmost point) is indicated by the horizontal errorbars; vertical errorbars give a (conservative) estimate of the systematic error on $\mu(B)$ of an object with apparent magnitude $I < 20.5$, $I \in [20.5, 21.5[$ and

Tab. 4.5 — Average inclination-corrected surface brightness properties of different simulated disk samples at $z \sim 0.7$ in the artificially redshifted SDSS data set. The values listed to the left and right of the vertical black line are the values obtained for galaxies with $r_{1/2} \geq 5$ kpc and $r_{1/2} \geq 7$ kpc, respectively. The information in this table is graphically represented in Figs. 4.6a and 4.6b.

T	$\overline{\mu(B)}$ $r_{1/2} \geq$5 kpc	$\overline{\mu(B)}$ $r_{1/2} \geq$7 kpc
type 2	$21.509^{+0.425}_{-0.322}$ ($\pm$0.089)	$21.718^{+0.361}_{-0.373}$ ($\pm$0.166)
type 2.3	$21.824^{+0.341}_{-0.290}$ ($\pm$0.133)	$21.862^{+0.254}_{-0.227}$ ($\pm$0.246)
type 2.2/type 2.1	$21.348^{+0.390}_{-0.176}$ ($\pm$0.114)	$21.655^{+0.518}_{-0.355}$ ($\pm$0.239)
type 2.0	$21.165^{+0.072}_{-0.216}$ ($\pm$0.149)	$21.181^{+0.056}_{-0.317}$ ($\pm$0.215)

$I \in$ [21.5, 22.5] (again from left to right). The errors in the determination of the surface brightness increase with the steepness of the surface brightness profile, thus they are given separately for pure disk galaxies (group of crosses in panel on the upper right) and for disk galaxies with a moderate or prominent bulge (group of crosses in panel 'disk galaxies w/ intermediate bulges') in the lower row.

The warped dashed and solid lines running diagonally across the lower part of the upper left panel in Figures 4.6a and 4.6b illustrate the considerations on completeness made in Section 4.2.3. The dashed track labeled "Scd, 5 (7) kpc" shows the path of a CWW Scd galaxy (Coleman et al. [25]) with apparent magnitude $I = 22.5$ and physical size of 5 (7) kpc. The solid line labeled "S0, 5 (7) kpc" shows the loci of an CWW S0 galaxy with the same magnitude as it is moved out to higher redshift. The distribution of surface brightness values in the disk galaxy population with $r_{1/2} \geq 7$ kpc is well fit by a Gaussian in all four redshift bins. This confirms that the expected log-normal distribution of sizes is sampled without biases when adopting a threshold of 7 kpc to limit our dataset. Even the data set extended to 5 kpc samples the expected log normal distribution well, indicating that incompleteness is small for the larger sample with $r_{1/2} \geq 5$ kpc as well. Still, in the light of a small incompleteness above 5 kpc discussed in Section 4.2.3, we consider our estimates of the surface brightness evolution for disks sizes down to 5 kpc as an upper limit to the actual brightness evolution of the intermediate-size disk galaxy population.

In Figure 4.7 we compare the surface brightness evolution derived in our study with the analysis of Lilly et al. [71] and Barden et al. [5]. The canonical Freeman value is shown in the figure with a grey band, the width of which reflects the range in disk opacities we consider (see also the final three paragraphs of Section 4.3.2). Barden et al. [5] used roughly 5700 GEMS disk galaxies to study the size-luminosity and the stellar mass-size relation since $z \sim 1$. Their analysis selected disks by the value of the Sérsic index ($n \leq 2.5$). In the interest of a consistent comparison with their results we have taken a subsample of COSMOS disk galaxies that does not contain the bulge-dominated sources since they are the only category which have a median Sérsic index larger than the GEMS selection cut at

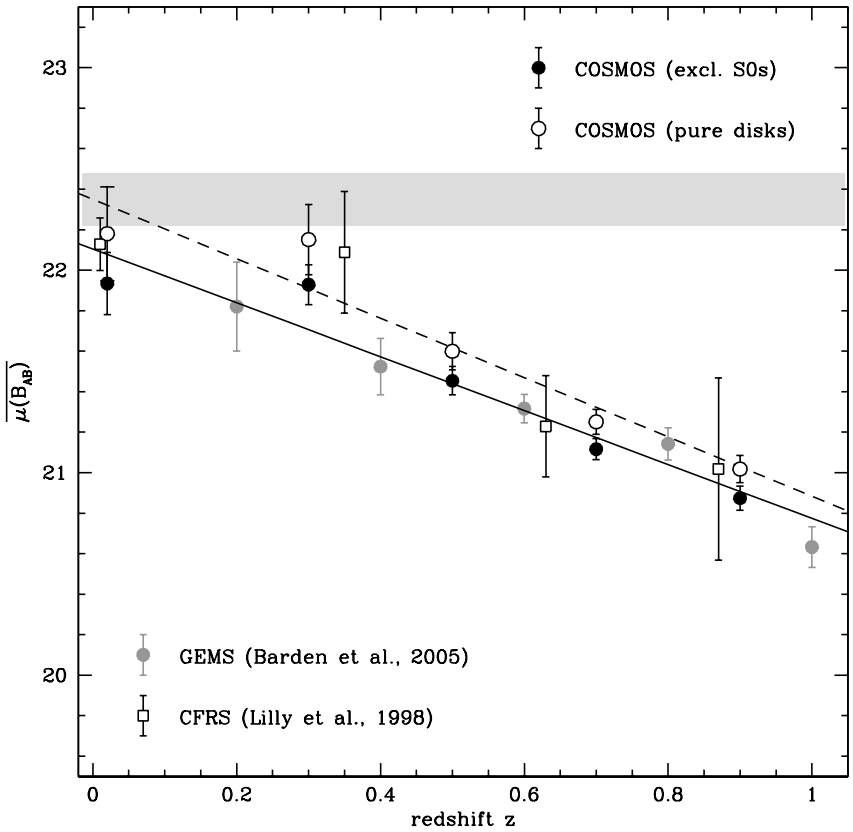

Fig. 4.7 — Comparison of the evolution in rest-frame B-band effective surface brightness of disk galaxies in the CFRS (open squares), the GEMS (grey points) and the COSMOS survey. In the latter case the evolution is shown both for pure disks (open black circles and dashed trend line) and a sample of disk galaxies from which bulge-dominated objects were excluded (black dots and solid line). The distinction was made to ease the comparison with disk galaxies studied in the GEMS survey (all objects with Sérsic index $n \leq 2.5$) and in the CFRS (for which the authors studied the evolution of the disk *component* in disk galaxies with and without bulge). All errors shown are 2σ statistical errors. The light grey horizontal band indicates the range of characteristic surface brightness values found in local disks (Freeman [46]) after correction to match the present analysis (see final paragraphs of Section 4.3.2).

$n = 2.5$. Furthermore, the GEMS measurements (plotted in grey) have been: (i) converted from rest-frame B-band central surface brightness to effective surface brightnesses using equation (4.4); (ii) corrected for different magnitude systems and filter transmissions using the iraf task `calcphot`; and (iii) rescaled to a zero colour gradient (as assumed for our COSMOS galaxies). The resulting correction in size was smaller than 5%. Our COSMOS median surface brightness values (shown only for the case with the inclination correction derived from disks with half light radii exceeding 5 kpc) are shown fin Figure 4.7 with filled black dots (and solid line) for the sample including all but the bulge-dominated disk galaxies, and with open black circles for a sample consisting only of bulgeless disks.

Tab. 4.6 — Average surface brightness (not corrected for inclination) properties of different COSMOS disk samples. The information in this table is graphically represented in Figs. 4.6a and 4.6b and organized as the content of Table 4.4.

T	redshift	$\overline{\mu(B)}$ $r_{1/2} \geq 5$ kpc	$\overline{\mu(B)}$ $r_{1/2} \geq 7$ kpc
type 2	0.3	$21.369^{+0.417}_{-0.402}$ (± 0.041)	$21.371^{+0.349}_{-0.350}$ (± 0.066)
	0.5	$21.135^{+0.362}_{-0.346}$ (± 0.034)	$21.208^{+0.300}_{-0.282}$ (± 0.053)
	0.7	$20.902^{+0.319}_{-0.324}$ (± 0.027)	$21.024^{+0.304}_{-0.278}$ (± 0.046)
	0.9	$20.704^{+0.353}_{-0.348}$ (± 0.032)	$20.911^{+0.302}_{-0.363}$ (± 0.057)
type 2.3	0.3	$21.580^{+0.429}_{-0.334}$ (± 0.084)	$21.562^{+0.411}_{-0.191}$ (± 0.151)
	0.5	$21.335^{+0.311}_{-0.269}$ (± 0.049)	$21.416^{+0.240}_{-0.239}$ (± 0.072)
	0.7	$21.048^{+0.301}_{-0.227}$ (± 0.032)	$21.216^{+0.218}_{-0.253}$ (± 0.051)
	0.9	$20.882^{+0.324}_{-0.256}$ (± 0.035)	$21.079^{+0.284}_{-0.256}$ (± 0.062)
type 2.2/	0.3	$21.410^{+0.408}_{-0.389}$ (± 0.050)	$21.434^{+0.342}_{-0.401}$ (± 0.083)
type 2.1	0.5	$21.057^{+0.382}_{-0.291}$ (± 0.044)	$21.113^{+0.269}_{-0.263}$ (± 0.067)
	0.7	$20.759^{+0.336}_{-0.300}$ (± 0.038)	$20.956^{+0.265}_{-0.280}$ (± 0.060)
	0.9	$20.505^{+0.326}_{-0.325}$ (± 0.051)	$20.732^{+0.336}_{-0.304}$ (± 0.086)
type 2.0	0.3	$20.878^{+0.313}_{-0.326}$ (± 0.092)	$21.174^{+0.367}_{-0.296}$ (± 0.107)
	0.5	$20.548^{+0.355}_{-0.270}$ (± 0.087)	$20.857^{+0.327}_{-0.312}$ (± 0.178)
	0.7	$20.335^{+0.388}_{-0.197}$ (± 0.085)	$20.588^{+0.436}_{-0.333}$ (± 0.230)
	0.9	$20.075^{+0.341}_{-0.235}$ (± 0.099)	$20.398^{+0.139}_{-0.287}$ (± 0.143)

The CFRS data of Lilly et al. [71] for the disk component are also shown as squares. Rescaling the measurements of Lilly et al. for the use of different filters was not sufficient to bring them into the vicinity of the GEMS and the COSMOS data points. We have thus applied a constant offset in surface brightness to the CFRS measurements such that the CFRS brightening trend (0.8±0.3 mag at $z \sim 0.67$) matches the trend line we derived for the bulgeless disk galaxies at $z \sim 0.8$ (i.e., where we sample rest-frame B light). After introducing this correction the evolution of pure disks as measured with the data of the CFRS and that of the COSMOS survey are consistent. This is also true for the GEMS measurements which agree very well with those made on the morphologically equivalent COSMOS sample of disk galaxies.
The small error bars on COSMOS measurements allow us to study the evolution of the different categories of disk galaxies in the following section.

The surface brightness evolution as a function of B/D-ratio

To trace the evolution of the disk galaxy population as a function of the bulge-to-disk ratio B/D we group the objects assigned to ZEST morphological type 2.2 and 2.1 into one group of galaxies termed 'disks with intermediate bulges'; these systems are intermediate between pure disks (ZEST type 2.3) and bulge-dominated disk galaxies (ZEST type 2.0). Figure 4.6 shows the evolution of rest-frame B-band surface brightness in the disk galaxy population as a whole (upper left corner) and for three B/D-categories mentioned above.

Tab. 4.7 — Average surface brightness (not corrected for inclination) properties of different simulated disk samples at $z \sim 0.7$ in the artificially redshifted SDSS data set. The information is structured as in Table 4.5 and graphically represented in Figs. 4.6a and 4.6b.

T	$\overline{\mu(B)}$ $r_{1/2} \geq$5 kpc	$\overline{\mu(B)}$ $r_{1/2} \geq$7 kpc
type 2	$21.509^{+0.425}_{-0.322}$ ($\pm$0.089)	$21.718^{+0.361}_{-0.373}$ ($\pm$0.166)
type 2.3	$21.824^{+0.341}_{-0.290}$ ($\pm$0.133)	$21.862^{+0.254}_{-0.227}$ ($\pm$0.246)
type 2.2/2.1	$21.348^{+0.390}_{-0.176}$ ($\pm$0.114)	$21.655^{+0.518}_{-0.355}$ ($\pm$0.239)
type 2.0	$21.165^{+0.072}_{-0.216}$ ($\pm$0.149)	$21.181^{+0.056}_{-0.317}$ ($\pm$0.215)

All medians and their associated errors shown for the COSMOS data set as a function of redshift in these figures are summarized in Table 4.4 and 4.6 (for inclination-corrected and uncorrected surface brightness, respectively). To enable a direct comparison of the median surface brightness of disks in the local universe we have plotted the identical information measured for the sample of artificially redshifted SDSS galaxies in each square of Figures 4.6a and 4.6b (cf. Tables 4.5/4.7 for the numerical values of median and associated errors for the SDSS$_{z=0.7}$ comparison sample). From Figures 4.6a and 4.6b it is evident that:

- surface brightness has decreased since $z \sim 1$ both in the disk galaxy population as a whole, as well as in each of the individual B/D-categories,
- the amount of fading since $z \sim 1$ is on average of order 1.4 mag in the rest-frame B-band if surface brightness values are corrected for inclination (dark grey points and solid trend line) and about 1 mag if optically thick disks are assumed such that no inclination correction needs to be applied (light grey points and dotted trend line),
- a linear evolution of the surface brightness fits the measurements between $z = 0.2$ and 1 well and – when extrapolated to low redshift – is in good agreement with the value measured in the local SDSS population,
- the average surface brightness increases with the importance of the bulge component, thus reflecting the higher central concentration of light in objects with a steeper surface brightness profile, and
- the surface brightness evolution in the largest disks with $r_{1/2} \geq 7$ kpc is quite similar to the evolution measured in objects larger than 5 kpc; it is reduced by about 0.3 mag in the largest objects for the bulge-dominated disk galaxies but nearly identical in the case of the total population and the disk galaxies with intermediate bulges or no bulge component at all.

The grey lines tracing the band of surface brightness values in Figures 4.6a and 4.6b demonstrate how well a linear model for the surface brightness evolution can fit the data.

Tab. 4.8 — Line parameters of the best-fit trend lines shown in Figs. 4.6a/4.6b and Figs. 4.8a/4.8b.

category	$\overline{\mu(B,z=0)}$	$d\overline{\mu(B,z)}/dz$	$\overline{\mu(B,z=0)}$	$d\overline{\mu(B,z)}/dz$
	$r_{1/2} \geq 5$ kpc [a]		$r_{1/2} \geq 7$ kpc [b]	
type 2	22.030±0.092	-1.302±0.161	22.218±0.054	-1.339±0.095
type 2.3	22.350±0.140	-1.467±0.244	22.583±0.079	-1.531±0.137
type 2.2/2.1	22.031±0.154	-1.485±0.268	22.238±0.061	-1.542±0.107
type 2.0	21.520±0.066	-1.486±0.115	21.588±0.160	-1.147±0.279
type 2	21.584±0.047	-0.951±0.083	21.690±0.041	-0.916±0.072
type 2.3	21.873±0.034	-1.114±0.059	21.857±0.022	-0.889±0.039
type 2.2/2.1	21.525±0.131	-1.053±0.230	21.697±0.038	-1.072±0.067
type 2.0	21.209±0.029	-1.257±0.050	21.312±0.097	-0.976±0.169

[a] Line parameters from data shown in Fig. 4.6a and summarized in Tables 4.4/4.5 (for inclination-corrected $\mu(B)$) and Tables 4.6/4.7 ($\mu(B)$ not corrected for inclination).

[b] Line parameters from data shown in Fig. 4.6b and summarized in Tables 4.4/4.5 (for inclination-corrected $\mu(B)$) and Tables 4.6/4.7 ($\mu(B)$ not corrected for inclination).

Note. — This table specifies the parameters returned by a linear least squares fit to the median values (including the SDSS data point as a constraint at $z \sim 0$) of the effective surface brightness, $\overline{\mu(B)}$, for various categories of disks in different redshift slices. The 2$^{\rm nd}$ and 4$^{\rm th}$ column (the former for disks with $r_{1/2} \geq 5$ kpc, the latter for a sample restricted to objects with $r_{1/2} \geq 7$ kpc) give the values of median effective surface brightness if the fitted trend is extrapolated to $z = 0$. Columns number 3 and 5 list the slope of the line, i.e., the inferred surface brightness increase in the galaxy population in the range $z \in [0, 1[$. In the upper half of the table the evolutionary trends for inclination-corrected surface brightness values are given, in the lower half the inferred evolution without application of an inclination correction.

In Table 4.8 we list the best fitting line parameters obtained from a linear regression on the median effective surface brightness values in the COSMOS data set to which the SDSS measurement was added as an additional constraint. As done in the graphical representation of the surface brightness evolution we list the evolutionary trends both for the case with (upper half of table) and without inclination correction (lower half).

In Figures 4.8a and 4.8b we summarize the information on the surface brightness evolution of different samples of disk galaxies reported in Figures 4.6a and 4.6b. Different disk galaxy samples are plotted with different lines and symbols in Figure 4.8. In Table 4.8 the result of the fits is summarized for both sets of galaxies with physical size above 5 and 7 kpc, respectively. The slope of the lines is equivalent to the amount of surface brightening $d\overline{\mu}/dz$ out to $z \sim 1$. We infer the following evolution for disks with $r_{1/2} \geq 5$ kpc if an opacity-dependent correction for inclination is applied (black points and trends lines): -1.30±0.16 mag for all disk galaxies, -1.47±0.24 mag for bulgeless systems, -1.49±0.27 mag for disks with intermediate bulges, and -1.49±0.12 mag for bulge-dominated disks. The evolution calculated when using only the largest disks is virtually the same in the case of the total population and of disks without a bulge or with an intermediate bulge

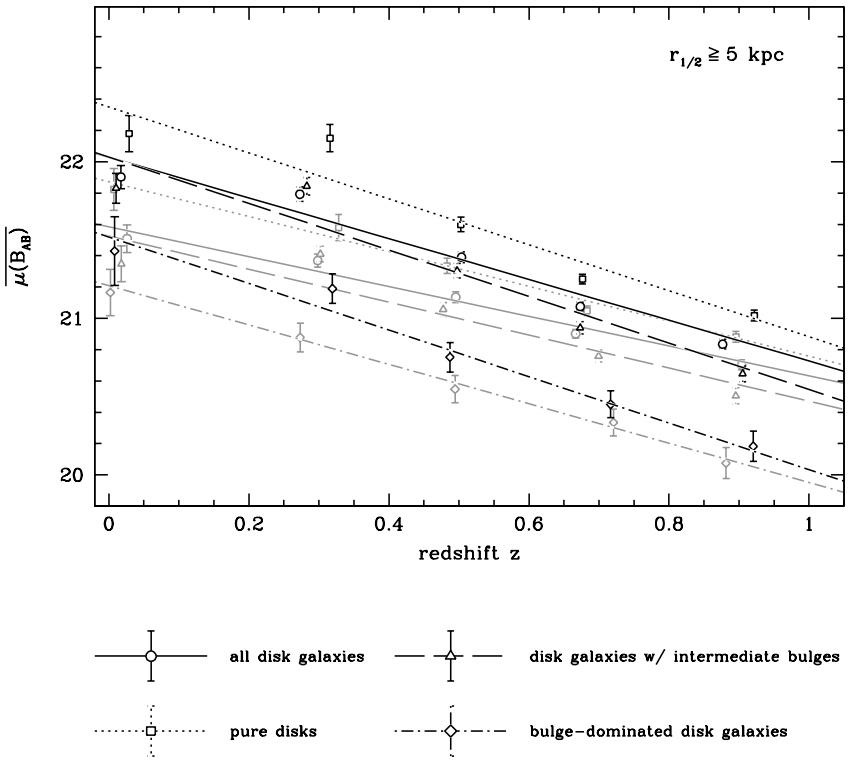

Fig. 4.8a — Evolution of median rest-frame B-band surface brightness $\overline{\mu(B)}$ in the disk galaxy population for sources with $r_{1/2} \geq 5$ kpc. Different morphological (sub-)classes of disks are plotted with different lines and symbols according to the scheme illustrated in the lower third of the figure. The black symbols and lines report the evolution derived for inclination-corrected surface brightness values; grey colouring has been used to show the evolution inferred if surface brightness values are not corrected for inclination (i.e. if perfectly optically thick disks are assumed). The measurements have been randomly moved away from the nominal bin centres at redshifts 0.3, 0.5, 0.7 and 0.9 to avoid the overlapping of points. Error bars give the standard error of the median. The line parameters of the least-square fit to the COSMOS points (which were additionally constrained by the local SDSS measurement at $z \sim 0$) are given in the left half of Table 4.8.

component. The most bulge-dominated systems show an evolution which is somewhat smaller, namely -1.15±0.28 mag.
We also plot (in grey) the fit for the evolution of surface brightness values if these are not corrected for inclination. The evolution found in this case is: -0.95±0.08 mag for all disk galaxies, -1.11±0.06 mag for bulgeless systems, -1.05±0.23 mag for disks with intermediate bulges, and -1.26±0.05 mag for bulge-dominated disks. As before the evolution of the largest bulge-dominated galaxies is seen to be reduced by about 0.3 mag while in the two other B/D-categories and in the global population the evolution of disk galaxy samples selected according to $r_{1/2} \geq 5$ kpc or 7 kpc agree well. This shows that the main conclusions of the analysis do not depend on the opacity of the disks out to $z \sim 1$.

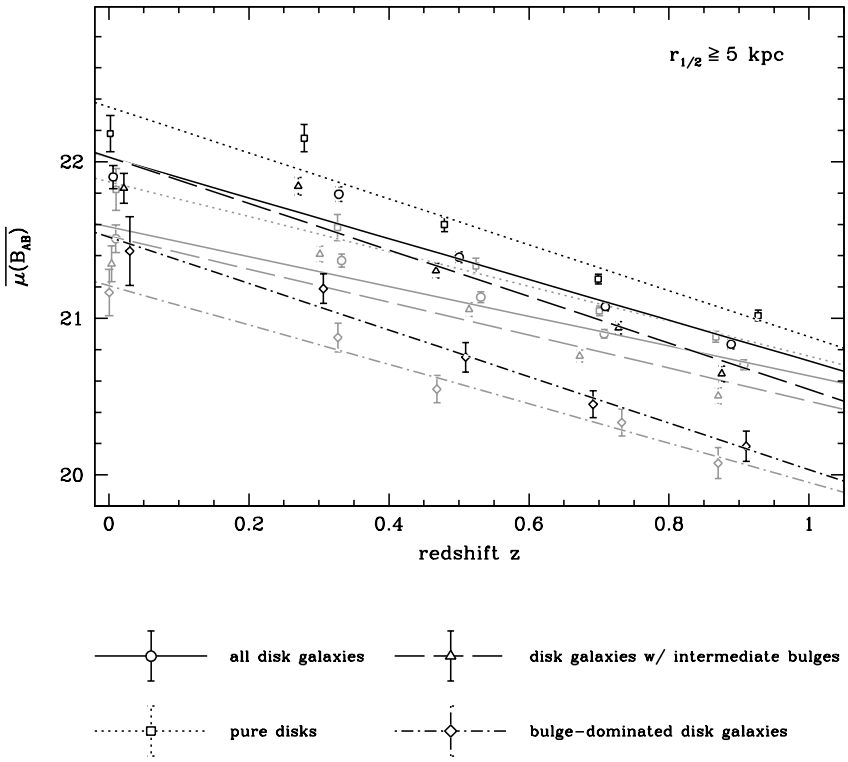

Fig. 4.8b — As in previous figure but using a sample of galaxies restricted to sources with $r_{1/2} \geq 7$ kpc. The line parameters are listed in the right-hand half of Table 4.8.

In the case of the pure disks the extrapolation of the linear fit to redshift zero provides a figure which can be compared with the canonical [46] value of $\mu_{\rm F} = 21.65$ mag arcsec^{-2} for the B-band central surface brightness. The central and effective surface brightness are related by

$$\mu(B) = \mu_0(B) + 2.5 \log \left(\frac{k(n)^{2n}}{n \cdot \Gamma(n)} \right) \ , \tag{4.4}$$

where n is the Sérsic index, $k(n)$ is the scaling factor in the Sérsic profile and $\Gamma(n)$ is the Gamma function. For an exponential disk with $n = 1$ the difference between central and effective surface brightness is $\mu(B) - \mu_0(B) = 1.12$. To compare with our data, the canonical Freeman value was also corrected for:

- The use of different B-filters (Johnson B vs. Subaru B) and magnitude scales (Vega magnitudes vs. AB magnitudes). This was done using the iraf task `calcphot` and the spectrum of an Scd galaxy taken from the ZEBRA library.
- The measured opacity of the disks. Freeman [46] assumes optically thin disks and

therefore apply an inclination correction with $C = 1$ in equation (4.1). For local galaxies in our analysis where we measure an upper limit of $C_{z\sim 0} = 0.46$ (cf. Section 4.3.1). In order to apply an average correction for all disks regardless of their orientation we calculated a mean flattening $\overline{q}$, which is obtained by averaging the observed axis ratio $q = b/a$ over all possible orientations. Using the relation between the inclination angle i and the observed axis ratio for objects with a minimal flattening q_0, one has:

$$\int_0^{\pi/2} q(i)\ \frac{di}{\pi/2} = \int_0^{\pi/2} \sqrt{(1-q_0^2)\ \cos^2(i) + q_0^2}\ \frac{di}{\pi/2} = 0.67\ . \tag{4.5}$$

The minimal flattening was assumed to be 0.2. With this the expression for the opacity-correction is $2.5(1 - C_{z\sim 0})\ \log(\overline{q})$.

The rescaled Freeman value becomes $\mu_{\mathrm{F,\ corr}} = 22.22$ if we wish to compare it with the evolutionary trend we derive assuming $C_{z\sim 0} = 0$; for the case of non-vanishing $C_{z\sim 0} = 0.46$ the according value is $\mu_{\mathrm{F,\ corr}} = 22.48$. Both for the sample of pure disk galaxies with half-light radii larger than 5 kpc as well as for the largest disks with $r_{1/2} \geq 7$ kpc the linear evolutionary trend lies within the range expected from the classical Freeman value (see light grey area in Figure 4.7). The extrapolation of the evolutionary trend from COSMOS galaxies at intermediate redshifts is thus consistent with both the $\mathrm{SDSS}_{z=0.7}$ comparison sample as well as with the Freeman relation.

Inspection of Figures 4.8a and 4.8b shows that the sample including all disk galaxies displays a slightly smaller surface brightness increase out to $z = 1$ than the one inferred for any of the B/D classes individually. This trend could be explained by the relative evolution in the number density of disks with different bulge-to-disk ratios already discussed in S07 (Chapter 3), and further elaborated later in this chapter.

4.3.3 Star formation histories

Figures 4.9a and 4.9b show the distributions of rest frame $(u^* - V)$-colours for the same four categories of disk galaxies of the previous section (both for the sample with half-light size larger than 5 kpc and 7 kpc; see Table 4.9 for the summary of the average colours in the COSMOS sample). Galaxy colours were calculated by linear interpolation of the ground-based photometry (ranging from u^* to K_s fluxes, see Section A.2.2) at the central wavelength of the CFHT u^*- and the Subaru V-band in the rest-frame of the galaxies. Qualitatively identical results were found if $(u^* - V)$-colours were derived from the best fit ZEBRA templates.

The open grey dots with asymmetric error bars indicate the median and the 2nd and 3rd inter-quartile range of the color difference in the redshift intervals $z \in$ [0.2, 0.4[, [0.4, 0.6[, [0.6, 0.8[and [0.8, 1[. Uncertainties in the individual measurement are shown by each member of the group of three crosses in the upper left panel. The horizontal errorbars

Tab. 4.9 — Values of rest frame $(u^* - V)$-colours for different categories of COSMOS disk galaxies, using only objects with $r_{1/2} \geq 5$ kpc or $r_{1/2} \geq 7$ kpc, respectively (cf. Figs. 4.9a and 4.9b).

T	redshift	$\overline{(u^* - V)}_0$ [a] $r_{1/2} \geq 5$ kpc	$\overline{(u^* - V)}_0$ $r_{1/2} \geq 7$ kpc
type 2	0.3	$1.089^{+0.232}_{-0.209}$ (± 0.021)	$1.239^{+0.171}_{-0.189}$ (± 0.033)
	0.5	$1.043^{+0.198}_{-0.195}$ (± 0.017)	$1.165^{+0.154}_{-0.147}$ (± 0.030)
	0.7	$0.940^{+0.215}_{-0.172}$ (± 0.015)	$1.006^{+0.183}_{-0.107}$ (± 0.023)
	0.9	$0.799^{+0.182}_{-0.158}$ (± 0.015)	$0.855^{+0.160}_{-0.144}$ (± 0.028)
type 2.3	0.3	$0.935^{+0.155}_{-0.147}$ (± 0.033)	$1.078^{+0.119}_{-0.113}$ (± 0.050)
	0.5	$0.891^{+0.158}_{-0.088}$ (± 0.019)	$1.048^{+0.124}_{-0.142}$ (± 0.040)
	0.7	$0.826^{+0.147}_{-0.119}$ (± 0.014)	$0.944^{+0.090}_{-0.096}$ (± 0.029)
	0.9	$0.700^{+0.138}_{-0.101}$ (± 0.014)	$0.758^{+0.113}_{-0.098}$ (± 0.025)
type 2.2/	0.3	$1.056^{+0.201}_{-0.188}$ (± 0.023)	$1.196^{+0.141}_{-0.164}$ (± 0.044)
	0.5	$1.097^{+0.179}_{-0.218}$ (± 0.024)	$1.207^{+0.137}_{-0.128}$ (± 0.038)
	0.7	$1.029^{+0.207}_{-0.186}$ (± 0.023)	$1.069^{+0.171}_{-0.113}$ (± 0.034)
	0.9	$0.914^{+0.178}_{-0.195}$ (± 0.025)	$0.951^{+0.166}_{-0.158}$ (± 0.039)
type 2.0	0.3	$1.408^{+0.076}_{-0.157}$ (± 0.026)	$1.413^{+0.062}_{-0.115}$ (± 0.040)
	0.5	$1.328^{+0.147}_{-0.114}$ (± 0.039)	$1.321^{+0.105}_{-0.169}$ (± 0.076)
	0.7	$1.265^{+0.115}_{-0.127}$ (± 0.034)	$1.208^{+0.152}_{-0.100}$ (± 0.058)
	0.9	$1.152^{+0.087}_{-0.088}$ (± 0.035)	$1.171^{+0.064}_{-0.070}$ (± 0.053)

[a] The values given correspond to the median, the standard error of the median (in brackets, cf. equation (4.3)) and the spread in the population measured by the 1st quartile (error in subscript) and the 3rd quartile (error in superscript).

show the 1σ-error on the photometric redshift for objects at $z \sim 0.25$ (cross at left), $z \sim 0.6$ (cross in middle) and $z \sim 0.95$ (right-most cross). Vertical errors mark the uncertainty in the determination of $(u^* - V)$-color.

The rest frame $(u^* - V)$-colours of the corresponding samples of SDSS galaxies are also shown in each of the four panels in Figure 4.9a and 4.9b at $z \sim 0$ using the same nomenclature as for the COSMOS sources. The values are listed in Table 4.10 (note that no errors are visible for bulge-dominated galaxies with $r_{1/2} \geq 7$ kpc as this sub-sample consists of only three sources with very similar $(u^* - V)$-colour). The colours for the SDSS galaxies were computed from the SDSS *ugriz*-photometry using the same approach of linear interpolation applied to the COSMOS galaxies.

The analysis of the evolving colour properties displayed in Figures 4.9a and 4.9b shows that:

- at all redshifts out to $z = 1$, the morphological classes contain successively redder objects moving from bulgeless disks to bulge-dominated galaxies, as it is seen in the local disk galaxy population;

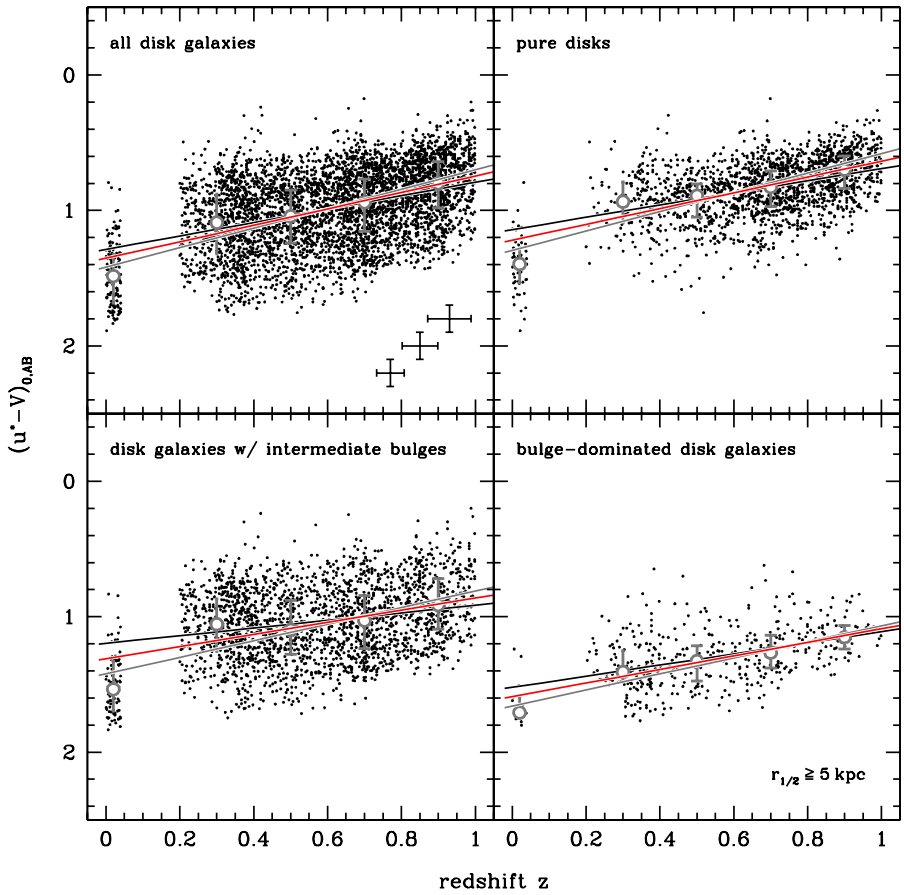

Fig. 4.9a — Rest-frame $(u^* - V)$-colours for disk galaxies with $r_{1/2} \geq 5$ kpc as a function of redshift. The open grey circles at $z \sim 0$ indicate the median in either of the four disk galaxy categories in the SDSS$_{z=0.7}$ comparison sample. Medians derived for COSMOS galaxies are plotted at $z \geq 0.2$.
Median values of rest-frame $(u^* - V)$-colours and their associated errors shown in this figure are listed in Table 4.9 for the COSMOS sources and in Table 4.10 for the SDSS$_{z=0.7}$ comparison sample. The "blueing" of the galaxy colours has been estimated by taking the average between two linear fits to the data; (1) a straight line fit to the median values using both the COSMOS and SDSS measurements (grey line), and (2) a linear regression (excluding the SDSS measurements) on the COSMOS data points (black line). The average evolutionary trend lines are plotted in red and their parameters specified in Table 4.11.

- the mean colors of the disk galaxy population as a whole, and of galaxies of different B/D-ratio, become steadily bluer as redshift increases;
- the detected amount of "blueing" ranges from 0.5 mag to 0.7 mag, depending on B/D-ratio;
- the slope of the relation $\overline{(u^* - V)}$ versus z tends to be steeper for pure disks than

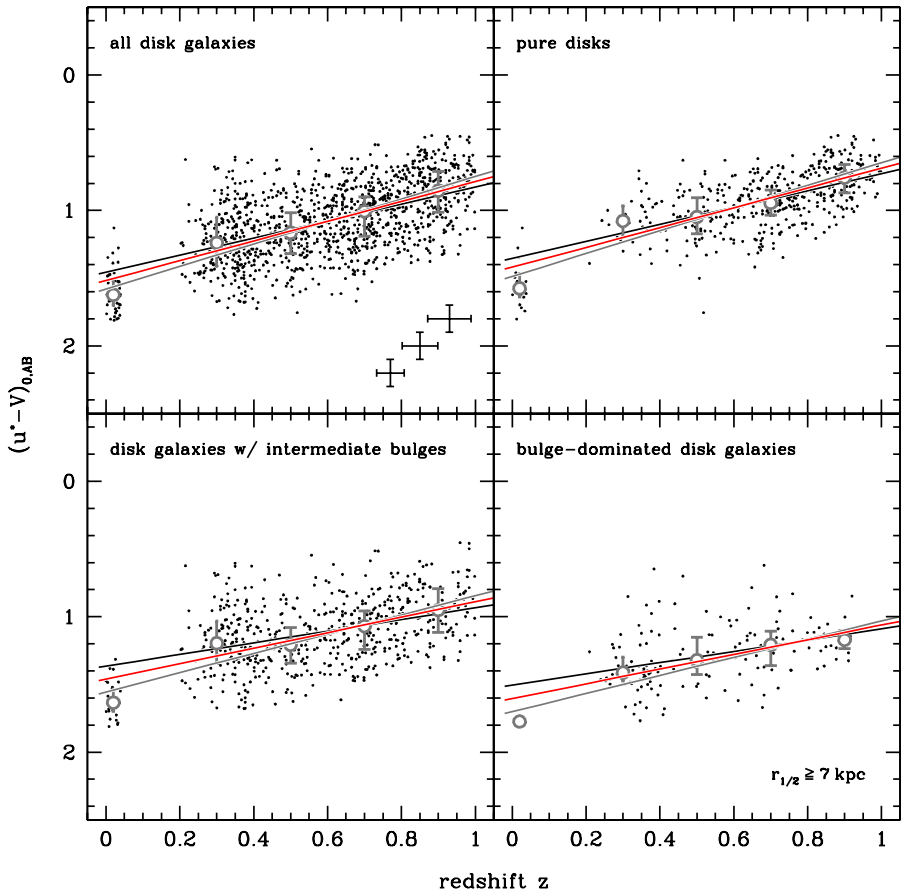

Fig. 4.9b — As in previous figure but using only galaxies with $r_{1/2} \geq 7$ kpc. Median values of rest-frame $(u^* - V)$-colours and their associated errors shown in this figure are listed in Table 4.9 for the COSMOS sources and in Table 4.10 for the $\mathrm{SDSS}_{z=0.7}$ comparison sample. (Symbols and colour coding as in Fig. 4.9a.)

for disk galaxies with a bulge and also steeper for the largest galaxies ($r_{1/2} \geq 7$ kpc) than for smaller ones ($r_{1/2} \geq 5$ kpc).

Two different linear regressions on the evolving values of $(u^* - V)$ were performed, one including and one excluding the SDSS value, and the average value of their slopes and y-axis intercepts were adopted to describe the fiducial shift in galaxy colours as a function of redshift. This inclusion of the SDSS value results in a slightly steeper evolutionary slope (plotted as a grey line in Figure 4.9). The fiducial average is plotted as a red line in Figures 4.9a and 4.9b and its parameters are listed in Table 4.11 for each of the disk galaxy samples.

In Figure 4.10a and 4.10b we plot grids of evolutionary tracks in the plane of rest-frame $(u^* - V)$-colour versus luminosity increase (dark grey grid for Bruzual and Charlot [13]

Tab. 4.10 — Values of rest frame $(u^* - V)$-colours for different simulated disk samples at $z \sim 0.7$ in the artificially redshifted SDSS data set. The values given to the left and right of the vertical separator list the values obtained for galaxies with $r_{1/2} \geq 5$ kpc and $r_{1/2} \geq 7$ kpc, respectively (see Figs. 4.9a and 4.9b for the graphical representation of the information given in the table).

T	$\overline{(u^* - V)}_0$ $r_{1/2} \geq$5 kpc	$\overline{(u^* - V)}_0$ $r_{1/2} \geq$7 kpc
type 2	1.485±0.039 (±0.179)	1.623±0.041 (±0.090)
type 2.3	1.396±0.060 (±0.129)	1.575±0.087 (±0.086)
type 2.2/type 2.1	1.536±0.051 (±0.184)	1.635±0.052 (±0.082)
type 2.0	1.708±0.065 (±0.079)	1.774±0.027 (±0.024)

Tab. 4.11 — Line parameters of the best-fit trend lines shown in red in Figs. 4.9a and 4.9b.

category	$\overline{(u^* - V)\,(z=0)}$	$d\overline{(u^* - V)\,(z)}/dz$	$\overline{(u^* - V)\,(z=0)}$	$d\overline{(u^* - V)\,(z)}/dz$
	$r_{1/2} \geq$ 5 kpc [a]		$r_{1/2} \geq$7 kpc [b]	
type2	1.354±0.069	-0.607±0.121	1.516±0.059	-0.729±0.102
type 2.3	1.217±0.100	-0.582±0.175	1.422±0.096	-0.738±0.164
type 2.2/type2.1	1.310±0.111	-0.450±0.193	1.464±0.085	-0.574±0.146
type 2.0	1.592±0.054	-0.510±0.094	1.602±0.088	-0.541±0.155

[a] Line parameters from data shown in Fig. 4.9a and summarized in Tables 4.9 and 4.10.

[b] Line parameters from data shown in Fig. 4.9b and summarized in Tables 4.9 and 4.10.

Note. — The line parameters represent the average of (1) a linear regression on the COSMOS measurements in the range $z \in [0.2, 1[$, and of (2) a linear least squares fit to the median values (including the SDSS data point as a constraint at $z \sim 0$) of rest-frame $(u^* - V)$-colours for various categories of disks in different redshift slices. The 2nd and 4th column (the former for disks with $r_{1/2} \geq 5$ kpc, the latter for a sample restricted to objects with $r_{1/2} \geq 7$ kpc) give the values of rest-frame $(u^* - V)$-colour at $z = 0$ by extrapolation of the fitted trend. Columns number 3 and 5 list the slope of the line, i.e., the inferred amount of "blueing" in the galaxy population in the range $z \in [0, 1[$.

models and light grey grid for Maraston [76] models). In both cases a Salpeter initial mass function is assumed and the spectra of composite stellar populations with different exponentially declining star formation rates are then used to calculate the galaxy colours and the luminosity as a function of age. The dashed lines in the two grids mark isochrones corresponding to 1, 3, 5, 7, 9, 11 and 13 Gyr after the onset of star formation. All flux changes are normalized to the present day flux (taken as the one at an age of 13 Gyr) which we use as our reference value when defining the scale on the vertical axis which measures the difference $\Delta M(B)$ in the flux emitted by the evolving stellar populations at a younger

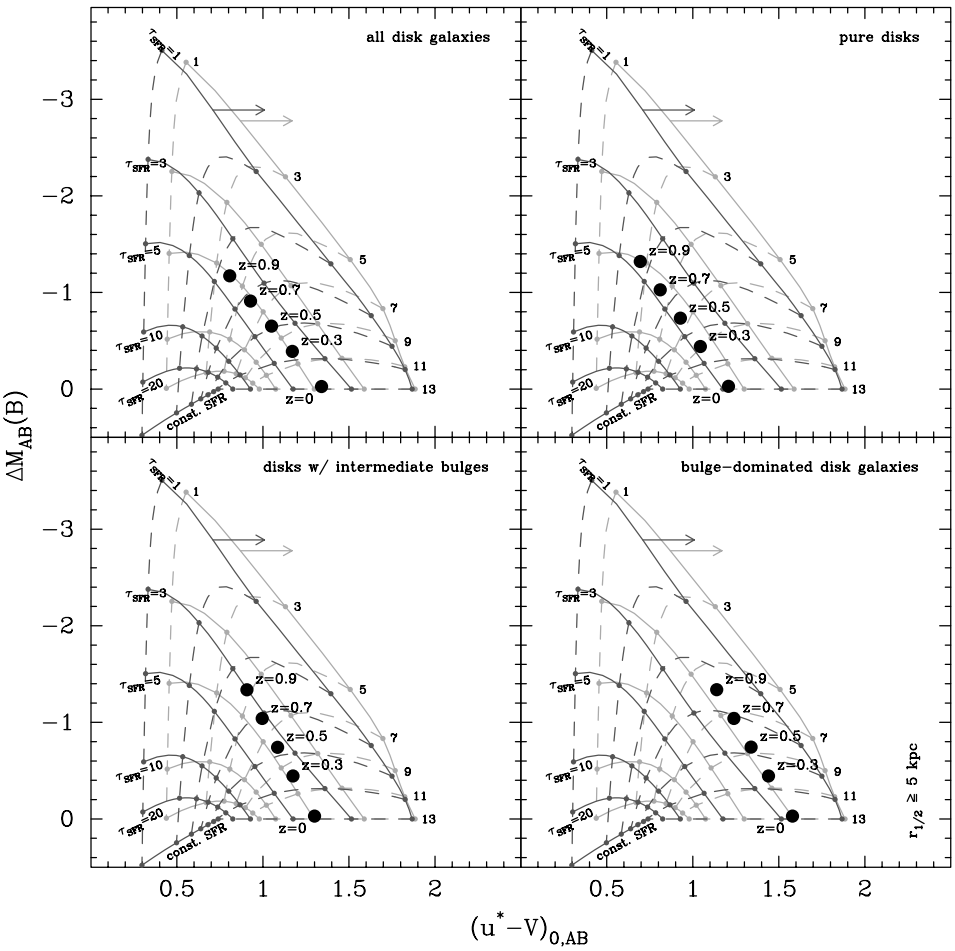

Fig. 4.10a — Average location of the disk galaxy population (objects with $r_{1/2} \geq 5$ kpc) and various sub-classes thereof with respect to rest-frame $(u^* - V)$-colours and luminosity increase, superimposed on population synthesis models (light grey grid – Maraston [76]; dark grey grid – Bruzual and Charlot [13]). Solid grid lines are lines of equal star formation history, dashed lines in the two grids are isochrones. The position of the black points labeled with $z = 0$, 0.3, 0.5, 0.7 and 0.9 is defined by the best fitting linear trends for the evolution of the rest-frame $(u^* - V)$-colour and for the increase in effective surface brightness (cf. Tables 4.8 and 4.11 for the parameters of the trend lines).

age and today. The solid lines are lines of constant star formation history (described by the exponential time constant $\tau_{\rm SFR}$); five evolutionary tracks with exponentially declining star formation are plotted, starting with $\tau_{\rm SFR} = 1$ Gyr on the right, followed by those with exponential time constants of 3, 5, 10 and 20 Gyr (from right to left). In addition to the lines of equal τ, the dark grey grid also includes the track for a constant star formation rate of $4M_\odot$/yr.

In both parts of Figure 4.10 the average properties of the COSMOS galaxy population

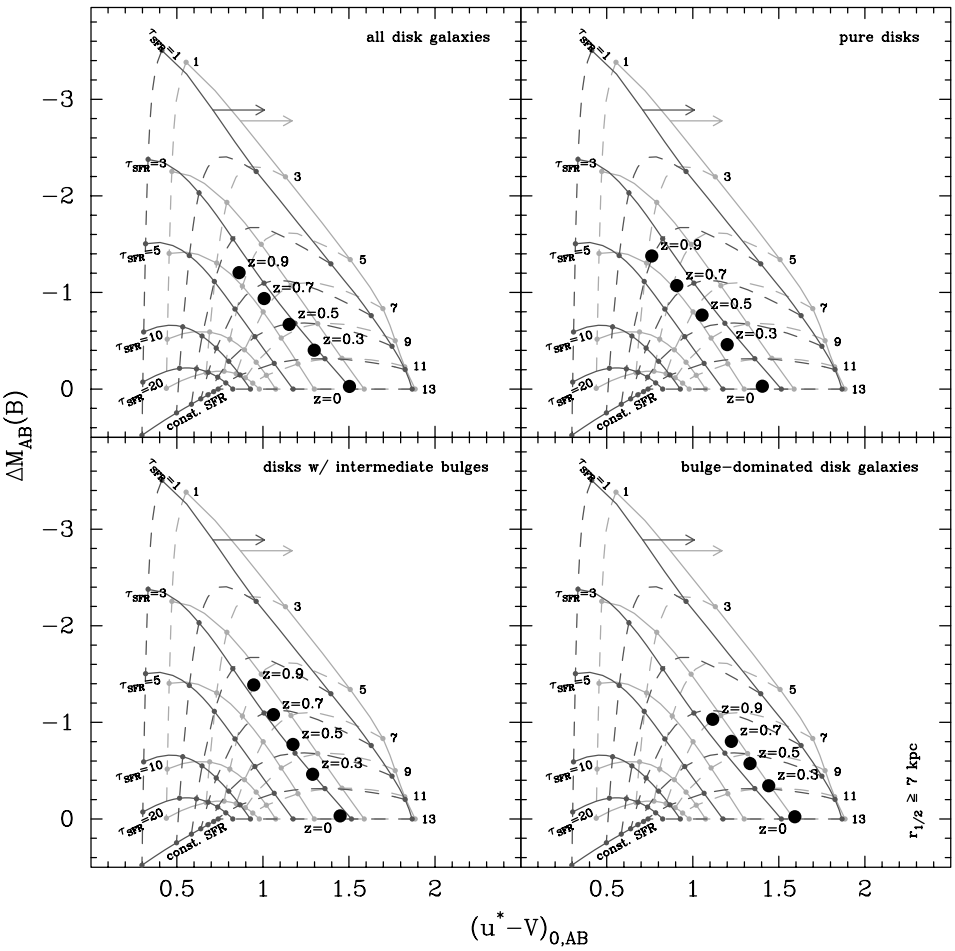

Fig. 4.10b — As in previous figure but using only galaxies with $r_{1/2} \geq 7$ kpc. The location of the points are defined by the line parameters given in Tables 4.8 (for the brightness increase) and Table 4.11 (for galaxy colour). All symbols and colour coding match those of Fig. 4.10a.

at redshifts $z = 0.3$, 0.5, 0.7 and 0.9 and those of the SDSS comparison sample at $z = 0$ are superimposed as black dots labeled with their redshift. Positions along the horizontal axis are determined by the linear fit to the colour evolution summarized in Table 4.11. Assuming that the sizes of the disk galaxies do not evolve strongly out to $z \sim 1$ (as shown in S07 and in this work), the change in the median surface brightness of the population is equivalent to a change in magnitude, $\Delta M(B)$, as calculated using the SED libraries of Bruzual and Charlot [13] and Maraston [76]. Thus the vertical axis in the figure implies the increase in surface brightness $\Delta\overline{\mu(B)}$ given by the relations listed in Table 4.8. We only show the evolution derived from inclination-corrected surface brightness values and will continue to refer mainly to these estimates for the rest of the analysis. The reader may resort to Table 4.8 to compare the difference in evolution resulting from using or neglecting corrections for inclination.

To assess the effects of dust reddening we repeat the computation of the grid points using the Galactic extinction law of Cardelli et al. [15] and the Small Magellanic Cloud extinction law of Pei [88]; the effects are virtually identical in the wavelength range containing the CFHT u^*- and the Subaru V-filter. The application of these corrections results in a shift of the evolutionary grid which is indicated by the dark and the light grey arrows for the two grids. The length of the arrow (0.3 mag) corresponds to the shift in $(u^* - V)$-colour brought about by a colour excess $E(B - V)$ of 0.2 mag[1].

For the disk galaxy population as a whole the inspection of 4.10a and 4.10b shows that:

- since $z \sim 1$ disk galaxies have evolved roughly parallel to the lines of constant $\tau_{\rm SFR}$ that describe an exponentially-decaying star formation rate; and
- the loci of the disk galaxy population as a whole favour star formation histories with an exponential time constant of roughly 5 Gyr. This result was already hinted at by a sample of a few dozen large disk galaxies studied by Lilly et al. [71], and is now put on solid ground by our COSMOS sample.

As already commented by previous authors, a declining star formation rate is thus the origin of the decline of the surface brightness of disk galaxies from higher redshifts to the local universe. With the large sample at hand we can advance the analysis and inspect the evolution of disk galaxies with and without bulges in detail.
The bulgeless disks behave as the whole population , i.e. have $\tau_{\rm SFR} \simeq 5$ Gyr. The integrated (i.e., disk plus bulge) star formation histories of bulge-dominated disk galaxies differ at face value from those of bulgeless disks: the star formation activity declines faster, the larger the bulge component. The effect can be well explained by considering a passively evolving contribution of the bulge component, as shown in Figure 4.11 where such a component has been added to the synthetic SEDs. The evolutionary tracks shown in Figure 4.11 include a bulge component that started its star formation 13 Gyr ago and exhausted it with an exponential time constant of $\tau_{\rm SFR} = 100$ Myr, and a disk component with a slowly declining star formation activity (given by the value of $\tau_{\rm SFR}$ labelling the solid lines in the figure). The contribution of the bulge component to the total flux of the galaxy in the B-band is 20% for disk galaxies with intermediate bulges (left panel) and 50% for bulge dominated galaxies (right), respectively.

The observed trends can thus be interpreted to indicate a similar star formation history over the past 8 billion years for all disks independent of whether or not they host a bulge component. Within the errors, these conclusions apply independent of whether the largest disks only (Figure 4.11) or also smaller disks ($r_{1/2} \in [5, 7[$ kpc) are considered.

[1] Note, that although the flux is reduced in the blue and green range of the electromagnetic spectrum, the application of the extinction law manifests itself as a purely horizontal shift because we calibrate the luminosity evolution by the value at 13 Gyr and the SED at this epoch is affected by the identical extinction as those at all other ages. If extinction properties were to change through cosmic time the "reddening vector" drawn in the plot would also have a non-vanishing component along the y-axis.

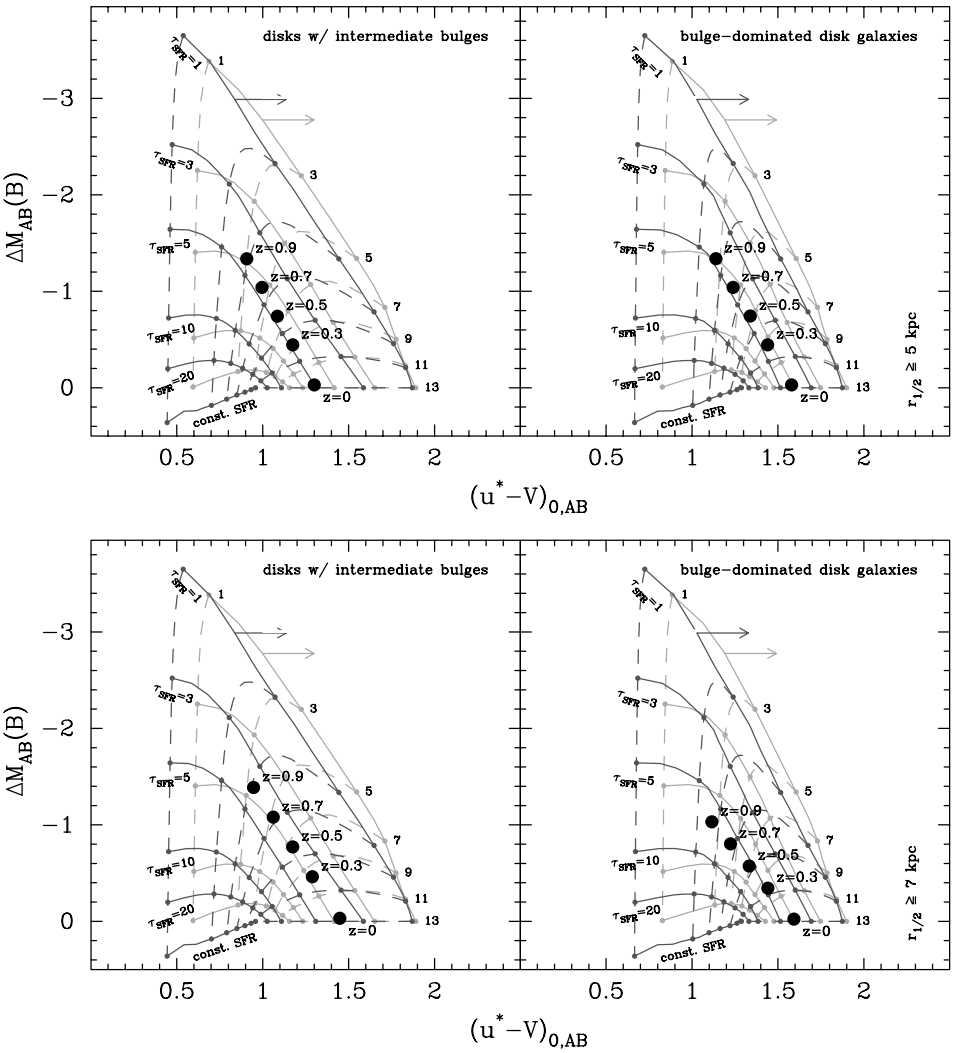

Fig. 4.11 — Evolution of disk galaxy categories with a non-negligible bulge component, compared with the expected evolutionary tracks if the SEDs of the synthetic galaxies are a combination of a bulge component and a disk. The measured evolution is shown separately for the largest disk galaxies with $r_{1/2} \geq 7$ kpc (*lower part* of figure) and a sample involving all objects with $r_{1/2} \geq 5$ kpc (*upper half* of figure). In drawing the stellar evolution grids the same nomenclature as the one of the previous figure was used. The grids show the fading and reddening expected of a stellar population which has an old bulge component (represented by a composite stellar population as old as the Hubble time with a very quickly declining star formation rate – a time constant $\tau_{\rm SFR} = 100$ Myr was chosen) and a disk component with more slowly declining star formation activity (given by the value of $\tau_{\rm SFR}$ labelling the solid lines in the figure). The contribution of the bulge component to the total flux of the galaxy in the B-band was taken as 20% and 50% for disk galaxies with intermediate bulges (*left*) and bulge-dominated galaxies (*right*), respectively.

4.4 The bivariate size-luminosity function

4.4.1 Definition

In S07 (Chapter 3 of this thesis) we discussed the evolution of the integrated size function of disk galaxies, without any attempt to investigate the dependence of such a size function on luminosity. Here we advance the analysis by studying the bivariate size-luminosity function. It measures the number of galaxies per unit comoving volume and per logarithmic unit of half-light radius $r_{1/2}$ (expressed in kpc) and unit rest-frame B-band magnitude $M(B)$. Since we are working with a magnitude-limited sample, it is necessary to correct for the fact that bright objects could be located in a larger volume of space and still enter our sample while the volume throughout which a faint object could be observed is smaller. As done in S07, the variation of sampling volume for the individual sources is accounted for by using the $V_{\rm max}$-formalism (Felten [42], Schmidt [110]) in which each galaxy is weighted with the reciprocal of the comoving volume it could occupy while still satisfying the selection criteria of the sample. We present the main concepts again for clarity.

1. The volume $V_{\rm max}$ is calculated for each source according to:

$$V_{\rm max} = \left(\frac{c}{H_0}\right)^3 \, d\Omega \, \left[\int_{z_{\rm min}}^{z_{\rm max}} \frac{dz}{\sqrt{\Omega_\Lambda + \Omega_m \, (1+z)^3}}\right]^3 , \tag{4.6}$$

   where

$$D(z) = \left(\frac{c}{H_0}\right) \, \int_0^z \frac{dz}{\sqrt{\Omega_\Lambda + \Omega_m \, (1+z)^3}} \tag{4.7}$$

   is the comoving distance in a ΛCDM cosmological model with $\Omega_\Lambda = 0.75$ and $\Omega_m = 0.25$. $d\Omega$ in the preceding formula is the effective solid angle covered by the survey, which is 6036 arcmin^2.
   For bright objects the larger value of $V_{\rm max}$ will lead to a reduced weighting factor, thereby correcting for their overabundance in the sample with respect to fainter members of the galaxy population (see S07 for further details).

2. With the knowledge of $V_{\rm max}$ the bivariate size-luminosity distribution is constructed by summing the appropriately weighted galaxies within a given interval in size and absolute magnitude:

$$\Phi(M, \log(r_{1/2}), z) \times \Delta M \times \Delta\log(r_{1/2}) = \sum_\gamma \frac{1}{V_{{\rm max},\gamma}} . \tag{4.8}$$

   The summation is carried out over all sources γ with a photometric redshift within the redshift bin under consideration.

3. The Poisson noise (owing to the statistical manner in which each bin is populated) in each bin of the bivariate size luminosity distribution is the dominant error affecting $\Phi(M, \log(r_{1/2}), z)$ (and exceeds the errors introduced by the uncertainties on sizes, magnitudes and photometric redshifts as shown in S07). The Poisson error is given by:

$$\sigma_P = \sqrt{\sum_{\gamma} \frac{1}{V^2_{\mathrm{max},\gamma}}} \tag{4.9}$$

where the summation includes all objects γ in a given bin.

In Figures 4.12a to 4.12d we show the 2-dimensional surface defined by the bivariate size-luminosity distribution $\Phi(M, \log(r_{1/2}), z)$ as a function of redshift. For each redshift slice centred on z = 0.3, 0.5, 0.7 and 0.9 (from top to bottom) the surface is viewed from two different angles: one almost parallel to the size axis (panel on the left) and the other approximately looking down the magnitude axis (right). In both views lines of constant radius are plotted in shades of red (growing lighter for larger sizes) and lines of constant magnitude in shades of blue (growing darker with increasing luminosity) in those regions of parameter space where the sample is complete in a given redshift bin. (The completeness limit is defined by the faintest observed magnitude at the bin centre in each redshift slice, i.e., $M(B)$ = -17.5, -19, -20 and -21 at z = 0.3, 0.5, 0.7 and 0.9 as can be seen by scrutinizing the upper part of Figure 4.1.) The binning was chosen such that bin limits always comply with completeness limits. Along the size axis we sample the surface between $\log(r_{1/2})$ = -.05 and 1.3 (i.e., for physical galaxy sizes ranging from 0.9 kpc to 20 kpc) in bins of width $\Delta\log(r_{1/2})$ = 0.15 centred on $\log(r_{1/2})$ = 0.025, 0.175,... etc. With respect to magnitude we plot a measurement every half of a magnitude with bin centres located at one quarter and three quarters of a magnitude, e.g., at -21.75, -21.25, -20.75,... etc. Poissonian errors are marked with a vertical black bar. Errors are not indicated in the incomplete regions of parameter space which are also kept in black and white as opposed to the complete part of the surface which is coloured as described above.

Panels (a) to (d) of Figure 4.12 show the evolution since $z \sim 1$ of $\Phi(M, \log(r_{1/2}), z)$ for the entire disk galaxy population, for the bulgeless disks and for disk galaxies with intermediate and strong bulge components (this order). Note that:

- the shape of the surface remains almost constant with redshift when the entire disk galaxy population is considered. In fact, the visual impression is that the characteristics of the rib lines are quite similar in those part of the plot which can be compared at all redshifts. This is especially clear if one looks at the red lines of constant size.

- vertical shifts of the surface $\Phi(M, \log(r_{1/2}), z)$ as a function of redshift occur in the individual B/D-disk categories but appear to be minor when all kinds of disk galaxies are combined (see Figure 4.12a), and

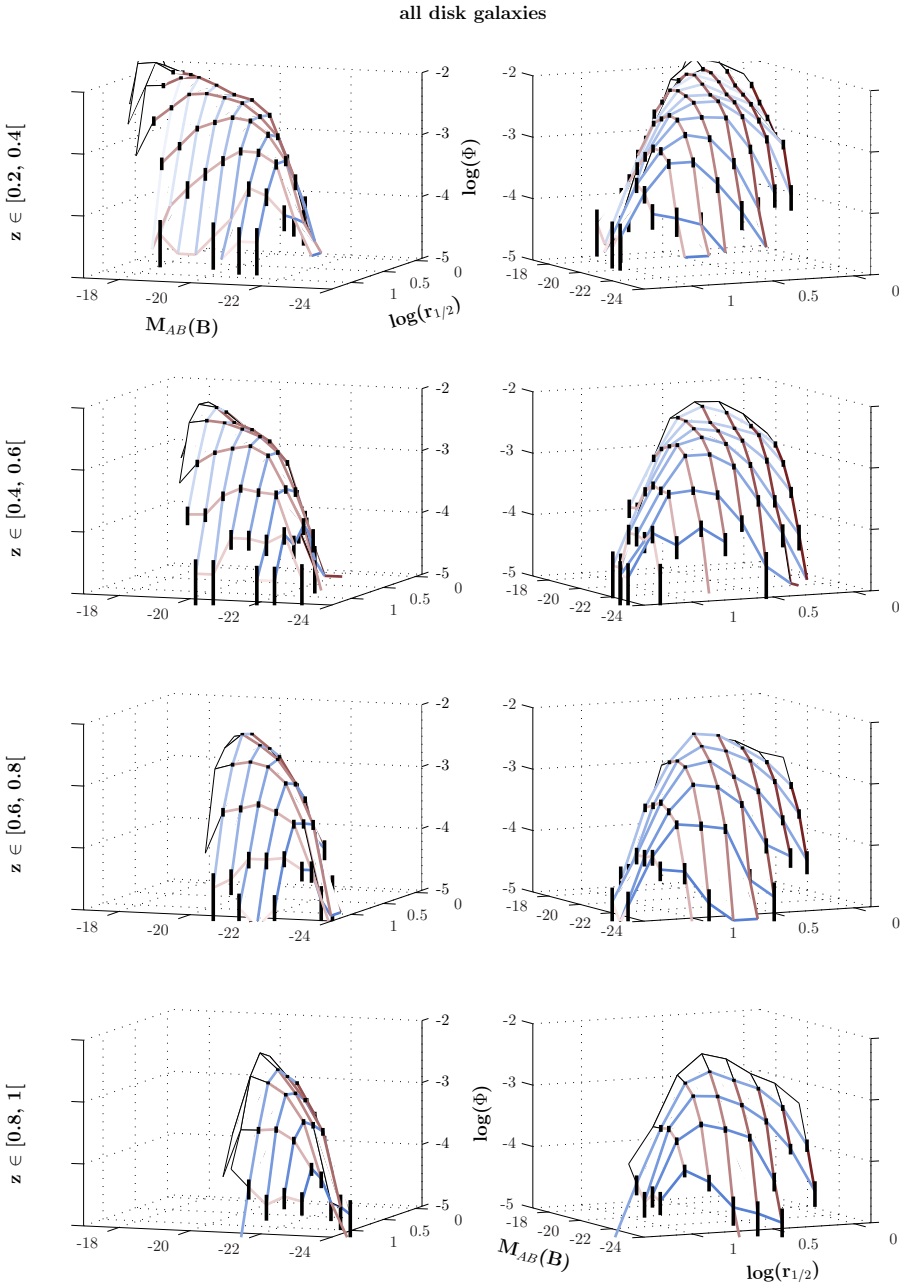

Fig. 4.12a — Evolution of the bivariate size-luminosity distribution of the entire disk galaxy population since $z \sim 1$. Views approximately parallel to the size axis (*panel on the left*) and to the magnitude axis (*right*) are shown. Lines of constant radius are plotted in shades of red (growing lighter for larger sizes) and lines of constant magnitude in shades of blue (growing darker with increasing luminosity) in those regions of the plot where the sample is complete. Poissonian errors (cf. equation (4.9)) on the measurements in the complete regions of the plot are marked with a vertical black bar.

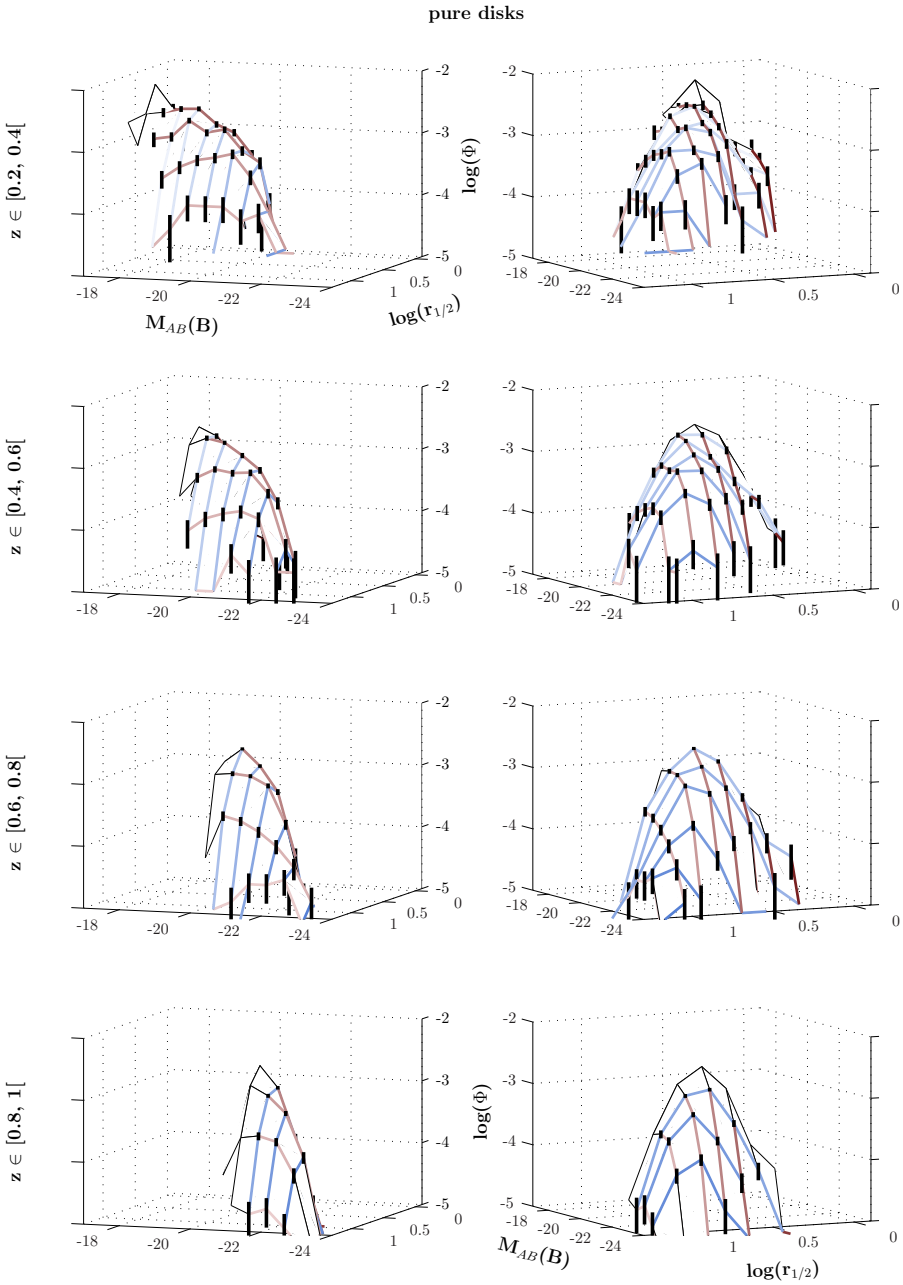

Fig. 4.12b — Evolution of the bivariate size-luminosity distribution of pure disk galaxies since $z \sim 1$. Colour schemes and projections as in Figure 4.12a.

- the smallest disk galaxies alone – and in particular those with a small or intermediate bulge component – determine the shape of the faint end slope of the luminosity function. The distribution of rest-frame absolute B-band magnitudes at a given size reflects the spread in surface brightness values and Figure 4.12 thus shows that both large objects with low surface brightness and small objects with high surface

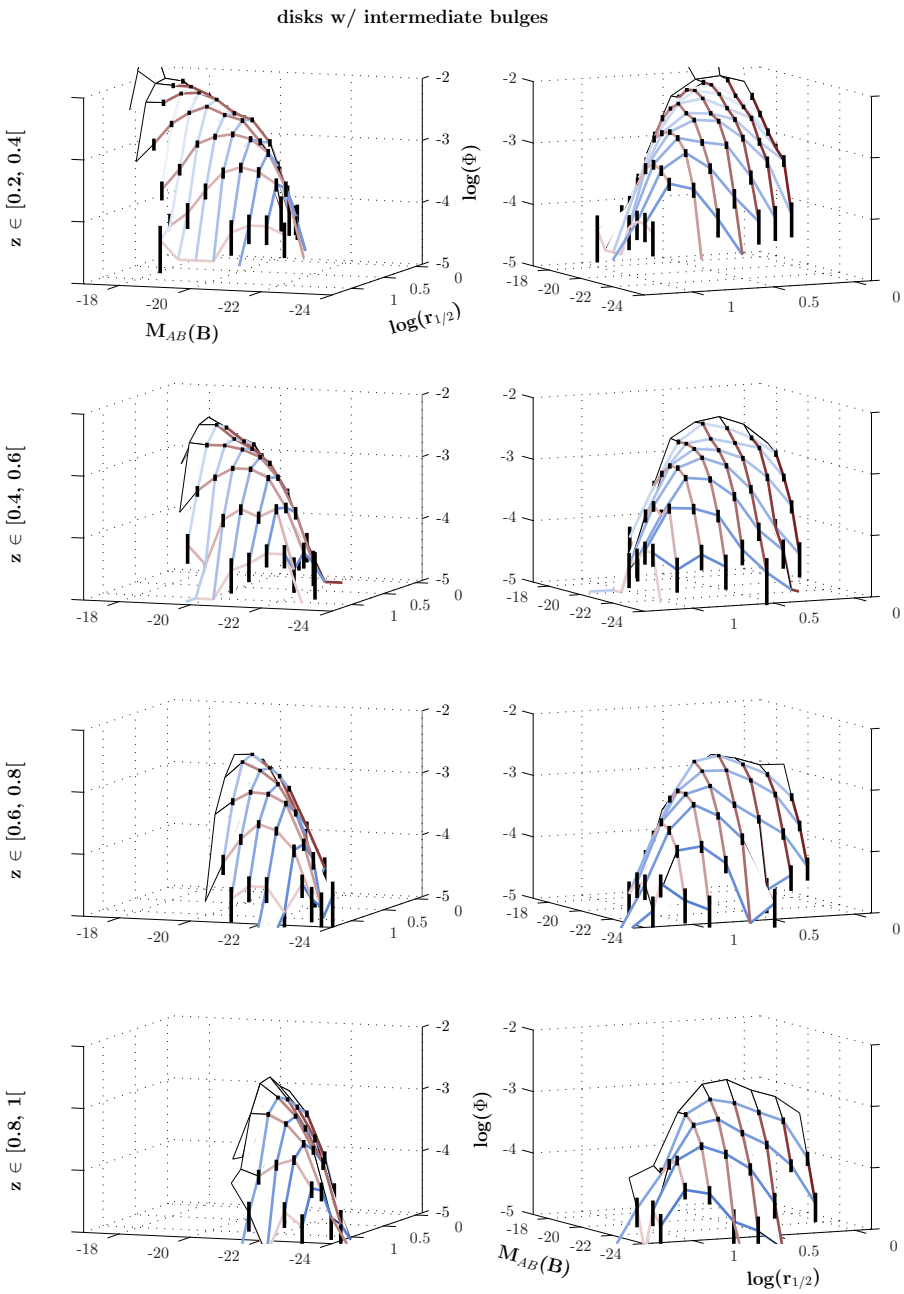

Fig. 4.12c — Evolution since $z \sim 1$ of the bivariate size-luminosity distribution of disk galaxies with intermediate bulge components. Colour schemes and projections as in Figure 4.12a.

brightness are rare.

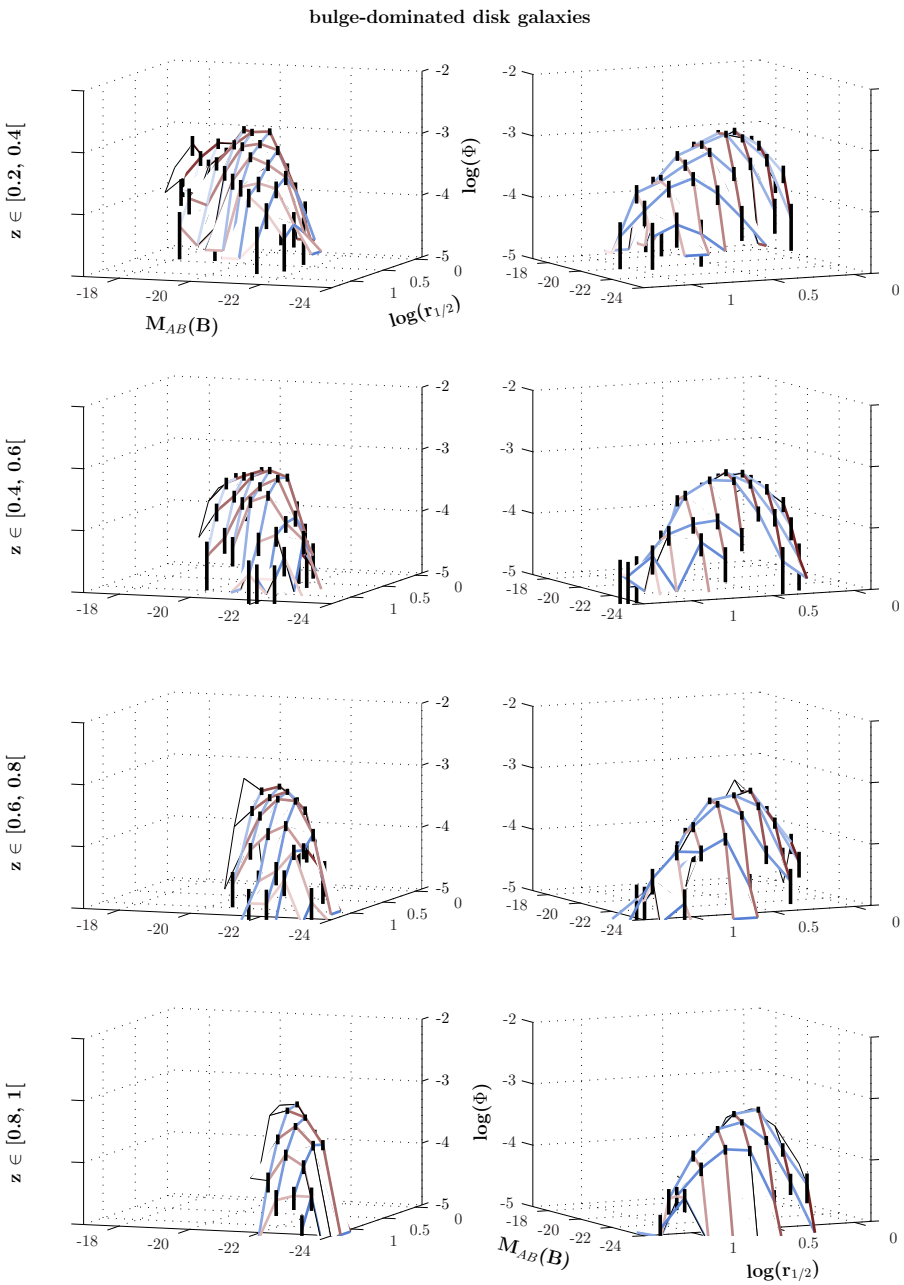

Fig. 4.12d — Evolution since $z \sim 1$ of the bivariate size-luminosity distribution of bulge-dominated disk galaxies. Colour schemes and projections as in Figure 4.12a.

4.4.2 Analytic parametrization of the bivariate size-luminosity function

We assume that the bivariate size-luminosity function can be described by the product of a distribution in luminosity - the Schechter function - and a log-normal distribution in size

at fixed luminosity (see also Chołoniewski [23], de Jong and Lacey [29], Ferguson et al. [44] and Ravindranath et al. [94]):

$$\Phi(L, r_{1/2})\ dL\ dr_{1/2} = \Phi^* \left(\frac{L}{L^*}\right)^{\alpha} \exp\left(-\frac{L}{L^*}\right) \frac{dL}{L^*} \times \frac{1}{\sqrt{2\pi}\sigma_{r_{1/2}}} \exp\left(\frac{(-1)\left[\ln\left((r_{1/2}/r^*_{1/2})(L/L^*)^{\beta}\right)\right]^2}{2\sigma_{r^2_{1/2}}}\right) \frac{dr_{1/2}}{r_{1/2}} \ . \tag{4.10}$$

Rewritten in terms of magnitude this expression becomes

$$\Phi(M,\log(r_{1/2}))\ dM\ d\log(r_{1/2}) = 0.4\ \ln(10)^2\ \Phi^* 10^{-0.4(\alpha+1)(M-M^*)} \exp\left(-10^{-0.4(M-M^*)}\right) dM \times \frac{1}{\sqrt{2\pi}\sigma_{r_{1/2}}} \exp\left(\frac{(-1)\left[\log(r_{1/2}/r^*_{1/2}) - 0.4\beta(M-M^*)\right]^2}{2(\sigma_{r_{1/2}}/\ln(10))^2}\right) d\log(r_{1/2}) \ . \tag{4.11}$$

The underlying assumption in this parametrization is that the most important factor that determines the sizes of disk galaxies is the angular momentum of their host halo which simulations of hierarchical clustering show to be drawn from a log-normal distribution. Further assumptions include that: (i) the disk circular velocity is equal to that of its singular isothermal halo; (ii) the disk mass M_D is a universal fraction of the total baryonic mass in the halo; (iii) disk mass and luminosity are related by $M_D \propto L^{\gamma}$ with $\gamma \approx 1$. Using the prediction that the mass of dark matter halos is proportional to the cube of the circular velocity, $M_{\rm DM} \propto v_c^3$, the median disk radius $r^*_{1/2}$ which shifts the log-normal component in equation (4.11) is expected to vary with luminosity as $r^*_{1/2} \propto L^{\beta} \sim L^{-1/3}$.

We fit the bivariate size-luminosity function described by equation (4.11) to both the disk galaxy population as a whole and to its individual B/D-categories in two steps. First we determine for each redshift bin the values of Φ^*, α and M^* by fitting a Schechter function to the luminosity functions of our disk galaxies. As implied by the results of Scarlata et al. [103], the luminosity function of COSMOS disk galaxies is unchanged apart from brightening due to a passively aging stellar population over the redshift range $z \in [0,\ 1[$. We therefore fix the faint end slope α to the value derived for the lowest redshift bin with $z \in [0.2,\ 0.4[$ because the faint disk galaxy population is sampled best in this redshift range. Within the errorbars, the values of M^* for the luminosity functions shown in solid lines are consistent with the values found by Scarlata et al. [103] at $z \sim 0.7$ in the COSMOS survey and Willmer et al. [136] with data from the DEEP2 spectroscopic survey (Davis et al. [28]). In the second step we use the values of Φ^*, M^* and α as

Tab. 4.12 — Best fit parameter values of the analytic form of the bivariate size-luminosity function (equation (4.11) in manuscript) for COSMOS disk galaxies in different bins of redshift.

category	redshift	Φ^*	α	$M^*(B)$	$r^*_{1/2}$ [kpc]	$\sigma_{r_{1/2}}$	β
type 2	$z \in [0.2, 0.4[$	0.0052±0.0003	-1.05±0.03	-20.64±0.05	4.21±0.04	0.42±0.01	-0.301±0.006
	$z \in [0.4, 0.6[$	0.0036±0.0001	-1.05±0.03	-20.71±0.03	3.96±0.03	0.44±0.01	-0.331±0.010
	$z \in [0.6, 0.8[$	0.0043±0.0001	-1.05±0.03	-20.89±0.02	3.79±0.02	0.42±0.01	-0.335±0.011
	$z \in [0.8, 1[$	0.0045±0.0002	-1.05±0.03	-21.04±0.03	3.37±0.05	0.44±0.01	-0.355±0.025
type 2.3	$z \in [0.2, 0.4[$	0.0016±0.0002	-0.92±0.09	-19.79±0.12	3.98±0.05	0.33±0.01	-0.253±0.013
	$z \in [0.4, 0.6[$	0.0014±0.0001	-0.92±0.09	-20.16±0.04	4.31±0.04	0.32±0.01	-0.267±0.018
	$z \in [0.6, 0.8[$	0.0025±0.0001	-0.92±0.09	-20.34±0.04	4.06±0.04	0.30±0.01	-0.335±0.019
	$z \in [0.8, 1[$	0.0027±0.0003	-0.92±0.09	-20.60±0.05	3.83±0.12	0.29±0.01	-0.405±0.039
type 2.2/	$z \in [0.2, 0.4[$	0.0036±0.0003	-1.10±0.03	-20.47±0.07	4.12±0.05	0.42±0.01	-0.331±0.008
type2.1	$z \in [0.4, 0.6[$	0.0022±0.0001	-1.10±0.03	-20.65±0.04	3.83±0.04	0.44±0.01	-0.395±0.013
	$z \in [0.6, 0.8[$	0.0023±0.0001	-1.10±0.03	-20.87±0.03	3.51±0.03	0.44±0.01	-0.459±0.017
	$z \in [0.8, 1[$	0.0019±0.0001	-1.10±0.03	-21.13±0.04	3.12±0.06	0.43±0.01	-0.457±0.037
type 2.0	$z \in [0.2, 0.4[$	0.0017±0.0001	0.27±0.09	-20.20±0.08	2.92±0.04	0.41±0.01	-0.499±0.019
	$z \in [0.4, 0.6[$	0.0007±0.0001	0.27±0.09	-20.34±0.04	2.61±0.04	0.37±0.01	-0.461±0.020
	$z \in [0.6, 0.8[$	0.0006±0.0001	0.27±0.09	-20.69±0.03	2.56±0.04	0.37±0.01	-0.502±0.024
	$z \in [0.8, 1[$	0.0006±0.0001	0.27±0.09	-20.74±0.04	2.11±0.08	0.36±0.01	-0.507±0.042

the starting point to derive the parameters of the size-component of the bivariate size-luminosity function. The values of the best-fitting parameters (obtained by a non-linear χ^2 minimization carried out with the Levenberg-Marquardt method) are given in Table 4.12. Following the usual interpretation of the diagonal elements of the covariance matrix $\mathcal{C}_{ij}$ as the σ^2 of the fitted parameter, the stated errors associated with the best-fit parameters of the analytic bivariate size-luminosity function correspond to $\sqrt{\mathcal{C}_{ii}}$.

In Figures 4.13a to 4.13d we show the density contours of the best-fitting bivariate size luminosity function superimposed on the observed bivariate size-luminosity distribution. The intensity of the colour scale and grey scale with which the data are plotted reflects the comoving space density of objects with a given size and luminosity. Shades of grey are used where the sample is not complete with respect to magnitude, and colours are used in regions where the sample is complete. We define the completeness limits as the faintest observable magnitude at the centre of each redshift slice (see also Figure 4.1) and use only these regions of parameters space to derive the best fit the bivariate size-luminosity function in equation (4.11).

The comparison of the contours and the pixelated intensity scale in Figure 4.13 shows that the analytic parametrization is a fair representation of the data. An assessment of Figures 4.13a to 4.13d and the best-fitting parameters in Table 4.12 reveals that:

- The exponent β which describes how the mode of the log-normal size component scales with luminosity, i.e., $r^*_{1/2} \propto L^\beta$, decreases as a function of redshift in all disk galaxy samples except the most bulge-dominated disk galaxies where it does not change noticeably between $z \sim 1$ and 0.2. The evolution in the other two B/D-

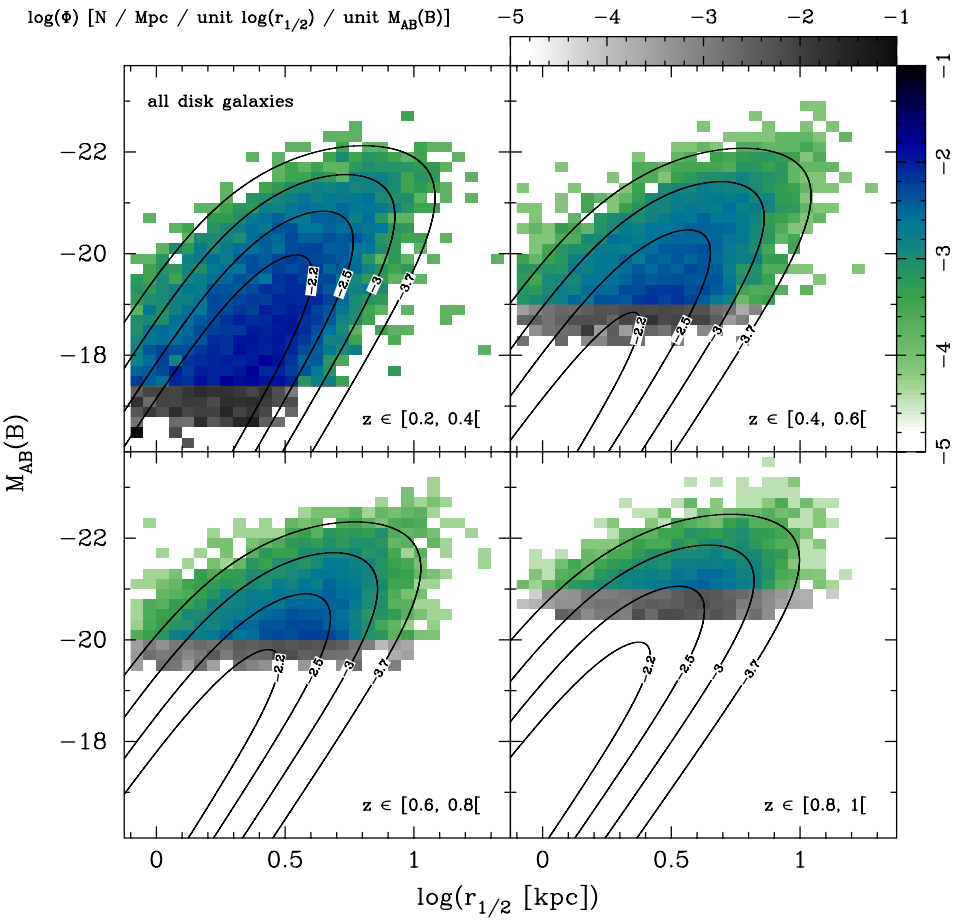

Fig. 4.13a — Contours of the best-fitting bivariate size-luminosity function (cf. equation (4.11)) derived from the fit to the total disk galaxy population in four redshift bins. The contours are 2×10^{-4}, 10^{-3}, 3.2×10^{-3} and 6.3×10^{-3} Mpc^{-3} log$(r_{1/2})^{-1}$ mag^{-1}. Behind the contours of the analytic bivariate size-luminosity function we show the bivariate size-luminosity distribution colour-coded in shades of grey where the sample is not complete with respect to magnitude. Completeness limits are set at the faintest observable magnitude at the centre of each redshift slice (cf. Figure 4.1). The intensity of the colour scale and grey scale reflects the comoving space density of objects with a given size and luminosity.

categories with respect to the value at $z \sim 1$ is approx 40% (bulgeless disks) and 30% (disks with intermediate bulges) and it manifests itself by a steepening of the contours with respect to the size-axis as one goes to lower redshift in Figures 4.13b and 4.13c. The tendency is also present in the whole sample including disk galaxies of all B/D-ratios (cf. Figure 4.13a) where the change amounts to 15% and values agree well with the theoretical (-1/3)-scaling (cf. first paragraph of this section).

- The widths of the log-normal distribution, $\sigma_{r_{1/2}}$ are smaller for pure disks than for

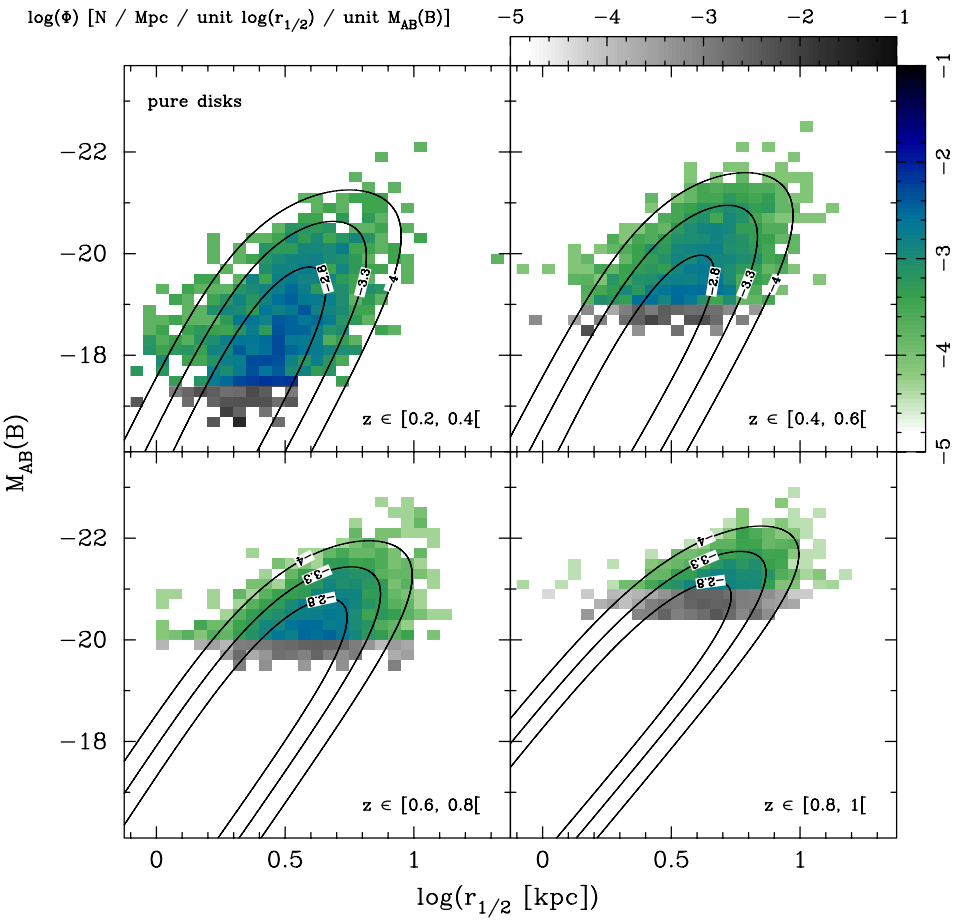

Fig. 4.13b — As in the preceding figure but using only a subset of pure disk galaxies.

bulged systems. For a given disk galaxy sample $\sigma_{r_{1/2}}$ remains more or less constant as a function of redshift and ranges from 0.3 to 0.4.

The evolution of characteristic sizes and luminosities – as expressed by $r^*_{1/2}$ and M^* – can be estimated from the horizontal and vertical shifts of the contour levels as a function of redshift. As can also be seen in Table 4.12 the values of $r^*_{1/2}$ hardly change in the range $z \in [0.2, 1[$ for the bulgeless disk population. In contrast, $r^*_{1/2}$ increases with cosmic time both in the total disk galaxy population and in the B/D-categories with non-negligible bulges.

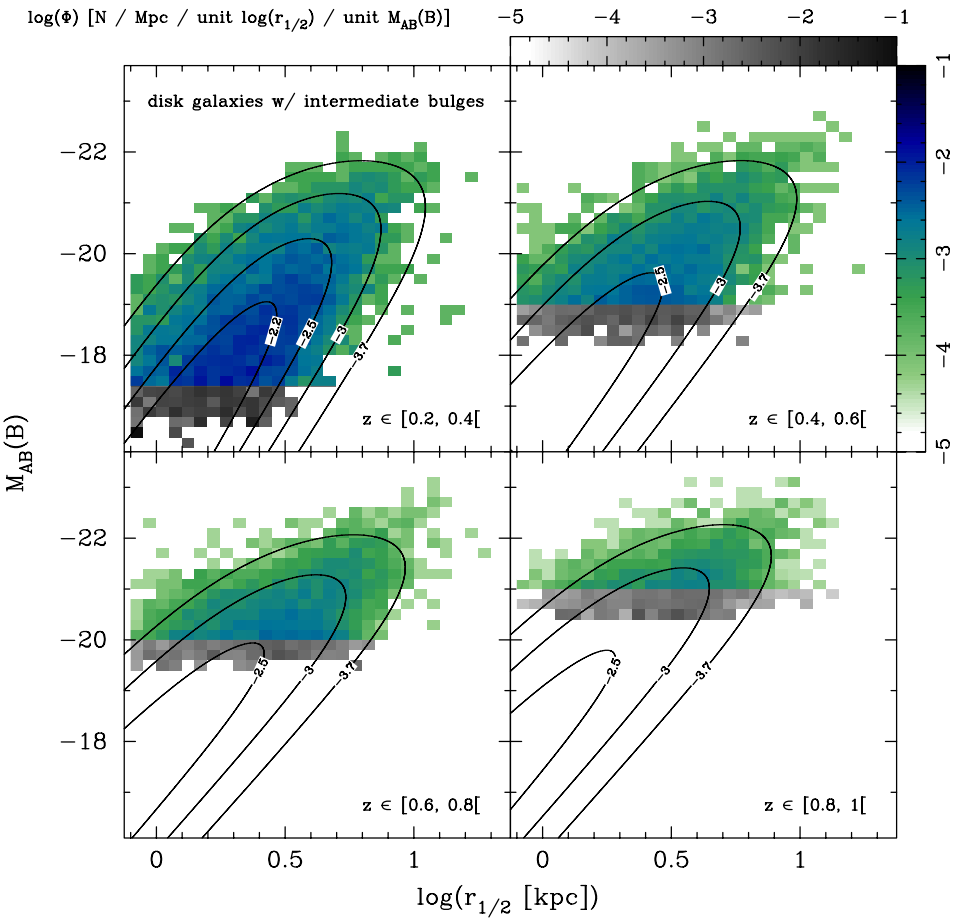

Fig. 4.13c — As in Figure 4.13a but for disk galaxies with intermediate bulges.

4.4.3 Luminosity-dependent evolution of disk galaxy sizes at $z < 1$

In Section 4.4.1 we already briefly considered some global properties in the shape of the surface defined by the bivariate size-luminosity function $\Phi(M, \log(r_{1/2}), z)$. In this section we assess the evolutionary changes in the disk galaxy population as a whole and in the different B/D-categories in more detail. These may manifest themselves as either shifts or changes in curvature of the surface $\Phi(M, \log(r_{1/2}), z)$.
Focusing on the disk galaxy population as a whole (see Figures 4.12a and 4.13a), we observe that:

- The normalization of $\Phi(M, \log(r_{1/2}), z)$ for all but the largest disk galaxies has remained almost unchanged since $z \sim 1$. Only the surface at $z \in [0.2,\ 0.4[$ is raised above the others which most likely is caused by the well-known large overdensity in the COSMOS field around $z \sim 0.3$ (the increased density in this redshift slice is also evidenced by the generally higher values of Φ^* from the luminosity function

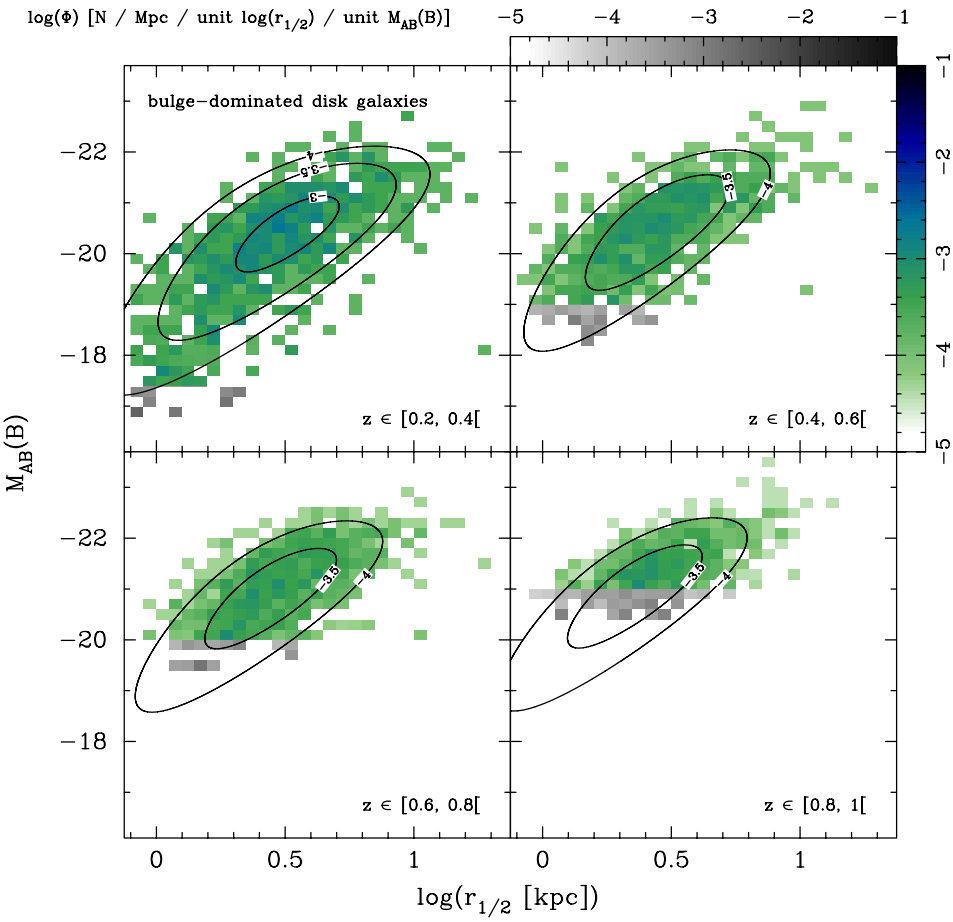

Fig. 4.13d — As in Figure 4.13a but for bulge-dominated disk galaxies.

fits of the previous section). We conclude that the population of disk galaxies with $r_{1/2} \leq 7$ kpc (i.e. $\log(r_{1/2}) \lesssim 0.9$) has experienced virtually only evolution along the magnitude axis (as evidenced by the rib lines at constant size which shift to brighter magnitudes as one goes to higher redshift). The amount of luminosity evolution is about 1 mag with a tendency to be larger in smaller galaxies than in large ones.

- The horizontal offset between the rib lines at constant magnitude (see Figure 4.12a) and the shifting of the contours in Figure 4.13a is evidence for increasing sizes in the disk galaxy population; the size evolution is larger at higher luminosities. Moreover, it appears that the slope of the size distribution at large sizes ($\log(r_{1/2}) \geq 0.8$) steepens at higher redshift as would be expected if the largest galaxies were rarer than they are today. This steepening appears only in the brightest magnitude bins.

- The number density of the brightest objects (i.e. those with $M(B) \leq$ -22) has decreased since $z \sim 1$. This is a consequence of the shift to higher luminosities of the magnitude distributions mentioned in the first point.

With Figures 4.12b to 4.12d and 4.13b to 4.13d we can repeat the analysis for disk galaxies with different B/D-ratios:

- Disk galaxies with intermediate bulges show features similar to those that characterize the evolution of the total disk galaxy population, namely; (i) the evolution of the luminosity as a function of redshift, and (ii) the shift of the size distributions at constant magnitude and – to a lesser extent – (iii) the increasing number of large objects as one goes from high to low redshift.

- There is a clear rise towards lower redshifts in the number density of bulge-dominated disks.

- A striking difference exists between bulgeless disks and disks with bulges: Whereas the former show a more or less constant or increasing number density at a given magnitude from $z = 0$ to higher redshift, the trend is inverted for disks with bulges. Bulgeless disk galaxies were more frequent at high redshift than they are today. The declining number density of these objects is distinguishable in the left-hand column of Figure 4.12b. It is also obvious, however, that luminosity evolution has occurred in pure disks just as it has in all the other disk galaxy categories.

To further inspect the origin of the observed trends we study the changes in characteristic size and abundance of galaxies in bins of evolving luminosity. The binning is chosen such as to follow the evolution of M^* in the B-band which is about 1 mag since $z \sim 1$ for pure disks, disk galaxies with intermediate bulges and bulge-dominated disks and approx. 0.7 for the total population (cf. Table 4.12). The results are illustrated in Figures 4.14a and 4.14b. Our magnitude bins are defined by $M(B) + z \in [M_{\rm min},\ M_{\rm max}[$ where $M_{\rm min}$ and $M_{\rm max}$ are the bright and faint magnitude limit of the bin, respectively. Bin limits are chosen such that the faint magnitude limit of the intermediate luminosity bin, $M(B)+z \in$ [-21.1, -20.1[, coincides with the magnitude completeness limit in the highest redshift slice. Doing so provides us with two luminosity bins in which we can follow disk evolution over the whole redshift range since $z \sim 1$ and one fainter bin which is fairly complete out to $z \sim 0.8$. (In fact, completeness is not perfect in the redshift slice $z \in [0.6,\ 0.8[$ where the faintest of the three magnitude bins includes objects with $M(B) + z \in$ [-19.8, -20.8[while the completeness limit is at $M(B) =$ -20.)

We define the "characteristic size" as the size-coordinate, $\mathcal{R}_{\rm bary}$, of the barycentre of the bivariate size-luminosity function $\Phi(M(B), \log(r_{1/2}), z)$ in a given evolving luminosity bin. The barycentre $\mathcal{R}_{\rm bary}$ is calculated by weighting the coordinate of each size-bin centre, $\log(r_{1/2,i})$, with the value of the bivariate size-luminosity function at that position (for all absolute magnitudes $M(B)_j$ within the magnitude range defined by the magnitude bin limits $M_{\rm min}$ and $M_{\rm max}$):

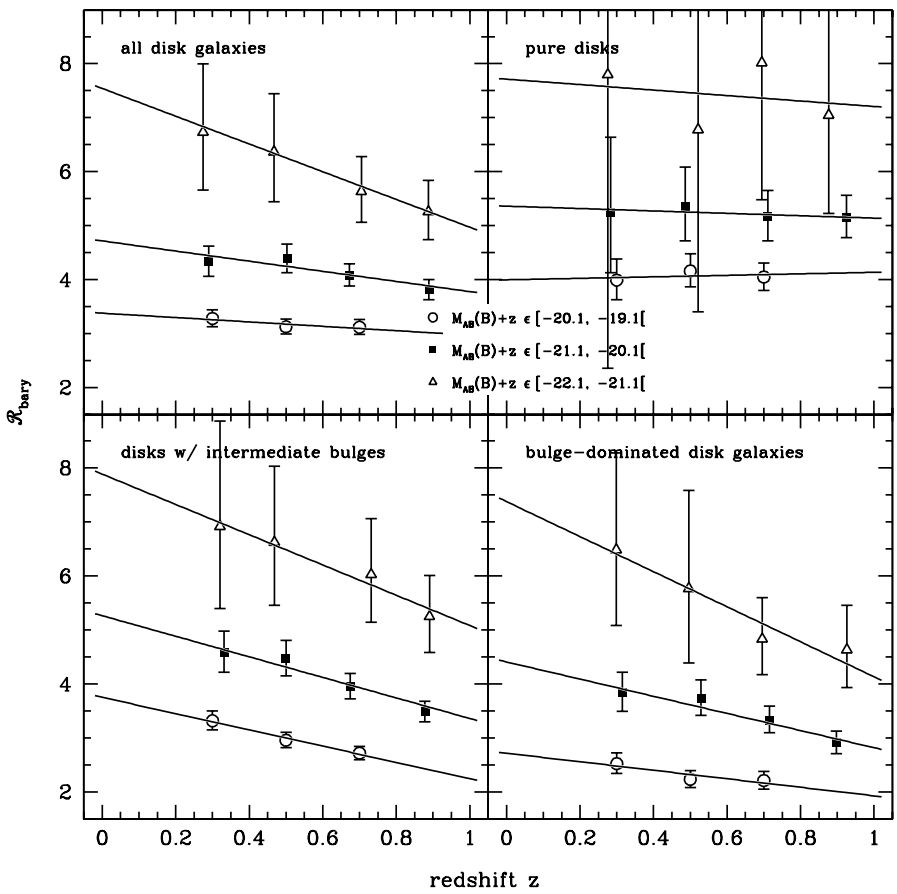

Fig. 4.14a — Evolution with redshift of the barycentre $\mathcal{R}_{\rm bary}$ of the bivariate size-luminosity function within three evolving magnitude bins (see legend). The evolution of the magnitude bins matches the amount of luminosity evolution observed in the bivariate size-luminosity function (cf. Figures 4.12 and 4.13 or Table 4.12). Triangles, squares, and circles denote the measurements in the brightest, intermediate and faintest bin studied. The faintest magnitude bin is not plotted for the highest redshift slice as it is not complete.

$$\mathcal{R}_{\rm bary} = \frac{\displaystyle\sum_{\substack{r_i \\ M_j+z\in[M_{\rm min},\ M_{\rm max}[}} \log(r_{1/2,i}) \times \Phi(M(B)_j, \log(r_{1/2,i}), z)}{\displaystyle\sum_{\substack{r_i \\ M_j+z\in[M_{\rm min},\ M_{\rm max}[}} \Phi(M(B)_j, \log(r_{1/2,i}), z)} \ . \tag{4.12}$$

Figure 4.14a shows the values of $\mathcal{R}_{\rm bary}$ for different luminosity bins and as a function of redshift. In Figure 4.14b we plot the value of the bivariate size luminosity function at

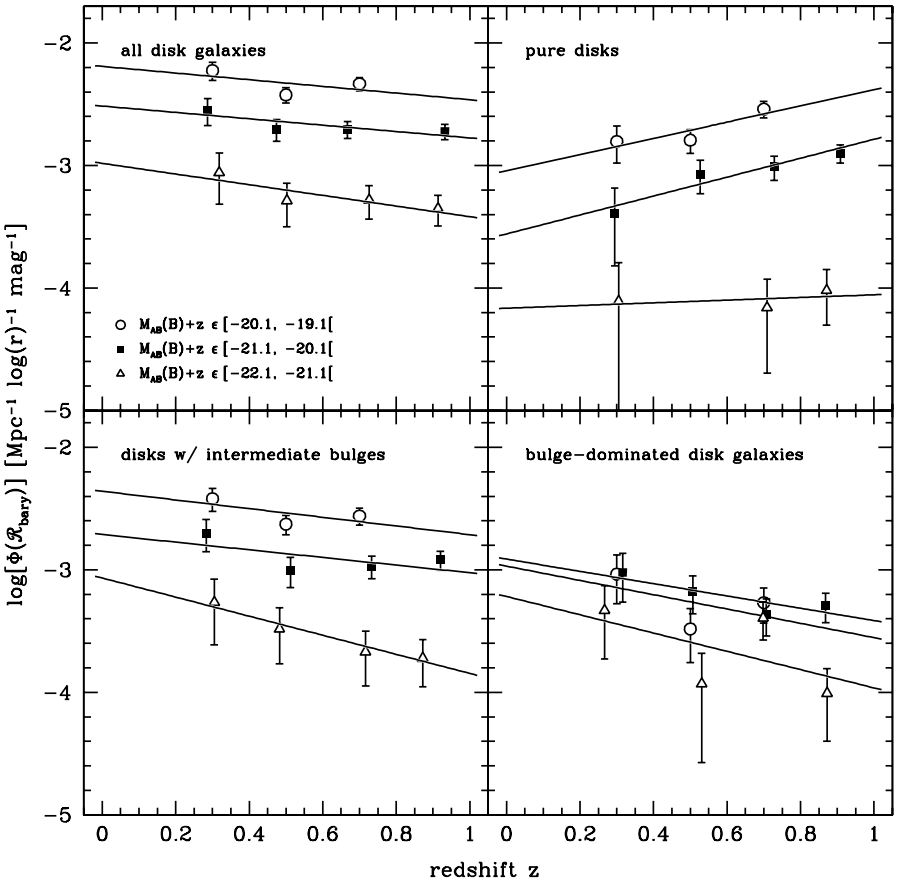

Fig. 4.14b — Evolution with redshift of the comoving space density at the barycentre $\mathcal{R}_{\rm bary}$ of the bivariate size-luminosity function within evolving magnitude bins. The luminosity evolution of the magnitude bins matches that observed in the bivariate size-luminosity function (cf. Figures 4.12 and 4.13 or Table 4.12). All symbols as in Figure 4.14a.

the position of the barycentre. Consideration of these two figures confirms that:

- In all three magnitude bins the value of $\mathcal{R}_{\rm bary}$ for pure disk galaxies has not changed as a function of redshift (see panel in the upper right corner of Figure 4.14a). This confirms the constancy of $r^*_{1/2}$, the mode of the log-normal size distribution of the analytic parametrization of the bivariate size-luminosity function, found in Section 4.4.2.
- For "bulged" disk galaxies the values of $\mathcal{R}_{\rm bary}$ consistently grow with cosmic time. The size evolution in a given evolving magnitude bin varies with luminosity in the sense that it is larger for more luminous objects. The gradient from low luminosity to high luminosity growth of $\mathcal{R}_{\rm bary}$ is steeper in bulge-dominated sources than in

disks with intermediate bulges (see lower two rows of Figure 4.14a). In the case of disk galaxies with intermediate bulges, the sizes in all magnitude bins were smaller by about 40% with respect to the present day value.

- In the disk galaxy population as a whole, and in the bulged disk galaxies, the detected size evolution is only about 10% in the range $M(B) + z \in$ [-20.1, -19.1[and 20% if $M(B) + z \in$ [-21.1, -20.1[. It reaches 30% for the brightest objects with $M(B) + z \in$ [-22.1, -21.1[. In the case of the bulge-dominated galaxies the evolution of characteristic sizes depends on luminosity in the same way but is raised by 10-15% with respect to the total population.
- The number density of the total disk galaxy population at the characteristic radius $\mathcal{R}_{\rm bary}$ has remained nearly constant in all luminosity bins out to $z = 1$ (see upper left quarter of Figure 4.14b).

Summarizing, the constancy of the number density in different luminosity bins is the result of a modestly increasing number density of disk galaxies with a non-negligible bulge component (lower half of Figure 4.14b) and a declining number density of the bulgeless disks over the same range in redshift.

4.5 The role of environment

4.5.1 Estimation of environmental density

The large statistical sample provided by COSMOS, and the large volume covered by the survey, which probes all relevant scales of the large-scale structure, allows us to investigate for the first time how the evolution of the disk galaxy population described above depends on the environmental density. In this section we give a short overview of the most important concepts and steps involved in the calculation of the density field (see Carollo et al. (2008; in preparation) for details).

When estimating densities for a survey based on a magnitude limited catalog one faces the problem of non-uniform sampling in redshift due to the cut in apparent magnitude. To compensate that the mean density $\langle\rho\rangle$ of catalogued objects at low redshift is far higher than at high redshifts we apply the $V_{\rm max}$ formalism. After computing the accessible volume for each galaxy the mean density at each redshift follows from (i) summing the reciprocal of the value of $V_{\rm max}$ for all galaxies with physical properties such that they could have been observed at that distance, and (ii) dividing this sum by the number of galaxies contributing to it. As the density estimation supplies absolute density values ρ, it is then possible to derive overdensities $\delta = \rho/\langle\rho\rangle - 1$ on an individual basis for each galaxy.
For the density estimation proper, the approach of kernel estimation is adopted which necessitates no prior assumptions about a parametric form for the sought probability density function. The kernel $K(x)$ is effectively a probability density which satisfies

$$\int K(x) d^n x = 1$$

where the integration is carried out over a specific part of the n-dimensional parameter space being investigated (in the present case redshift z plus right ascension and declination (α, δ)). If the probability distributions within the individual dimensions of parameter space are independent the kernel may be written as a product kernel, i.e.

$$K(x) = \prod_{j=1}^{n} K_j(x_j) \ .$$

In our case we assume statistical independence between z and (α, δ) such that the kernel becomes

$$K(z, \alpha, \delta) = \sum_{k=1}^{N_g} K(\alpha - \alpha_k, \delta - \delta_k) K_k(z) \ , \tag{4.13}$$

where the summation over k reflects that each of the N_g galaxies in the catalog has different coordinates (α_k, δ_k) on the sky and a different probability distribution with distance which is described by the kernel $K_k(z)$. $K_k(z)$ incorporates the information of the redshift distribution of the objects resulting from running ZEBRA on the catalog and the angular kernel K(α,δ) is an as yet unspecified kernel that is used to estimate the density in thin redshift slices of width dz. In the present analysis an Epanechnikov kernel (Epanechnikov [39]) was chosen which is a kernel of finite support combining the properties of a top hat and a Gaussian kernel. Its shape is described by

$$K(\alpha, \delta | R_E) = \begin{cases} \frac{2}{\pi R_E^2} \left(1 - r^2/R_E^2\right) & \text{if } r < R_E \\ 0 & \text{otherwise} \ , \end{cases} \tag{4.14}$$

with $r = \sqrt{\alpha^2 + \delta^2}$ and a cut-off scale of 3.5 Mpc. This size was found to reproduce the density distribution well in density estimation trials using mock catalogs specially produced for the COSMOS field (Bschorr et al. 2008, in preparation). The mock catalogs provide known redshift distributions and artificial photometry such that the entire procedure of density calculation (including the redshift estimation with ZEBRA) can be simulated in a reliable way.

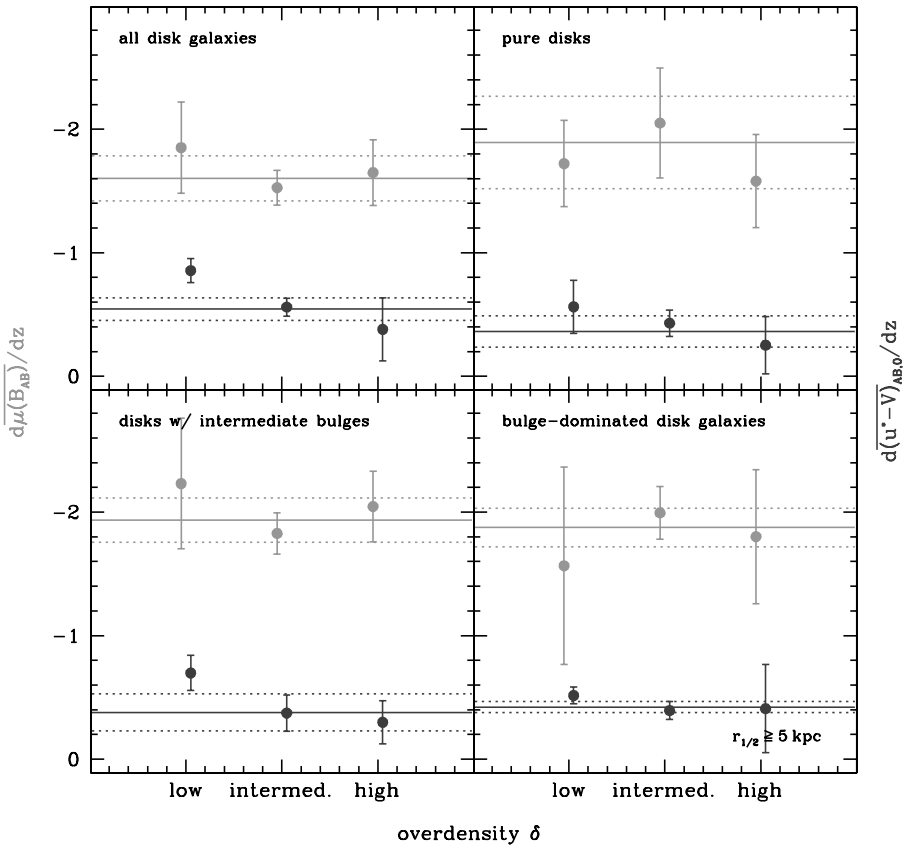

Fig. 4.15a — Variation of the evolution of rest-frame B-band effective surface brightness $\overline{\mu(B)}$ (light grey) and rest-frame $(u^* - V)$-colour (dark grey) with the density of the environment (using all sources with $r_{1/2} \geq 5$ kpc). The slopes $d\overline{\mu(B)}/dz$ and $d\overline{(u^* - V)}_0/dz$ represent the best-fitting linear trend to the evolution of the median values of surface brightness and colour in different environments. In each panel the solid horizontal line gives the evolution of the pertinent disk galaxy sample averaged over all environments. Dashed lines denote the uncertainty in the evolution in the total disk galaxy population. The evolutionary trends shown are computed by taking the average evolution observed for the cases where (i) percentiles are computed individually for each redshift bin, and (ii) the percentiles are computed for the entire range $z \in [0.2, 1[$.

4.5.2 Results

In Figures 4.15a and 4.15b we show the slopes of the best-fitting linear evolutionary trends to the values of the median surface brightness $\overline{\mu(B)}$ and median rest-frame colour $\overline{(u^* - V)}_0$ as a function of environmental density. The evolution of surface brightness and galaxy colour is calculated in a similar way as described in Sections 4.3.2 and 4.3.3, respectively. However, here we do not use the local $\mathrm{SDSS}_{z=0.7}$ comparison sample to constrain the trend lines at $z \sim 0$, since no information on the environmental density is available for the

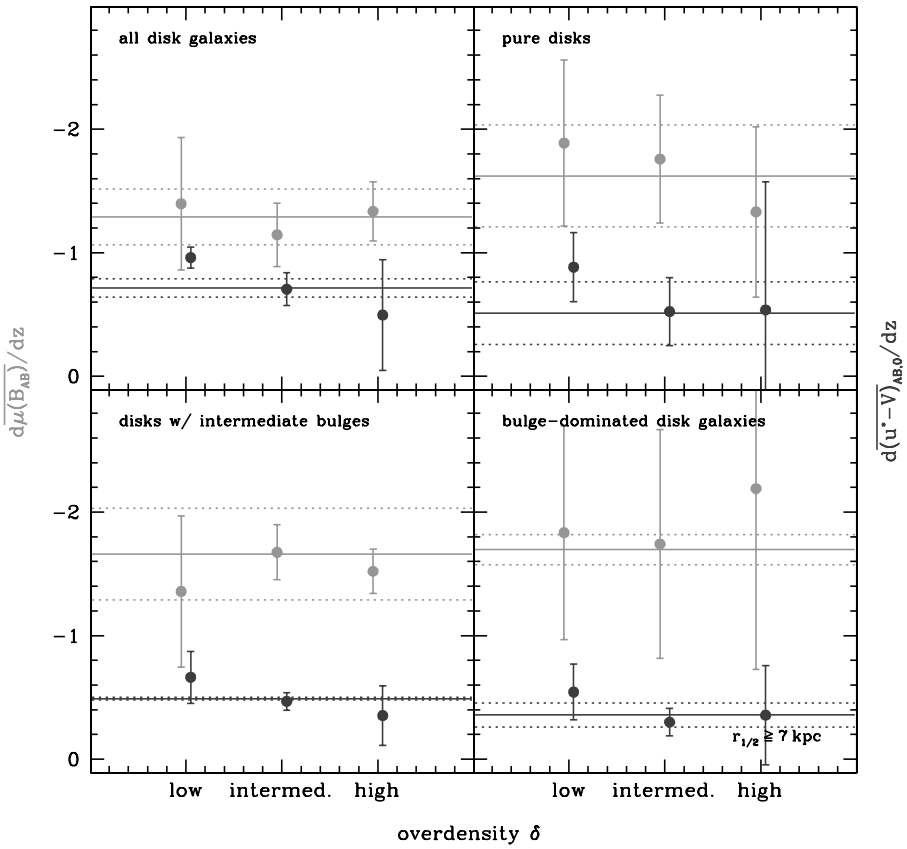

Fig. 4.15b — As in previous figure but for objects with $r_{1/2} \geq 7$ kpc.

SDSS dataset. We define a region to be of high or low density if its environmental density lies above the 75$^{\rm th}$ or below the 25$^{\rm th}$ percentile of the distribution of measurements of comoving overdensity δ, respectively. Those parts of the overdensity distribution which lie between the 25$^{\rm th}$ and 75$^{\rm th}$ percentile have been termed "intermediate". The evolutionary trends shown in Figure 4.15 are computed by averaging the evolution obtained if high and low density are defined as either (i) from the distribution of overdensites over the entire redshift range $z \in [0, 1[$, or (ii) from the distribution of overdensities in each of the four redshift slices $z \in [0.2, 0.4[$, $[0.4, 0.6[$, $[0.6, 0.8[$ and $[0.8, 1[$ individually (implying in the latter case that the division of low, intermediate and high density regions occurs at different values of δ in each bin of redshift).

In Figure 4.15a, the evolutionary trend for the rest-frame B-band effective surface brightness, $d\overline{\mu(B)}/dz$, and for the rest-frame colour $d\overline{(u^* - V)}_0/dz$ are plotted in light and dark grey, respectively, for disk galaxies with $r_{1/2} \geq 5$ kpc. The horizontal lines (solid line – measured evolution; dotted lines – error on evolutionary trend) show the evolution of these two quantities if galaxies in all environments are included. The symbols with error bars give the evolutionary estimates in regions of low, intermediate and high density, plotted from left to right along the horizontal axis. The same formalism is used in Figure

4.15b, which plots similar quantities for the sample with half-light radius larger than 7 kpc.

While surface brightness evolution is independent of environment the evolution of galaxy colours is clearly affected by it. In denser environments the colour evolution is reduced with respect to low density regions of the universe where it evolves most.

4.6 Discussion & conclusions

Using a sample of over 27,000 disk galaxies in the redshift interval $0.2 \leq z < 1$, distributed throughout the 1.64 deg^2 field of the COSMOS field, we find, consistent with previous work, that (1) the median surface brightness in the disk galaxy population has decreased by about 1-1.4 magnitudes since $z \sim 1$, and that (2) the luminosity evolution in the disks is due to an increased star formation rate at earlier epochs. Exploiting the large sample offered by COSMOS, we furthermore infer that the amount of surface brightness evolution over the past eight billion years is similar for all disks, independent of whether or not they host a bulge, and of the strength of the bulge-to-disk ratio. Changes in the relative abundance of bulged and bulgeless disks conspire to produce a weaker evolution in surface brightness in the disk galaxy population as a whole in comparison with the individual B/D-categories.

Our investigation of the bivariate evolution of the comoving number density of disk galaxies as a function of their luminosity and physical size shows that the typical sizes of bulgeless disk galaxies have hardly changed over the past eight billion years. The distribution of disk galaxies with a non-negligible bulge component on the other hand has continuously evolved toward larger sizes since $z = 1$ to today. Typical sizes of bulge-dominated galaxies have changed by about 30% over this time span. The evolution in size has been accompanied by a change in the relative number densities of galaxies with different B/D ratios: bulgeless disks have decreased in number density, while bulged disk galaxies have become more abundant, from $z \sim 1$ to $z = 0$.

Environment does play a role in the evolution of disk galaxies. The colour evolution of disks becomes progressively weaker, the denser the environment. In contrast, surface brightness and luminosity evolution depend weakly – if at all – on environment. This leads us to hypothesize that in the past disks in denser environments may have experienced a globally accelerated evolution compared to disks in low density environments. We will dedicate future work to testing this hypothesis.

4.7 Appendix: Errors on $\mu(B)$, $M(B)$, $r_{1/2}$ & $(u^* - V)_0$

1. The effective rest-frame B-band surface brightness is given by the expression

$$\mu(B) = C - 2.5\,\log\left(\frac{F}{2}\right) + 2.5\,\log\left(\pi R_{1/2}^2\right) + 2.5\,\log(q) - 10\,\log(1+z) - K_{F814W,B}(z)\ ,$$

where F is the total GIM2D flux, q the axis ratio and $K_{F814W,B}(z)$ the K-correction[2]. Propagation of errors results in an associated error of

$$\begin{aligned}\Delta\mu &= \left[\left(\frac{\partial\mu}{\partial F}\right)^2 \Delta F^2 + \left(\frac{\partial\mu}{\partial R_{1/2}}\right)^2 \Delta R_{1/2}^2 + \left(\frac{\partial\mu}{\partial q}\right)^2 \Delta q^2 + \left(\frac{\partial\mu}{\partial z}\right)^2 \Delta z^2\right]^{1/2} \\ &= \frac{2.5}{\ln(10)}\left[\left(\frac{\Delta F}{F}\right)^2 + 4\,\left(\frac{\Delta R_{1/2}}{R_{1/2}}\right)^2 + \left(\frac{\Delta q}{q}\right)^2 + 16\,\left(\frac{\Delta z}{1+z}\right)^2\right]^{1/2}\ .\end{aligned}$$

In deriving an expression for $\Delta\mu$ the error in the K-correction due to a false assignment of ZEBRA spectral type was not accounted for. It should, however, be small compared to the other contributions.

2. The rest-frame B-band absolute magnitude and its error are

$$M(B) = I - 5\,\log(D_L(z)) - K_{F814W,B}(z) - 25\ ,$$

and

$$\begin{aligned}\Delta M(B) &= \left[\left(\frac{\partial M}{\partial I}\right)^2 \Delta I^2 + \left(\frac{\partial M}{\partial D_L(z)}\right)^2 \Delta D_L^2\right]^{1/2} \\ &= \frac{2.5}{\ln(10)}\left[\left(\frac{\Delta F}{F}\right)^2 + 4\,\left(\frac{\Delta D_L(z)}{D_L(z)}\right)^2\right]^{1/2} \\ &= \frac{2.5}{\ln(10)}\left[\left(\frac{\Delta F}{F}\right)^2 + \left(\frac{(c/H_0)(1+z)}{D_L(z)\sqrt{\Omega_\Lambda + \Omega_m(1+z)^3}} + \frac{1}{1+z}\right)^2 \Delta z^2\right]^{1/2}\ .\end{aligned}$$

[2] The K-correction is defined through the equation $I = M(B) + 5\,\log(D_L(z)/10\ pc) + K_{I,B}$ (cf. Hogg et al. [57]).

Here it was used that $I = C - 2.5\log(F)$ and $D_L(z)$ is the luminosity distance. The error on the latter is calculated as follows:

$$\begin{aligned}
\Delta D_L(z) &= \Delta\left[(1+z)\cdot\frac{c}{H_0}\int_0^z \frac{dz}{\sqrt{\Omega_\Lambda+\Omega_m(1+z)^3}}\right] \\
&= \left(\frac{c}{H_0}\right)\left[\frac{(1+z)\ \Delta z}{\sqrt{\Omega_\Lambda+\Omega_m(1+z)^3}} + \Delta z\int_0^z \frac{dz}{\sqrt{\Omega_\Lambda+\Omega_m(1+z)^3}}\right] \\
&= \left[\frac{(c/H_0)(1+z)}{\sqrt{\Omega_\Lambda+\Omega_m(1+z)^3}} + \frac{D_L(z)}{1+z}\right]\Delta z\ .
\end{aligned}$$

3. The error in physical size, parametrized by the half-light radius in units of kpc, $r_{1/2} \propto D_A(z)\cdot R_{1/2}$, is

$$\begin{aligned}
\Delta r_{1/2} &= C\left[\left(\frac{\partial r_{1/2}}{\partial R_{1/2}}\right)^2 \Delta R_{1/2}^2 + \left(\frac{\partial M}{\partial D_A(z)}\right)^2 \Delta D_A^2\right]^{1/2} \\
&= C\left[\left(D_A(z)\ \Delta R_{1/2}\right)^2 + \left(R_{1/2}\ \Delta D_A(z)\right)^2\right]^{1/2} \\
&= C\ R_{1/2}\left[\left(\frac{\Delta R_{1/2}}{R_{1/2}}\right)^2 D_A(z)^2 + \left(\frac{(c/H_0)}{\sqrt{\Omega_\Lambda+\Omega_m(1+z)^3}} - D_A(z)\right)^2\left(\frac{\Delta z}{1+z}\right)^2\right]^{1/2}
\end{aligned}$$

where the uncertainty on the angular diameter distance $D_A(z)$ was computed analogously to that for $D_L(z)$ in point (2) and the constant C contains all factors used in the conversion from observed half-light radius in units of pixels to physical size expressed in kpc.

4. The error in the rest-frame colour $(u^* - V)_0$ is – in the worst case – the sum of the errors in the rest-frame u^*- and V-magnitudes. The error in the ground-based flux measurements is typically abound 0.05 mag, implying an error of order 0.1 on the rest-frame $(u^* - V)$-colour.

The uncertainty in GIM2D quantities contributing to the errors in $\mu(B)$, $M(B)$ and $r_{1/2}$ were estimated based on simulations presented in Section 2.1.3. We use the values listed below as upper estimates of the errors in GIM2D measurements. Errors are larger for objects with a steeper surface brightness profile. To account for this fact we specify errors separately for galaxies with a small or negligible bulge component and those with a large or moderate bulge. Since our simulations included only pure exponential disks and de Vaucouleur bulges the error for the bulged disks is derived by interpolating between these two categories; the error of the measurements for a non-negligibly bulged disk is

thus assumed to be that of a pure exponential disks plus half of the difference between the errors derived for a de Vaucouleur profile and an exponential disk.

- Axis ratio q: $\frac{\Delta q}{q} \approx 0.1$ for all objects, to a good approximation and independent of magnitude.
- Half-light radius $R_{1/2}$: $\frac{\Delta R_{1/2}}{R_{1/2}} \approx 0.15$ for type 2.3 and 2.2 disk galaxies
  $\frac{\Delta R_{1/2}}{R_{1/2}} \approx 0.225$ for type 2.1 and 2.0 disk galaxies
- Total flux F: $\frac{\Delta F}{F} \approx 0.1$ for disk galaxies of type 2.3 and 2.2 with $I < 20.5$
  $\frac{\Delta F}{F} \approx 0.15$ for disk galaxies of type 2.1 and 2.0 with $I < 20.5$
  $\frac{\Delta F}{F} \approx 0.15$ for disk galaxies of type 2.3 and 2.2 with $I \in [20.5, 21.5]$
  $\frac{\Delta F}{F} \approx 0.225$ for disk galaxies of type 2.1 and 2.0 with $I \in [20.5, 21.5]$
  $\frac{\Delta F}{F} \approx 0.25$ for disk galaxies of type 2.3 and 2.2 with $I > 21.5$
  $\frac{\Delta F}{F} \approx 0.324$ for disk galaxies of type 2.1 and 2.0 with $I > 21.5$.

The error bars shown in Figures 4.6a and 4.6b are based on theses values.

Science does not know its debt to imagination.

Ralph Waldo Emmerson

5 Summary & Outlook

In this thesis we show that:

- The fitting of both analytic surface brightness laws as well as "non-parametric" measures of galaxy structure can be successfully applied to HST images of distant galaxies in the COSMOS field. When combined the two approaches allow the division of the galaxy population into distinct morphological classes in an automated fashion, which is indispensable for large data sets containing tens of thousands of galaxies.
- The majority of the larger members of the disk galaxy population reaches their present size by $z \sim 1$. The number density of disk galaxies of intermediate sizes ($r_{1/2} \sim$ 5-7 kpc) remains nearly constant from $z \sim 1$ to today. Unless the growth and destruction of such systems exactly balanced in the last eight billion years, they must have neither grown nor been destroyed over this period. The number density of the largest disks ($r_{1/2} > 7$ kpc) increased by a factor of about 2 since $z \sim 1$.
- The relative abundance of bulged and pure disk galaxies changes with cosmic time. Bulge-dominated systems have become more abundant since $z \sim 1$ while the number density of pure disk galaxies has declined. The observational signature of this is a constancy – or even slight decrease – in the number density of large bulgeless disks since $z \sim 1$ while large disks with a bulge seem to have been less abundant at early times. Internal secular transformations which lead to the formation of a central spheroidal component may be responsible for shifting the balance in favour of more bulge-dominated disk galaxies.
- The surface brightness of large disk galaxies decreases by about 1-1.4 mag since $z \sim 1$. For both pure disk galaxies and the most bulge-dominated systems the amount of surface brightness evolution is similar, implying that the star formation history in galactic disks has been similar regardless of the presence and size of the central bulge.

- The amount of luminosity evolution since $z \sim 1$ can be explained by exponentially declining star formation rates with a time constant of about 5 Gyr for the disks independent of the bulges' size.
- The bivariate size-luminosity distribution is well fit by a log-normal distribution in size and a Schechter function in luminosity. For pure disk galaxies the peak of the size distribution has not changed since $z \sim 1$. The size distribution of disk galaxies which possess a bulge has evolved towards larger sizes in the last 8 billion years. On average, disk galaxies with a non-negligible bulge-component have grown by about 30% since $z \sim 1$.
- Surface brightness evolution depends only weakly on environment, while the evolution of rest-frame $(u^* - V)$-colours varies as a function of environmental density. The evolution is weaker in dense regions implying that disk galaxies in such overdensities had already formed most of their stars by $z \sim 1$.

There are many open questions concerning the evolution of disk galaxies that merit further investigation in future work. In view of the findings of this thesis it strikes us as especially interesting to study:

- The growth of mass in galactic disks

  At any redshift, observations of galaxies at different wavelengths reveal different components of their stellar populations and facilitate the disentangling of distinct morphological substructures and their evolutionary histories. Furthermore, information in different passbands allows one to consistently trace the redshift evolution of galactic structures at similar rest-frame wavelengths, and thus in similar components of the stellar population. The foreseen installation of the WFC3 camera onboard the HST in 2008 will hopefully provide images in the near-infrared at HST-resolution for the COSMOS field. This will allow the comparison of previous measurements of rest-frame B-band sizes with rest-frame I-band sizes, permitting a study of stellar population gradients and the growth of mass inside the disks as a function of other known galactic and environmental properties.

- The growth of mass in galactic bulges

  Several studies (see e.g., Kormendy and Kennicutt [67] or Carollo [16] for reviews and references) suggest that large disk galaxies accumulated a substantial fraction of their bulge mass through internal dynamical evolution over the last 8 billion years. Both internal bar instabilities or external influence from satellite interactions may bring about non-axisymmetric distortions of the disk potential that can funnel gas toward the galactic centre, and lead to enhanced star formation and bulge growth (e.g., Aguerri et al. [3], Steinmetz and Navarro [122]). The evolutionary trends in disk galaxies of different B/D ratios presented in chapters 3 and 4 supports this scenario, providing the first evidence at high redshifts for a large role of secular evolution in transforming bulgeless disks into bulged disks. Bulge-to-disk decomposition would therefore be useful to compare the statistical structural and colour properties of

bulges to those of their disks since $z \sim 1$. The available information on the COSMOS galaxies and their environment will allow for deeper insight into time-scales and processes underlying bulge formation.

- Substructure in galactic disks as an indicator of the role of internal dynamical evolution

  The role of internal disk dynamical instabilities in driving galactic evolution is expected to be large, but quantification of how this happens is still scarce. In addition to bulge-growing bar instabilities, the development and properties of spiral structure can also be important in the life of a disk galaxy. With the quantification and parametrization of bar and spiral structure for a sample of 33,000 COSMOS disk galaxies it will be possible to produce observational constraints on the properties and development of disk instabilities with cosmic time. The residuals from analytic surface brightness fits are a particularly promising way to study the non-smooth and non-symmetric galactic light and to determine, for instance, the 'winding-strength' and the degree of rotational symmetry of spiral patterns, bar strength and morphology or also the clumpiness of spiral disks (an indication of the distribution of the centres of star formation activity), both in barred and unbarred disk galaxies. The development of quantitative measures of spiral and internal structure also are a prerequisite for the assessment of how the environment affect the internal evolution and dynamics of the disk galaxy population.

Appendix

A.1 A local galaxy sample redshifted to $z \sim 0.7$

The comoving volume of the universe sampled by the ACS COSMOS data at redshifts smaller than $z \sim 0.05$ is only approximately 1.6×10^3 Mpc^3, and includes a mere 150 galaxies. Due to cosmic sampling variance and small number statistics the objects at these lowest redshifts are thus inadequate as a meaningful $z \sim 0$ calibration for studies of galaxy evolution.

To overcome this limitation we used the SSDS-based data set of artificial galaxy images as constructed and presented by Kampczyk et al. [62]. In this thesis it served as a reference sample with which the evolutionary trends (e.g., of the size function or of surface brightness) at intermediate redshift derived from COSMOS galaxies could be linked to the properties of the galaxy population in the local universe. The artificial SDSS galaxies simulate how the local universe would appear if observed in the COSMOS survey at a redshift $z = 0.7$. They were extracted from the SDSS-DR4 galaxy catalog[1] and define a volume-limited sample of 1813 galaxies with $M(B) <$ -18.5 in the redshift interval 0.015 $< z <$ 0.025. The absolute B-band magnitude $M(B)$ was derived from the SDSS g mag-

[1] The SDSS survey provides homogenous color information and spectroscopic redshfits for more than 10^6 galaxies with magnitude $r < 17.77$ (Strauss et al. [123]). We expect the SDSS-based sample of Kampczyk et al. [62] to be unbiased with respect to environmental effects and fully representative of the local galaxy population down to a limiting magnitude of $M(B)$ -18.5 for the following reasons: (1) The photometric and spectroscopic SDSS data are virtually complete down to $r \sim 17.8$ (Strauss et al. [123]), i.e., well below the considered absolute magnitude cut. Specifically, the surface brightness cut applied for the selection of the SDSS spectroscopic targets ($\mu < 23$ mag arcsec^{-2}) and mechanical constraints of the spectrograph (which exclude galaxies in pairs closer than 55") remove less than 1% and ∼6% of targets brighter than $r = 17.77$, respectively. Most importantly, the fraction of excluded galaxies does not depend on the galaxy magnitude; (2) It is extracted from a sample of ∼700,000 SDSS galaxies over a volume of 2.5×10^5 Mpc^3, which encompasses the full range of local environmental densities, from voids to galaxy clusters.
The website of SDSS data release no. 4 is `http://www.sdss.org/dr4/`.

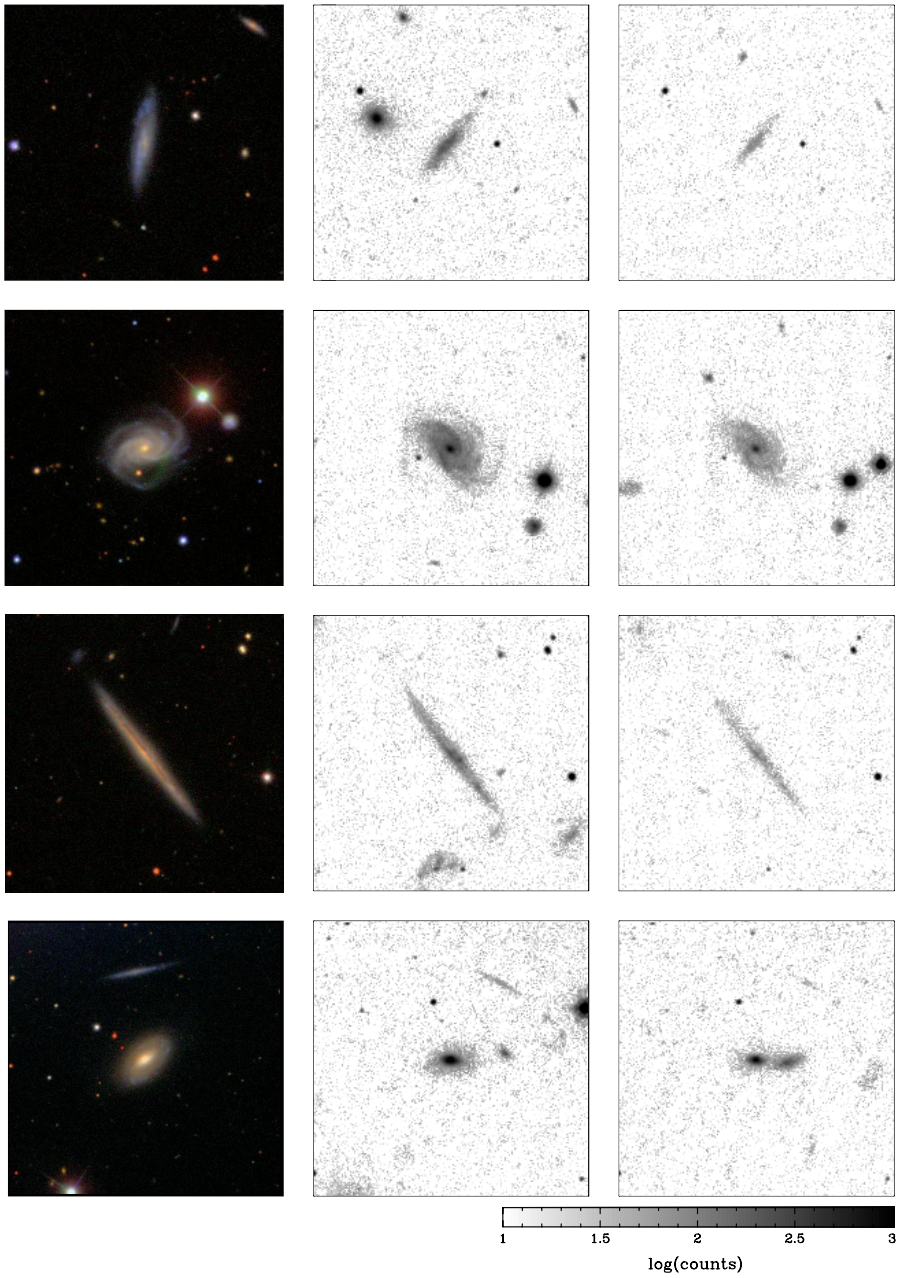

Fig. A.1 — Examples of four SDSS disk galaxies and their simulated appearance at $z \sim 0.7$. The leftmost stamp shows the original SDSS image, the stamp on the right the same galaxy at $z \sim 0.7$ as it would be seen by the HST ACS in a COSMOS tile. The central column shows the original galaxy redshifted and brightened by $\Delta\mu = z$. Each stamp has a physical size of 73.5 kpc. In the simulated COSMOS images (2nd and 3rd column) the SDSS galaxy may appear in the vicinity of a real COSMOS galaxy due to coincidental superpositions.

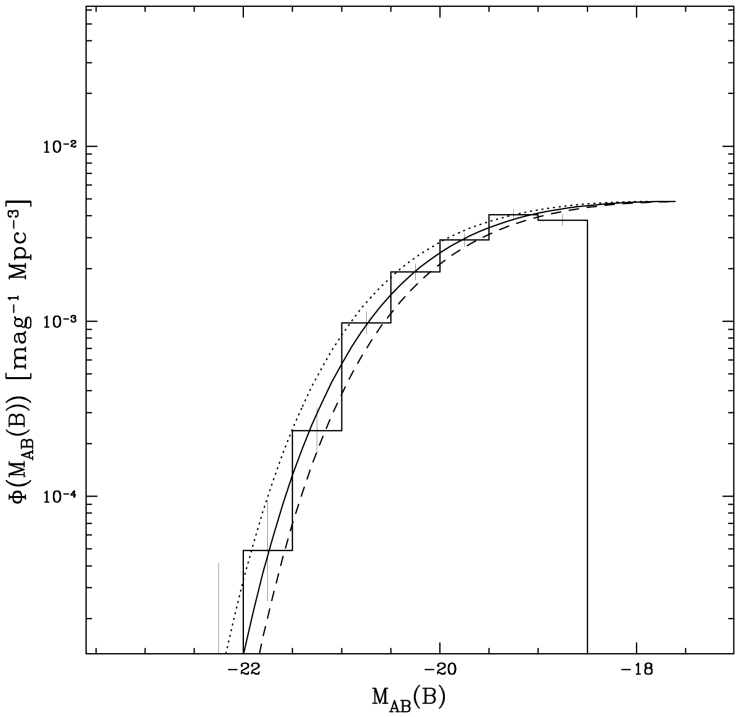

Fig. A.2 — The rest-frame $B-$band luminosity function for the SDSS galaxy sample of Kampczyk et al. [62], which was use to extend the evolutionary trends measured in the COSMOS sample at $z > 0.2$ to the local volume (solid histogram). It is normalized using the $g-$band luminosity function of Blanton et al. [10], converted to the B-band magnitude using the average transformation (solid line) between a 12 Gyr-old single burst SED with a solar metallicity (dotted line) and a single-burst 0.1 Gyr-old SED with a similar metallicity (dashed line).

nitude by applying a $K-$correction computed on the basis of the observed $g - r$ colour and redshift of each galaxy.

The SDSS g-band at $z = 0$ almost perfectly matches the ACS F814W (I) band at $z = 0.7$. To simulate how the local galaxies (observed in the SDSS g-band) would appear, in the absence of evolution, in the F814W COSMOS ACS images at a redshift $z = 0.7$, it is thus only necessary to account for the different pixel scales and PSFs, and cosmological surface brightness dimming. The SDSS$_{z=0.7}$-simulated images include no size evolution but have versions both with and without the evolution of surface brightness (cf. Figure A.1). They were randomly added to the COSMOS ACS images to reproduce their typical noise properties and to simulate random overlapping of galaxies due to projection effects.

The simulated SDSS$_{z=0.7}$ galaxies were analyzed with the same procedures used for the real COSMOS data. This not only applies to structural measurements but also to source detection. SExtractor was run to detect the sources and to measure their $I-$band magnitudes, position angles and ellipticities. In particular, the same SExtractor configuration

parameters that were used to generate the COSMOS-catalog (Leauthaud et al. [70]) were adopted for the extraction of the $\mathrm{SDSS}_{z=0.7}$ objects. About 6% of the $\mathrm{SDSS}_{z=0.7}$ galaxies were not recovered by SExtractor.

If the size or luminosity functions, or the bivariate size-luminosity distribution, of COSMOS galaxies are to be compared to that of the set of artificially redshifted galaxies this necessitates the prior knowledge of the number density of the SDSS comparison sample. Direct computation of this figure would require careful tracking of the spectroscopic sampling rate, redshift completeness, and practical difficulties encountered in the selection of the sample (see also the previous footnote). It is thus preferable to compute the effective volume based on the average density of the much larger full SDSS sample. To this end the (unnormalized) luminosity function of the 1813 simulated galaxies was compared with the absolute luminosity function of the full SDSS (Blanton et al. [10]).
The rest-frame $B-$band luminosity function for the simulated $\mathrm{SDSS}_{z=0.7}$ sample is shown in Figure A.2 (*solid histogram*). Being based on a volume-limited, random selection of the local galaxy population, this luminosity function will have the same shape as the global $z = 0$ $B-$band luminosity function. The total number of SDSS galaxies with $M(B) <$ -18.5 is calculated by integrating the $B-$band luminosity function recovered from the $g-$band luminosity function of Blanton et al. [10] and then applied as normalization to the solid histogram. To convert g-band to B-band magnitudes, we considered two extreme SEDs: a young (0.1 Gyr) single burst stellar population with solar metallicity, and an old (12 Gyr) single burst stellar population with the same metallicity. The corresponding transformations are: $B = g + 0.02$, and $B = g + 0.36$. In Figure A.2 we show the luminosity functions calculated using the normalization derived adopting the "old" SED (dotted line), the "young" SED (dashed line), and the average of the two (solid line). For all comparisons of evolutionary trends between COSMOS data and the local universe in this thesis, we have adopted the SDSS $B-$band luminosity function derived with the average SED correction.

A.2 The COSMOS Survey

The Cosmic Evolution Survey (COSMOS)[2] was begun in 2003 with a Hubble Space Telescope (HST) Legacy survey to map an area of approximately 2 deg^2 in a region of the sky which was to be accessible for complementary or follow-up observations with the most powerful astronomical facilities already in use or planned for future commissioning. The choice of a field near the celestial equator was inevitable if telescopes on both the northern and the southern hemisphere were to participate in the project. It is centred at R.A. = $10^{\mathrm{h}}00^{\mathrm{m}}28.6^{\mathrm{s}}$, decl. = $+02°12'12.0''$ (J2000.0) and has the shape of a $1.4° \times 1.4°$ square[3], aligned east-west and north-south in the constellation Sextant. It is devoid of bright X-

[2] The COSMOS web site is `http://www.astro.caltech.edu/~cosmos`. Publically released COSMOS data sets can be obtained from `http://irsa.ipac.caltech.edu/data/COSMOS`. IRSA also supplies a cutout capability derived from the full-field HST ACS mosaic, which can be made with any field centre and size.

[3] In a flat cosmology with $\Omega_\Lambda = 0.75$, $\Omega_m = 0.25$ and $H_0 = 70$ km s^{-1} Mpc^{-1} an angular scale of 1.4° corresponds to a comoving scale of 20.1, 55.0 and 83.3 Mpc at $z \sim 0.2$, 0.6 and 1, respectively.

ray, UV and radio sources. Furthermore, it was chosen to have among the lowest and most uniform far infrared cirrus backgrounds and also exceptionally low and uniform extinction ($E_{B-V} \simeq 0.02$ mag) compared to other equatorial fields. Since the field had not been previously observed in the context other surveys (e.g., the HDF-N/S, GOODS/CDF-N/S, the Lockman Hole or the Groth strip) most of the complementary observations had to be initiated and carried out in parallel to the HST-program. At the time of writing the following observatories on the Earth were or had been involved in gathering data in the COSMOS field: VLT, SUBARU, KPNO, CTIO, CFHT, UKIRT, Magellan (all in the IR/optical), IRAM (sub-mm) and VLA (radio). Space-based observations were carried out with XMM-Newton (X-rays), GALEX (UV), HST (optical/near-IR) and Spitzer Space Telescope (mid- and far-IR). In the future the potential of new observatories like the Atacama Large Millimeter/Sub-millimeter Array (ALMA), the Extended Very Large Array (EVLA), the Square Kilometer Array (SKA), the Thirty Meter Telescope (TMT) or SCUBA2 on the James Clerk Maxwell Telescope (JCMT) will be harnessed.

About three million galaxies and active galactic nuclei (AGNs) have been detected down to $I = 27.5$ (10σ) in the COSMOS field. The survey probes a volume in the high redshift universe which approaches the one covered by the SDSS at $z \leq 0.1$ (approximately 10^7 h^{-3} Mpc^3, cf. Figure 1 in Scoville et al. [113]). The large data set has both an unprecedented statistical relevance and also suffers less from cosmic sampling variance than earlier surveys at intermediate and high redshift. It is being used to address the following issues:

1. the evolution of galaxies, clusters, large-scale structure and dark matter on mass scales up to $2{\times}10^{14}$ $M_\odot$,
2. the formation, assembly, and evolution of galaxies and the star formation in galaxies as a function of large-scale structure environment, morphology, and redshift,
3. the nature, morphology, and clustering properties of different galaxy populations and their evolution with redshift,
4. the evolution of AGNs and the dependence of black hole growth on galaxy morphology and environment,
5. the reconstruction of the dark matter distribution using weak gravitational lensing, and
6. the mass and luminosity distribution of the earliest galaxies, AGNs and intergalactic gas at $z =$ 3-6 and their clustering.

In the COSMOS field it is thus possible to study the growth of galaxies, AGNs, and dark matter structure – from voids to the most massive clusters – until a look-back time of about 10 billion years. The availability of multi-wavelength data from X-rays to radio is crucial both to provide as much information as possible on individual objects (e.g., on (obscured) star formation rate, active nuclei, metallicity, or the internal dynamics) as well as to detect entire populations of galaxies at high redshifts which are usually not

accessible to surveys limited to IR/optical wavelengths. The following paragraphs are a brief summary of those COSMOS data sets which were used for the work presented in this Ph.D. thesis.

A.2.1 Hubble Space Telescope observations

The COSMOS HST Legacy survey (Scoville et al. [112]) is the largest HST survey ever undertaken. It consists of 592 single-orbit $I(F814W)$-band exposures (central wavelength 8332 Å) with the Advanced Camera for Surveys' (ACS) Wide-Field Channel (WFC) detector.
HST and ACS orbit the Earth at a height of 593 km. The circular orbit has a period of 96 to 97 minutes and is inclined by 28.5° with respect to the equatorial plane of the Earth. Thanks to its combination of detector area and high quantum efficiency the ACS camera surpasses previous instruments such that HST imaging discovery efficiency was improved by about a factor of 10 after its installation. ACS is mounted in one of the instrument bays behind the HST primary mirror and has three independent cameras that provide wide-field, high resolution, and ultraviolet imaging capabilities respectively, using a broad variety of filters. In addition, coronagraphic, polarimetric, and grism capabilities make it a versatile instrument for a wide range of scientific objectives.
The ACS CCDs are thinned, backside-illuminated full-frame devices cooled by thermoelectric cooler (TEC) stacks housed in sealed, evacuated dewars with fused silica windows. The spectral response of the WFC CCDs is optimized for imaging at visible to near-IR wavelengths. As with all CCD detectors, there is noise (readout noise) and time (read time) associated with reading out the detector following an exposure. For full-frame readouts between successive identical exposures, the minimum time is 135 seconds for the WFC. However, this can be reduced to as little as ∼35 seconds for WFC subarray readouts. The dynamic range for a single exposure is ultimately limited by the depth of the CCD full well (∼85,000 e^- for the WFC).
At the conclusion of each exposure, the acquired data is read out from the detector and placed in the internal buffer memory of ACS, where it is stored until it can be transferred to the HST solid state data recorder (and thereafter to the ground). The internal buffer memory is large enough to hold one WFC image.

For the principal part of the COSMOS HST Legacy Survey the field was imaged to a point source limiting depth of $I \simeq 27.2$ mag (5σ) in a $0.24''$ diameter aperture. Furthermore, nine of the allocated orbits were used for $g(F475W)$-imaging with the aim of evaluating the need for full field coverage in a second filter. Parallel observations were carried out with the NICMOS (F160W H-band filter at 1.6μm) and WFPC2 (F300W U- and F450W B-filters) cameras that cover roughly 6% and 55% of the ACS-field respectively.

Figure A.3 shows how the COSMOS HST ACS survey compares in area and depth with previous surveys; the Hubble Deep Fields (HDFs; Williams et al. [134, 135]) which imaged a 5 arcmin^2 area, GOODS which covered a larger area (130 arcmin^2, Giavalisco et al. [52]), GEMS (Rix et al. [96]) which was larger than GOODS (800 arcmin^2) but at

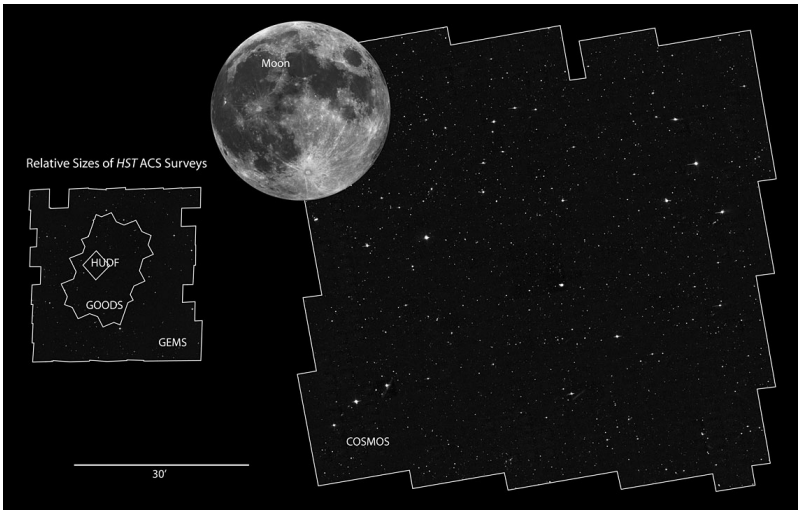

(*a*)

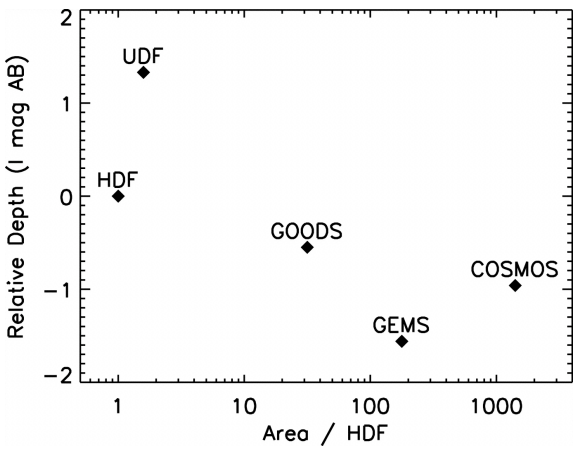

(*b*)

Fig. A.3 — (*a*) Comparison of relative sizes of the COSMOS field (right), the moon and three other HST ACS surveys (GEMS, GOODS and HUDF). With an area of approximately 1.7 deg^2 the HST COSMOS field is about 10 times larger than the moon. (*b*) Relative field areas and sensitivities of major HST surveys at ∼8000 Å compared to the HDF survey. COSMOS has 9 times the area of GEMS, the next largest survey, with sensitivity just 1.4 times less than GOODS (taken from Scoville et al. [112]).

shallower depth and the Ultra Deep Survey (Beckwith et al. [7]) which has unrivaled depth but at 11 arcmin^2 only a small area.
The F814W filter (7300-9500 Å) has particularly good transmission characteristics (∼95%) which is an important advantage for a survey with the size of COSMOS which places high demands on telescope time. In particular, the filter provides an additional 0.5 mag of depth for a given exposure time relative to the narrower F775W (SDSS i) filter on HST which was used in the GEMS, GOODS and UDF surveys.

The ACS WFC field of view measures $202'' \times 202''$ which is divided into two CCD arrays separated by a gap of $4.5''$. The pixel size of the images used for the analysis of this Ph.D. thesis is $0.5''$ (a COSMOS-internal release with a resolution of $0.3''$/px was created for the weak-lensing analysis). During each orbit of the space telescope four equal-length exposures of 507 seconds (i.e., a total of 2028 seconds) were obtained in a four-position dither pattern designed to shift bad pixels (about 2-6% of the detector pixels get hit by cosmic rays during one orbit of the telescope) and to fill the gap between the two ACS CCD arrays. Adjacent pointings in the mosaic were positioned with roughly 4% overlap in order to provide at least three-exposure coverage at the edge of each pointing and four-exposure coverage over about 95% of the survey area. The measured FWHM of the PSF in the ACS I-band filter is approximately $0.1''$ as a result of the convolution of the intrinsic width of the PSF from the HST optics ($\sim 0.085''$) with the detector pixels and the pixel size of the final image.
The read noise of the WFC detector is 5 e^-/pixel and the dark current rate 0.0038 e^-/s/pixel. The camera is mounted $\sim 6'$ off-axis from the principal optical axis of HST and is also tilted with respect to the focal plane of the telescope which results in a significant amount of skew distortion across the field. The pixels are thus projected as skew trapezoids on the sky with changing shapes across the detector. This distortion is removed during data processing after the acquisition of the data.

During the acquisition of the HST ACS data in Cycle 12 and 13 the guidestar positions were not yet corrected for their proper motion. This lead to an uncertainty of up to $2''$ in the absolute astrometric positioning of the individual HST pointings. In order to correct for this uncertainty the ACS data set was tied into ground-based CFHT I-band imaging (Aussel et al. 2008, in preparation) with the USNO-B1.0 (Monet et al. [83]) reference frame offsets established from the COSMOS VLA survey (Schinnerer et al. [109]). The absolute registration of all ACS data in the COSMOS archive is accurate to approximately $0.05''$-$0.10''$ over the entire field. The flux calibration of the ACS is tied in to the standard STSci ACS calibration which is accurate to better than 0.05% in absolute zero point. All descriptions of the ACS data processing including drizzling, flux calibration, registration, and mosaicking is provided in Koekemoer et al. [66].

A.2.2 Ancillary multi-wavelength observations of the COSMOS field

Ground-based imaging with 4 m and 8 m-class telescopes in the optical/near-IR, as well as near-IR data from the Spitzer-IRAC camera is an essential part of the COSMOS survey in the absence of multi-band information with HST. In the rest of this section we give a brief overview of the data with which photometric redshift estimates were derived by ZEBRA (Feldmann et al. [41]) for the galaxy sample studied in this thesis.

SUBARU Suprime-Cam observations

The COSMOS field has been imaged in multiple optical broad and narrow bands with the prime-focus camera (Suprime-Cam) at the 8.2 m Subaru telescope (see Taniguchi et al. [125] and Capak et al. [14] for a description of observations and data processing). At the time of writing the program COSMOS-21 was being carried out which – after conclusion of the project – will provide photometry in 21 filters. For the redshift estimates used in this Ph.D. thesis only six filters were employed; the Johnson broadband filters B (4460 Å) and V (5484 Å) and the SDSS broadband filters g' (4723 Å), r' (6213 Å), i' (7641 Å) and z' (8855 Å).
The Suprime-Cam consists of 10 CCD chips covering a wide field of view ($34'\times27'$ at a resolution of $0.2''$/pixel) such that a total of nine pointings is necessary to image the whole COSMOS area. At 3σ the point source detection limit ranged from $z' \simeq 25$ to $B \simeq 27$ within a $3''$ diameter aperture. Due to the high sensitivity of Suprime-Cam objects brighter than 19th magnitude were saturated in typical exposures which makes the astrometric registration of the Subaru data very difficult. To enable the astrometric calibration against, e.g., the SDSS astrometric catalog of the data set a series of short supplementary exposures were thus also taken in each band. The FWHM of the PSF ranged from $< 1''$ to $\sim1.6''$ for observations in the different filters. Once calibrated, all images were smoothed with a Gaussian kernel to a FWHM of $1.5''$ to ensure consistent aperture photometry (optimized for a $3''$ aperture) across all bands.

CFHT MegaPrime data

Deep u^* (3798 Å) and shallow i^* (7684 Å) imaging of the COSMOS field was obtained with the Megaprime camera on the 3.6 m Canada-France-Hawai'i telescope (CFHT). Observations were taken under excellent seeing conditions with FWHM $< 1''$ in five sets of dithered exposures forming a pentagonal coverage of the COSMOS field that is four times deeper in the centre than at the edges. Megaprime has a 1 deg^2 field that is imaged by 36 CCD detectors. The 5σ depth in a $3''$ aperture is 26.5 in the u^*-band. Since objects as bright as 15th magnitude were unsaturated in MegaPrime exposures accurate astrometric registration was feasible with the CFHT data which was used as a reference for COSMOS data sets with greater positional uncertainty.

CTIO ISPI and KPNO Flamingos

Two instruments were employed to image the COSMOS field in the near-IR K_s-band; the Flamingos camera on the Kitt Peak 4 m and the Infrared Side Port Imager (ISPI) camera on the Cerro Tololo Infrared Observatory (CTIO) 4 m telescope. Both have a field of view slightly larger than $10'\times10'$ such that full coverage of the field was achieved after 81 pointings. The infrared array detectors of Flamingo and ISPI are sensitive to wavelengths between 0.9μm to 2.4μm and average exposure times of approximately 25 minutes with

both instruments resulted in a 5σ detection limit of 21.2 in a $3''$ aperture. As in the case of the Subaru and CFHT data sets all images were smoothed with Gaussian kernel with FWHM $1.5''$.

Spitzer-IRAC data from the S-COSMOS survey

The COSMOS Spitzer Survey (S-COSMOS) is a Legacy program designed to carry out a uniform deep survey of the full 2 deg^2 COSMOS field in all seven Spitzer bands (3.6, 4.5, 5.6 and 8.0μm with the IRAC-camera and 24.0, 70.0 and 160.0μm with MIPS). During the analysis of this Ph.D. thesis only the near-IR IRAC bands at 3.6 and 4.5μm were supplied as input to the estimation of photometric redshifts with ZEBRA.
The IRAC camera has two fields of view, each one reserved for two channels: one for the 3.6 and 5.6μm detectors, and one for the 4.5 and 8.0μm detectors. They were used to image the COSMOS field to a depth of 20 minutes in a multiple-pass strategy aimed at identifying asteroids (a significant contaminant for IR-surveys in fields near the ecliptic plane) and rejecting cosmic rays; a total of about 500 pointings were each observed 12 times for 100 seconds. Since the two fields of view of IRAC are separated by $7'$, the area observed was significantly larger than the HST COSMOS field.

Bibliography

[1] R. G. Abraham, S. van den Bergh, K. Glazebrook, R. S. Ellis, B. X. Santiago, P. Surma, and R. E. Griffiths. The Morphologies of Distant Galaxies. II. Classifications from the Hubble Space Telescope Medium Deep Survey. *ApJS*, 107:1–22, November 1996. doi: 10.1086/192352.

[2] R. G. Abraham, S. van den Bergh, and P. Nair. A New Approach to Galaxy Morphology. I. Analysis of the Sloan Digital Sky Survey Early Data Release. *ApJ*, 588: 218–229, May 2003. doi: 10.1086/373919.

[3] J. A. L. Aguerri, M. Balcells, and R. F. Peletier. Growth of galactic bulges by mergers. I. Dense satellites. *A&A*, 367:428–442, February 2001. doi: 10.1051/0004-6361: 20000441.

[4] W. E. Baggett, S. M. Baggett, and K. S. J. Anderson. Bulge-Disk Decomposition of 659 Spiral and Lenticular Galaxy Brightness Profiles. *AJ*, 116:1626–1642, October 1998. doi: 10.1086/300525.

[5] M. Barden, H.-W. Rix, R. S. Somerville, E. F. Bell, B. Häußler, C. Y. Peng, A. Borch, S. V. W. Beckwith, J. A. R. Caldwell, C. Heymans, K. Jahnke, S. Jogee, D. H. McIntosh, K. Meisenheimer, S. F. Sánchez, L. Wisotzki, and C. Wolf. GEMS: The Surface Brightness and Surface Mass Density Evolution of Disk Galaxies. *ApJ*, 635: 959–981, December 2005. doi: 10.1086/497679.

[6] J. Barnes and G. Efstathiou. Angular momentum from tidal torques. *ApJ*, 319: 575–600, August 1987. doi: 10.1086/165480.

[7] S. V. W. Beckwith, M. Stiavelli, A. M. Koekemoer, J. A. R. Caldwell, H. C. Ferguson, R. Hook, R. A. Lucas, L. E. Bergeron, M. Corbin, S. Jogee, N. Panagia, M. Robberto, P. Royle, R. S. Somerville, and M. Sosey. The Hubble Ultra Deep Field. *AJ*, 132: 1729–1755, November 2006. doi: 10.1086/507302.

[8] M. A. Bershady, A. Jangren, and C. J. Conselice. Structural and Photometric Classification of Galaxies. I. Calibration Based on a Nearby Galaxy Sample. *AJ*, 119:2645–2663, June 2000. doi: 10.1086/301386.

[9] E. Bertin and S. Arnouts. SExtractor: Software for source extraction. *A&AS*, 117: 393–404, June 1996.

[10] M. R. Blanton, D. W. Hogg, N. A. Bahcall, I. K. Baldry, J. Brinkmann, I. Csabai, D. Eisenstein, M. Fukugita, J. E. Gunn, Ž. Ivezić, D. Q. Lamb, R. H. Lupton, J. Loveday, J. A. Munn, R. C. Nichol, S. Okamura, D. J. Schlegel, K. Shimasaku, M. A. Strauss, M. S. Vogeley, and D. H. Weinberg. The Broadband Optical Properties of Galaxies with Redshifts $0.02 < z < 0.22$. *ApJ*, 594:186–207, September 2003. doi: 10.1086/375528.

[11] G. R. Blumenthal, S. M. Faber, J. R. Primack, and M. J. Rees. Formation of galaxies and large-scale structure with cold dark matter. *Nature*, 311:517–525, October 1984.

[12] R. Bouwens and J. Silk. Models of Disk Evolution: Confrontation with Observations. *ApJ*, 568:522–538, April 2002. doi: 10.1086/341670.

[13] G. Bruzual and S. Charlot. Stellar population synthesis at the resolution of 2003. *MNRAS*, 344:1000–1028, October 2003. doi: 10.1046/j.1365-8711.2003.06897.x.

[14] P. Capak, H. Aussel, M. Ajiki, H. J. McCracken, B. Mobasher, N. Scoville, P. Shopbell, Y. Taniguchi, D. Thompson, S. Tribiano, S. Sasaki, A. W. Blain, M. Brusa, C. Carilli, A. Comastri, C. M. Carollo, P. Cassata, J. Colbert, R. S. Ellis, M. Elvis, M. Giavalisco, W. Green, L. Guzzo, G. Hasinger, O. Ilbert, C. Impey, K. Jahnke, J. Kartaltepe, J.-P. Kneib, J. Koda, A. Koekemoer, Y. Komiyama, A. Leauthaud, O. Lefevre, S. Lilly, C. Liu, R. Massey, S. Miyazaki, T. Murayama, T. Nagao, J. A. Peacock, A. Pickles, C. Porciani, A. Renzini, J. Rhodes, M. Rich, M. Salvato, D. B. Sanders, C. Scarlata, D. Schiminovich, E. Schinnerer, M. Scodeggio, K. Sheth, Y. Shioya, L. A. M. Tasca, J. E. Taylor, L. Yan, and G. Zamorani. The First Release COSMOS Optical and Near-IR Data and Catalog. *ApJS*, 172:99–116, September 2007. doi: 10.1086/519081.

[15] J. A. Cardelli, G. C. Clayton, and J. S. Mathis. The relationship between infrared, optical, and ultraviolet extinction. *ApJ*, 345:245–256, October 1989. doi: 10.1086/167900.

[16] C. M. Carollo. The Inner Properties of Late-type Galaxies. In L. C. Ho, editor, *Coevolution of Black Holes and Galaxies*, pages 231–+, 2004.

[17] C. M. Carollo. The Centers of Early- to Intermediate-Type Spiral Galaxies: A Structural Analysis. *ApJ*, 523:566–574, October 1999. doi: 10.1086/307753.

[18] C. M. Carollo, M. Stiavelli, and J. Mack. Spiral Galaxies with WFPC2. II. The Nuclear Properties of 40 Objects. *AJ*, 116:68–84, July 1998. doi: 10.1086/300407.

[19] C. M. Carollo, M. Stiavelli, P. T. de Zeeuw, M. Seigar, and H. Dejonghe. Hubble Space Telescope Optical-Near-Infrared Colors of Nearby $R^{1/4}$ and Exponential Bulges. *ApJ*, 546:216–222, January 2001. doi: 10.1086/318265.

[20] C. M. Carollo, M. Stiavelli, M. Seigar, P. T. de Zeeuw, and H. Dejonghe. Spiral Galaxies with HST/NICMOS. I. Nuclear Morphologies, Color Maps, and Distinct Nuclei. *AJ*, 123:159–183, January 2002. doi: 10.1086/324725.

[21] C. M. Carollo, C. Scarlata, M. Stiavelli, R. F. G. Wyse, and L. Mayer. Old and Young Bulges in Late-Type Disk Galaxies. *ApJ*, 658:960–979, April 2007. doi: 10.1086/511125.

[22] C. L. Carroll. *Alice's Adventures in Wonderland*. Macmillan Publishers Ltd, 1865.

[23] J. Chołoniewski. Bivariate luminosity function of E and S0 galaxies. *MNRAS*, 214: 197–202, May 1985.

[24] L. Ciotti and G. Bertin. Analytical properties of the $R^{1/m}$ law. *A&A*, 352:447–451, December 1999.

[25] G. D. Coleman, C.-C. Wu, and D. W. Weedman. Colors and magnitudes predicted for high redshift galaxies. *ApJS*, 43:393–416, July 1980. doi: 10.1086/190674.

[26] C. J. Conselice, M. A. Bershady, and A. Jangren. The Asymmetry of Galaxies: Physical Morphology for Nearby and High-Redshift Galaxies. *ApJ*, 529:886–910, February 2000. doi: 10.1086/308300.

[27] O. Dahari. The nuclear activity of interacting galaxies. *ApJS*, 57:643–664, April 1985. doi: 10.1086/191021.

[28] M. Davis, S. M. Faber, J. Newman, A. C. Phillips, R. S. Ellis, C. C. Steidel, C. Conselice, A. L. Coil, D. P. Finkbeiner, D. C. Koo, P. Guhathakurta, B. Weiner, R. Schiavon, C. Willmer, N. Kaiser, G. A. Luppino, G. Wirth, A. Connolly, P. Eisenhardt, M. Cooper, and B. Gerke. Science Objectives and Early Results of the DEEP2 Redshift Survey. In P. Guhathakurta, editor, *Discoveries and Research Prospects from 6- to 10-Meter-Class Telescopes II. Edited by Guhathakurta, Puragra. Proceedings of the SPIE, Volume 4834, pp. 161-172 (2003).*, volume 4834 of *Presented at the Society of Photo-Optical Instrumentation Engineers (SPIE) Conference*, pages 161–172, February 2003.

[29] R. S. de Jong and C. Lacey. The Local Space Density of SB-SDM Galaxies as Function of Their Scale Size, Surface Brightness, and Luminosity. *ApJ*, 545:781–797, December 2000. doi: 10.1086/317840.

[30] R. E. de Souza, D. A. Gadotti, and S. dos Anjos. BUDDA: A New Two-dimensional Bulge/Disk Decomposition Code for Detailed Structural Analysis of Galaxies. *ApJS*, 153:411–427, August 2004. doi: 10.1086/421554.

[31] G. de Vaucouleurs, A. de Vaucouleurs, H. G. Corwin, Jr., R. J. Buta, G. Paturel, and P. Fouque. Book-Review - Third Reference Catalogue of Bright Galaxies. *Third Reference Catalogue of Bright Galaxies (New York: Springer)*, 82:621–+, December 1991.

[32] V. P. Debattista, C. M. Carollo, L. Mayer, and B. Moore. Bulges or Bars from Secular Evolution? *ApJL*, 604:L93–L96, April 2004. doi: 10.1086/386332.

[33] V. P. Debattista, C. M. Carollo, L. Mayer, and B. Moore. The Kinematic Signature of Face-On Peanut-shaped Bulges. *ApJj*, 628:678–694, August 2005. doi: 10.1086/431292.

[34] V. P. Debattista, L. Mayer, C. M. Carollo, B. Moore, J. Wadsley, and T. Quinn. The Secular Evolution of Disk Structural Parameters. *ApJ*, 645:209–227, July 2006. doi: 10.1086/504147.

[35] A. C. Doyle. The Adventure of the Speckled Band. *The Strand Magazine*, February 1892.

[36] A. C. Doyle. The Adventure of the Reigate Squires. *The Strand Magazine*, June 1893.

[37] O. J. Eggen, D. Lynden-Bell, and A. R. Sandage. Evidence from the motions of old stars that the Galaxy collapsed. *ApJ*, 136:748–767, November 1962.

[38] E. Emsellem, M. Cappellari, R. F. Peletier, R. M. McDermid, R. Bacon, M. Bureau, Y. Copin, R. L. Davies, D. Krajnović, H. Kuntschner, B. W. Miller, and P. T. de Zeeuw. The SAURON project - III. Integral-field absorption-line kinematics of 48 elliptical and lenticular galaxies. *MNRAS*, 352:721–743, August 2004. doi: 10.1111/j.1365-2966.2004.07948.x.

[39] V. A. Epanechnikov. Nonparametric estimation of a multidimensional probability density. *Theor. Probab. Appl.*, 14:153–158, 1969.

[40] S. M. Fall and G. Efstathiou. Formation and rotation of disc galaxies with haloes. *MNRAS*, 193:189–206, October 1980.

[41] R. Feldmann, C. M. Carollo, C. Porciani, S. J. Lilly, P. Capak, Y. Taniguchi, O. L. Fèvre, A. Renzini, N. Scoville, M. Ajiki, H. Aussel, T. Contini, H. McCracken, B. Mobasher, T. Murayama, D. Sanders, S. Sasaki, C. Scarlata, M. Scodeggio, Y. Shioya, J. Silverman, M. Takahashi, D. Thompson, and G. Zamorani. The Zurich Extragalactic Bayesian Redshift Analyzer and its first application: COSMOS. *MNRAS*, 372:565–577, October 2006. doi: 10.1111/j.1365-2966.2006.10930.x.

[42] J. E. Felten. On Schmidt's Vm estimator and other estimators of luminosity functions. *ApJ*, 207:700–709, August 1976.

[43] A. M. N. Ferguson and C. J. Clarke. The evolution of stellar exponential discs. *MNRAS*, 325:781–791, August 2001. doi: 10.1046/j.1365-8711.2001.04501.x.

[44] H. C. Ferguson, M. Dickinson, M. Giavalisco, C. Kretchmer, S. Ravindranath, R. Idzi, E. Taylor, C. J. Conselice, S. M. Fall, J. P. Gardner, M. Livio, P. Madau, L. A. Moustakas, C. M. Papovich, R. S. Somerville, H. Spinrad, and D. Stern. The Size Evolution of High-Redshift Galaxies. *ApJL*, 600:L107–L110, January 2004. doi: 10.1086/378578.

[45] I. Ferreras, T. Lisker, C. M. Carollo, S. J. Lilly, and B. Mobasher. Evolution of Field Early-Type Galaxies: The View from GOODS CDFS. *ApJ*, 635:243–259, December 2005. doi: 10.1086/497292.

[46] K. C. Freeman. On the Disks of Spiral and S0 Galaxies. *ApJ*, 160:811–830, June 1970.

[47] Z. Frei, P. Guhathakurta, J. E. Gunn, and J. A. Tyson. A Catalog of Digital Images of 113 Nearby Galaxies. *AJ*, 111:174–+, January 1996. doi: 10.1086/117771.

[48] M. Fukugita and P. J. E. Peebles. The Cosmic Energy Inventory. *ApJ*, 616:643–668, December 2004. doi: 10.1086/425155.

[49] M. Fukugita, C. J. Hogan, and P. J. E. Peebles. The Cosmic Baryon Budget. *ApJ*, 503:518–530, August 1998. doi: 10.1086/306025.

[50] G. Gamow. The role of turbulence in the evolution of the universe. *Phys. Rev.*, 86 (2):251, Apr 1952. doi: 10.1103/PhysRev.86.251.

[51] G. Gamow and E. Teller. On the origin of great nebulae. *Phys. Rev.*, 55(7):654–657, Apr 1939. doi: 10.1103/PhysRev.55.654.

[52] M. Giavalisco, H. C. Ferguson, A. M. Koekemoer, M. Dickinson, D. M. Alexander, F. E. Bauer, J. Bergeron, C. Biagetti, W. N. Brandt, S. Casertano, C. Cesarsky, E. Chatzichristou, C. Conselice, S. Cristiani, L. Da Costa, T. Dahlen, D. de Mello, P. Eisenhardt, T. Erben, S. M. Fall, C. Fassnacht, R. Fosbury, A. Fruchter, J. P. Gardner, N. Grogin, R. N. Hook, A. E. Hornschemeier, R. Idzi, S. Jogee, C. Kretchmer, V. Laidler, K. S. Lee, M. Livio, R. Lucas, P. Madau, B. Mobasher, L. A. Moustakas, M. Nonino, P. Padovani, C. Papovich, Y. Park, S. Ravindranath, A. Renzini, M. Richardson, A. Riess, P. Rosati, M. Schirmer, E. Schreier, R. S. Somerville, H. Spinrad, D. Stern, M. Stiavelli, L. Strolger, C. M. Urry, B. Vandame, R. Williams, and C. Wolf. The Great Observatories Origins Deep Survey: Initial Results from Optical and Near-Infrared Imaging. *ApJL*, 600:L93–L98, January 2004. doi: 10.1086/379232.

[53] G. J. Glasser. Variance Formulas for the Mean Difference and Coefficient of Concentration. *J. Amer. Stat. Assoc.*, 57:648–654, 1962.

[54] F. Governato, L. Mayer, J. Wadsley, J. P. Gardner, B. Willman, E. Hayashi, T. Quinn, J. Stadel, and G. Lake. The Formation of a Realistic Disk Galaxy in Λ-dominated Cosmologies. *ApJ*, 607:688–696, June 2004. doi: 10.1086/383516.

[55] A. W. Graham and S. P. Driver. A Concise Reference to (Projected) Sérsic $R^{1/n}$ Quantities, Including Concentration, Profile Slopes, Petrosian Indices, and Kron Magnitudes. *Publications of the Astronomical Society of Australia*, 22:118–127, 2005. doi: 10.1071/AS05001.

[56] J. E. Gunn. The evolution of galaxies. In H. A. Brueck, G. V. Coyne, and M. S. Longair, editors, *Astrophysical Cosmology Proceedings*, pages 233–259, 1982.

[57] D. W. Hogg, I. K. Baldry, M. R. Blanton, and D. J. Eisenstein. The K correction. *ArXiv Astrophysics e-prints*, October 2002.

[58] J. H. Jeans. Philos. Trans. Roy. Soc. London. *ApJ*, 199:1–53, 1902.

[59] S. Jogee, F. D. Barazza, H.-W. Rix, I. Shlosman, M. Barden, C. Wolf, J. Davies, I. Heyer, S. V. W. Beckwith, E. F. Bell, A. Borch, J. A. R. Caldwell, C. J. Conselice, T. Dahlen, B. Häussler, C. Heymans, K. Jahnke, J. H. Knapen, S. Laine, G. M. Lubell, B. Mobasher, D. H. McIntosh, K. Meisenheimer, C. Y. Peng, S. Ravindranath, S. F. Sanchez, R. S. Somerville, and L. Wisotzki. Bar Evolution over the Last 8 Billion Years: A Constant Fraction of Strong Bars in the GEMS Survey. *ApJL*, 615:L105–L108, November 2004. doi: 10.1086/426138.

[60] I. T. Jolliffe. Discarding Variables in a Principal Component Analysis. I: Artificial Data. *J. Appl. Statistics*, 21:160–173, 1972. doi: 10.2307/2346488.

[61] H. F. Kaiser. The Application of Electronic Computers to Factor Analysis. *Educ. Psychol. Measurements*, 20:141–151, 1960.

[62] P. Kampczyk, S. J. Lilly, C. M. Carollo, C. Scarlata, R. Feldmann, A. Koekemoer, A. Leauthaud, M. T. Sargent, Y. Taniguchi, and P. Capak. Simulating the Cosmos: The Fraction of Merging Galaxies at High Redshift. *ApJS*, 172:329–340, September 2007. doi: 10.1086/516594.

[63] I. Kant. *Allgemeine Naturgeschichte und Theorie des Himmels.* Königsberg, 1755.

[64] I. D. Karachentsev and O. G. Kashibadze. Masses of the local group and of the M81 group estimated from distortions in the local velocity field. *Astrophysics*, 49:3–18, January 2006. doi: 10.1007/s10511-006-0002-6.

[65] G. Kauffmann, A. Nusser, and M. Steinmetz. Galaxy formation and large-scale bias. *MNRAS*, 286:795–811, April 1997.

[66] A. M. Koekemoer, H. Aussel, D. Calzetti, P. Capak, M. Giavalisco, J.-P. Kneib, A. Leauthaud, O. Le Fèvre, H. J. McCracken, R. Massey, B. Mobasher, J. Rhodes, N. Scoville, and P. L. Shopbell. The COSMOS Survey: Hubble Space Telescope Advanced Camera for Surveys Observations and Data Processing. *ApJS*, 172:196–202, September 2007. doi: 10.1086/520086.

[67] J. Kormendy and R. C. Kennicutt, Jr. Secular Evolution and the Formation of Pseudobulges in Disk Galaxies. *ARA&A*, 42:603–683, September 2004.

[68] J. E. Krist and R. N. Hook. NICMOS PSF variations and tiny tim simulations. In S. Casertano, R. Jedrzejewski, T. Keyes, and M. Stevens, editors, *The 1997 HST Calibration Workshop with a New Generation of Instruments, p. 192*, pages 192–+, January 1997.

[69] P. S. Laplace. *Exposition du Système du Monde.* Paris, 1796.

[70] A. Leauthaud, R. Massey, J.-P. Kneib, J. Rhodes, D. E. Johnston, P. Capak, C. Heymans, R. S. Ellis, A. M. Koekemoer, O. Le Fèvre, Y. Mellier, A. Réfrégier, A. C. Robin, N. Scoville, L. Tasca, J. E. Taylor, and L. Van Waerbeke. Weak Gravitational Lensing with COSMOS: Galaxy Selection and Shape Measurements. *ApJS*, 172:219–238, September 2007. doi: 10.1086/516598.

[71] S. Lilly, D. Schade, R. Ellis, O. Le Fevre, J. Brinchmann, L. Tresse, R. Abraham, F. Hammer, D. Crampton, M. Colless, K. Glazebrook, G. Mallen-Ornelas, and T. Broadhurst. Hubble Space Telescope Imaging of the CFRS and LDSS Redshift Surveys. II. Structural Parameters and the Evolution of Disk Galaxies to Z approximately 1. *ApJ*, 500:75–+, June 1998. doi: 10.1086/305713.

[72] S. J. Lilly, L. Tresse, F. Hammer, D. Crampton, and O. Le Fevre. The Canada-France Redshift Survey. VI. Evolution of the Galaxy Luminosity Function to z approximately 1. *ApJ*, 455:108–124, December 1995. doi: 10.1086/176560.

[73] S. J. Lilly, O. L. Fèvre, A. Renzini, G. Zamorani, M. Scodeggio, T. Contini, C. M. Carollo, G. Hasinger, J.-P. Kneib, A. Iovino, V. Le Brun, C. Maier, V. Mainieri, M. Mignoli, J. Silverman, L. A. M. Tasca, M. Bolzonella, A. Bongiorno, D. Bottini, P. Capak, K. Caputi, A. Cimatti, O. Cucciati, E. Daddi, R. Feldmann, P. Franzetti, B. Garilli, L. Guzzo, O. Ilbert, P. Kampczyk, K. Kovac, F. Lamareille, A. Leauthaud, J.-F. L. Borgne, H. J. McCracken, C. Marinoni, R. Pello, E. Ricciardelli, C. Scarlata, D. Vergani, D. B. Sanders, E. Schinnerer, N. Scoville, Y. Taniguchi, S. Arnouts, H. Aussel, S. Bardelli, M. Brusa, A. Cappi, P. Ciliegi, A. Finoguenov, S. Foucaud, R. Franceschini, C. Halliday, C. Impey, C. Knobel, A. Koekemoer, J. Kurk, D. Maccagni, S. Maddox, B. Marano, G. Marconi, B. Meneux, B. Mobasher, C. Moreau, J. A. Peacock, C. Porciani, L. Pozzetti, R. Scaramella, D. Schiminovich, P. Shopbell, I. Smail, D. Thompson, L. Tresse, G. Vettolani, A. Zanichelli, and E. Zucca. zCOSMOS: A Large VLT/VIMOS Redshift Survey Covering $0 < z < 3$ in the COSMOS Field. *ApJS*, 172:70–85, September 2007. doi: 10.1086/516589.

[74] D. N. C. Lin and J. E. Pringle. The formation of the exponential disk in spiral galaxies. *ApJL*, 320:L87–L91, September 1987. doi: 10.1086/184981.

[75] J. M. Lotz, J. Primack, and P. Madau. A New Nonparametric Approach to Galaxy Morphological Classification. *AJ*, 128:163–182, July 2004. doi: 10.1086/421849.

[76] C. Maraston. Evolutionary population synthesis: models, analysis of the ingredients and application to high-z galaxies. *MNRAS*, 362:799–825, September 2005. doi: 10.1111/j.1365-2966.2005.09270.x.

[77] F. R. Marleau and L. Simard. Quantitative Morphology of Galaxies in the Hubble Deep Field. *ApJ*, 507:585–600, November 1998. doi: 10.1086/306356.

[78] D. H. McIntosh, E. F. Bell, H.-W. Rix, C. Wolf, C. Heymans, C. Y. Peng, R. S. Somerville, M. Barden, S. V. W. Beckwith, A. Borch, J. A. R. Caldwell, B. Häußler, K. Jahnke, S. Jogee, K. Meisenheimer, S. F. Sánchez, and L. Wisotzki. The Evolution of Early-Type Red Galaxies with the GEMS Survey: Luminosity-Size and Stellar Mass-Size Relations Since z=1. *ApJ*, 632:191–209, October 2005. doi: 10.1086/432786.

[79] R. Michard and J. Marchal. Quantitative morphology of E-S0 galaxies. III. Coded and parametric description of 108 galaxies in a complete sample. *AA&S*, 105:481–501, June 1994.

[80] T. Mizuno and K.-I. Oikawa. Two-Dimensional Decomposition of a Disky Elliptical Galaxy, NGC 4621. *PASJ*, 48:591–600, August 1996.

[81] H. J. Mo, S. Mao, and S. D. M. White. The formation of galactic discs. *MNRAS*, 295:319–336, April 1998.

[82] B. Mobasher, P. Capak, N. Z. Scoville, T. Dahlen, M. Salvato, H. Aussel, D. J. Thompson, R. Feldmann, L. Tasca, O. Lefevre, S. Lilly, C. M. Carollo, J. S. Kartaltepe, H. McCracken, J. Mould, A. Renzini, D. B. Sanders, P. L. Shopbell, Y. Taniguchi, M. Ajiki, Y. Shioya, T. Contini, M. Giavalisco, O. Ilbert, A. Iovino, V. Le Brun, V. Mainieri, M. Mignoli, and M. Scodeggio. Photometric Redshifts of Galaxies in COSMOS. *ApJS*, 172:117–131, September 2007. doi: 10.1086/516590.

[83] D. G. Monet, S. E. Levine, B. Canzian, H. D. Ables, A. R. Bird, C. C. Dahn, H. H. Guetter, H. C. Harris, A. A. Henden, S. K. Leggett, H. F. Levison, C. B. Luginbuhl, J. Martini, A. K. B. Monet, J. A. Munn, J. R. Pier, A. R. Rhodes, B. Riepe, S. Sell, R. C. Stone, F. J. Vrba, R. L. Walker, G. Westerhout, R. J. Brucato, I. N. Reid, W. Schoening, M. Hartley, M. A. Read, and S. B. Tritton. The USNO-B Catalog. *AJ*, 125:984–993, February 2003. doi: 10.1086/345888.

[84] T. Naab and J. P. Ostriker. Are disk galaxies the progenitors of giant ellipticals? *ArXiv Astrophysics e-prints*, February 2007.

[85] C. A. Norman, J. A. Sellwood, and H. Hasan. Bar Dissolution and Bulge Formation: an Example of Secular Dynamical Evolution in Galaxies. *ApJ*, 462:114–124, May 1996. doi: 10.1086/177133.

[86] J. B. Oke. Absolute Spectral Energy Distributions for White Dwarfs. *ApJS*, 27: 21–35, February 1974.

[87] P. J. E. Peebles. Origin of the Angular Momentum of Galaxies. *ApJ*, 155:393–401, February 1969.

[88] Y. C. Pei. Interstellar dust from the Milky Way to the Magellanic Clouds. *ApJ*, 395:130–139, August 1992. doi: 10.1086/171637.

[89] C. Y. Peng, L. C. Ho, C. D. Impey, and H.-W. Rix. Detailed Structural Decomposition of Galaxy Images. *AJ*, 124:266–293, July 2002. doi: 10.1086/340952.

[90] A. A. Penzias and R. W. Wilson. Measurement of the Flux Density of CAS a at 4080 Mc/s. *ApJ*, 142:1149–1155, October 1965.

[91] V. Petrosian. Surface brightness and evolution of galaxies. *ApJL*, 209:L1–L5, October 1976.

[92] E. Pignatelli, G. Fasano, and P. Cassata. GASPHOT: a tool for Galaxy Automatic Surface PHOTometry. *A&A*, 446:373–388, January 2006. doi: 10.1051/0004-6361: 20041704.

[93] W. H. Press and P. Schechter. Formation of Galaxies and Clusters of Galaxies by Self-Similar Gravitational Condensation. *ApJ*, 187:425–438, February 1974.

[94] S. Ravindranath, H. C. Ferguson, C. Conselice, M. Giavalisco, M. Dickinson, E. Chatzichristou, D. de Mello, S. M. Fall, J. P. Gardner, N. A. Grogin, A. Hornschemeier, S. Jogee, A. Koekemoer, C. Kretchmer, M. Livio, B. Mobasher, and R. Somerville. The Evolution of Disk Galaxies in the GOODS-South Field: Number Densities and Size Distribution. *ApJL*, 604:L9–L12, March 2004. doi: 10.1086/382952.

[95] J. D. Rhodes, R. J. Massey, J. Albert, N. Collins, R. S. Ellis, C. Heymans, J. P. Gardner, J.-P. Kneib, A. Koekemoer, A. Leauthaud, Y. Mellier, A. Refregier, J. E. Taylor, and L. Van Waerbeke. The Stability of the Point-Spread Function of the Advanced Camera for Surveys on the Hubble Space Telescope and Implications for Weak Gravitational Lensing. *ApJS*, 172:203–218, September 2007. doi: 10.1086/516592.

[96] H.-W. Rix, M. Barden, S. V. W. Beckwith, E. F. Bell, A. Borch, J. A. R. Caldwell, B. Häussler, K. Jahnke, S. Jogee, D. H. McIntosh, K. Meisenheimer, C. Y. Peng, S. F. Sanchez, R. S. Somerville, L. Wisotzki, and C. Wolf. GEMS: Galaxy Evolution from Morphologies and SEDs. *ApJS*, 152:163–173, June 2004. doi: 10.1086/420885.

[97] B. Robertson, N. Yoshida, V. Springel, and L. Hernquist. Disk Galaxy Formation in a Λ Cold Dark Matter Universe. *ApJ*, 606:32–45, May 2004. doi: 10.1086/382871.

[98] N. Roche, K. Ratnatunga, R. E. Griffiths, M. Im, and A. Naim. Galaxy surface brightness and size evolution to Z of about 4. *MNRAS*, 293:157–176, January 1998.

[99] T. E. O. Rosse. Observations on the Nebulae. *Philosophical Transactions Series I*, 140:499–514, 1850.

[100] B. S. Ryden. The Ellipticity of the Disks of Spiral Galaxies. *ApJ*, 601:214–220, January 2004. doi: 10.1086/380437.

[101] M. T. Sargent, C. M. Carollo, S. J. Lilly, C. Scarlata, R. Feldmann, P. Kampczyk, A. M. Koekemoer, N. Scoville, J.-P. Kneib, A. Leauthaud, R. Massey, J. Rhodes, L. A. M. Tasca, P. Capak, H. J. McCracken, C. Porciani, A. Renzini, Y. Taniguchi, D. J. Thompson, and K. Sheth. The Evolution of the Number Density of Large Disk Galaxies in COSMOS. *ApJS*, 172:434–455, September 2007. doi: 10.1086/516584.

[102] M. T. Sargent, C. M. Carollo, S. J. Lilly, P. Oesch, C. Scarlata, T. Bschorr, O. Hahn, P. Kampczyk, R. Feldmann, A. M. Koekemoer, N. Scoville, J.-P. Kneib, A. Leauthaud, R. Massey, J. Rhodes, L. A. M. Tasca, P. Capak, C. Porciani, A. Renzini, Y. Taniguchi, and D. J. Thompson. The bivariate size-luminosity evolution of disk galaxies. *ApJ*, submitted.

[103] C. Scarlata, C. M. Carollo, S. Lilly, M. T. Sargent, R. Feldmann, P. Kampczyk, C. Porciani, A. Koekemoer, N. Scoville, J.-P. Kneib, A. Leauthaud, R. Massey, J. Rhodes, L. Tasca, P. Capak, C. Maier, H. J. McCracken, B. Mobasher, A. Renzini, Y. Taniguchi, D. Thompson, K. Sheth, M. Ajiki, H. Aussel, T. Murayama, D. B. Sanders, S. Sasaki, Y. Shioya, and M. Takahashi. COSMOS Morphological

Classification with the Zurich Estimator of Structural Types (ZEST) and the Evolution Since z = 1 of the Luminosity Function of Early, Disk, and Irregular Galaxies. *ApJS*, 172:406–433, September 2007. doi: 10.1086/516582.

[104] C. Scarlata, C. M. Carollo, S. J. Lilly, R. Feldmann, P. Kampczyk, A. Renzini, A. Cimatti, C. Halliday, E. Daddi, M. T. Sargent, A. Koekemoer, N. Scoville, J.-P. Kneib, A. Leauthaud, R. Massey, J. Rhodes, L. Tasca, P. Capak, H. J. McCracken, B. Mobasher, Y. Taniguchi, D. Thompson, M. Ajiki, H. Aussel, T. Murayama, D. B. Sanders, S. Sasaki, Y. Shioya, and M. Takahashi. The Redshift Evolution of Early-Type Galaxies in COSMOS: Do Massive Early-Type Galaxies Form by Dry Mergers? *ApJS*, 172:494–510, September 2007. doi: 10.1086/517972.

[105] D. Schade, S. J. Lilly, D. Crampton, F. Hammer, O. Le Fevre, and L. Tresse. Canada-France Redshift Survey: Hubble Space Telescope Imaging of High-Redshift Field Galaxies. *ApJL*, 451:L1–L4, September 1995. doi: 10.1086/309677.

[106] D. Schade, R. G. Carlberg, H. K. C. Yee, O. Lopez-Cruz, and E. Ellingson. Evolution of Galactic Disks in Clusters and the Field at $0.1 < z < 0.6$ in the CNOC Survey. *ApJL*, 465:L103–L106, July 1996. doi: 10.1086/310144.

[107] D. Schade, S. J. Lilly, O. Le Fevre, F. Hammer, and D. Crampton. Canada-France Redshift Survey. XI. Morphology of High-Redshift Field Galaxies from High-Resolution Ground-based Imaging. *ApJ*, 464:79–91, June 1996. doi: 10.1086/177301.

[108] P. Schechter. An analytic expression for the luminosity function for galaxies. *ApJ*, 203:297–306, January 1976.

[109] E. Schinnerer, V. Smolčić, C. L. Carilli, M. Bondi, P. Ciliegi, K. Jahnke, N. Z. Scoville, H. Aussel, F. Bertoldi, A. W. Blain, C. D. Impey, A. M. Koekemoer, O. Le Fevre, and C. M. Urry. The VLA-COSMOS Survey. II. Source Catalog of the Large Project. *ApJS*, 172:46–69, September 2007. doi: 10.1086/516587.

[110] M. Schmidt. Space Distribution and Luminosity Functions of Quasi-Stellar Radio Sources. *ApJ*, 151:393–409, February 1968.

[111] C. Scorza and R. Bender. The internal structure of disky elliptical galaxies. *A&A*, 293:20–43, January 1995.

[112] N. Scoville, R. G. Abraham, H. Aussel, J. E. Barnes, A. Benson, A. W. Blain, D. Calzetti, A. Comastri, P. Capak, C. Carilli, J. E. Carlstrom, C. M. Carollo, J. Colbert, E. Daddi, R. S. Ellis, M. Elvis, S. P. Ewald, M. Fall, A. Franceschini, M. Giavalisco, W. Green, R. E. Griffiths, L. Guzzo, G. Hasinger, C. Impey, J.-P. Kneib, J. Koda, A. Koekemoer, O. Lefevre, S. Lilly, C. T. Liu, H. J. McCracken, R. Massey, Y. Mellier, S. Miyazaki, B. Mobasher, J. Mould, C. Norman, A. Refregier, A. Renzini, J. Rhodes, M. Rich, D. B. Sanders, D. Schiminovich, E. Schinnerer, M. Scodeggio, K. Sheth, P. L. Shopbell, Y. Taniguchi, N. D. Tyson, C. M. Urry, L. Van Waerbeke, P. Vettolani, S. D. M. White, and L. Yan. COSMOS: Hubble Space Telescope Observations. *ApJS*, 172:38–45, September 2007. doi: 10.1086/516580.

[113] N. Scoville, H. Aussel, M. Brusa, P. Capak, C. M. Carollo, M. Elvis, M. Giavalisco, L. Guzzo, G. Hasinger, C. Impey, J.-P. Kneib, O. LeFevre, S. J. Lilly, B. Mobasher, A. Renzini, R. M. Rich, D. B. Sanders, E. Schinnerer, D. Schminovich, P. Shopbell, Y. Taniguchi, and N. D. Tyson. The Cosmic Evolution Survey (COSMOS): Overview. *ApJS*, 172:1–8, September 2007. doi: 10.1086/516585.

[114] J. L. Sérsic. *Atlas de galaxias australes*. Cordoba, Argentina: Observatorio Astronomico, 1968.

[115] K. Sheth, M. W. Regan, N. Z. Scoville, and L. E. Strubbe. Barred Galaxies at $z > 0.7$: NICMOS Hubble Deep Field-North Observations. *ApJL*, 592:L13–L16, July 2003. doi: 10.1086/377329.

[116] J. Silk. Cosmic Black-Body Radiation and Galaxy Formation. *ApJ*, 151:459–+, February 1968.

[117] L. Simard, D. C. Koo, S. M. Faber, V. L. Sarajedini, N. P. Vogt, A. C. Phillips, K. Gebhardt, G. D. Illingworth, and K. L. Wu. The Magnitude-Size Relation of Galaxies out to z˜1. *ApJ*, 519:563–579, July 1999. doi: 10.1086/307403.

[118] L. Simard, C. N. A. Willmer, N. P. Vogt, V. L. Sarajedini, A. C. Phillips, B. J. Weiner, D. C. Koo, M. Im, G. D. Illingworth, and S. M. Faber. The DEEP Groth Strip Survey. II. Hubble Space Telescope Structural Parameters of Galaxies in the Groth Strip. *ApJS*, 142:1–33, September 2002. doi: 10.1086/341399.

[119] G. F. Smoot, C. L. Bennett, A. Kogut, E. L. Wright, J. Aymon, N. W. Boggess, E. S. Cheng, G. de Amici, S. Gulkis, M. G. Hauser, G. Hinshaw, P. D. Jackson, M. Janssen, E. Kaita, T. Kelsall, P. Keegstra, C. Lineweaver, K. Loewenstein, P. Lubin, J. Mather, S. S. Meyer, S. H. Moseley, T. Murdock, L. Rokke, R. F. Silverberg, L. Tenorio, R. Weiss, and D. T. Wilkinson. Structure in the COBE differential microwave radiometer first-year maps. *ApJL*, 396:L1–L5, September 1992. doi: 10.1086/186504.

[120] J. Sommer-Larsen, M. Götz, and L. Portinari. Galaxy Formation: Cold Dark Matter, Feedback, and the Hubble Sequence. *ApJ*, 596:47–66, October 2003. doi: 10.1086/377685.

[121] D. N. Spergel, L. Verde, H. V. Peiris, E. Komatsu, M. R. Nolta, C. L. Bennett, M. Halpern, G. Hinshaw, N. Jarosik, A. Kogut, M. Limon, S. S. Meyer, L. Page, G. S. Tucker, J. L. Weiland, E. Wollack, and E. L. Wright. First-Year Wilkinson Microwave Anisotropy Probe (WMAP) Observations: Determination of Cosmological Parameters. *ApJS*, 148:175–194, September 2003. doi: 10.1086/377226.

[122] M. Steinmetz and J. F. Navarro. The hierarchical origin of galaxy morphologies. *New Astronomy*, 7:155–160, June 2002. doi: 10.1016/S1384-1076(02)00102-1.

[123] M. A. Strauss, D. H. Weinberg, R. H. Lupton, V. K. Narayanan, J. Annis, M. Bernardi, M. Blanton, S. Burles, A. J. Connolly, J. Dalcanton, M. Doi, D. Eisenstein, J. A. Frieman, M. Fukugita, J. E. Gunn, Ž. Ivezić, S. Kent, R. S. J. Kim, G. R.

Knapp, R. G. Kron, J. A. Munn, H. J. Newberg, R. C. Nichol, S. Okamura, T. R. Quinn, M. W. Richmond, D. J. Schlegel, K. Shimasaku, M. SubbaRao, A. S. Szalay, D. Vanden Berk, M. S. Vogeley, B. Yanny, N. Yasuda, D. G. York, and I. Zehavi. Spectroscopic Target Selection in the Sloan Digital Sky Survey: The Main Galaxy Sample. *AJ*, 124:1810–1824, September 2002. doi: 10.1086/342343.

[124] E. Swedenborg. *Opera Philosophica et Mineralia (Principia, Vol. I)*. Dresden, 1734.

[125] Y. Taniguchi, N. Scoville, T. Murayama, D. B. Sanders, B. Mobasher, H. Aussel, P. Capak, M. Ajiki, S. Miyazaki, Y. Komiyama, Y. Shioya, T. Nagao, S. S. Sasaki, J. Koda, C. Carilli, M. Giavalisco, L. Guzzo, G. Hasinger, C. Impey, O. LeFevre, S. Lilly, A. Renzini, M. Rich, E. Schinnerer, P. Shopbell, N. Kaifu, H. Karoji, N. Arimoto, S. Okamura, and K. Ohta. The Cosmic Evolution Survey (COSMOS): Subaru Observations of the HST Cosmos Field. *ApJS*, 172:9–28, September 2007. doi: 10.1086/516596.

[126] A. Toomre. Mergers and Some Consequences. In B. M. Tinsley and R. B. Larson, editors, *Evolution of Galaxies and Stellar Populations*, pages 401–+, 1977.

[127] I. Trujillo and J. A. L. Aguerri. Quantitative morphological analysis of the Hubble Deep Field North and Hubble Deep Field South - I. Early- and late-type luminosity-size relations of galaxies out to z˜ 1. *MNRAS*, 355:82–96, November 2004. doi: 10.1111/j.1365-2966.2004.08292.x.

[128] I. Trujillo and M. Pohlen. Stellar Disk Truncations at High z: Probing Inside-Out Galaxy Formation. *ApJL*, 630:L17–L20, September 2005. doi: 10.1086/491472.

[129] I. Trujillo, N. M. Förster Schreiber, G. Rudnick, M. Barden, M. Franx, H.-W. Rix, J. A. R. Caldwell, D. H. McIntosh, S. Toft, B. Häussler, A. Zirm, P. G. van Dokkum, I. Labbé, A. Moorwood, H. Röttgering, A. van der Wel, P. van der Werf, and L. van Starkenburg. The Size Evolution of Galaxies since z∼3: Combining SDSS, GEMS, and FIRES. *ApJ*, 650:18–41, October 2006. doi: 10.1086/506464.

[130] T. S. van Albada. Dissipationless galaxy formation and the R to the 1/4-power law. *MNRAS*, 201:939–955, December 1982.

[131] C. F. von Weizsäcker. The Evolution of Galaxies and Stars. *ApJ*, 114:165–186, September 1951.

[132] S. D. M. White. Angular momentum growth in protogalaxies. *ApJ*, 286:38–41, November 1984. doi: 10.1086/162573.

[133] S. D. M. White and C. S. Frenk. Galaxy formation through hierarchical clustering. *ApJ*, 379:52–79, September 1991. doi: 10.1086/170483.

[134] R. E. Williams, B. Blacker, M. Dickinson, W. V. D. Dixon, H. C. Ferguson, A. S. Fruchter, M. Giavalisco, R. L. Gilliland, I. Heyer, R. Katsanis, Z. Levay, R. A. Lucas, D. B. McElroy, L. Petro, M. Postman, H.-M. Adorf, and R. Hook. The Hubble Deep Field: Observations, Data Reduction, and Galaxy Photometry. *AJ*, 112:1335–+, October 1996. doi: 10.1086/118105.

[135] R. E. Williams, S. Baum, L. E. Bergeron, N. Bernstein, B. S. Blacker, B. J. Boyle, T. M. Brown, C. M. Carollo, S. Casertano, R. Covarrubias, D. F. de Mello, M. E. Dickinson, B. R. Espey, H. C. Ferguson, A. Fruchter, J. P. Gardner, A. Gonnella, J. Hayes, P. C. Hewett, I. Heyer, R. Hook, M. Irwin, D. Jones, M. E. Kaiser, Z. Levay, A. Lubenow, R. A. Lucas, J. Mack, J. W. MacKenty, P. Madau, R. B. Makidon, C. L. Martin, L. Mazzuca, M. Mutchler, R. P. Norris, B. Perriello, M. M. Phillips, M. Postman, P. Royle, K. Sahu, S. Savaglio, A. Sherwin, T. E. Smith, M. Stiavelli, N. B. Suntzeff, H. I. Teplitz, R. P. van der Marel, A. R. Walker, R. J. Weymann, M. S. Wiggs, G. M. Williger, J. Wilson, N. Zacharias, and D. R. Zurek. The Hubble Deep Field South: Formulation of the Observing Campaign. *AJ*, 120:2735–2746, December 2000. doi: 10.1086/316854.

[136] C. N. A. Willmer, S. M. Faber, D. C. Koo, B. J. Weiner, J. A. Newman, A. L. Coil, A. J. Connolly, C. Conroy, M. C. Cooper, M. Davis, D. P. Finkbeiner, B. F. Gerke, P. Guhathakurta, J. Harker, N. Kaiser, S. Kassin, N. P. Konidaris, L. Lin, G. Luppino, D. S. Madgwick, K. G. Noeske, A. C. Phillips, and R. Yan. The Deep Evolutionary Exploratory Probe 2 Galaxy Redshift Survey: The Galaxy Luminosity Function to $z \sim 1$. *ApJ*, 647:853–873, August 2006. doi: 10.1086/505455.

[137] T. Wright. *An Original Theory or New Hypothesis of the Universe Founded Upon the Laws of Nature, and Solving by Mathematical Principles the General Phaenomena of the Visible Creation; and Particularly the Via Lactea.* London, 1750.

Publications

The Role of Environment in the Redshift Evolution of Disk Galaxies in COSMOS: Surface Brightness, Sizes & Star Formation Histories.
M. T. Sargent, C. M. Carollo, S. J. Lilly, C. Scarlata, T. Bschorr, O. Hahn, P. Kampczyk, A. M. Koekemoer, N. Scoville, J.-P. Kneib, A. Leauthaud, R. Massey, P. Oesch, J. Rhodes, L. A. M. Tasca, P. Capak, H. J. McCracken, C. Porciani, A. Renzini, Y. Taniguchi, D. J. Thompson, and K. Sheth.
ApJ, submitted. [102]

The Evolution of the Number Density of Large Disk Galaxies in COSMOS.
M. T. Sargent, C. M. Carollo, S. J. Lilly, C. Scarlata, R. Feldmann, P. Kampczyk, A. M. Koekemoer, N. Scoville, J.-P. Kneib, A. Leauthaud, R. Massey, J. Rhodes, L. A. M. Tasca, P. Capak, H. J. McCracken, C. Porciani, A. Renzini, Y. Taniguchi, D. J. Thompson, and K. Sheth.
ApJS, 172:434-455, September 2007. [101]

COSMOS Morphological Classification with the Zurich Estimator of Structural Types (ZEST) and the Evolution Since z = 1 of the Luminosity Function of Early, Disk, and Irregular Galaxies.
C. Scarlata, C. M. Carollo, S. Lilly, M. T. Sargent, R. Feldmann, P. Kampczyk, C. Porciani, A. Koekemoer, N. Scoville, J.-P. Kneib, A. Leauthaud, R. Massey, J. Rhodes, L. Tasca, P. Capak, C. Maier, H. J. McCracken, B. Mobasher, A. Renzini, Y. Taniguchi, D. Thompson, K. Sheth, M. Ajiki, H. Aussel, T. Murayama, D. B. Sanders, S. Sasaki, Y. Shioya, and M. Takahashi.
ApJS, 172:406-433, September 2007. [103]

The Redshift Evolution of Early-Type Galaxies in COSMOS: Do Massive Early-Type Galaxies Form by Dry Mergers?
C. Scarlata, C. M. Carollo, S. J. Lilly, R. Feldmann, P. Kampczyk, A. Renzini, A. Cimatti,

C. Halliday, E. Daddi, M. T. Sargent, A. Koekemoer, N. Scoville, J.-P. Kneib, A. Leauthaud, R. Massey, J. Rhodes, L. Tasca, P. Capak, H. J. McCracken, B. Mobasher, Y. Taniguchi, D. Thompson, M. Ajiki, H. Aussel, T. Murayama, D. B. Sanders, S. Sasaki, Y. Shioya, and M. Takahashi.
ApJS, 172:494510, September 2007. [104]

Simulating the Cosmos: The Fraction of Merging Galaxies at High Redshift.
P. Kampczyk, S. J. Lilly, C. M. Carollo, C. Scarlata, R. Feldmann, A. Koekemoer, A. Leauthaud, M. T. Sargent Y. Taniguchi, and P. Capak.
ApJS, 172:329-340, September 2007. [62]

Curriculum vitæ

Contact information

Departement Physik	*Phone*:	+41 (0)44 633 29 38
Institut für Astronomie	*Fax*:	+41 (0)44 633 12 38
ETH Zürich, HPT D18	*E-mail*:	markmr@phys.ethz.ch
Wolfgang-Pauli-Str. 16	*Web*:	`www.exp-astro.phys.ethz.ch/sargent`
CH-8093 Zürich		
Schweiz/Switzerland		

Personal information

Date of Birth:	September 17th, 1979
Place of Birth:	Kilchberg ZH, Switzerland
Citizenship:	Swiss & Canadian
Marital Status:	Single
Mother Tongues:	German, English
Other Languages:	fluency and good written knowledge of French and Italian, conversational Irish-Gaelic, basic Russian, Latin (reading)

Education

Ph.D. candidate, ETH Zürich 2004-2007
Title: The Evolution of Disk Galaxies in the COSMOS-Survey
Advisor: Prof. Dr. C.M. Carollo

ETH diploma in physics (equivalent to M.Sc.), ETH Zürich *Title*: Dynamics of the Eurasian plate *Advisor*: Prof. Dr. S. Goes	1999-2004
Eidgenössische Matur Typus B (classical languages), Kantonsschule Stadelhofen, Zürich, Switzerland	1994-1999

Research interests

Galaxy evolution at high and low redshift, disk galaxies, galaxy morphology, internal dynamical evolution and internal structure of galaxies, stellar populations, interstellar medium

Research experience

Ph.D. student, Institute of Astronomy, ETH Zürich	2004-2007
Scientific employee of the Institute of Geophysics (Geodynamics group), ETH Zürich	2004

Teaching experience

Various duties including organising and composing exercises, and delivering lessons as teaching assistant for the following courses:

Introductory Physics for environmental sciences students	2004/2005
Fundamentals of Electromagnetism for physics students	2005
Introductory Quantum Mechanics for physics students	2006
Fundamentals of Astrophysics for physics students	2006
Introductory Physics for material sciences students	2007
Fundamentals of Astrophysics for physics students	2007

Public outreach

'*Night of Physics*': Involvement in organizing an open house celebrating the 150th anniversary of the ETH Zürich and the '*World Year of Physics*'	Summer 2005

'*Physics for Kids & Teens*': Introducing primary school children to astronomy during the festivities for the '*World Year of Physics*' at the ETH Zürich	Spring 2005
Part time employee of the Planetarium Zürich	1999-2001

Military service

Basic military service (training as radio operator) in Fribourg, Switzerland	1999
Yearly repetition courses	since 2000

Computer skills

Operating systems:	Mac, Unix/Linux, Sun/Solaris and MS Windows
Languages:	Perl & PDL, shell-programming (bash & csh), `iraf`, LaTeX & HTML. Basic C++, Fortran77 & IDL
Numerical & plotting packages:	SuperMongo, PGPLOT, Mathematica, Matlab & Gnuplot

Hobbies/other interests

Sports, woodworking, history & philosophy of science, hiking, playing the piano, languages & reading